An Elementary Error Model for Terrestrial Laser Scanning

A thesis accepted by the Faculty of Aerospace Engineering and Geodesy
of the University of Stuttgart in fulfillment of the requirements
for the degree of Doctor of Engineering Sciences (Dr.-Ing.)

by

Gabriel A. Kerekes

born in Arad, Romania

Main referee:	Prof. Dr.-Ing. habil. Dr. h.c. Volker Schwieger
Co-referee:	Prof. Dr.-Ing. Hans-Berndt Neuner
Co-referee:	Prof. Dr. Corinna Harmening
Day of the exam:	12.12.2022

Institute of Engineering Geodesy
University of Stuttgart
2023

Table of contents

Abstract

Terrestrial Laser Scanning (TLS) is a recent method in engineering geodesy area-wise deformation analysis. After a TLS scan, the result for each epoch is a point cloud that describes the object's geometry. For each point cloud, the stochastic properties are important for a reliable decision concerning the current object geometry. Generally, the stochastic properties are described by a stochastic model. Currently, stochastic models for TLS observations are highly disputed and incomplete. A realistic stochastic model is necessary for typical applications like structural deformation analysis for buildings and civil engineering constructions.

This work presents a method to define a stochastic model in form of a synthetic variance-covariance matrix (SVCM) for TLS observations. It relies on the elementary error theory defined by Bessel and Hagen at the beginning of the 19th century and adapted for geodetic observations by Pelzer and Schwieger at the end of the 20th century. According to this theory, different types of errors that affect TLS measurements are classified into three groups: non-correlating, functional correlating, and stochastic correlating errors.

For each group, different types of errors are studied based on the error sources that affect TLS observations. These types are classified as instrument-specific errors, environment-related errors, and object surface-related errors. Regarding instrument errors, calibration models for high-end laser scanners are studied. For the propagation medium of TLS observations, the effects of air temperature, air pressure and vertical temperature gradient on TLS distances and vertical angles are studied. An approach based on time series theory is used for extracting the spatial correlations between observation lines. For the object's surface properties, the effect of surface roughness and reflectivity on the distance measurement is considered. Both parameters affect the variances and covariances in the stochastic model. For each of the error types, examples based on own research or literature are given.

After establishing the model, four different study cases are used to exemplify the utility of a fully populated SVCM. The scenarios include real objects measured under laboratory and field conditions and simulated objects. The first example outlines the results from the SVCM based on a simulated wall with an analysis of the variance and covariance contribution. In the second study case, the role of the SVCM in a sphere adjustment is highlighted. A third study case presents a deformation analysis of a wooden tower. Finally, the fourth example shows how to derive an optimal TLS station point based on the SVCM trace.

All in all, this thesis brings a contribution by defining a new stochastic model based on the elementary error theory in the form a SVCM for TLS measurements. It may be used for purposes such as analysis of error magnitude on scanned objects, adjustment of surfaces, or finding an optimal TLS station point position with regard to predefined criteria.

Zusammenfassung

Terrestrisches Laserscanning (TLS) ist eine in der Ingenieurgeodäsie für die Deformationsanalyse angewandte Messmethode. Nach einem Scanvorgang erhält man pro Epoche eine Punktwolke, die die Objektgeometrie beschreibt. Die stochastischen Eigenschaften der Punktwolke sind wichtig für eine zuverlässige Aussage über den Objektzustand. Allgemein sind diese Eigenschaften durch das stochastische Modell definiert. Aktuell sind stochastische Modelle für TLS Messungen ein forschungsrelevantes Thema. Ein realistisches stochastisches Modell ist für Anwendungen von TLS Messvorgängen beim Monitoring wie z.B. Bauwerküberwachung notwendig.

Diese Arbeit stellt eine Methode zur Erstellung eines stochastischen Modells in Form einer synthetischen Varianz-Kovarianz-Matrix (SVKM) für TLS Beobachtungen vor. Sie basiert auf der am Anfang des 19. Jahrhunderts von Bessel und Hagen definierten Elementarfehlertheorie. Am Ende des 20. Jahrhunderts wurde die Theorie von Pelzer und Schwieger für geodätische Beobachtungen adaptiert. Basierend auf dem Elementarfehlermodel werden die verschiedenen Arten von Fehlern, die auf TLS Messungen einen Einfluss haben, in drei Gruppen eingeteilt: nicht korrelierende, funktional korrelierende und stochastisch korrelierende Fehler.

Für jede Gruppe werden TLS Fehlerquellen in unterschiedliche Fehlerarten eingeteilt. Diese Arten werden als instrumentenspezifische Fehler, umgebungsbezogene (atmosphärische) Fehler und objektoberflächenbezogene Fehler klassifiziert. In Bezug auf die Instrumentenfehler werden Kalibrierungsmodelle für High-End-Laserscanner untersucht. Für die atmosphärischen Elementarfehler werden die Auswirkungen von Lufttemperatur, Luftdruck und vertikalem Temperaturgradienten auf TLS Distanzen und Zenitwinkel untersucht. Ein Ansatz zusammen mit Elementen aus der Zeitreihentheorie wird verwendet, um die räumlichen Korrelationen zwischen Beobachtungslinien zu ermitteln. Bei den Oberflächeneigenschaften des Objekts wird der Einfluss von Oberflächenrauigkeit und Reflektivität auf die Entfernungsmessung berücksichtigt. Beide Parameter beeinflussen die Varianzen und Kovarianzen im hier definierten stochastischen Modell. Für jede Fehlerart werden Beispiele anhand eigener Recherchen oder Literatur gegeben.

Nach Erstellung der SVKM werden vier verschiedene Beispiele verwendet, um die Anwendbarkeit einer vollbesetzten Matrix zu veranschaulichen. Die Szenarien beinhalten sowohl reale Objekte, die unter Labor- und Feldbedingungen gemessen wurden als auch simulierte Objekte. Die Ergebnisse der ersten Studie stellen die zu erwarteten Varianzen und Kovarianzen und deren Anteile auf einer simulierten Wand. Eine zweite Anwendung stellt die Rolle der SVCM in einer Kugelausgleichung dar. Die dritte Studie zeigt eine Deformationsanalyse eines Holzturms. Bei der letzten Anwendung wird ein optimaler TLS Standpunkt basierend auf der SVCM Spur ermittelt.

Zusammenfassend, liefert diese Arbeit einen Beitrag durch die Definition eines neuen stochastischen Modells auf Basis des Elementarfehlermodels in Form eines SVCM für TLS-Messungen. Es kann für die Analyse der Punktfehler an gescannten Objekten, Ausgleichung von geometrische Primitiven bzw. Freiformflächen und das Finden einer optimalen TLS Standpunktposition nach vordefinierten Kriterien verwendet werden.

1. Introduction

1.1 Motivation

One of the main scopes in engineering geodesy is deformation and displacement monitoring of structures such as buildings, bridges, towers, dams, tunnels, or other infrastructure (cf. Staiger, 2003; Uren and Price, 2010; Kuhlmann et al., 2014; Wunderlich et al., 2016). In all measurement methods, geodetic sensors are used to acquire data continuously or within different epochs with the purpose of comparing the current object state with past states (cf. Wieser et al., 2018). The temporal discretization depends on the monitored object and expected deformations. Regarding the spatial discretization of measured positions on the monitored object, point-wise approaches are still dominant (Scaioni et al., 2018; Wieser et al., 2018). Well-established geodetic sensors and methods like GNSS, total station, optical plumbing, leveling, etc. are used for decades in point-wise monitoring (cf. Welsch and Heunecke, 2001). Although highly reliable, point-wise acquisition methods have their limitations for objects with complex shapes like curved façades, high-rise buildings, or arch dams. In these cases, area-wise deformation analysis extends the application spectrum by measuring wide areas of the observed object (cf. Harmening and Neuner, 2016; Wunjaz, 2016; Kuhlmann and Holst, 2018). The current thesis contributes to a subclass of these methods, namely Terrestrial Laser Scanning (TLS) for monitoring by defining a stochastic model for TLS.

For the point-wise methods mentioned above, the uncertainty budget, also known as the stochastic model, is well studied and broadly accepted (Ogundare, 2016). The situation is different for area-wise methods (e.g. TLS applications). Up to now, it is still unsatisfactory (cf. Neuner et al., 2016; Kuhlmann and Holst, 2018). Generally, a stochastic model is a mathematical model that describes real-life phenomena that are characterized by the presence of uncertainty (Borovkov, 2014). Measurements together with their uncertainty are important for decision-making. Decisions have consequences that range from a mere inconvenience to loss of life, including economic loss or profit. For this reason, measurement uncertainty ought to be considered whenever a measurement result is used to inform decisions and actions (Possolo & Iyer, 2017). The main challenge is to have as much knowledge as possible about the process influencing factors. Having this, the stochastic model is representative for the uncertainty and the results of that measurement can be considered realistic. There are many ways of defining a stochastic model, but for direct and indirect measurements (cf. Niemeier, 2008), it can be expressed by a variance-covariance matrix (VCM) (cf. Matthias, 1992) based on the assumption of normal probability distributions. This matrix is also named uncertainty matrix or covariance matrix in other sources, but this thesis uses the VCM denotation as a convention. Depending on the matrix structure (e.g. diagonal, fully populated) the uncertainty of the measured physical phenomena is either well or poorly represented. If the existing physical correlations between all observations are unknown, the VCM is reduced to a diagonal matrix poorly resembling the complex nature of all the interactions. If the observations are truly independent, and therefore no correlations exist, the diagonal VCM is the correct choice. In any case, using an inappropriate VCM may lead to wrong decisions in the TLS deformation analysis (Zhao et al., 2019) or failure to issue timely alerts (Teunissen et al., 2020).

Trying to overcome this issue, the current work defines the stochastic model in form of a VCM based on the Elementary Error Theory. This theory is applied to TLS observations with the goal of creating an overarching TLS stochastic model. It includes elementary errors for three

types of errors based on their correlating effects. These are non-correlating, functional correlating, and stochastic correlating errors. Furthermore, they are grouped into instrument-specific errors (laser scanner), environment-specific errors (observation propagation medium) and object surface-specific errors. The classification is made based on multidisciplinary research from scientific fields like metrology, mechanics, statistics, optical physics, microclimatology, material science, civil engineering, etc. Empirical findings of the author or findings from literature, technical specifications, and assumptions are used to define the so-called synthetic variance-covariance matrix (SVCM). After the definition, examples of applications are given, and the model is presented for simulated data in different scenarios and real-world measurements.

1.2 Literature review related to TLS stochastic models and own contributions

This section offers a short review of currently available stochastic models in TLS applications, restricting the applications to static laser scanning related to monitoring. Neuner et al. (2016) offer a comprehensive overview of the available point cloud modeling methods used in engineering geodesy together with their stochastic models. Although there are multiple methods of describing uncertainty propagation in measurements (see sec. 2.1), the uncertainty budget in static TLS is not yet an established subject (Neuner et al., 2016). The main reason is the complexity of factors that contribute to TLS uncertainty. Three categories of influencing factors can be distinguished and generally accepted by the scientific community (cf. Wunderlich et al., 2016): the instrument, the propagation environment, and object surface properties. A strict isolation is hardly possible, but efforts are made to study the effects of each category, e.g. instrument errors (cf. Muralikrishnan, 2021), environment (cf. Friedli, 2020; Kerekes & Schwieger, 2020) or surface properties (cf. Chaudhry, 2021). The most commonly used methods in TLS are based on the variance-covariance propagation law, Monte Carlo Method, or empirically defined models. The first two are additionally explained in chapter 2. Some examples that use these methods for TLS applications are mentioned here.

A few of the many studies that apply the variance-covariance propagation law for TLS applications are the ones from Lipkowski and Mettenleiter (2019), Hartzell et al. (2015), or Lichti (2007). The variance-covariance propagation law is also the underlying base of the TLS elementary error model (cf. Kauker and Schwieger, 2017; Kerekes and Schwieger, 2020 and 2021) developed in this contribution. As seen later in this thesis, this approach also considers correlations, although correlations may also be considered in empirical-based models (cf. Chen et al. 2015, Schmitz et al. 2021).

Another approach for uncertainty modeling is by using Monte Carlo simulations. Although generating large data samples may be problematic for point clouds because of the high number of points, this method was used, among others, in laser scanning applications by Koch (2008), Alkhatib et al. (2009), Aichinger and Schwieger (2018), Zhao (2019) and Heinz et al. (2020).

An empirical approach has been recently introduced by Wujanz et al. (2017) in TLS applications. It uses the radiometric information of scanned surfaces for describing the measurement uncertainty of TLS ranges. Based on the intensity of the reflected laser beams, the respective range measurement is attributed a level of uncertainty according to predefined exponential functions valid for the scanner in case. Although simple and powerful, intensity-based models neglect instrumental systematic errors and do not consider existing correlations in the point cloud. A similar measurement-driven approach is defined by Mukupa et al. (2017)

in which the focus is likewise set on intensities. The idea of concentrating on radiometric information to describe uncertainty (Habib, 2009) is well spread in other LiDAR applications (e.g. airborne) and may be justified by the radar equation, which jointly models some of the uncertainty sources.

Regarding the current thesis, several publications on the topic (Kauker and Schwieger 2015, Kauker and Schwieger, 2017; Kerekes and Schwieger 2020, Kauker and Schwieger, 2021) have contributed to the theoretical basis and have given impulses for new research directions. Continuing this line of work, the following topics have been improved, researched in more depth, or completely changed. A different and newer functional model has been adopted for laser scanners of panoramic type and a model for scanners with hybrid architecture has been introduced. The atmospheric parameters are treated as elementary errors and are now included in the stochastic correlating group. Previously, they were treated as functional correlating, but this was sufficient only due to the experiments in laboratory conditions. Additionally, a measurement-based approach combined with microclimate information is used to find values for the variances and covariances of the atmospheric parameters. The influence is not only considered for distances but also for angles. Regarding the next type of errors, a completely different approach is developed for the object surface properties. The impact of this error group is asserted using the physical properties of scanned surfaces and technical TLS specifications. Finally, all error types are quantified in the fully populated SVCM. Although the focus of this work is on defining the stochastic model in form of a SVCM, its validity, and potential have been exemplified in several applications that are shortly presented next.

1.3 Applications in engineering geodesy

This work presents only a few applications from current engineering geodesy tasks using the SVCM as a stochastic model. Examples are given on real and simulated objects with different sizes, ranging from a few decimeters to a few hundred meters. For the few decimeter level, a sphere adjustment is performed; for the few meter level, a 14-meter experimental wooden tower is used and finally for the few hundred-meter level, a concrete arch dam that expands over 400 m is used. Point clouds are acquired in all cases with high-end laser scanners, a fact that can be seen in other publications on area-wise monitoring (cf. Holst et al., 2017; Mukupa et al., 2016; Scaioni, 2018; Wujanz, 2016). The SVCM presented in this thesis has been conducted for examples with a reduced number of points in the TLS point cloud. Although the validity of the methodology remains undisturbed, technical processing restrictions that are valid at the time of writing, constrain the matrix sizes to 150000 x 150000 in Matlab (Mathworks©) depending mostly on the RAM memory of the system. This may be a small number for point clouds, but it is always a matter of choosing sufficient points representative for the object geometry. There are possible solutions to extend the capabilities, but the focus was not set on this aspect, and may be improved if necessary.

The first application presents features of a SVCM for a simulated object. The object resembles commonly met geometric primitives in TLS, like planes of a façade. The analysis serves as a basis for judging the expected errors of position of object points for different scan configurations. Additionally, the resulting spatial correlations are analyzed.

A second application shows the importance of correlations in sphere estimation. A Gauss-Helmert adjustment is performed with the SVCM as the stochastic model. Outcomes point out the benefits of considering correlations.

In the third example, a deformation analysis based on estimated surfaces is conducted with point clouds acquired in two epochs separated by approximately one year. Among the most interesting outcomes, is the fact that existing deformations cannot be detected and classified as statistically significant without the appropriate SVCM. This highlights the importance of the fully populated SVCM in a deformation analysis.

The last application shows the utility of the SVCM in planning purposes and estimating a priori variances of a point cloud. Similar to simulations of geodetic networks, different locations for TLS station points in relation to the monitored object are simulated and give information about the magnitude of variances (covariances if required) at each position. This offers the user indication about the optimal scan position, given that the geometry of the monitored object and surrounding topography is roughly known.

1.4 Structure of the thesis

Continuing the introduction, chapter two offers a brief overview of uncertainty propagation and then lays the theoretical background necessary for constructing the SVCM. The elementary error theory is presented starting with a short historical overview and continuing with the introduction of groups of elementary errors. At the end of the chapter, the different types of errors that affect TLS measurements are classified into the above-mentioned groups. In the following three chapters, the mentioned types of errors are extensively treated. Chapter 3 is about instrument-specific errors and treats laser scanners from a mechanical/optical point of view with a focus on two scanner architectures. In chapter 4, the errors caused by the propagation medium of TLS observations are treated. The effect of some of the most common atmospheric parameters is studied on TLS distances and vertical angles. An approach based on time series theory is used for computing the correlations between observation lines. Next, chapter 5 studies the effect of two main object surface properties on distance measurements. They result in both variances and covariances of the TLS distances. Each of the abovementioned three chapters can be read independently or in the desired order, although the author's recommendation is to read them consecutively because this reflects the development order. Chapter 6 gives examples of the defined SVCM based on simulated and real data. The results of simulations and field measurements are presented and discussed according to the same criteria used to judge the quality of geodetic network adjustments (e.g. variance and volume criteria). Finally, chapter 7 ends this contribution with conclusions and gives an outlook.

2. Synthetic covariance matrix for TLS point clouds

2.1 About uncertainty propagation

According to the International Vocabulary of Metrology (VIM) a measurement is the process of obtaining one or more quantity values that can reasonably be attributed to a quantity. The quantity intended to be measured is called measurand (International Organization of Legal Metrology, 2007). The true value of the measurand is the value of the quantity, which, if known, would ideally reflect, both qualitatively and quantitatively, the corresponding property of the object according to the purpose of the measurement (Rabinovich, 2018). Any measurement, independent of its scope, is performed with measurement instruments. Instruments are imperfect and every measurement is an experimental procedure, characterized by uncertainty. The term uncertainty, may be misinterpreted (Possolo and Iyer, 2017) or used with different meanings according to the science branch. In an attempt to overcome this issue, the Joint Committee for Guides in Metrology (JCGM) emitted the Guide to the Expression of Uncertainty in Measurement (GUM) for the first time in 1995. An updated version dates from 2008 (Joint Committee for Guides in Metrology, 2008). The much disputed GUM provides a universal way of describing uncertainty in measurements conducted with scientific activities, industrial activities, calibration, testing and inspection laboratories, or evaluation and accreditation bodies. The overall scope is to express the result of a measurement as the best estimate of the measurand, along with the associated measurement uncertainty.

There are several possibilities for describing measurement uncertainty. Possolo and Iyer (2017) provide a recent review of concepts, models, methods, and computations commonly used for measurement uncertainty evaluations. In the current work, only a brief presentation is given for the two most commonly used methods in geodetic measurements: the variance-covariance propagation law (sometimes called Gauss's law) and Monte Carlo method. Other methods based on empirical measurements may also be considered for TLS (cf. Wujanz et al., 2017, Chen et al., 2015) or methods based on Bayesian statistics (cf. Koch, 1990), but it is out of scope to present all of them in this work. In any case, a probabilistic representation of measurement uncertainty is used and results are evaluated in a model-based manner. For more in-depth knowledge related to probability and statistics, handbooks like Freedman et al. (2007) and DeGroot and Schervish (2011) or specific for geodesy, Niemeier (2008) and Pelzer (1985) are recommended.

The variance-covariance propagation law can be considered the oldest method among all others. In his work, C. F. Gauß presented a method of describing how the uncertainties in independent input variables of a differentiable function *f* propagate on the output results of the same function (Gauß, 1823). This method is incorporated in the GUM and is widely used in many technical applications. The influence of an input variable x_i $(i = 1..z)$ on the final product y can be estimated with total differential calculus (cf. Niemeier, 2008). For example, the influence of each input variable x_i on a function $y = f(x_1, x_2, \dots, x_z)$ is directly given by the first-order partial derivative $\partial f / \partial x_i$, also called sensitivity coefficients. The quality of the estimation depends on how close to linear the function f is in the neighborhood of $(x_1, x_2, \dots, x_z)$. This neighborhood is often defined by the intervals covered by the standard uncertainties of each input variable (Lafarge and Possolo, 2015). The measurement equation encompassed by *f*, expresses the measurand as a function of a finite set of input variables for

which estimates and uncertainty evaluations are available. It assumes that all input and output values are quantitative and that the partial derivatives of *f* with respect to its arguments exist. The measurement equation usually describes a physical law or relation known to hold true for the values of inputs and the true value of the output (Possolo and Iyer, 2017). If the process may be expressed by a differentiable function and the random variables are independent (uncorrelated), then the variance of the result is estimated by:

$$\sigma_y^2 = \left(\frac{\partial f}{\partial x_1}\right) \cdot \sigma_{x1}^2 + \left(\frac{\partial f}{\partial x_2}\right)^2 \cdot \sigma_{x2}^2 + \cdots + \left(\frac{\partial f}{\partial x_z}\right)^2 \cdot \sigma_{xz}^2. \tag{2.1}$$

The equivalent expression of eq. 2.1 written in matrix form is $\boldsymbol{\Sigma_{yy}} = \boldsymbol{A} \cdot \boldsymbol{\Sigma_{xx}} \cdot \boldsymbol{A^T}$, where the matrix $\boldsymbol{\Sigma_{yy}}$ represents the VCM for functions *f* which may have several outputs; the matrix $\boldsymbol{\Sigma_{xx}}$ contains the variances (and possibly covariances) of input variables x_i, and the matrix $\boldsymbol{A}$ contains the partial derivatives $\partial f / \partial x_i$. This form of the variance-covariance propagation law has been presented because it is frequently used in the current work.

It can be seen, that this approach assumes linear or linearized models. If the relation between the function variables is non-linear (which is the case in most geodetic observations, cf. chapters 3, 4 and 5 for TLS observations) and/or the variances of the input variables are large, then the variance-covariance propagation law may offer false estimates. Another important underlying assumption made for the input variables is that they are normally distributed. An exception applies if the number of input variables is very large (e.g. theoretically ∞), case in which they do not need to fulfill this condition according to the central limit theorem. In any case, the outcomes of the variance propagation law are normally distributed and the statistical parameters are completely described by their expected value and standard deviation (Caspary and Wichmann, 2007). This is also the underlying assumption in this thesis (cf. sec. 2.3).

There are situations in which obtaining partial derivatives for the assumed model is difficult or impossible. This is admittedly recognized in the GUM by mentioning that the relation between measurand and input quantities may be complicated, may not be written down explicitly, may be determined experimentally, or exists only as an algorithm that must be evaluated numerically (Possolo & Elster, 2014). For some of these cases, the alternative is to use the so-called Monte Carlo Method (Metropolis and Ulam, 1949). In Monte Carlo simulations, for each random variable, m_c samples are generated based on known or assumed statistical distributions of the input variables. Alternatively, samples from measurements may likewise be available without the need of knowing their statistical properties. Regarding the measurement equation (model), there is no requirement of knowing whether it is a linear or non-linear model. For each of the generated m_c samples, the model output is computed and afterwards, the properties (e.g. probability distribution function, mean value, standard deviation) can be analyzed (cf. Schweitzer and Schwieger, 2011). Some advantages of Monte Carlo approaches are that they may produce as many correct significant digits in its results as required; they do not involve the computation of derivatives; are applicable even when *f* is markedly non-linear; provide the necessities to characterize the whole probability distribution of the output quantity (Possolo and Iyer, 2017). Regarding disadvantages, if the input variables are correlated, the (joint) probability distribution must be considered for the sample generation. Another disadvantage may be the high number of model runs necessary for each value in the sample.

In the current thesis, there is no emphasis on comparing the mentioned methods for propagating uncertainty. There is a vast spectrum of scientific papers that treat this subject, but for the curious reader, the online NIST Uncertainty Machine offers the possibility to freely compare methods of propagating uncertainty. The user is allowed to assign a probability distribution to the input variables and conduct simulations of a self-defined model. Lafarge and Possolo (2020), the NIST uncertainty machine handbook authors, give a short comparison of the variance propagation law (called Gauss's formula in the publication) and the Monte Carlo Method, both as presented in the GUM.

2.2 Historical overview of the elementary error theory

The origin of the hypothesis of elementary errors dates back to the beginning of the 19th century, a time in which scientists in Europe showed high interest in probability theory and statistics. Often defined as the fathers of the hypothesis of elementary errors, Friedrich Wilhelm Bessel (1784-1846) and Gotthilf Hagen (1797-1884) jointly hold the merit for its discovery.

From a historical point of view, Bessel paved the way with his courses on astronomy at the University of Königsberg for the "invention" of the hypothesis by one of his favorite disciples Hagen. As can be seen from the unpublished exchange of letters between them, the sole credit of an explicit formulation and justification of the hypothesis of elementary errors has to be assigned to Hagen (Fischer, 2011). Works of other scientists like Daniel Bernoulli, Thomas Young, and even Carl Friedrich Gauss are closely related to the idea of elementary errors, but none of them reached a final form. This changed after Hagen clearly formulated the hypothesis about elementary errors, resorting to the principles of use of measurement instruments (Fischer, 2011). In his work, Hagen (1837) made the following assumption:

> "…the error in the result of any measurement is the algebraic sum of an infinitely large number of elementary errors ("elementäre Fehler"), which are all equally large and of which each single one can be just as positive as negative."

After publication, Hagen's (1837) and Bessel's (1838) work was not immediately accepted or further developed in the error theory. Some of the early applications besides measurements are found in statistics of biological and social phenomena, but for more details and other applications, the reader is advised to consult Fischer (2011), chapter 3. In the current work, only aspects relevant to geodetic measurements are shortly addressed. First in general and then with the focus on multidimensional observations. For additional theoretical aspects, Pelzer (1985) and Schwieger (1999) are recommended.

2.3 Elementary error theory

According to the elementary error theory, geodetic observations can be treated as random quantities. It is considered that systematic deviations in a measurement process are either avoided or corrected in the processing. Therefore, systematic deviations are not addressed further.

Each realization l of a measured random quantity L differs from its expectation μ_l by a random deviation ε (Pelzer, 1985):

$$\mu_l = l - \varepsilon. \tag{2.2}$$

It is assumed that the random deviation ε is a sum of q numerous, small elementary errors Δ_i.

$$\varepsilon = \sum_{i=1}^{q} \Delta_i, \tag{2.3}$$

with absolute values supposed to be equal, but with varying signs:

$$\Delta_i = \pm\Delta \quad \text{with } i = 1 \dots q. \tag{2.4}$$

The occurrence of positive and negative values is equally possible (Hagen, 1837), therefore, the central limit theorem (cf. Pelzer, 1985) states that the expectation μ_ε (denoted also with $E(\varepsilon)$ for coherence with other authors) of the random deviation is 0:

$$\mu_\varepsilon = E(\varepsilon) = \sum_{i=1}^{q} \mathrm{E}(\Delta_i) = 0. \tag{2.5}$$

Also following the central limit theorem, a statement about the variance σ^2 of the measured random quantity L can be made as follows:

$$\sigma^2 = E(\varepsilon^2) = \sum_{i=1}^{q} E(\Delta_i^2) = q \cdot \Delta^2. \tag{2.6}$$

If the number of elementary errors is very high ($q \to \infty$) and implicitly their absolute values decrease, becoming infinitely small, the assumption of standard normal (Gaussian) distribution is valid for the random deviation ε. Implicitly, the measured random quantity L also follows the same standard normal distribution with the variance defined by eq. 2.6:

$$L \sim N(\mu_l, \sigma^2) \quad \text{and} \quad \varepsilon \sim N(0, \sigma^2). \tag{2.7}$$

Up to eq. 2.7, the hypothesis of elementary errors has been presented for a single random quantity, similar to how Hagen explains it with one-dimensional data. However, geodetic observations generally have more dimensions. They may consist of spatial 1D, 2D or 3D information, temporal data, or a combination of all together. With regard to this, the hypothesis is extended to n-dimensional vectors. Hence, the random quantity vector $\boldsymbol{L}$ is composed of n random quantities L_i. For each value in eq. 2.2 and 2.5, the equivalent vector form is given by:

$$\boldsymbol{\mu_l} = \boldsymbol{l} - \boldsymbol{\varepsilon} \quad \text{and} \quad \boldsymbol{\mu_\varepsilon} = E(\boldsymbol{\varepsilon}) = \mathbf{0}. \tag{2.8}$$

Since the random vector has n values, the equation for variance (see eq. 2.6) becomes the equation of the variance-covariance matrix (VCM) $\boldsymbol{\Sigma_{ll}}$:

$$E(\boldsymbol{\varepsilon}^2) = \boldsymbol{\Sigma_{ll}} \tag{2.9}$$

where $\boldsymbol{\Sigma_{ll}}$ is fully populated with the expectation of each random deviation as follows:

$$\boldsymbol{\Sigma_{ll}} = \begin{bmatrix} E(\varepsilon_1^2) & E(\varepsilon_1 \cdot \varepsilon_2) & E(\varepsilon_1 \cdot \varepsilon_3) & \cdots & E(\varepsilon_1 \cdot \varepsilon_n) \\ E(\varepsilon_2 \cdot \varepsilon_1) & E(\varepsilon_2^2) & E(\varepsilon_2 \cdot \varepsilon_3) & \cdots & E(\varepsilon_2 \cdot \varepsilon_n) \\ E(\varepsilon_3 \cdot \varepsilon_1) & E(\varepsilon_3 \cdot \varepsilon_2) & E(\varepsilon_3^2) & \vdots & E(\varepsilon_3 \cdot \varepsilon_n) \\ \vdots & \vdots & \vdots & \ddots & \vdots \\ E(\varepsilon_n \cdot \varepsilon_1) & E(\varepsilon_n \cdot \varepsilon_2) & E(\varepsilon_n \cdot \varepsilon_3) & \cdots & E(\varepsilon_n^2) \end{bmatrix}. \tag{2.10}$$

Instead of the expectations, the variances σ_n^2 and covariances σ_{1n} can be used for expressing the VCM in a simpler manner:

$$\boldsymbol{\Sigma_{ll}} = \begin{bmatrix} \sigma_1^2 & \sigma_{12} & \sigma_{13} & \cdots & \sigma_{1n} \\ \sigma_{21} & \sigma_2^2 & \sigma_{23} & \cdots & \sigma_{2n} \\ \sigma_{31} & \sigma_{32} & \sigma_3^2 & \vdots & \sigma_{3n} \\ \vdots & \vdots & \vdots & \ddots & \vdots \\ \sigma_{n1} & \sigma_{n2} & \sigma_{n3} & \cdots & \sigma_n^2 \end{bmatrix}. \tag{2.11}$$

Thus, the matrix $\boldsymbol{\Sigma_{ll}}$ is a square, symmetric, positive-semidefinite matrix. Often nothing more is known about the VCM, but sometimes it is known that $\boldsymbol{\Sigma_{ll}}$ has a certain form or pattern (Graybill, 1969). Examples of patterned matrices are diagonal matrices with reoccurring values (e.g. each third element on the main diagonal) or full matrices that contain values of covariances only between some elements. This feature may be helpful in computing the matrix inverse. The main topic of this thesis addresses VCMs as in eq. 2.11 and how they can be defined for TLS observations.

Generally, the theory of multivariate analysis focuses on the analysis of the VCM, meaning that it may be necessary to compute the determinant of $\boldsymbol{\Sigma_{ll}}$, the eigenvalues or the inverse of $\boldsymbol{\Sigma_{ll}}$ if it exists (Graybill, 1969). Common geodetic quality indicators rely directly on these values. This is especially relevant for some applications discussed in chapter 6. Most of the theories and applications of multivariate analysis involve the normal distribution, as this is the most common distribution observed in nature (an idea known as Queteletism). It is also the most frequent probability distribution assumed for geodetic measurements (Möser et al. 2012).

Analog to eq. 2.7 in which it was seen that the normal distribution is valid for all random quantities L, the same can be assumed for the multivariate vector $\boldsymbol{L}$ and the corresponding random deviation vector $\boldsymbol{\varepsilon}$. Instead of a single variance value, the vector's stochastic properties are described by $\boldsymbol{\Sigma_{ll}}$:

$$\boldsymbol{L} \sim N(\boldsymbol{\mu_l}, \boldsymbol{\Sigma_{ll}}) \quad \text{and} \quad \boldsymbol{\varepsilon} \sim N(\boldsymbol{0}, \boldsymbol{\Sigma_{ll}}). \tag{2.12}$$

It is possible to classify multi-dimensional data into different classes according to the nature of the stochastic and functional properties of elementary errors Δ_i. The following paragraphs explain how the elementary error groups were defined according to Pelzer (1985) and Schwieger (1999). Similar explanations have already been given in papers on the topic (cf. Kauker and Schwieger, 2017, Kerekes and Schwieger, 2020), but only briefly. Because of this, the following section expands the classification for understanding.

2.4 Groups of elementary errors

2.4.1 Non-correlating elementary errors

In his work, Pelzer (1985) decomposes the random deviation vector $\boldsymbol{\varepsilon}$ into two groups of elementary errors. In this section, the first one, called the non-correlating group is addressed.

It is considered that each of the n observations in $\boldsymbol{L}$, is influenced by p non-correlating elementary error types. They are depicted by δ_{ik} where i is the observation number and $k=1\ldots p$ denotes the elementary error type. Following these conventions, each non-correlating error vector $\boldsymbol{\delta_k}$ contains only one error type and has the form:

$$\boldsymbol{\delta_k} = \begin{bmatrix} \delta_{1k} \\ \delta_{2k} \\ \vdots \\ \delta_{nk} \end{bmatrix} \text{ where } k = 1 \ldots p. \tag{2.13}$$

Following the same principle as in eq. 2.5:

$$\boldsymbol{\mu_{\delta_k}} = E(\boldsymbol{\delta_k}) = \mathbf{0} \text{ where } k = 1 \ldots p. \tag{2.14}$$

An additional property for the expectation between non-correlating elementary errors is the stochastic independence between the types (e.g. k and j to the type):

$$E\left(\boldsymbol{\delta_k} \cdot \boldsymbol{\delta_j}\right) = \mathbf{0} \text{ for } k \neq j. \tag{2.15}$$

Moreover, the individual (single) non-correlating elementary errors are also stochastically independent per definition, therefore:

$$E\left(\delta_{ik} \cdot \delta_{jk}\right) = 0 \text{ for } i \neq j \text{ and } i, j = 1 \ldots n. \tag{2.16}$$

If $i = j$, then the diagonal elements are addressed, and as seen in eq. 2.6, the variance is:

$$E\left(\delta_{ik} \cdot \delta_{jk}\right) = \sigma_{ik}^2 \text{ for } i = j. \tag{2.17}$$

As demonstrated in eq. 2.9 and 2.10 for the general case, applying the statements from eq. 2.16 and 2.17 will result in a VCM with the following form:

$$\boldsymbol{\Sigma_{\delta_k \delta_k}} = \begin{bmatrix} \sigma_{1k}^2 & 0 & 0 & \cdots & 0 \\ 0 & \sigma_{2k}^2 & 0 & \cdots & 0 \\ 0 & 0 & \sigma_{3k}^2 & \cdots & 0 \\ \vdots & \vdots & \vdots & \ddots & \vdots \\ 0 & 0 & 0 & \cdots & \sigma_{nk}^2 \end{bmatrix}. \tag{2.18}$$

This means that $\boldsymbol{\Sigma_{\delta_k \delta_k}}$ is a diagonal matrix, respecting eq. 2.16 (no covariances of the elementary errors). Besides this assumption, each non-correlating elementary error type k has the same variance σ_k^2 on each observation i from the total n observations. This leads to the following simplification:

$$\boldsymbol{\Sigma_{\delta_k \delta_k}} = \sigma_k^2 \cdot \boldsymbol{I}_{(n \cdot n)} = \sigma_k^2 \cdot \begin{bmatrix} 1 & 0 & 0 & \cdots & 0 \\ 0 & 1 & 0 & \cdots & 0 \\ 0 & 0 & 1 & \cdots & 0 \\ \vdots & \vdots & \vdots & \ddots & \vdots \\ 0 & 0 & 0 & \cdots & 1 \end{bmatrix}. \tag{2.19}$$

The impact of the non-correlating errors δ_{ik} on the observations in $\boldsymbol{L}$ is defined with the help of first-order partial derivatives (cf. sec. 2.1 variance-covariance propagation law), which numerically define a local linearization of the function in matter. The partial derivatives are

further referred to as influencing factors and in the case of non-correlating elementary errors denoted by d_{ik}. The matrix containing the influencing factors has the following form:

$$\boldsymbol{D_k} = \begin{bmatrix} d_{1k} & 0 & 0 & \cdots & 0 \\ 0 & d_{2k} & 0 & \cdots & 0 \\ 0 & 0 & d_{3k} & \cdots & 0 \\ \vdots & \vdots & \vdots & \ddots & \vdots \\ 0 & 0 & 0 & \cdots & d_{nk} \end{bmatrix} = \begin{bmatrix} \frac{\partial L_1}{\partial \delta_{1k}} & 0 & 0 & \cdots & 0 \\ 0 & \frac{\partial L_2}{\partial \delta_{2k}} & 0 & \cdots & 0 \\ 0 & 0 & \frac{\partial L_3}{\partial \delta_{3k}} & \cdots & 0 \\ \vdots & \vdots & \vdots & \ddots & \vdots \\ 0 & 0 & 0 & \cdots & \frac{\partial L_n}{\partial \delta_{nk}} \end{bmatrix}. \tag{2.20}$$

The impact of each elementary error type k is given by the diagonal matrix $\boldsymbol{D_k}$ on each of the n observations. The concrete value for d_{ik} is easily obtained because in most cases, the model (function) in which the elementary errors play a role, is known. Computing $\partial L_i / \partial \delta_{ik}$ is straightforward.

Finally, the random deviation vector $\boldsymbol{\varepsilon_\delta}$ for all p non-correlating elementary error types is:

$$\boldsymbol{\varepsilon_\delta} = \sum_{k=1}^{p} \boldsymbol{D_k} \cdot \boldsymbol{\delta_k}, \tag{2.21}$$

where $\boldsymbol{\varepsilon_\delta}$ has the same dimensions as the total number of observations in $\boldsymbol{L}$. The corresponding part in the VCM denoted by $\boldsymbol{\Sigma_{ll,\delta}}$, is defined after applying the variance-covariance propagation law on eq. 2.21 and the conventions in eq. 2.19 and 2.20:

$$\boldsymbol{\Sigma_{ll,\delta}} = \sum_{k=1}^{p} \boldsymbol{D_k} \cdot \boldsymbol{\Sigma_{\delta_k \delta_k}} \cdot \boldsymbol{D_k^T} = \sum_{k=1}^{p} \sigma_k^2 \cdot \boldsymbol{D_k^2}. \tag{2.22}$$

If non-correlating errors are the only ones considered in observation processes (due to lack of knowledge of other types), then the complete variance-covariance matrix $\boldsymbol{\Sigma_{ll}}$ is a diagonal matrix. Correlations that possibly exist are neglected in this case, but this assumption is very often encountered in geodetic measurements.

2.4.2 Functional correlating elementary errors

In contrast to non-correlating elementary errors, the functional correlating errors, as defined by Pelzer (1985), do not influence only one value in the random deviation vector $\boldsymbol{\varepsilon}$, but may affect several (even all) measurement quantities. Regarding this principle, they have a correlating effect on the observations.

Another differentiating feature of functional correlating errors ξ_s is that the number of elementary errors m is not dependent on the number of observations. The same principle as in eq. 2.5 about the expectation applies:

$$\boldsymbol{\mu_{\xi_s}} = E(\xi_s) = \boldsymbol{0} \text{ where } s = 1 \ldots m, \tag{2.23}$$

and correlations with the other group of non-correlating errors are excluded by definition:

$$E(\boldsymbol{\xi} \cdot \boldsymbol{\delta_k}) = \boldsymbol{0} \text{ where } k = 1 \ldots p. \tag{2.24}$$

Regarding the individual (single) functional correlating elementary errors, they are also stochastically independent per definition, therefore:

$$E\left(\xi_s \cdot \xi_j\right) = 0 \;\text{ for }\; s \neq j \;\text{ and }\; s, j = 1 \ldots m. \tag{2.25}$$

For the diagonal elements $s = j$ are addressed, and as seen in eq. 2.6, the variance is:

$$E\left(\xi_s \cdot \xi_j\right) = \sigma_s^2 \text{ for } s = j, \tag{2.26}$$

case in which, the variance-covariance matrix of the functional correlating errors is:

$$\boldsymbol{\Sigma}_{\xi\xi} = \begin{bmatrix} \sigma_1^2 & 0 & 0 & \cdots & 0 \\ 0 & \sigma_2^2 & 0 & \cdots & 0 \\ 0 & 0 & \sigma_3^2 & \cdots & 0 \\ \vdots & \vdots & \vdots & \ddots & \vdots \\ 0 & 0 & 0 & \cdots & \sigma_m^2 \end{bmatrix}. \tag{2.27}$$

The structure of the influencing matrix defines the main difference between non-correlating errors and functional correlating errors. This matrix contains the influencing factors of functional correlating errors f_{is} on the observations in $\boldsymbol{L}$. Knowing the model after which $\boldsymbol{L}$ is determined, the influencing matrix is defined as a fully populated matrix:

$$\boldsymbol{F} = \begin{bmatrix} f_{11} & f_{12} & f_{13} & \cdots & f_{1m} \\ f_{21} & f_{22} & f_{23} & \cdots & f_{2m} \\ f_{31} & f_{32} & f_{33} & \cdots & f_{3m} \\ \vdots & \vdots & \vdots & \ddots & \vdots \\ f_{n1} & f_{n2} & f_{n3} & \cdots & f_{nm} \end{bmatrix} = \begin{bmatrix} \frac{\partial L_1}{\partial \xi_1} & \frac{\partial L_1}{\partial \xi_2} & \frac{\partial L_1}{\partial \xi_3} & \cdots & \frac{\partial L_1}{\partial \xi_m} \\ \frac{\partial L_2}{\partial \xi_1} & \frac{\partial L_2}{\partial \xi_2} & \frac{\partial L_2}{\partial \xi_3} & \cdots & \frac{\partial L_2}{\partial \xi_m} \\ \frac{\partial L_3}{\partial \xi_1} & \frac{\partial L_3}{\partial \xi_2} & \frac{\partial L_3}{\partial \xi_3} & \cdots & \frac{\partial L_3}{\partial \xi_m} \\ \vdots & \vdots & \vdots & \ddots & \vdots \\ \frac{\partial L_n}{\partial \xi_1} & \frac{\partial L_n}{\partial \xi_2} & \frac{\partial L_n}{\partial \xi_3} & \cdots & \frac{\partial L_n}{\partial \xi_m} \end{bmatrix}. \tag{2.28}$$

Each of the m functional correlating elementary errors ξ_s will have theoretically, an impact on each observation in $\boldsymbol{L}$. In special cases in which each functional correlating elementary error ξ_s affects only one observation, then that specific elementary error needs to be moved to the non-correlating error group by definition.

Returning to the random deviation vector, the group of functional correlating errors is:

$$\boldsymbol{\varepsilon}_\xi = \boldsymbol{F} \cdot \boldsymbol{\xi}\,, \tag{2.29}$$

and the matrix/vector dimensions are $F_{(n \cdot m)}$ and $\xi_{(m \cdot 1)}$. The corresponding VCM is obtained after applying the variance propagation law:

$$\boldsymbol{\Sigma}_{ll,\xi} = \boldsymbol{F} \cdot \boldsymbol{\Sigma}_{\xi\xi} \cdot \boldsymbol{F}^{\boldsymbol{T}}. \tag{2.30}$$

To avoid confusion, the same rule as in eq. 2.24, also applies to the random deviation vectors between the elementary error groups:

$$E\left(\boldsymbol{\varepsilon}_\xi \cdot \boldsymbol{\varepsilon}_\delta\right) = \boldsymbol{0}. \tag{2.31}$$

Given the nature of each matrix in eq. 2.30, after the multiplication of one fully populated, one diagonal and the transverse of the first fully populated matrix, the result is also a fully populated matrix (cf. Thompson, 1969). Hence, the functional correlating errors define correlations between the observations (Schwieger, 1999).

2.4.3 Stochastic correlating elementary errors

The previous two groups of elementary errors imply knowledge about the measurement process in a detailed manner. Specifically, the stochastic nature of these elementary error groups is known and there is no doubt that they are stochastically independent. This means that a classification of the elementary errors in the two groups is possible because the process is well understood and elementary errors are separable in these two types. But there are cases in which a measurement process is so complex or the measurement system cannot be fully modeled. For these cases, a third group of elementary errors has been introduced by Schwieger (1999), called the stochastic correlating elementary errors.

Denoted by γ_{ih}, stochastic correlating elementary errors can be correlated with each other, in contrast to the non-correlating and functional correlating errors. Following the previous conventions, there can be q stochastic correlating errors, grouped in the generic vector $\boldsymbol{\gamma_h}$. The stochastic correlating errors can be used where the measurement process cannot be separated into stochastic independent error groups.

As generally valid, the expectation for the vector $\boldsymbol{\gamma_h}$ is:

$$\boldsymbol{\mu}_{\boldsymbol{\gamma_h}} = E(\boldsymbol{\gamma_h}) = \mathbf{0} \text{ where } h = 1 \dots q, \tag{2.32}$$

but the covariance for elementary error of the same type h is:

$$E(\gamma_{ih} \cdot \gamma_{jh}) = \sigma_{ijh} \text{ for } i \neq j \text{ and } i,j = 1 \dots n, \tag{2.33}$$

and for diagonal elements*:*

$$E(\gamma_{ih} \cdot \gamma_{jh}) = \sigma_{ih}^2 \text{ for } i = j \text{ and } i,j = 1 \dots n. \tag{2.34}$$

Accordingly, variances and covariance lead to q fully populated VCMs that have the following form:

$$\boldsymbol{\Sigma}_{\boldsymbol{\gamma_h}\boldsymbol{\gamma_h}} = \begin{bmatrix} \sigma_{1h}^2 & \sigma_{12h} & \sigma_{13h} & \cdots & \sigma_{1nh} \\ \sigma_{12h} & \sigma_{2h}^2 & \sigma_{23h} & \cdots & \sigma_{2nh} \\ \sigma_{13h} & \sigma_{23h} & \sigma_{3h}^2 & \cdots & \sigma_{3nh} \\ \vdots & \vdots & \vdots & \ddots & \vdots \\ \sigma_{1nh} & \sigma_{2nh} & \sigma_{3nh} & \cdots & \sigma_{nh}^2 \end{bmatrix}. \tag{2.35}$$

In case the variances σ_{ih}^2 are identical for all observations, the VCM $\boldsymbol{\Sigma}_{\boldsymbol{\gamma_h}\boldsymbol{\gamma_h}}$ will have a simplified form:

$$\boldsymbol{\Sigma}_{\boldsymbol{\gamma_h}\boldsymbol{\gamma_h}} = \sigma_h^2 \cdot \mathbf{R}_{\boldsymbol{\gamma_h}\boldsymbol{\gamma_h}} = \sigma_h^2 \cdot \begin{bmatrix} 1 & \rho_{12h} & \rho_{13h} & \cdots & \rho_{1nh} \\ \rho_{12h} & 1 & \rho_{23h} & \cdots & \rho_{2nh} \\ \rho_{13h} & \rho_{23h} & 1 & \cdots & \rho_{3nh} \\ \vdots & \vdots & \vdots & \ddots & \vdots \\ \rho_{1nh} & \rho_{2nh} & \rho_{3nh} & \cdots & 1 \end{bmatrix}, \tag{2.36}$$

where $\mathbf{R}_{\gamma_h \gamma_h}$ is the correlation matrix containing correlation coefficients ρ_{ijh} (also called Pearson product-moment correlation coefficient). The latter can be obtained by:

$$\rho_{ij} = \frac{\sigma_{ij}}{\sigma_i \cdot \sigma_j}. \tag{2.37}$$

The correlation coefficients can be used to determine the covariances σ_{ij} between two elementary errors, if their correlation function and variances are known. Obtaining values for the correlation coefficients is possible with the help of correlation functions or after analyzing empirical data. Another possibility is to use covariance functions directly. In the lack of empirical data, many stochastic processes encountered in physical systems in nature can be generally described by different correlation functions, e.g. exponential functions (Martin, 1968). Despite this, there are cases in which correlations are negligible because of their reduced dimensions (Heunecke, 2004). Specific correlation functions are addressed in the context of the elementary error type later in chapters 4 and 5.

As deduced from the structure of matrix $\mathbf{\Sigma}_{\gamma_h \gamma_h}$, if covariances inherit the value 0, the respective observations *i* and *j* are not correlated with respect to the stochastic correlating elementary error type *h*. If this is the case for the complete matrix $\mathbf{\Sigma}_{\gamma_h \gamma_h}$, with other words, no correlations are defined, the respective error type *h* is reclassified as non-correlating.

Another exception is the case in which correlation coefficients in matrix $\mathbf{R}_{\gamma_h \gamma_h}$ show strong positive or negative correlations (1 or -1). If this occurs, the respective observations are functionally dependent, and that elementary error type is reclassified in the functional correlating error group.

Regarding the stochastic relation between stochastic elementary error types, the *q* error types are normally not dependent on each other stochastically:

$$E(\boldsymbol{\gamma_h} \cdot \boldsymbol{\gamma_j}) = \mathbf{0} \quad \text{where} \quad h, j = 1 \dots q \quad \text{and} \; h \neq j \tag{2.38}$$

There are exceptions to eq. 2.38. In these cases, the separation between elementary error types cannot be completely respected due to the physical dependency of these error types, a fact that will be explained in chapter 4. The elementary error model as introduced by Schwieger (1999) is expanded by this first novelty in the current work.

Additionally, the classification of elementary error types should be made in such a way that no stochastic dependency with the other groups of non-correlating and functional correlating errors exist:

$$E(\boldsymbol{\gamma_h} \cdot \boldsymbol{\xi}) = E(\boldsymbol{\gamma_h} \cdot \boldsymbol{\delta_k}) = \mathbf{0} \quad \text{where} \quad h = 1 \dots q \quad \text{and} \; k = 1 \dots p, \tag{2.39}$$

and implicitly for the random deviation error vectors:

$$E(\boldsymbol{\varepsilon_\gamma} \cdot \boldsymbol{\varepsilon_\xi}) = E(\boldsymbol{\varepsilon_\gamma} \cdot \boldsymbol{\varepsilon_\delta}) = 0. \tag{2.40}$$

As in the previous two groups, the influencing factors can be defined in the diagonal matrixes with partial derivatives:

$$\boldsymbol{G_h} = \begin{bmatrix} g_{1h} & 0 & 0 & \cdots & 0 \\ 0 & g_{2h} & 0 & \cdots & 0 \\ 0 & 0 & g_{3h} & \cdots & 0 \\ \vdots & \vdots & \vdots & \ddots & \vdots \\ 0 & 0 & 0 & \cdots & g_{nh} \end{bmatrix} = \begin{bmatrix} \frac{\partial L_1}{\partial \gamma_{1h}} & 0 & 0 & \cdots & 0 \\ 0 & \frac{\partial L_2}{\partial \gamma_{2h}} & 0 & \cdots & 0 \\ 0 & 0 & \frac{\partial L_3}{\partial \gamma_{3h}} & \cdots & 0 \\ \vdots & \vdots & \vdots & \ddots & \vdots \\ 0 & 0 & 0 & \cdots & \frac{\partial L_n}{\partial \gamma_{nh}} \end{bmatrix}. \tag{2.41}$$

As seen in the matrix depicted by eq. 2.41, the elementary error model described up to now, uses a simple diagonal matrix. During the research conducted within this thesis, this proved to be insufficient for modelling the complex influences of stochastic correlating errors introduced in chapters 4 and 5. To overcome these issues, instead of single elements g_{ih} on the diagonal of $\boldsymbol{G_h}$, block matrices are introduced on the main diagonal for each of the i observations. By this means, the observations' influencing factors are modeled in a similar, but not identical manner to the functional correlating errors (not a fully populated influencing matrix). This comprises the second novelty of the elementary error model, as shown later on concrete examples.

Finally, the corresponding random deviation vector $\boldsymbol{\varepsilon_\gamma}$ for stochastic correlating errors is:

$$\boldsymbol{\varepsilon_\gamma} = \sum_{h=1}^{q} \boldsymbol{G_h} \cdot \boldsymbol{\gamma_h}. \tag{2.42}$$

Applying the variance propagation law once more on the error vector $\boldsymbol{\varepsilon_\gamma}$, the corresponding fully populated variance-covariance matrix $\boldsymbol{\Sigma}_{\boldsymbol{ll,\gamma}}$ is:

$$\boldsymbol{\Sigma}_{\boldsymbol{ll,\gamma}} = \sum_{h=1}^{q} \boldsymbol{G_h} \cdot \boldsymbol{\Sigma}_{\boldsymbol{\gamma_h \gamma_h}} \cdot \boldsymbol{G_h^T} = \sum_{h=1}^{q} \sigma_h^2 \cdot \boldsymbol{G_h} \cdot \mathbf{R}_{\boldsymbol{\gamma_h \gamma_h}} \cdot \boldsymbol{G_h^T}. \tag{2.43}$$

By its form, the VCM $\boldsymbol{\Sigma}_{\boldsymbol{ll,\gamma}}$ is fully populated and leads to correlations between the observations.

2.4.4 Obtaining values for the variances of elementary errors

If numerical values for the variances of elementary errors σ^2 are available (e.g. from empirical data), then they can be directly used in the corresponding VCM of the respective elementary error vector. Alternatively, if no values are available, an estimation can be made according to the best knowledge available for the observation phenomenon (instrument & method). With regard to this, the maximum error of an elementary error (e.g. $\delta_{ik}[max]$) is estimated. With this information, Pelzer (1985) recommends deducing the standard deviation σ_k based on the probability distribution of the respective elementary error. Examples of three types of probability distribution functions are given by Pelzer (1985):

Normal distribution: $\sigma \approx 0.3 \cdot EE[max]$ (2.44)

Rectangular distribution: $\sigma \approx 0.6 \cdot EE[max]$ (2.45)

Triangular distribution: $\sigma \approx 0.4 \cdot EE[max]$ (2.46)

As one may observe, a very similar approach is described in the GUM in both cases – from empirical data or assumed after eq. 2.44-2.46. Although the current thesis maintains the conventions used by Pelzer, the definitions from GUM are shortly mentioned for informative purposes. Thereafter, there are two ways of evaluating uncertainty together with the probability density function that describes or is assumed to describe the model in the GUM. These are called Type A and Type B. The first one, Type A evaluations are data-based and involve replicated readings (or observations) obtained under conditions of repeatability. Type B evaluations are employed by means other than the statistical analysis of series of observations. They are based on expert knowledge and scientific judgment of everything that is known about the input quantities. Examples of such sources are expert knowledge derived from past measurements for the same or similar quantities, experience with the behavior and properties of relevant materials, instruments and measurement methods, manufacturers' specifications, information from calibration certificates, material certificates, uncertainties assigned to reference data taken from handbooks (Possolo & Elster, 2014).

In the following chapters of this thesis, there are cases in which empirical standard deviations are available (cf. chapters 3 and 4) for different elementary errors, but there are also cases in which assumptions about the standard deviations need to be made based on eq. 2.44-2.46.

2.5 The synthetic variance-covariance matrix from the elementary error model

The elementary error model, as generally described before, was elegantly presented in Pelzer (1985) and included only non-correlating and functional correlating errors at that time. Later, the model was extended by Schwieger (1999) in his thesis by the stochastic correlating part. Following the two authors and the theory in sec. 2.3 and 2.4, an overview is given for all types of errors.

According to the group of errors, the random deviation $\boldsymbol{\varepsilon}$ is the sum of all random deviation vectors in each group (see eq. 2.22, 2.30, 2.43):

$$\boldsymbol{\varepsilon} = \boldsymbol{\varepsilon}_{\boldsymbol{\delta}} + \boldsymbol{\varepsilon}_{\boldsymbol{\xi}} + \boldsymbol{\varepsilon}_{\boldsymbol{\gamma}}, \tag{2.45}$$

$$\boldsymbol{\varepsilon} = \sum_{k=1}^{p} \boldsymbol{D_k} \cdot \boldsymbol{\delta_k} + \boldsymbol{F} \cdot \boldsymbol{\xi} + \sum_{h=1}^{q} \boldsymbol{G_h} \cdot \boldsymbol{\gamma_h}, \tag{2.46}$$

where the non-correlating error vectors $\boldsymbol{\delta_k}$, functional correlating error vector $\boldsymbol{\xi}$, and stochastic correlating error vectors $\boldsymbol{\gamma_h}$ and their corresponding influencing matrices are jointly modeled.

The corresponding VCM $\boldsymbol{\Sigma}_{\boldsymbol{ll}}$ is likewise obtained by addition of the individual VCM presented in eq. 2.22, 2.30 and 2.42 because elementary error groups are not correlated with each other (see eq. 2.40), thus:

$$\boldsymbol{\Sigma_{ll}} = \boldsymbol{\Sigma}_{\boldsymbol{ll},\boldsymbol{\delta}} + \boldsymbol{\Sigma_{ll,\xi}} + \boldsymbol{\Sigma}_{\boldsymbol{ll},\boldsymbol{\gamma}}, \tag{2.47}$$

$$\boldsymbol{\Sigma_{ll}} = \sum_{k=1}^{p} \sigma_k^2 \cdot \boldsymbol{D_k^2} + \boldsymbol{F} \cdot \boldsymbol{\Sigma_{\xi\xi}} \cdot \boldsymbol{F^T} + \sum_{h=1}^{q} \boldsymbol{G_h} \cdot \boldsymbol{\Sigma}_{\boldsymbol{\gamma_h \gamma_h}} \cdot \boldsymbol{G_h^T}. \tag{2.48}$$

This represents the equation of the synthetic variance-covariance matrix (SVCM). The reason for naming it "synthetic" (constructed) is its definition. The word originates from the Latin "syntheticus" and Greek "synthetikos" meaning "expert in putting together" (Collins dictionary, 2018). After estimating variances and covariances for each group of elementary errors and computing the influencing factors (partial derivatives), the SVCM is complete and synthesizes the stochastic model of the respective observation process. For ease of understanding, the overview after Schwieger (1999) is updated here (Tab 2.1).

Table 2.1 Overview of the elementary error model.

Elementary error group (EEG)	**non-correlating**	**functional correlating**	**stochastic correlating**
Denotation	$\boldsymbol{\delta_{ik}}$	$\boldsymbol{\xi_s}$	$\boldsymbol{\gamma_{ih}}$
Number of elementary errors (EE)	$n \cdot p$ $i = 1 \dots n$ $k = 1 \dots p$	m $s = 1 \dots m$	$n \cdot q$ $i = 1 \dots n$ $h = 1 \dots q$
VCM of the EEG	unity matrix $\sigma_k^2 \cdot I_{(n \cdot n)}$	diagonal matrix $\boldsymbol{\Sigma_{\xi\xi}}$	fully populated matrix $\boldsymbol{\Sigma_{\gamma_h \gamma_h}}$
Stochastic properties of the EEG	not correlated	not correlated	correlated
Matrix of influencing factors	diagonal matrix $\boldsymbol{D_k}$	fully populated matrix $\boldsymbol{F}$	diagonal (block) matrix $\boldsymbol{G_h}$
Effects of EE on…	one observation	more (all) observations	more observations
EEG part in the VCM $\boldsymbol{\Sigma_{ll}}$	$\sum_{k=1}^{p} \sigma_k^2 \cdot \boldsymbol{D_k^2}$	$\boldsymbol{F \cdot \Sigma_{\xi\xi} \cdot F^T}$	$\sum_{h=1}^{q} \boldsymbol{G_h \cdot \Sigma_{\gamma_h \gamma_h} \cdot G_h^T}$.
Stochastic effect of the EEG part	not correlated	correlated	correlated

To the author's best knowledge, applications of the elementary error model for geodetic measurements can be found in a reduced number of publications. In this sense, only the recent (after the late 20th century) relevant ones are mentioned. In Augath (1985), the elementary error model is applied to electronic distance measurement (EDM) instruments. Matthias (1992) uses the model to derive correlations in precise levelling. Later, the model is applied to GNSS observations by Schwieger (1999). Among the more recent applications, Kauker and Schwieger (2017) apply the elementary error for TLS and define a SVCM.

The main subject of the current contribution continues the line of work started at the Institute of Engineering Geodesy (IIGS) at the University of Stuttgart in 2014 by adapting, extending, and improving the elementary error model for TLS measurements. In the upcoming section, a classification of the influences on TLS measurements is made based on the elementary error groups defined in sec 3.2. Each of the error sources is treated extensively in chapters 3, 4, and 5.

2.6 Classification of TLS errors

The known error sources are first identified and classified into a group of the SVCM. This is necessary because it is not self-evident that all error sources (e.g. instrument errors) of the same type fall into the same group of elementary errors. The principle used in this thesis for classifications of TLS errors may be referred to as a bottom-up approach. In this case, several

steps are needed: the complete enumeration of all relevant sources of uncertainties, a description of how they affect the measurement result, and finally, the quantification of the contribution they make to the uncertainty of the result (Possolo and Iyer, 2017).

As valid for any measurement instrument, laser scanners are realizations of an idealistic measurement system, therefore affected by physical manufacturing limitations. All manufacturing and assembly imperfections of the laser scanner affect the observations. This gives a first category of errors that are called instrument-specific or simply instrument errors in this work. Some instrument errors influence more or all observations in the same way, leading to highly correlated results. A functional dependency between these instrument errors and the results is often defined by the instrument construction principle (system architecture) and the used calibration model. One example is the zero point error of the EDM unit that affects all distance measurements in the same way. This leads to the first classification of instrument errors in the functional correlating group. However, there are other instrument-related errors that have a random effect on the observations. In many technical specifications, the term "noise" (e.g. range noise) is found. In this work, this is understood as a random error and therefore, classified in the non-correlating group. Currently researched instrument errors, based on literature, are introduced and discussed in chapter 3.

Another important error source is the propagation environment (atmosphere) of the electromagnetic waves (cf. Rüeger, 1990). There are many complex parameters describing the environment between the scanner and the measured object, but only the ones known to have an important impact on EDM measurements are studied. These are air temperature, air pressure, and vertical temperature gradient. They are classified in the stochastic correlating group because each of them influences each observation differently. Moreover, the environment elementary error types are correlated to each other (cf. eq. 2.35) but also between each type by their nature (cf. Geiger et al., 2003). In this sense, eq. 2.38 cannot be completely fulfilled, therefore the definition of the stochastic correlating group of errors is extended in this work. Details about their inclusion into the SVCM are the main topic of chapter 4.

Additional TLS error sources are caused by the measured object properties such as surface roughness and reflectivity. As with environment errors, the object surface-related errors are classified into the stochastic correlating group because surface features of an object (e.g. concrete wall) show similar or reoccurring properties. The only elementary error group that can handle correlations within the same error type is the stochastic correlating group (cf. tab. 2.1). In previous publications on the topic (cf. Kauker and Schwieger, 2017) these types of errors proved to be the most difficult to define and handle. Chapter five of this work, addresses the issue through a novel approach, based on the physical properties of surfaces and technical specifications of laser scanners.

According to other authors (cf. Soudarissanane, 2016), scanning geometry is also considered an error source. But in this work, it is not included as a separate error source, because most (if not all) of the errors considered in the SVCM (see tab. 2.2) are dependent on scanning geometry. This means, for example, that with increasing distance between the scanner and the object, the variances also increase (see sec. 6.1 and 6.3). A simple example is the effect caused by angular measurement noise on the TLS points at different distances. With increasing distance the effect of the angular noise increases linearly, therefore the geometry dependency is given.

Depending on applications, if scans from multiple station points need to be referenced in the same coordinate system, an additional error source, commonly called registration or georeferencing errors must be considered. This type of error is addressed in several works in literature (cf. Reshetyuk, 2009 Soudarissanane, 2016), but its inclusion in the elementary error model is out of scope for the current thesis and planned for future work.

Table 2.2 Classification of TLS error sources in the SVCM.

Type of correlation according to the elementary error group	**Error source**
non-correlating	Instrument
functional correlating	Instrument
stochastic correlating	Measurement environment Object surface properties

In this chapter, the theory of elementary errors was resumed in an extensive and accessible manner. The elementary error groups were defined and their stochastic properties are highlighted. All in all, this chapter represents the underlying fundament for all upcoming applications and many equations will be referenced from here.

3. Instrument-specific errors

3.1 TLS generalities and conventions

Terrestrial Laser Scanners (TLSs) are active optical multi-sensor systems used to remotely measure the three-dimensional geometry of objects with backscattering surface properties (cf. Mettenleiter et al., 2015; Staiger, 2003). The result of a TLS scan is a bundle of points, called point cloud that resembles the shape of the real scanned object. Additionally, radiometric information (intensities) of the respective object surface is acquired and, if RGB cameras are integrated, color information can be assigned to the geometry. Laser scanners got more precise, compact, and affordable in the past 20 years (Wieser et al., 2019), reaching performances of very high scan rates (e.g. up to 2 million points per second) and high accuracy (e.g. range noise of 0.1 mm). Since scanners became commercially available, numerous studies, mostly from the scientific community, reconfirm their performance in different test scenarios within laboratory and field conditions (cf. Muralikrishnan, 2021; Kersten and Lindstaedt, 2022). For more details about laser scanners, the interested reader can find general reviews and working principles in the above-mentioned references and additional sources like Shan and Toth (2018), Kuhlmann and Holst (2018), or Vosselman and Maas (2010). For a detailed historical development of laser scanners, Spring (2020a and 2020b) offers a very rich literature review from multilingual and multidisciplinary sources.

There are several possibilities to define polar and Cartesian coordinate systems, but the one used throughout this thesis is presented in fig. 3.1 and described by eq. 3.1-3.6.

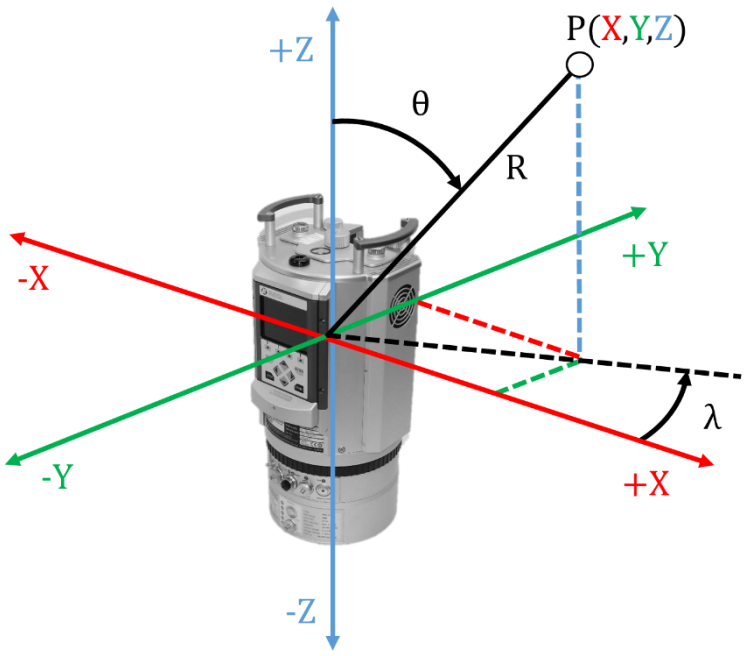

Figure 3.1. Conventions used for Cartesian coordinates and polar observations

The conventions for TLS observations and coordinates are represented by the mathematical relations between range (R), horizontal angle (λ), vertical angle (θ), and Cartesian coordinates (X, Y, Z) as follows:

$$R = \sqrt{X^2 + Y^2 + Z^2}, \tag{3.1}$$

$$\lambda = \text{atan}(Y/X), \tag{3.2}$$

$$\theta = \text{acos}(Z/R), \tag{3.3}$$

$$X = R \cdot \cos(\lambda) \cdot \sin(\theta), \tag{3.4}$$

$$Y = R \cdot \sin(\lambda) \cdot \sin(\theta), \tag{3.5}$$

$$Z = R \cdot \cos(\theta). \tag{3.6}$$

In other literature sources that are related to the TLS observations (R, λ, θ), the terminology used for these observations may be different, e.g. azimuth or direction instead of horizontal angle or zenith angle instead of vertical angle or generally spherical coordinates, but they all refer to the same observed values (cf. Chow et al., 2013; Neitzel, 2006b).

By default, TLS users have access to point clouds directly in Cartesian coordinates and an additional parameter describing the radiometric properties of the scanned points. The origin of the Cartesian coordinate system is the scanner axis intersection point, which receives the coordinates (0, 0, 0). The point clouds are relative to the origin. Only in exceptional cases, the user can export raw data from the scanner or scanner software and work directly in the observation space. For this reason, the conversion from X, Y, Z coordinates to polar measurements in observation space is made according to eq. 3.1-3.3 if the values are not available. The equations are valid only under the mentioned conditions in which the scanner is the origin.

In the following sections, emphasis is put on instrument errors for two types of TLSs commonly used in engineering geodesy. The distinction is made only according to their architecture, presented in sec. 3.2. Next, non-correlating errors are defined in general for TLSs with the matrix structure that will be used in this work. Afterwards, for each TLS type, a calibration model is presented based on existing models in the literature (sec. 3.4 and 3.5) with their integration into the elementary error model.

3.2 Instrument types

Classifying laser scanners can be done according to several principles: (i) the distance measuring principle, (ii) the scanning mechanism, and (iii) the working range. Only the first two have a direct influence in the elementary error model, while the third is considered a scanner-specific capability that does not change the model.

The first criterion (i) differentiates between TLSs that use time-of-flight (TOF), phase difference, or a combination for the distance measurement. The main differences are measurement rate (also called scanning speed) and distance measurement accuracy. The latter is important and needs to be introduced into the elementary error model. Most manufacturers specify the range measurement accuracy differently, but common forms are range noise, range uncertainty, RMS (Root-Mean Square), and standard deviation. It is usually taken from technical specifications or white papers of the specific scanner. Efforts have been made by scientists to reach a common form of how range accuracy is given (Wunderlich et al. 2013), but manufacturers are free to specify this information as they prefer. Generally, phase-based

scanners are known to have better distance measurement accuracies than TOF scanners (Toth and Petrie, 2018), a fact that has been recently reconfirmed (cf. Suchocki, 2020). Exceptions to this rule are TOF scanners that use waveform digitizing technology or digital TOF. An extra category is not used here, since each manufacturer uses different terms to define this method. Some examples of TLSs from different manufacturers commonly used nowadays in engineering geodesy are given based on the distance measurement principle (i):

- Time-of-flight TLS: Riegl VZ600i, Trimble X7, Leica RTC360, Leica P40, Teledyne Optech Polaris, Stonex X300, Topcon GLS-2000 etc.;
- Phase-based TLS: Zoller+Fröhlich Imager 5016, Surphaser 400, Faro Focus S, Trimble X12 etc.

The list is far from complete and even if all scanners available today would be enumerated, the list would be outdated by the time of publication. For a good overview of the latest TLS from some of the most known manufacturers, the magazine or website Geo-matching (Geomares, 2022) is recommended.

Regarding criterion (ii) the scanning mechanism defines the scanner field-of-view (FOV), meaning that only a limited part of the volume around the scanner is measurable. With regard to this principle, Staiger (2003) classifies TLSs into three groups based solely on the scanner FOV (fig. 3.2). He distinguishes between panoramic scanners (fig. 3.2a), hybrid scanners (fig. 3.2b) and camera scanners (fig. 3.2c).

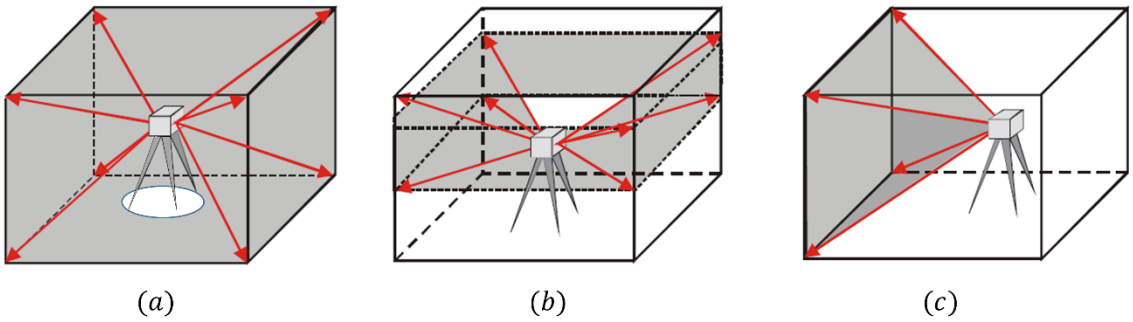

Figure 3.2. Classification of TLSs according to their field-of-view (a) Panoramic TLS, (b) Hybrid TLS, (c) Camera TLS (Staiger, 2003)

Panoramic scanners have the advantage of being able to measure most of the surrounding volume. Full angular coverage of 360° in the horizontal plane is obtained by the rotating platform (scanner head) around the vertical axis. Nowadays, this is a standard feature for all scanners. The advantage of panoramic scanners over all other types is the large vertical FOV, with values of up to 320°. The uncovered angle under the scanner is a physical limitation by the scanner head and tripod that leads to an empty space (void) in the full-dome point cloud. Nonetheless, panoramic scanners are implied in a wide range of reality capture applications, especially in indoor set-ups, e.g. industrial buildings, churches, etc. Also, outdoor applications that require geometry information above the scanner (e.g. tunnels, high-rise buildings) profit from this type of scanner.

The second type, called hybrid scanners, have the same full angular coverage in the horizontal plane but are limited in the vertical FOV to values usually reaching from 60° up to 120°. These limitations are given by the scanning mechanism, which contains either a rotating polygon

mirror or oscillating mirrors. The laser beam is deflected by this mirror and due to the mounting plane and mirror size, the beam can be deflected only within a relatively narrow vertical angle. A hybrid scanner is easily distinguishable by the scanner head, which has one side opening window. Nevertheless, this type of scanner is mostly found in outdoor long-range applications like open-pit mining, landslide monitoring, or general mapping applications in which no overhead information is needed (Petrie and Toth, 2018).

Finally, camera scanners have a limited FOV and resemble, in this sense, a normal photogrammetric camera. This is the architecture that some of the first scanners (e.g. Cyrax) used. Horizontal coverage was obtained by manually rotating the scanner. Two oscillating mirrors deflect the laser beam resulting in a raster pattern on the captured object. Current TLS manufacturers do not use this type of architecture, mainly because of the limited FOV.

According to the scanning range criterion (iii), even relatively new classifications (c.f. Shan and Toth, 2018) become outdated, due to the rapid development in TLSs. Therefore, no more emphasis will be put on scanning range, as it does not change the TLS elementary error model.

In the following sections, the elementary error model is implemented for only two types of scanners. According to the previous classification regarding the FOV (ii), the first one is a panoramic scanner (a) – the Leica HDS 7000 (equivalent of Zoller + Fröhlich Imager 5010) and the second a hybrid scanner (b) – the Riegl VZ2000. A more specific classification is needed, based solely on the scanning mechanism. This is relevant because different types of scanning mechanisms are prone to instrument-specific errors only applicable to that kind of scanner. In Joeckel and Stober (2008), equations describing the correction terms and geometric reductions for three kinds of scanners are given. However, these equations are only general, because the ones specific for the scanners in use are proprietary information of the TLS manufacturers. Luckily, the technical specifications of the two scanners used in this work indicate the mirror type (scanning mechanism). It is not always obvious from visual inspections. The Leica HDS7000 uses a 45° inclined monogon mirror. These types of mirrors have only one facet centered on the rotational axis (horizontal axis), sometimes referred to as truncated mirrors (cf. Stutz, 2012). Concerning the second scanner, the Riegl VZ2000 uses a three-facet reflective regular polygon mirror. More details about these types of mirrors are given in sec. 3.5 and appendix 1. Figure 3.3 shows a schematic non-scaled representation of the scanning mechanism of these two scanners and their relation to the EDM unit and scanner axes.

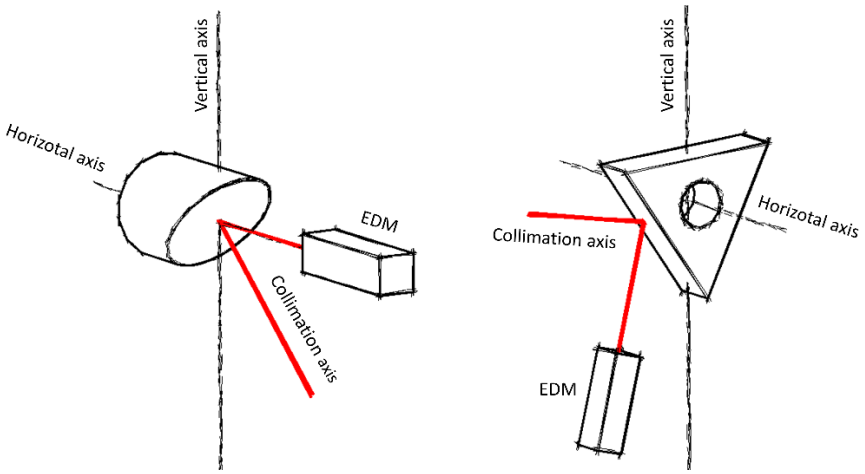

Figure 3.3. Schematic representation of scanning mechanism for panoramic scanners of type (a) with a 45° rotating monogon mirror (left); a three facet polygon mirror (right) for hybrid scanners of type (b).

3.3 Instrument-specific non-correlating errors

In any case, the technical specifications sheet can be used to obtain numerical values for variances introduced into the non-correlating elementary error group. For each measured polar element (R, λ, θ), there is a non-correlating elementary error type that affects each of the n observations with the same variance. In this sense, the three non-correlating elementary error types are:

- $\boldsymbol{\delta_\lambda}$ – horizontal angle noise;
- $\boldsymbol{\delta_\theta}$ – vertical angle noise;
- $\boldsymbol{\delta_R}$ – range noise.

The single TLS components (angle encoders and EDM) used to measure the aforementioned polar elements are, as all measurement systems, prone to random errors. The term "noise" depicts the remaining deviation after systematic effects have been corrected, which is understood in this work as a synonym for random deviation. It is beyond the purpose of this work to explain how the internal noise of angle encoders and EDM are established. Technical explanations can be found in Buchner et al. (2021) for EDM and white papers of encoders manufacturers (cf. Dr. Johannes Heidenhain GmbH, 2022) for optical angle encoders.

For each polar element, a different and independent TLS component is used, for e.g. angle encoders for the horizontal angle, angle encoders for the rotating mirror, and EDM unit for the distances (cf. Mettenleiter et al. 2015), and therefore the condition of stochastic independency for non-correlating error types stated in eq. 2.15 is satisfied:

$$E(\boldsymbol{\delta_\lambda} \cdot \boldsymbol{\delta_\theta}) = E(\boldsymbol{\delta_\lambda} \cdot \boldsymbol{\delta_R}) = E(\boldsymbol{\delta_\theta} \cdot \boldsymbol{\delta_R}) = \mathbf{0}. \tag{3.1}$$

The effect on each of the n observations is the same in the case of each non-correlating error type, therefore the VCM for each type is according to eq. 2.19 a scaled matrix:

$$\boldsymbol{\Sigma}_{\boldsymbol{\delta_\lambda}\boldsymbol{\delta_\lambda}} = \sigma_\lambda^2 \cdot \boldsymbol{I}_{(n \cdot n),} \tag{3.2}$$

$$\boldsymbol{\Sigma}_{\boldsymbol{\delta_\theta}\boldsymbol{\delta_\theta}} = \sigma_\theta^2 \cdot \boldsymbol{I}_{(n \cdot n),} \tag{3.3}$$

$$\boldsymbol{\Sigma}_{\boldsymbol{\delta_R}\boldsymbol{\delta_R}} = \sigma_R^2 \cdot \boldsymbol{I}_{(n \cdot n)}. \tag{3.4}$$

In what concerns the influencing matrix, the observation noise affects each observation directly in observation space (Schwieger, 1999, Kauker and Schwieger, 2017); in other words, the matrix $\mathbf{D}_{\boldsymbol{\delta_\lambda}} = \mathbf{D}_{\boldsymbol{\delta_\theta}} = \mathbf{D}_{\boldsymbol{\delta_R}} = \boldsymbol{I}$ is in each case the unity matrix. This results in the corresponding part of the VCM of non-correlating errors (see eq. 2.48, 3.2-3.4 and tab. 2.1) like follows:

$$\boldsymbol{\Sigma}_{\boldsymbol{ll},\boldsymbol{\delta_\lambda}} = \boldsymbol{\Sigma}_{\boldsymbol{\delta_\lambda}\boldsymbol{\delta_\lambda}} = \sigma_\lambda^2 \cdot \boldsymbol{I}_{(n \cdot n),} \tag{3.5}$$

$$\boldsymbol{\Sigma}_{\boldsymbol{ll},\boldsymbol{\delta_\theta}} = \boldsymbol{\Sigma}_{\boldsymbol{\delta_\theta}\boldsymbol{\delta_\theta}} = \sigma_\theta^2 \cdot \boldsymbol{I}_{(n \cdot n)}, \tag{3.6}$$

$$\boldsymbol{\Sigma}_{\boldsymbol{ll},\boldsymbol{\delta_R}} = \boldsymbol{\Sigma}_{\boldsymbol{\delta_R}\boldsymbol{\delta_R}} = \sigma_R^2 \cdot \boldsymbol{I}_{(n \cdot n)}. \tag{3.7}$$

In order to handle data easier, the individual matrices from eq. 3.5-3.7 are grouped into a VCM $\boldsymbol{\Sigma}_{\boldsymbol{ll-NC}}$ that contains the variances for each observation type in diagonal block matrices:

$$\boldsymbol{\Sigma}_{ll-NC} = \begin{bmatrix} \sigma_\lambda^2 & 0 & 0 & \cdots \\ 0 & \sigma_\theta^2 & 0 & \cdots \\ 0 & 0 & \sigma_R^2 & \cdots \\ \vdots & \vdots & \vdots & \ddots \end{bmatrix}. \tag{3.8}$$

This convention is applied to all other matrixes in this work. Each of the total n observations has its own block of 3x3, therefore the complete matrix size will be *(3n x 3n)*. Numeric values for matrixes with the structure from eq. 3.8 are given in tab. 3.1. They are taken from the original technical specifications of the two scanners (Leica Geosystems AG, 2011, Riegl Laser Measurement Systems GmbH, 2015). Note that for the Riegl VZ2000 angular noise values, there was no explicit indication in the technical specification. Therefore, the values in tab. 3.1 are those of the "angle measurement resolution" as indicated by the manufacturer. Data sheets of newer Riegl scanners now include an indication for angular accuracy, e.g. Riegl VZ400i and Riegl VZ2000i (Riegl Laser Measurement Systems GmbH, 2022). Some TLS manufacturers indicate the range noise for several distances and in relation to the target reflectivity (e.g. Basis Software Inc., 2021). In this work, this dependency is likewise modeled, but in the stochastic correlating group, as seen later (sec. 5.3.2).

Table 3.1. Values for the non-correlating errors of two scanners used in this work.

Correlation type	TLS	Range noise	Horizontal angle noise	Vertical angle noise
non-correlating errors	Leica HDS 7000	σ_R= 0.5 [mm]	σ_λ= 7.9 [mgon]	σ_θ= 7.9 [mgon]
non-correlating errors	Riegl VZ2000	σ_R= 5 [mm]	σ_λ= 0.55 [mgon]	σ_θ= 1.66 [mgon]

Here is it worth mentioning, that the VCM in eq. 3.8 is used by most practitioners for evaluating the measurement uncertainty in coordinate space (X, Y, Z) using the variance propagation law. The influencing matrices in this case are obtained by computing partial derivatives of the Cartesian coordinates (eq. 3.4-3.6) with regard to each of the polar elements. This is straightforward and not exemplified here. An example can be read in Lipkowski and Mettenleiter (2019).

3.4 Panoramic scanners

Generally, instruments for measuring angles and distances are prone to manufacturing errors, assembling errors, and displacements of different elements (Fialovszky, 1991). Terrestrial laser scanners are not an exception to this rule and therefore comparable with Total Stations (TS) or theodolites in many aspects (cf. Lichti and Lampard, 2008, Lichti, 2010). Apart from the beam deflecting system, the three axes (cf. fig. 3.3) are identical, therefore many errors that are well-known in TS or theodolites (cf. Stahlberg, 1997) have been adapted/integrated into TLS calibration models. Rietdorf et al. (2004) and Neitzel (2006a) can be counted among the first studies that applied such calibration models for TLS. The primer tested it on a self-developed laser scanner, whilst the second conducted experiments with a panoramic scanner, Z+F Imager 5003. Similarities between some TS systematics errors and how they can be corrected are also highlighted by Lichti (2017) with a ray-tracing approach. These are only a few examples of existing TLS calibration models. Although there are arguments about why to use one or another, none of them have been adopted as a standard for calibrating laser scanners.

Furthermore, there are special error parameters that can be modeled only for panoramic scanners.

However, there is a calibration model developed by the National Institute of Standards and Technology (NIST) that led to the definition of a standard procedure for evaluating the performance of laser scanners (NIST, 2016). After major TLS manufacturers tested their scanners at the NIST laboratory in a "run-off" in May 2016, a common standard was defined and it is meant to evaluate the instrument's precision along the three axes in a complete manner. The purpose is to reach a common set of technical specifications that all (or most) TLS manufacturers will use. Currently, the standard is published under the name ASTM E3125-17 and the first realizations of this standard are presented by Wang et al. (2020) and Muralikrishnan (2021). It is expected that this test procedure will be widely adopted in the TLS community and therefore, the calibration parameters (CPs) will be commonly understood. For this reason, the CPs in the NIST model are adopted as additional instrument elementary errors.

In consequence, the TS-similar model (cf. Kauker and Schwieger, 2017) is replaced by the abovementioned NIST model. This was defined by Muralikrishnan et al. (2015) and uses a set of 18 CPs also called mechanical and optical misalignments to model the instrumental errors of panoramic laser scanners. Throughout this contribution, these CPs are considered instrument-related elementary errors, but they will be further addressed as CPs to maintain coherence with other publications. Also, the same denotation x_i is maintained for comprehension. Not all 18 parameters are determinable through typical calibration routines. For this reason, a simplified version of this model has been adapted by Medić et al. (2017) and used for high-end panoramic scanners. From the 18 CPs, they determine 10 as relevant (see tab. 3.2) in reducing most of the systematic instrumental errors, but thorough this thesis, only the random component of the CPs is of interest.

Table 3.2. Parameter of TLS calibration model (Muralikrishnan et al., 2015, Medić et al., 2017).

CP	Tilts/Angular Errors	CP	Offsets/Metric Errors
x_4	Vertical index error	x_{1n}	Horizontal beam offset
x_{5n}	Horizontal beam tilt	x_{1z}	Vertical beam offset
x_{5z}	Vertical beam tilt	x_2	Horizontal axis offset
x_6	Collimation axis error	x_3	Mirror offset
x_7	Horizontal axis error (tilt)	x_{10}	Zero point error

Besides the graphical representation of the CPs, more detailed explanations are not given here, since they have been extensively discussed by Muralikrishnan et al. (2015) and Medić et al. (2017). The following figures (inspired by Muralikrishnan et al., 2015; Medić et al., 2017; Muralikrishnan, 2021) illustrate the CPs separately for clearness. They are designed with a CAD program and perspectives are changed in order to have a clear view. In reality, the scanner may be affected by several or all CPs, some of which are hard to separate and sensitive only to special calibration setups (two-face measurements, in-line measurements, etc.). The reason for representing the parameters graphically is to offer an impression about the absolute value of each CP and more important, along which axis does its variation (slightly different values compared to the actual position) have an influence on the observations. In all cases, the ideal position of the components (green) and the actual position (red) are represented. Note that the 45° monogon rotating mirror is not annotated in the figures because it is self-evident.

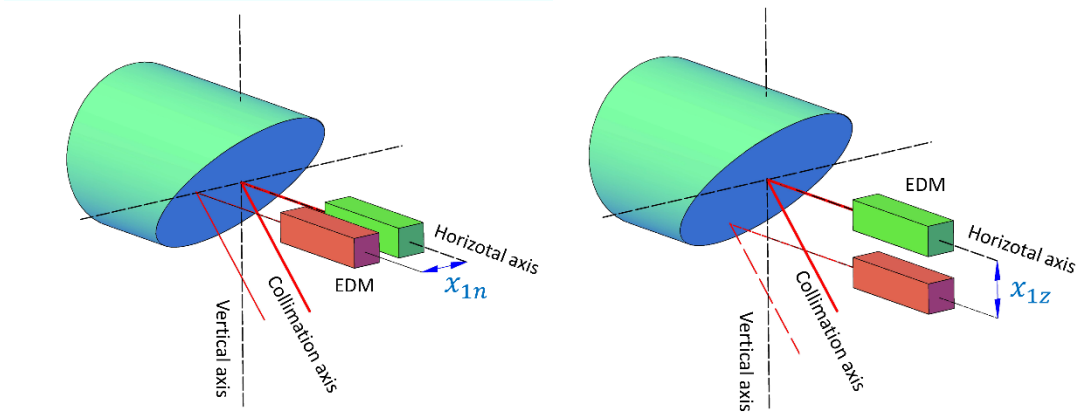

Figure 3.4. Schematic representation of scanning mechanism and the horizontal beam offset x_{1n} (left) and vertical beam offset x_{1z} (right). Green=ideal position, red=actual position.

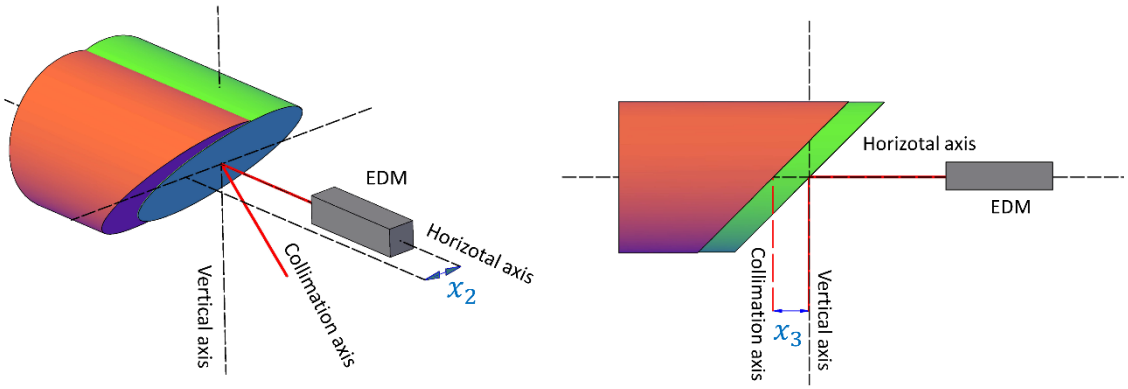

Figure 3.5. Schematic representation of scanning mechanism and the horizontal axis offset x_2 (left) and mirror offset x_3 (right). Green=ideal position, red=actual position.

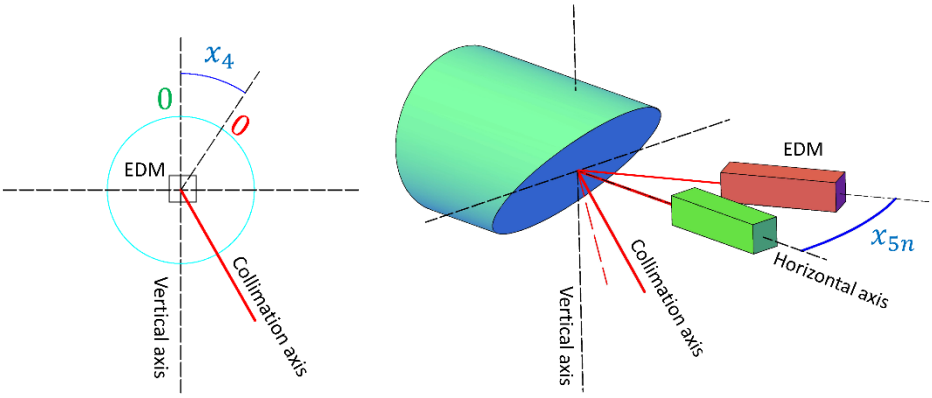

Figure 3.6. The vertical index error x_4 with horizontal axis normal to the view (left) and horizontal beam tilt x_{5n} (right). Green=ideal position, red=actual position.

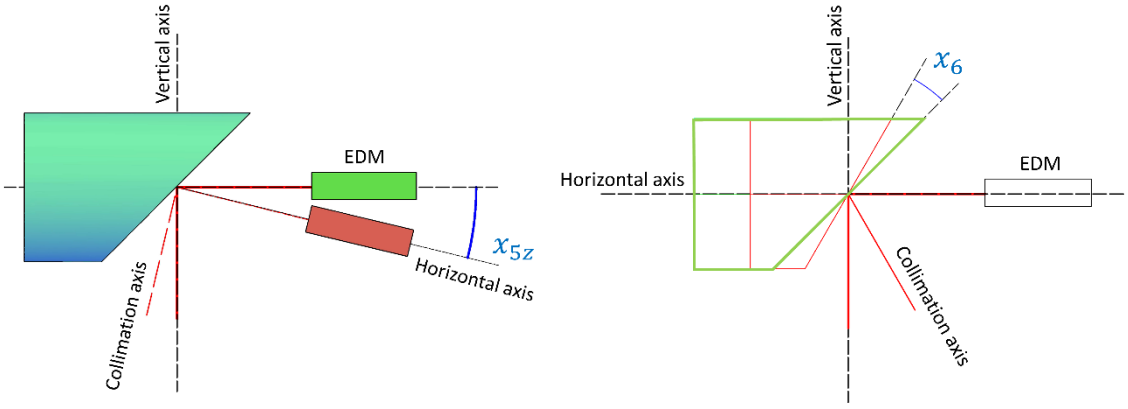

Figure 3.7. Side view representation of scanning mechanism and the vertical beam tilt x_{5z} (left) and collimation axis error x_6 (right). Green=ideal position, red=actual position.

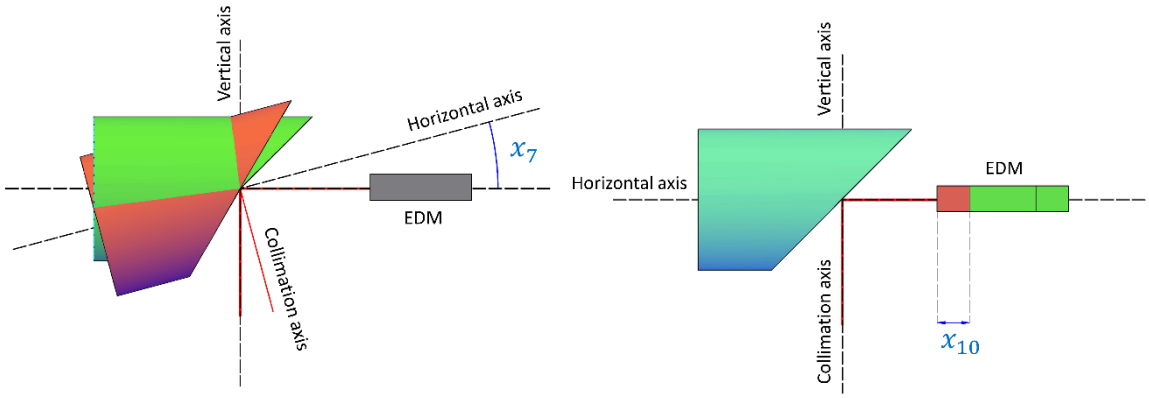

Figure 3.8. Side view representation of scanning mechanism and the horizontal axis error/tilt x_7 (left) and zero point error x_{10} (right). Green=ideal position, red=actual position.

It is arguable that not all instrument-specific errors are taken into consideration in this calibration model, but this fact is also admitted by the model authors. In some cases, additional correction parameters like the scale factor or cyclic phase errors (Fialovszky, 1991) for distance measurements or tumbling error (cf. Neitzel, 2006c, Chow et al., 2012) for the angles may be relevant and can be included in the model. The reason why this is not done here is related to the operating range of the scanner in cause and undergoing research on some topics, e.g. cyclic phase errors (Wieser et al., 2022). The ambiguity of the Leica HDS7000 can be solved up to 187 m, therefore a scale factor in a sense of a ppm correction is negligible at these distances. As regards the tumbling error, Neitzel (2006c) estimates the effect on the plane coordinates in the mm interval (e.g. up to 3 mm at 15 m caused by a tumbling error of 0.2 mm/m), which was presumed to be related to the asymmetrical scanner body. This type of construction is not used in newer TLSs.

In Kerekes and Schwieger (2021) two calibration models are presented and compared with the same data set and equivalent variances. One is a TS model (cf. Neitzel, 2006a) and the second is the currently used NIST model. Outcomes point out that both models try to represent the instrumental errors of panoramic TLS as well as possible considering the following two criteria: some error sources may not be relevant in certain situations and the effect of some error sources can be neglected for individual observation types (R, λ, θ). For example, the TS similar model considers a scale factor that may be advantageous for panoramic scanners that

have an extended range measurement capability (e.g. Z+F Imager 5016 up to 350 m). There is, however, no scale factor in the NIST model. Also, the tumbling error is included in the TS model and neglected in the NIST model. The main reason for choosing the latter was already highlighted at the beginning of sec. 3.3. Moreover, it can be observed from the representation of the CPs in the NIST model, that some parameters are specific only for panoramic scanners with 45° rotating mirrors (e.g. x_{1z}, x_3) which makes it appropriate for modeling errors of this specific type of TLS. The model's popularity is proven by the number of recent publications that deal with scanner self-calibration or assert the stability of the parameters regarding changing environment conditions (cf. Wang et al., 2017, Medić et al., 2019, Janßen et al., 2021).

Finally, the CPs are mathematically modeled as additive correction terms Δp (cf. Muralikrishnan et al., 2015, Chow et al., 2012) to the measured polar coordinates, e.g. $p_{corrected} = p_{measured} + \Delta p$. Only correction terms Δp are given here, where p is replaced in each case with the corresponding quantity:

$$\Delta\lambda = \frac{x_{1z}}{R\tan\theta} + \frac{x_3}{R\sin\theta} + \frac{x_{5z} - x_7}{\tan\theta} + \frac{2x_6}{\sin\theta} + \frac{x_{1n}}{R}, \tag{3.9}$$

$$\Delta\theta = \frac{(x_{1n} + x_2)\cos\theta}{R} + x_4 + x_{5n}\cos\theta - \frac{x_{1z}\sin\theta}{R} - x_{5z}\sin\theta, \tag{3.10}$$

$$\Delta R = x_2\sin\theta + x_{10}. \tag{3.11}$$

Equations 3.9 to 3.11 also simultaneously show the linear dependences between the CPs. This is given by the same geometry influencing factors (e.g. range and function of vertical angles) between CPs within the additive correction terms (e.g. x_3 and x_6 or x_{1z} and x_{5z}).

Another remark on the CPs interdependency is related to the apparently identical effect on the observations that some pairs of CPs have (e.g. fig. 3.4 left and fig. 3.5 left or fig. 3.5 right and fig. 3.8 right). Regarding the zero point error x_{10} and mirror offset x_3, one might say that both of them affect the ranges in the same manner, therefore they are not separable. However, x_3 is also modeled for the horizontal angle corrections term $\Delta\lambda$, therefore separation is possible because x_3 is sensitive to two-face measurements in the horizontal angle direction. The same applies to x_{1n} and x_2, which cannot be distinguished based on their graphical representation, but lead to different effects on the observations. Both show a two-face sensitivity in the vertical angle direction, however, x_2 is additionally sensitive in the distance measurement direction while the scanner is placed in line and in between two targets (Muralikrishnan et al., 2015).

Applying the elementary error theory to this model is straightforward. In the following example, the structure of the influencing matrix and VCM of functional correlating errors are presented for a single observation. As presumed, for more observations, the matrices are scaled accordingly. The variances of the CPs are arranged in the VCM of the functional correlating errors as follows:

$$\boldsymbol{\Sigma}_{\xi\xi} = \begin{pmatrix} {\sigma_{x_{1n}}}^2 & 0 & 0 & 0 & 0 & 0 & 0 & 0 & 0 & 0 \\ 0 & {\sigma_{x_{1z}}}^2 & 0 & 0 & 0 & 0 & 0 & 0 & 0 & 0 \\ 0 & 0 & {\sigma_{x_2}}^2 & 0 & 0 & 0 & 0 & 0 & 0 & 0 \\ 0 & 0 & 0 & {\sigma_{x_3}}^2 & 0 & 0 & 0 & 0 & 0 & 0 \\ 0 & 0 & 0 & 0 & {\sigma_{x_4}}^2 & 0 & 0 & 0 & 0 & 0 \\ 0 & 0 & 0 & 0 & 0 & {\sigma_{x_{5n}}}^2 & 0 & 0 & 0 & 0 \\ 0 & 0 & 0 & 0 & 0 & 0 & {\sigma_{x_{5z}}}^2 & 0 & 0 & 0 \\ 0 & 0 & 0 & 0 & 0 & 0 & 0 & {\sigma_{x_6}}^2 & 0 & 0 \\ 0 & 0 & 0 & 0 & 0 & 0 & 0 & 0 & {\sigma_{x_7}}^2 & 0 \\ 0 & 0 & 0 & 0 & 0 & 0 & 0 & 0 & 0 & {\sigma_{x_{10}}}^2 \end{pmatrix}. \tag{3.12}$$

The same order as on the main diagonal in eq. 3.12 must be respected along the lines of the influencing matrix $\boldsymbol{F}$, therefore the partial derivatives of each observation group (R, λ, θ) must be placed accordingly with regard to the mentioned diagonal. Finally, the influencing matrix as presented in eq. 2.28 and according to the conventions in eq. 3.8 (first line-horizontal angle λ, second-vertical angle θ, and third-range R) has the following structure:

$$\boldsymbol{F} = \begin{pmatrix} \frac{1}{R} & \frac{1}{R\tan(\theta)} & 0 & \frac{1}{R\sin(\theta)} & 0 & 0 & \frac{1}{\tan(\theta)} & \frac{2}{\sin(\theta)} & -\frac{1}{\tan(\theta)} & 0 \\ \frac{\cos(\theta)}{R} & -\frac{\sin(\theta)}{R} & \frac{\cos(\theta)}{R} & 0 & 1 & \cos(\theta) & -\sin(\theta) & 0 & 0 & 0 \\ 0 & 0 & \sin(\theta) & 0 & 0 & 0 & 0 & 0 & 0 & 1 \end{pmatrix}. \tag{3.13}$$

The corresponding part in the SVCM (depicted by letters with indices p), is given by:

$$\boldsymbol{F} \cdot \boldsymbol{\Sigma}_{\xi\xi} \cdot \boldsymbol{F}^{\boldsymbol{T}} = \begin{pmatrix} a_p & d_p & 0 \\ d_p & b_p & e_p \\ 0 & e_p & c_p \end{pmatrix}, \tag{3.14}$$

$$a_p = \frac{4\,{\sigma_{\mathrm{x6}}}^2}{\sin(\theta)^2} + \frac{{\sigma_{\mathrm{x7}}}^2}{\tan(\theta)^2} + \frac{{\sigma_{\mathrm{x5z}}}^2}{\tan(\theta)^2} + \frac{{\sigma_{\mathrm{x1n}}}^2}{R^2} + \frac{{\sigma_{\mathrm{x3}}}^2}{R^2\sin(\theta)^2} + \frac{{\sigma_{\mathrm{x1z}}}^2}{R^2\tan(\theta)^2}, \tag{3.15}$$

$$b_p = {\sigma_{\mathrm{x5n}}}^2\cos(\theta)^2 + {\sigma_{\mathrm{x5z}}}^2\sin(\theta)^2 + {\sigma_{\mathrm{x4}}}^2 + \frac{{\sigma_{\mathrm{x2}}}^2\cos(\theta)^2}{R^2} + \frac{{\sigma_{\mathrm{x1n}}}^2\cos(\theta)^2}{R^2} + \frac{{\sigma_{\mathrm{x1z}}}^2\sin(\theta)^2}{R^2}, \tag{3.16}$$

$$c_p = {\sigma_{\mathrm{x2}}}^2\sin(\theta)^2 + {\sigma_{\mathrm{x10}}}^2, \tag{3.17}$$

$$d_p = \frac{{\sigma_{\mathrm{x1n}}}^2\cos(\theta)}{R^2} - \frac{{\sigma_{\mathrm{x5z}}}^2\sin(\theta)}{\tan(\theta)} - \frac{{\sigma_{\mathrm{x1z}}}^2\sin(\theta)}{R^2\tan(\theta)}, \tag{3.18}$$

$$e_p = \frac{{\sigma_{\mathrm{x2}}}^2\cos(\theta)\sin(\theta)}{R}. \tag{3.19}$$

According to eq. 3.14, it can be seen which groups of observations show functional correlations just based on the matrix structure. In this sense, there is no correlation between the terms a_p (eq. 3.15) and c_p (eq. 3.17), therefore horizontal angles and distance measurements do not show functional relations according to this calibration model. There are no common influencing CPs between the terms a_p and c_p in this case.

All other non-diagonal terms d_p (eq. 3.18) and e_p (eq. 3.19) indicate that functional correlations should be expected between the respective observation groups. Basically, they resemble the common CPs for each of the pairs a_p and b_p, as well as b_p and c_p, respectively. Their values are directly influenced by the variances of the common CPs as seen in eq. 3.18 and 3.19. But this does not give any hint about the correlation strength (e.g. high positive or negative correlation). Besides the CP variances, each term contains numerical values of the observations, in this case only distances and vertical angles (see eq. 3.15 to 3.19), meaning that their correlations will also depend on the value of individual observations. Similar values for neighboring points lead to high correlations in this case, which is not a surprise since the origin of the observations is the same instrument (Heunecke, 2004) and the scanning geometry is similar. Concrete examples of correlation levels are given for one study case in chapter 6.

Concerning the main diagonal elements a_p, b_p, and c_p, a special effect can be seen for the terms b_p, and c_p. According to eq. 3.16, the variance of one of the CPs - ${\sigma_{\mathrm{x4}}}^2$ has a direct additive effect in the VCM. If this is compared to how non-correlating errors ${\sigma_{\theta}}^2$ (see. sec. 3.2) affect vertical angles, the exact same additive effect is seen here. One might be tempted to classify the vertical index error x_4 as a non-correlating error at this point, due to its identical effect on the variances. This is false because the vertical index error x_4 also has an effect on the covariances, therefore correlations. If the same operation as in eq. 3.14 is performed for two observations (using appropriately scaled matrices), this becomes obvious, between two observations of the same type. The same phenomenon applies to the zero point error x_{10} when compared to range noise ${\sigma_{\mathrm{R}}}^2$. Only judging by variances, there is no difference between two elementary errors affecting the observations; however, the correlations make a difference.

Another note is made with respect to scanning geometry that other authors consider a separate error source (cf. Kuhlmann and Holst, 2018). In each term of the functional correlating error group, the observations influence the magnitude of variances and covariances, either directly or inversely proportionally. For this reason, choosing a different scanner station point leads to other values of the observations, and thereafter other values in the VCM. This means that there is no need for a separate category in which scanning geometry is classified as an independent error group. The variances and covariance are per nature related to the scanning geometry (see eq. 3.14), especially with the distances and vertical angles. A counterargument may be that the angle of incidence between the scanned object and TLS beams is neglected here. Nevertheless, angles of incidence are considered in the elementary error model in the object surface-related errors as influencing factors. This is treated later in section 5.4.

Returning to the TLS calibration model for panoramic scanners, numerical values for the variances of the CPs are obtained after a TLS calibration. In this work, the Leica HDS7000 has been calibrated within the COLLECTOR project in November 2020 in a specially designed calibration field at the University of Bonn. This calibration field is designed according to the specifications proposed by NIST, therefore the target distribution and appropriate scanner station points allow the determination of a set of 10 CPs. The remaining 8 CPs from the complete NIST model (18 CPs) cannot be obtained in this calibration field. In any case, the results of calibration are the mean value for each parameter and its corresponding standard deviations. The latter are included in the elementary error model. They are considered realistic and preferred over the values from other publications on the topic with the same scanner (cf. Kerekes and Schwieger, 2021). Table 3.3 shows only the values for the CP's standard deviations.

Table 3.3. Overview of the instrumental elementary errors for the Leica HDS 7000 with standard deviations (Courtesy from COLLECTOR project)

Correlation type	CP name [unit]	Standard deviation
Functional correlating errors	x_{1n} [mm]	$\sigma_{x_{1n}}$ = 0.140
	x_{1z} [mm]	$\sigma_{x_{1z}}$ = 0.220
	x_2 [mm]	σ_{x_2} = 0.020
	x_3 [mm]	σ_{x_3} = 0.130
	x_4 [mgon]	σ_{x_4} = 0.448
	x_{5n} [mgon]	$\sigma_{x_{5n}}$ = 1.738
	x_{5z} [mgon]	$\sigma_{x_{5n}}$ = 1.598
	x_6 [mgon]	σ_{x_6} = 0.272
	x_7 [mgon]	σ_{x_7} = 1.929
	x_{10} [mm]	$\sigma_{x_{10}}$ = 0.060

3.5 Hybrid scanner

Calibration models for hybrid terrestrial laser scanners are among the least studied models in the engineering geodesy community. The reasons are manifold.

First, most of the tasks met in TLS are related to midrange surveys of scenes including building-scale objects (Spring, 2020b). Scanners that measure up to 400 m are sufficient for most 3D scenes in civil engineering and cultural heritage projects.

Second, the scanning mechanism of hybrid scanners with polygon mirrors is more complex than the mechanism of panoramic scanners with monogon mirrors (cf. Joeckel and Stober, 2008) because of additional reductions that need to be made (cf. fig. 3.9 right). To name only some examples, rotating polygon mirror scanners have a sinusoidal varying rangefinder systematic effect due to the offset of the mirror surfaces from the rotation axis (Lichti & Skaloud, 2010). This type of variation is shown for a mirror with 3 facets and an opening window (FOV) of 100° in fig. 3.9 left. Although the laser beam falls on the complete length of each facet while the mirror rotates, only a restricted area of the facet deflects the beam outside of the scanner's housing, in other words within the FOV. This is also the explanation for the typically restricted FOV of hybrid scanners. The three colored areas in fig. 3.9 left depict the FOV interval for each facet, also referred to as the active area of the mirror. Moreover, the EDM source can be mounted in different inclinations with respect to the vertical axis and not necessarily parallel to it as in fig. 3.9. This induces additional reductions that need to be made.

Third, calibration models used by TLS manufacturers are proprietary information, therefore confidential.

Fourth, high-end scanners of this type are generally more expensive, a fact that is understandable if one considers the intricacies involved in manufacturing high-quality polygon mirrors (Stutz, 2012).

Due to these reasons, the number of publications that deal with the calibration of terrestrial hybrid scanners with polygon mirrors is, to the author's best knowledge, very reduced. Nevertheless, the key references are mentioned in this section.

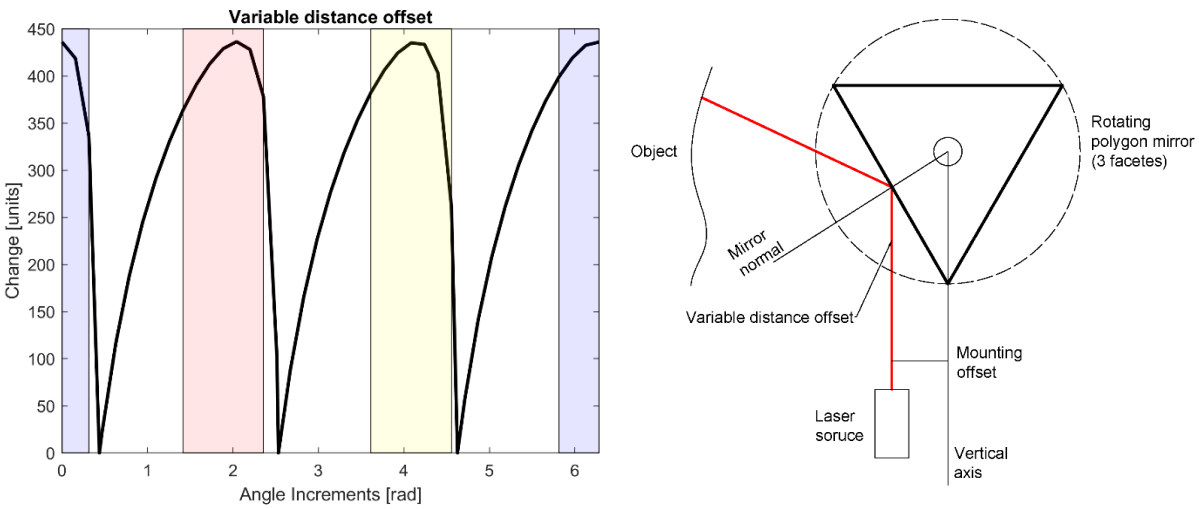

Figure 3.9. Left: Variable distance offset caused by the rotating polygon mirror and offset between EDM and vertical axis; colors depict the active area for each facet. Right: schematic example scanning mechanism and beam path for a polygon scanning head.

A similar calibration model as the one presented in sec. 3.4 has been defined for hybrid laser scanners by Lichti (2007) and Chow (2013). It is not specific only for scanners with polygon mirrors, therefore sources of errors like the ones mentioned above are not completely addressed. Nevertheless, it will be used in this work because it was verified for a hybrid scanner similar to the Riegl VZ2000 (Schneider, 2009) and numeric values are available. According to the author's best knowledge, no specific calibration model has been published up to now, a fact that is understandable due to the following reasons. The main challenge is to determine the magnitude of the CPs. Other types of calibration fields and special instruments are needed for this purpose. To start with, almost all CPs of panoramic scanners are obtained by two-face scanning scenarios. In the case of hybrid scanners, there is physically no second face, because the field of view of the hybrid scanners is only on one side of the scanner. In this case, calibrations that include terms sensitive to two-face measurements cannot be considered. Another issue that requires special conditions has to do with the maximum measurement range. Usually, scanners with this type of architecture are long-range scanners, therefore CPs specific for long ranges, like a scale factor, can only be obtained if calibration lines (e.g. pillars) with long distances (up to 3 km) are available and accessible. Regarding this aspect, calibration procedures that are applied to total stations are recommended for distance-specific CPs. Another argument is that scanners of this type are mostly used in less frequently met applications like rock cliff monitoring, and open pit mining if compared to other 3D acquisition applications (e.g. for 3D modeling). Finally, the TLS manufacturer calibration model remains confidential and a similar standard as the one presented by NIST is not available up to now.

An alternative calibration model that adapts a TS model again has been introduced by González-Aguilera et al. (2011). In comparison with the one mentioned above, it is less complex and the authors developed a self-calibration software (CalibTLS) that estimates the CPs after a scan routine. But it will not be used in this work, because it is considered less representative of hybrid TLS.

The functional model defined by Lichti (2007) and Chow et al. (2013) foresees correction terms for the observations that are added analog to the model in sec. 3.4. The ones applicable for the

current TLS are depicted with letters *a* for the calibration terms of horizontal angles, *b* for calibration terms of vertical angles, and finally, *c* for the measured distance calibration terms. This convention is maintained for coherence with the mentioned publications, although there are some parameters that are identical or similar to the NIST model (cf. sec. 3.4). A parallel is likewise given here for the ones that have an equivalent. Their name and brief meaning are explained in table 3.4. For more details about these parameters and which ones apply to certain scanners, the reader is advised to consult Chow et al. (2013).

Table 3.4. Parameter of TLS calibration model (Schneider, 2009, Chow et al. 2013).

Type	CP	Tilts/Angular Errors	Equivalent in NIST model (sec. 3.4)
Tilts/ Angular Errors	b_1	collimation axis error	x_6
	b_2	horizontal axis error	x_7
	b_6 , b_7	non-orthogonality of the plane containing the horizontal angle encoder and the vertical axis	partially x_{5z}
	b_8	empirical parameter for compensation of remaining systematic effects (possibly wobbling of the horizontal axis)	no equivalent
	c_0	vertical circle index error	x_4
	c_4	empirical parameter to model a sinusoidal errors function of the horizontal direction with period of 120° (cosine term)	no equivalent
Offsets/ Metric Errors	a_0	zero point error	x_{10}
	a_1	scale error	no equivalent
	a_2	quadric scale error	no equivalent
	b_3, b_4	horizontal circle eccentricities	x_2
	b_5	eccentricity of the collimation axis with respect to the vertical axis	x_3
	c_1, c_2	vertical circle eccentricities	x_{5n} and x_{5z}
	c_3	eccentricity of the collimation axis with respect to the horizontal axis	x_{1n}

Only the terms used in the model simplified by Schneider (2009) are adopted. The simplification is justified by the fact that not all of the CPs can be determined as significant after a calibration. He applied it for a Riegl LMS-420i (similar construction as Riegl VZ2000) and could determine some of the CPs as significant for the calibrated results. Some of them are negligible, some are not determinable or separable, and therefore the used model is restricted to the minimum number of CPs that can be identified with a given calibration field.

Following Schneider (2009), the CPs for each observation for a hybrid scanner can be defined as:

$$\Delta\lambda = b_1 \sec(\theta) + b_2 \tan(\theta) + b_3 \sin(\lambda) + b_4 \cos(\lambda) + \arcsin\left(\frac{b_5}{R}\right) + b_6 \sin(2\lambda) + b_7 \cos(2\lambda) + b_8 \cos(3\lambda), \tag{3.20}$$

$$\Delta\theta = c_0 + c_1 \sin(\theta) + c_2 \cos(\theta) + \arcsin(c_3/R) + c_4 \cos(3\lambda), \tag{3.21}$$

$$\Delta R = a_0 + a_1 R + a_2 R^2. \tag{3.22}$$

Out of all 15 CPs, only seven of them have numerical values in the above-mentioned publication. The reasons are related to the limited range in the calibration field and the impossibility of two-face measurements. Therefore, the partial derivatives in the influencing matrix $\boldsymbol{F}$ and corresponding VCM are given only for the estimated seven CPs. If more complex calibration fields are available and other CPs can be determined, the same principle applies.

Analog to the panoramic scanner, the structures of the influencing matrix and VCM of functional correlating errors are exemplified for one observation. The variances of the determined CPs are arranged in the VCM of the functional correlating errors as follows:

$$\boldsymbol{\Sigma_{\xi\xi}} = \begin{pmatrix} {\sigma_{a_0}}^2 & 0 & 0 & 0 & 0 & 0 & 0 \\ 0 & {\sigma_{a_1}}^2 & 0 & 0 & 0 & 0 & 0 \\ 0 & 0 & {\sigma_{b_4}}^2 & 0 & 0 & 0 & 0 \\ 0 & 0 & 0 & {\sigma_{b_6}}^2 & 0 & 0 & 0 \\ 0 & 0 & 0 & 0 & {\sigma_{c_0}}^2 & 0 & 0 \\ 0 & 0 & 0 & 0 & 0 & {\sigma_{c_1}}^2 & 0 \\ 0 & 0 & 0 & 0 & 0 & 0 & {\sigma_{c_4}}^2 \end{pmatrix}. \tag{3.23}$$

The corresponding influencing matrix as presented in eq. 2.28 is arranged as before with the elements on the first line-horizontal for angle λ, second line for vertical angle θ and third line for range R has the following structure:

$$\boldsymbol{F} = \begin{pmatrix} 0 & 0 & \cos(\lambda) & \sin(2\lambda) & 0 & 0 & 0 \\ 0 & 0 & 0 & 0 & 1 & \sin(\theta) & \cos(3\lambda) \\ 1 & R & 0 & 0 & 0 & 0 & 0 \end{pmatrix}. \tag{3.24}$$

The corresponding part in the SVCM (depicted by letters with indices h), is given by:

$$\boldsymbol{F \cdot \Sigma_{\xi\xi} \cdot F^T} = \begin{pmatrix} f_h & 0 & 0 \\ 0 & g_h & 0 \\ 0 & 0 & h_h \end{pmatrix}, \tag{3.25}$$

$$f_h = {\sigma_{\mathrm{b4}}}^2 \cos(\lambda)^2 + {\sigma_{\mathrm{b6}}}^2 \sin(2\,\lambda)^2, \tag{3.26}$$

$$g_h = {\sigma_{\mathrm{c0}}}^2 + {\sigma_{\mathrm{c1}}}^2 \sin(\theta)^2 + {\sigma_{\mathrm{c4}}}^2 \cos(3\,\lambda)^2, \tag{3.27}$$

$$h_h = R^2\, {\sigma_{\mathrm{a1}}}^2 + {\sigma_{\mathrm{a0}}}^2. \tag{3.28}$$

This is true only for the model that considers the CPs variances shown in eq. 3.23. In this case, the multiplied matrices lead to blocks of diagonal matrices (here only for one observation) as presented in eq. 3.25. In contrast to the previous model (sec. 3.4), the CPs are separated for each observation group (see tab 3.4), therefore covariances between the groups of observations (horizontal angles, vertical angles, and ranges) do not exist by definition. It can also be seen that there is no common CP that appears in two or more corrections terms (cf. eq. 3.20-3.22). Although the matrix in eq. 3.25 should belong to the non-correlating group due to its off-diagonal values, it still belongs to the functional correlating group, a fact that becomes clear when matrices for more than two observations are computed. They all have covariances in the upper and lower triangle and are therefore fully populated.

In contrast to the variances and covariances obtained for the calibration model for panoramic scanners (cf. eq. 3.15-3.19) where only the vertical angles and ranges play a role, here all groups are involved. This also leads to numeric values that are similar if the observations of neighboring points are analyzed (e.g. similar polar elements).

It should also be noted that a model with numeric values for all 15 CPs (cf. tab 3.4) is more complex and correct, but in lack of realistic values for the variances, it is not included in the elementary error model in this approach. As already highlighted (cf. Appendix 1), calibration models for hybrid laser scanners are less studied, but if this improves in the future and a better model than the one from eq. 3.20-3.22 is available, it can be easily integrated into the elementary error model in the same way realized here. The methodology remains the same.

Finally, the numerical values for CPs obtained in Schneider (2009) in a calibration field with the maximal possible measurable distance of 60 m for the Riegl LMS-Z420i are assumed to be representative values for the scanner used in this work, the Riegl VZ2000.

Table 3.5. Overview of the instrumental elementary errors used for the Riegl VZ2000 here as standard deviations (Schneider, 2009)

Correlation type	CP name [unit]	Standard deviation
Functional correlating errors	a_0 [mm]	$\sigma_{a_0} = 0.34$
	a_1 [ppm]	$\sigma_{a_1} = 40$
	b_4 [mgon]	$\sigma_{b_4} = 3.18$
	b_6 [mgon]	$\sigma_{b_6} = 1.91$
	c_0 [mgon]	$\sigma_{c_0} = 1.08$
	c_1 [mgon]	$\sigma_{c_1} = 1.85$
	c_4 [mgon]	$\sigma_{c_4} = 0.64$

These values are used in applications presented in chapter 6. The analysis highlights their contribution to the uncertainty budget on one side and also their importance for the statistical evaluation of deformations with the aid of fully populated VCMs on the other side.

4. Atmosphere-specific errors

4.1 The lower atmosphere

Most authors that consider the propagating environment of TLS observations as an error source, refer to this medium as the "atmosphere" (cf. Zhao, 2019; Kuhlmann & Holst, 2018; Ogundare, 2016). In all cases, the authors definitely refer to the lower layers of the atmosphere, more precisely the lower part of the troposphere, called the boundary layer (see fig. 4.1). It can be up to a few thousand meters above the surface, but for convenience, the term atmosphere and boundary layer will be considered the same throughout this work. Studying the atmospheric parameters in this layer is a science in itself, therefore the focus here is only on the influencing sources that are relevant for TLS measurements. General information about the complex nature of the atmosphere can be obtained from handbooks (Geiger et al., 2003; Jacobson, 2005; Stull, 1988).

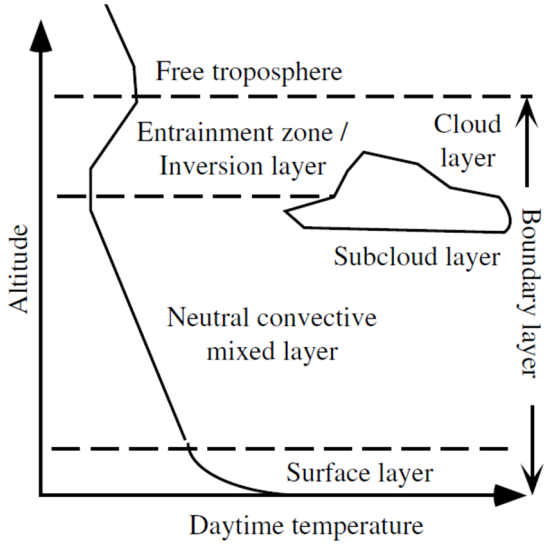

Figure 4.1. Example of air temperature change in the atmosphere's boundary level during daytime (Jacobson, 2005).

Andrews (2019) presents the common division of the lower atmosphere into two major regimes, first the atmospheric boundary layer (ABL) and the free atmosphere. The ABL is considered the lowest layer of the troposphere, roughly 1-2 km above the Earth's surface. In this layer, the surface heating leads to convective instability (cf. Kassera and Pietsch, 2020; Geiger et al., 2003), therefore to strong optical turbulence. The first couple of hundred meters above ground define the surface layer, approximately 10% of the ABL, where its properties are determined by the air-to-ground differences in atmospheric parameters. In all TLS applications, the observation lines fall within this layer. Exceptions are applications of long-range scanning in mountainous areas (cf. De Wekker and Kossmann, 2015; Voordendag et al., 2021) or open pit mining (Long et al., 2018). Regarding the free atmosphere, it refers to the layers above the ABL in which the effect of the Earth's surface heating becomes negligible.

Besides this rough separation, a more detailed one must be made according to local conditions and their influence on atmospheric conditions. Scientists refer to this as microclimate. The microclimate of a particular location can be defined as the statistical state of the atmosphere in

the layer being affected directly by the characteristic of the underlying surface. Processes that determine the microclimate of a location involve time scales that vary from a few seconds to several years. Depending on this scale, one may refer to a microclimate variation as the weather in the sense of changes from day to day. Moreover, local topography is also important if areas contain features with extreme height differences, e.g. deep valleys, canyons, glaciers, or high-rise buildings in urban areas (Rotach and Calanca, 2003). In fig. 4.2 each of the microclimate zones depicted with M1…M11 is strongly affected by the natural and artificial features in that area, topography, and atmospheric conditions. In this sense, the more is known about each zone, the closer the modeling of those zones will be to reality. Nevertheless, it is not expected that the modeling can be entirely deterministic because there are so many unknown factors and phenomena that interfere (Box et al., 2008). This diminishes the general character of the assumed model for that zone.

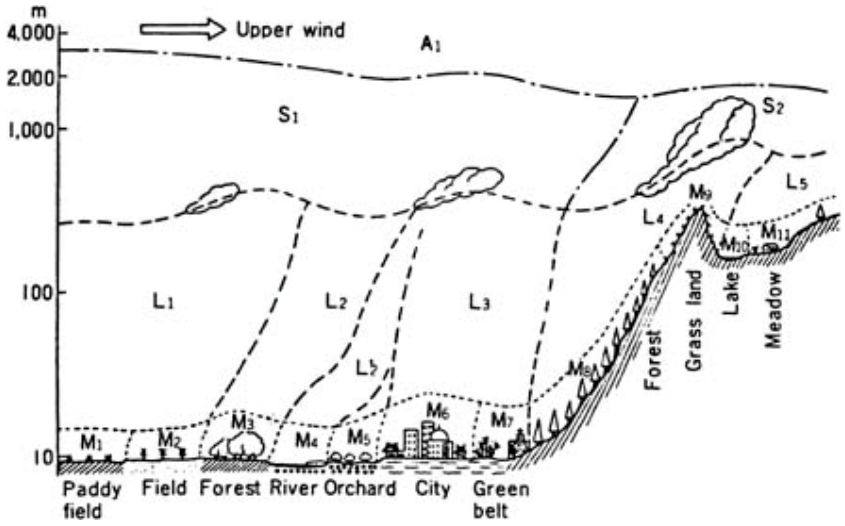

Figure 4.2. The microclimate zones in a schematic representation by Yoshino M. M. (1987)

Regardless of the effects on specific geodetic observations, the atmosphere can cause several effects on light. Sunlight shining on dust or ice crystals in the atmosphere can produce a lot of optical spectacles like rainbows, halos, blue sky, red sunset, coronas, green flash, and many more optical phenomena. Additionally, phenomena like rain, snow, sleet, fog, haze, pollution, etc., are atmospheric factors that affect visibility. All these factors can also affect the transmission of electromagnetic radiation through the atmosphere, in particular optical waves. The three main atmospheric processes that affected optical wave propagation are absorption, scattering, and refractive-index fluctuations. The latter is especially important in geodetic measurements defined by a slightly different term, the refraction coefficient. Absorption is a mechanism by which the atmosphere is heated. Scattering occurs in the visible and infrared (IR) wavelengths when the radiation propagates to certain air molecules and particles. Both absorption and scattering through the gases and particles in the atmosphere give rise primarily to the attenuation of an optical wave. Refraction index fluctuations lead to irradiance fluctuations, beam broadening, and loss of spatial coherence of the optical wave. These are all effects that lead to errors in applications that imply the transmission of optical waves through the atmosphere (Andrews, 2019). The subject was intensively discussed in the 80' by the geodetic community. Concrete examples are given in the review articles in Brunner (1984b) after the general assembly of the International Association of Geodesy 1982 in Tokyo. A specific review on the consideration of these effects in geodetic measurements (e.g. leveling,

vertical angle measurements) is given among many, by Flach (2000). These resources are, of course, only a starting point for the interested reader.

4.2 Atmospheric elementary errors

Out of the many parameters describing the microclimate of an area, only a few are considered in this work. The choice is made based on the physical laws upon which formulas for refraction are defined in geodesy (Vaníček and Krakiwsky, 1982) and their importance in corrections applied to distance measurements (cf. Rinner and Benz, 1966; Rueger, 1990; Pollinger, 2012). Some of them are also the ones used to compute the actual value of the refraction coefficient, as seen later. These are:

- *air temperature (t),*
- *air pressure (p),*
- *vertical temperature gradient (VGT).*

The atmospheric temperature on the surface of the earth varies from point to point, but also varies with time, being influenced by two main cycles – seasonal and diurnal (Vaníček and Krakiwsky, 1982). In consequence, air temperature as derived from local measurements in the area of interest is likewise subject to these changes. It is considered the most influential parameter on the refraction index of air (see later in sec. 4.4) for instruments that use wavelengths in the infrared spectrum. Throughout this work, the focus is set on the influences caused by variations in air temperature due to the propagation of terrestrial observations through different layers of the boundary layer and not on correcting distances in any way. This is only generally modeled here, even though specific influences like vegetation, wind, and solar radiation may lead to even stronger variations in different areas (cf. fig. 4.2). It is beyond the purpose of this thesis to research this in detail.

The second atmospheric parameter is air pressure. This is actually a measure of air density. Like temperature, the air density varies from place to place and is also time-dependent. In general terms, it decreases rapidly with height above the earth's surface. Air pressure is merely the hydrostatic pressure or weight of a column of air on a unit area. The relation between air temperature and air pressure is given by the equation of state of an ideal gas (not presented here), however, it is valid only for dry air. This state rarely occurs in the atmosphere's lower layers (Vaníček and Krakiwsky, 1982), therefore the functional relation is not valid. In contrast to air temperature, changes in pressure have a smaller influence on the propagation of optical and electromagnetic waves (see later in sec. 4.4).

In what concerns the vertical temperature gradient, the first step is to consider the vertical separation of the lower atmospheric boundary layer. Hirt et al. (2010) use the terms higher, intermediate, and lower atmosphere to define the variation of the VGT within a limited height above the ground. The same classification is adopted here in the lack of a better approximation of the local conditions, like the empirical one defined with sensors mounted on a balloon chord or vertical rod (Friedli, 2020). By the term "higher atmosphere", the author refers to the layers from 100 m and more above ground level. The VGT in this part has values around −0.006 K/m and is fairly independent of the Earth's surface temperature (Hirt et al. 2010). The next layer called the intermediate one is considered between 20–30 m and 100 m is weakly influenced by the ground temperature and has an average value for the VGT of −0.01 K/m. This is where the refraction coefficient has an average value of +0.15 and it is also the layer in which the Gaussian

value (+0.13) is most appropriate. One level lower, the first layer, is the one most prone to variations in ground temperature and the VGT reaches maximum fluctuations here. The previous studies, summarized in Hirt et al. (2010), showed variations of the refraction coefficient between −3.5 K/m and 3.5 K/m. These values indicate a rectangular distribution, and obtaining the standard deviation can be done as presented in sec. 2.4.4. Noteworthy are the empirical findings of Hennes (2006) in which the local refraction coefficient reaches values of −2.9 (meaning a VGT of −0.5 K/m) that leads to a concave curvature of the light path. This is the exact opposite of the common belief about the chord being convex (towards the ground) in almost all cases. Nevertheless, a less drastic value of −0.2 K/m is used in the current study, resembling an average value for this layer. In other related research studies (cf. Nikolitsas and Lambrou, 2019), general models, like the one from Kukkamaki (1938) are adopted. A graphical representation is given in the next section.

These three meteorological parameters comprise the atmospheric elementary errors used in the current work. The approach and conventions for their values are presented in the following subsections. Other parameters also affect the transmittance of electromagnetic waves through the atmosphere, e.g. relative humidity, carbon dioxide concentration, gaseous mixture, aerosols, bacteria, wind speed, and net radiation. However, they have a relatively small contribution to distance measurements and are usually studied for fundamental research as pointed out by Ciddor (1996). To name one example, if the carbon dioxide concentration changes from 300 ppm to 600 ppm (prognosis for the year 2070), the error in the refractive index (see eq. 4.1-4.2) would be 0.05 ppm (Rüeger, 1990). The relative humidity (equivalent partial water vapor) is classified into the same category, as demonstrated later. Although the elementary error model may be extended by these parameters, it is restricted to three elementary errors as mentioned before. This is done on one side due to their practical relevance in EDM measurements. On the other side, the choice is inspired by other set-ups used to acquire the local weather conditions at geodetic infrastructure facilities like the Geodetic Observatory Wettzell (Klügel et al., 2018) or in TLS monitoring applications.

As mentioned before, there is no general formula that describes the change of these parameters with regard to height. But there are general patterns that can be observed for air temperature and air pressure in the observation area. These are discussed in detail after the background for obtaining values for these elementary errors on TLS observations is explained. The following subsections present the stochastic nature of these errors and their effects on distance measurements and vertical angle measurements. The influence on horizontal angle measurements is not treated here, because it occurs in relatively rare cases. It may be relevant for scanning applications in which the observation lines run parallel and very close to prolonged objects of different temperatures such as walls, galleries of dams, tunnel walls, etc. (Ogundare, 2016). These kinds of setups are generally avoided in TLS applications.

4.3 On the stochastic nature of atmospheric parameters

In chapter two, three groups of errors have been defined. According to the nature of the stochastic relations between different types of elementary errors, the atmospheric parameters are classified as stochastic correlating. They can be correlated with each other, in contrast to the non-correlating or functional correlating errors, and can influence observations in a compound way. In sections 4.1 and 4.2 it was seen that the interactions and variations of atmospheric parameters are interrelated and very complex, therefore their effect on the measurement process cannot be strictly separated into stochastic independent error groups.

Nevertheless, their contribution to the TLS uncertainty can be taken into consideration by the approach presented here.

If TLS monitoring is considered, detailed planning of the measurement campaign should be made like in any other terrestrial precision measurement campaign (e.g. total station network measurement, precision leveling, GB-SAR, etc.). In this kind of setups the atmospheric parameters are usually considered for data correction. Common practices are to measure these parameters at the station point and in some cases near the observed object or other station points. Consequently, corrections are calculated based on averaged values of these parameters. Unlike in airborne laser scanning, where the average between aircraft and the ground temperature is a good approximation of the real situation (Beraldin and Blais, 2010), terrestrial observations are prone to near-ground boundary layer fluctuations. In addition to this, it was shown (cf. Friedli et al., 2019, Hirt et al., 2010) that even within a short time span, the atmospheric parameters may be subject to strong variations and there is no straightforward method of correcting the systematic effects. This is another reason for modeling the impacts on the observations stochastically, according to the complex relations of the atmospheric parameters.

Describing the interrelations can be achieved in the form of a VCM with the structure presented in eq. 2.35 in which the elementary errors are air temperature (t), air pressure (p), and VGT – depicted with the indices (g) for readability. On one side, this respects the stochastic properties of this group as stated in chapter two for the same elementary error types; e.g. temperature leads to correlations between different observations. This principle applies to air pressure and VGT likewise. On the other side, the definition is extended by the introduction of correlations between different types of elementary errors, e.g. air temperature and VGT or air temperature and air pressure, which are physically correlated with each other as explained in sec. 4.2. In this sense, the VCM will have the following structure:

$$\boldsymbol{\Sigma}_{\gamma\gamma,atm} = \begin{bmatrix} s_{t1}^2 & s_{t1p1} & s_{t1g1} & s_{t1t2} & s_{t1p2} & s_{t1g2} & \cdots \\ & s_{p1}^2 & s_{p1g1} & s_{p1t2} & s_{p1p2} & s_{p1g2} & \cdots \\ & & s_{g1}^2 & s_{g1t2} & s_{g1p2} & s_{g1g2} & \cdots \\ & & & s_{t2}^2 & s_{t2p2} & s_{t2g2} & \cdots \\ & & & & s_{p2}^2 & s_{p2g2} & \cdots \\ & & & & & s_{g2}^2 & \cdots \\ & & & & & & \ddots \end{bmatrix}. \tag{4.1}$$

Indices depict the variance or covariance of the atmospheric parameters for the TLS observation lines depicted by 1, 2…n. In this context, observation line means the vector connecting the scanner station point and the object point. The elements in the VCM $\boldsymbol{\Sigma}_{\gamma\gamma,atm}$ are additionally displayed in three colors according to the stochastic properties of each element. Red elements represent variances of the respective parameter (e.g. temperature) along an observation line. For each atmospheric parameter, values are assigned for each observation line. Green elements depict the covariances between the atmospheric parameters of a single observation line. Blue elements represent the covariances between atmospheric parameters of pairs of observation lines. It is challenging to obtain numeric values for all these elements, considering the complex and dynamic nature of the lower atmosphere. This is explained in the following paragraphs with the help of a simulated example. The approach is an improved version of the one presented by Kerekes and Schwieger (2020). Computational difficulties have

been solved and covariances are obtained between all observations and not based on average correlation coefficients.

An important notice is that the derived correlations are related to the spatial properties of the scanned object (e.g. shape, size, etc.) and the local topography of the scanning environment. Therefore, all references made to existing correlations must be interpreted as spatial correlations. Other types of correlations, like temporal correlations, are the subject of ongoing research and are not addressed here.

As in any terrestrial electro-optical measurement, an observation line represents the vector described by the light that travels from the instrument to the measured object and back. Along this observation line, the atmospheric conditions may vary. This depends on several factors such as the distance between the instrument and the object, and the region of the microclimate through which the observation is made. In any case, the light is perturbed along the whole path and the effects are not always negligible. In order to evaluate the variation of air temperature, air pressure, and VGT along the path, pre-knowledge about these parameters and local measurements for some of them are used in a combined way with spatial information.

Suppose a laser scanner is placed at a certain distance near a high-rise object and observations are possible from the base to the top of that object. It is most probable that the atmospheric parameters are very different at the bottom of the object and at its top. If the digital terrain model (DTM) of the area is available, then the local topography can be considered (fig. 4.3). Based on this, a realistic idea about the atmospheric parameters can be obtained.

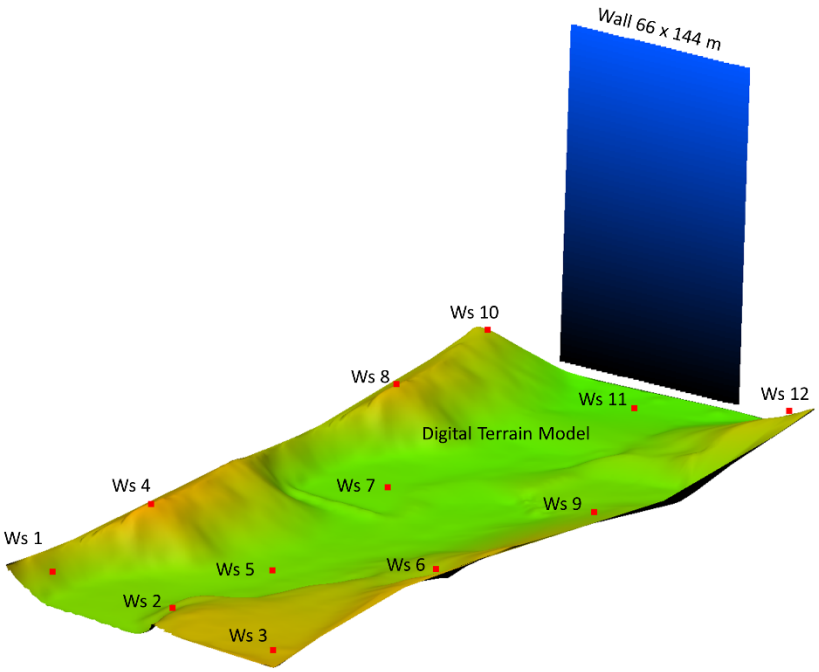

Figure 4.3. Example of scanned object (wall) with DTM and positions of weather stations (Ws).

In the next step, the separation limits of the temperature gradient layers (cf. sec. 4.2) are defined as assumed surfaces with an offset from ground level according to the abovementioned limits (fig. 4.4). The yellow surface defines the separating layer at about 25 m between the lower and intermediate atmosphere; the red layer is the separation between

intermediate and higher atmosphere at about 100 m above the ground. In order to have a better overview of the further steps, a vertical section (dotted black line fig 4.4 right) is extracted.

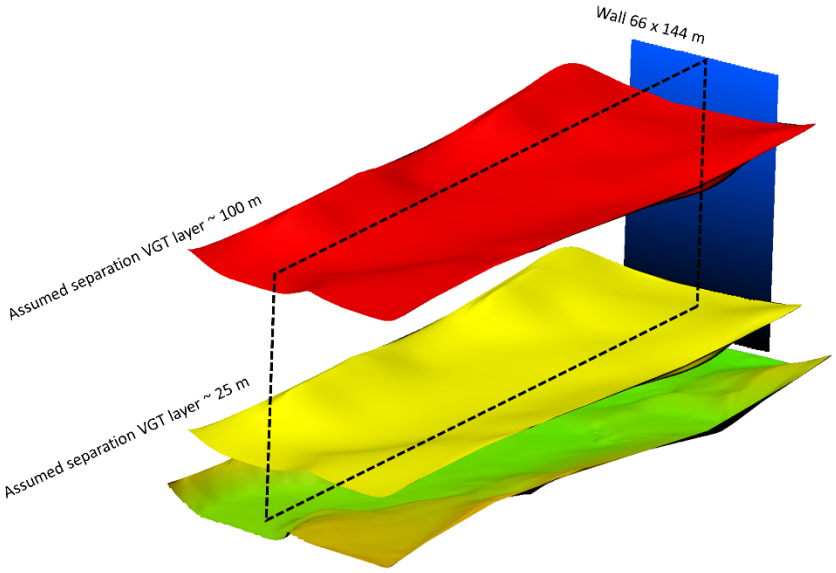

Figure 4.4. Spatial separation of assumed vertical temperature gradient (VGT) layers. The dotted plane represents a section, used for a simplified representation in fig. 4.6.

A similar vertical separation is made also for air pressure. The assumed model for air pressure decrease with height is less complex. In the first couple of hundred meters of the lower atmosphere, air pressure shows a linear decrease with height. The highest values are at ground level and after that, they decrease with increasing height above ground. Unlike the VGT, it is less prone to quick variations. Exceptions are sudden drops of pressure in case of an approaching storm. Air pressure can be easily measured on-site with portable weather stations or barometers. Most times, the measured values at different locations with a height difference between them, correspond with extrapolated values computed with the air pressure gradient value. This condition is met if the atmosphere is stable and according to the Deutscher Wetterdienst Lexikon (Deutscher Wetterdienst, 2022), the pressure gradient throughout the mentioned atmospheric layers is $\partial p/\partial z = -0.125$ hPa. In other words, with each meter in height, pressure drops by 0.125 hPa.

Now that the DTM is available and the separation of atmospheric layers is made, it is necessary to know the position of the scanner and the point cloud within the DTM. This is often referred to as georeferencing if the DTM is in an absolute coordinate system. The scanner position can be achieved either by direct georeferencing (e.g. scanner is equipped with GNSS) or by indirect means (e.g. targets with coordinates in another coordinate system).

An additional requirement is having measured values of the atmospheric parameters on-site and their position that can be georeferenced onto the DTM. In most cases, the air temperature and air pressure are measured near the laser scanner, usually at the instrument height. For the approach presented here, this is not sufficient. The recommendation is to record air temperature and air pressure from several locations that surround the area of interest between the scanner and scanned object as homogeneously as possible. In the ideal case, weather stations or low-cost weather loggers are placed in the area of interest. This is necessary for the spatial interpolation of air temperature and air pressure, later needed for information along

the whole observation line. By this means, a more realistic description of the local conditions is obtained, in contrast to the case where atmospheric parameters are recorded only at the station point.

The observation lines are given by the vectors that connect the TLS and object points. If this is represented graphically, one can see which observation line passes through which atmospheric layer (cf. fig. 4.4). Along each observation line, so-called synthetic points are generated by interpolation along the line. Point spacing between the synthetic points depends on the chosen number of points along all observation lines. This number is constant for all observation lines. The resulting intervals between the synthetic points of each observation line are different and mainly depend on the shape of the object. For example, if the scanned object represents a nearly flat landslide, an observation line at the bottom of the landslide is shorter than one at the top, but both will have the same number of synthetic points. In other words, they are equidistant for each observation line.

For each of the synthetic points, individual values for *t*, *p*, and *VGT* are interpolated or extrapolated based on their location in space and the aforementioned DTM model (fig. 4.5).

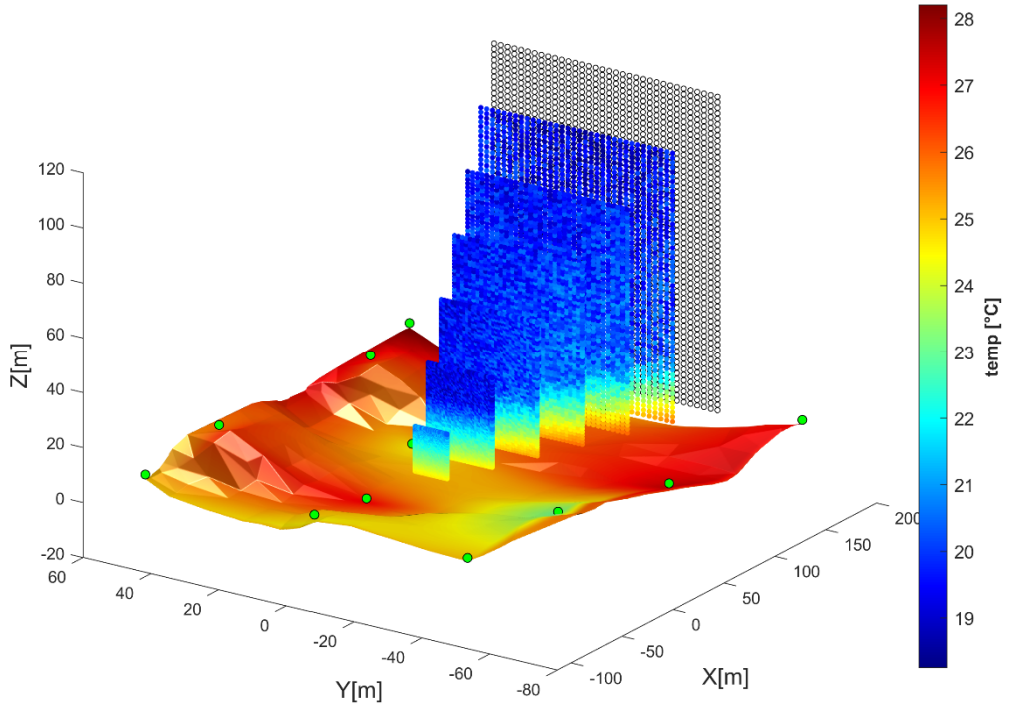

Figure 4.5. Interpolated values for the synthetic points colored based on temperature. The location of the weather station points is depicted by green circles on the DTM.

By this method, each observation line contains a series of values for all three atmospheric parameters. Only two of them are depicted by the blue lines in fig. 4.6, but the same principle applies for all the rest. For example, observation line 1 has a series of temperature values depicted by $t_{11}, t_{12} \ldots t_{1u}$ where u is the number of synthetic points for an observation line. This results in *u+1* equal intervals for the respective observation line. The same applies to the other two parameters p and *VGT*. Note that for the VGT, only the assumed values (not measured) are used here. The number of synthetic points can be freely chosen depending on

the length of the observation line and the variation of the local topography. The user should keep in mind that a small number of synthetic points along the observation line may not be representative of the change in atmospheric parameters. This is the same principle according to which a small sample number from a population is not representative for the average value, whilst by increasing the number of samples (e.g. towards ∞), the population standard deviation is almost equal to the sample standard deviation (Gotthardt, 1960). Finding an optimal number in this sense requires an empirical approach in which the user should verify after which number of sample points the variance (see eq. 4.1) still changes and would have a significant effect on the observations (see eq. 4.4-4.5 and 4.12-4.13). To exemplify this, if the change in the variance for temperature is 0.01° then this will affect the distance measurement by 0.01 ppm, which is by common sense negligible.

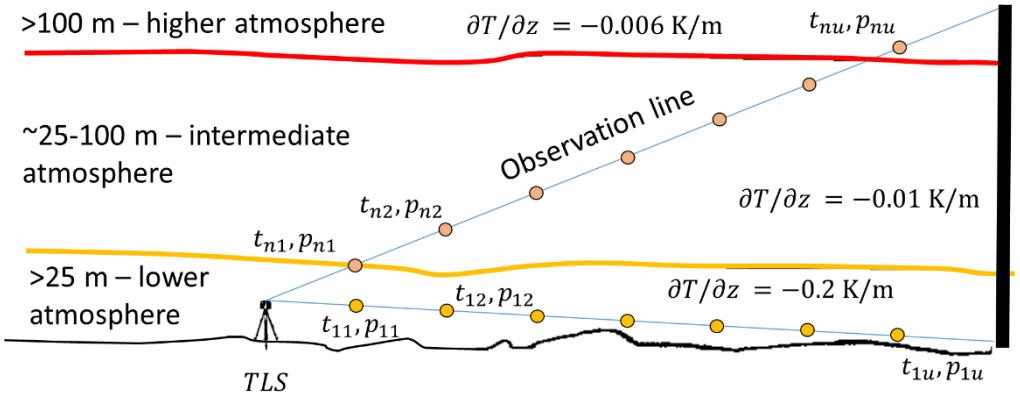

Figure 4.6. Section of the DTM and representation of observation lines (light blue) and equally spaced synthetic points per observation line (pink and yellow).

Having series of values for all three parameters along all observation lines allows the computation of variances and covariances along and between each observation line according to:

$$s_{ap}^2 = \frac{1}{u-1} \cdot \sum_{i=1}^{u} (ap_i - \overline{ap_i})^2, \tag{4.2}$$

$$s_{ap_i,ap_j} = \frac{1}{u-1} \cdot \sum_{i,j=1}^{u} (ap_i - \overline{ap_i}) \cdot (ap_j - \overline{ap_j}), \tag{4.3}$$

where s_{ap}^2 is the empirical variance computed for each of the three atmospheric parameters. The values ap_i and ap_j stand for the atmospheric parameters consecutively denoted by t_i, p_i, g_i , and u is the number of synthetic points; s_{ap_i,ap_j} is the empirical covariance between each of the atmospheric parameters. The latter is computed in the same manner for series that belong to the same observation line (e.g. covariance between air pressure and air temperature), but also for the series of different observations. This approach assumes stationarity along the observation lines for that single realization (state) of the atmospheric conditions. Although this is rarely true for natural phenomena, as stated by Heunecke et al. (2013), stationarity is commonly assumed in many applications in geodesy. Stationarity is defined as the transitional invariance of a statistic over the given interval, be it spatial or temporal (Lynch, 2012). It is however well-known that stationarity issues pose a problem very often and the users need to content themselves with a more or less self-defined quasi-stationarity (Schönwiese, 2013).

After the description given for the number of samples required along an observation line, one can see that weak-stationarity is assumed. This means that the mean and variance should be stationary along an observation line, for the chosen number of sample points.

With the help of the empirical variances and covariances, the VCM $\boldsymbol{\Sigma}_{\gamma\gamma,atm}$ in eq. 4.1 is constructed as a fully populated matrix. For ease of understanding, this is exemplified graphically (fig. 4.7) for two observation lines, as in the conventions of eq. 4.1.

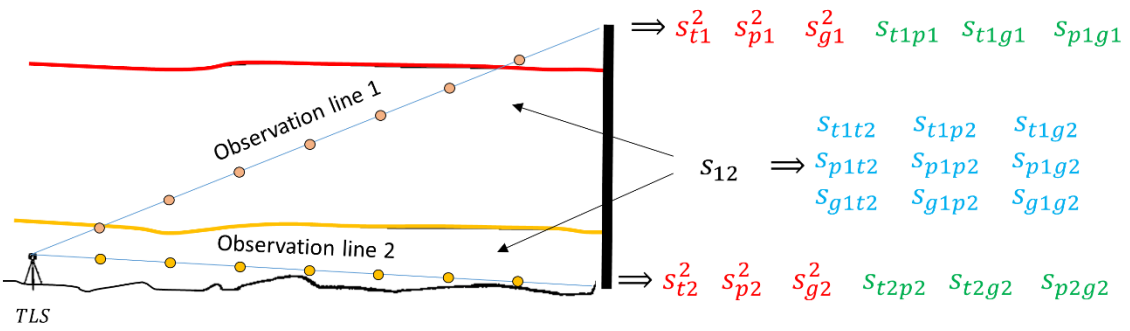

Figure 4.7. Graphical representation of the workflow for obtaining empirical variances and covariances for pairs of observation lines.

A drawback of this method is evidently the high computational cost. Some examples are given regarding the number of operations necessary for n TLS observations. Each observation will lead to three variances, therefore only to fill the main diagonal of the VCM matrix, $(3 \cdot n)$ operations are needed. In what concerns the rest of the elements, the matrix is symmetric, therefore it is sufficient if only the upper or the lower triangular elements are calculated and then mirrored. The covariances in this case lead to a number of $C_2^{3n} = 3n!/(2 \cdot (3n-2)!)$ operations. In other words, all possible unique combinations of two elements (from two series taken each time) need to be computed. The numeric example of the wall point cloud contains 1972 observations, therefore the number of operations needed for computing covariances is $C_2^{5916} = 17\,496\,570$. The required time to compute these values in Matlab is less than two minutes. With these values, the VCM as stated in eq. 4.7 is fully populated and represents the existing variances and covariances of the atmospheric parameters along the observations.

4.4 The influence of atmospheric parameters on the observations

Up to now, variations in atmospheric parameters have been presented, with emphasis on their spatial distribution. In order to obtain a concrete measure of their impact on the TLS observations, the influencing coefficients (e.g. partial derivatives) according to the measurement process must be obtained. In this section, the effects of these changes are presented based on the established EDM literature.

4.4.1 Influence on the distance measurement

Similar to EDM of total stations, distance measurements in TLS, are influenced significantly by changes in air temperature and air pressure; in any case for long distances. Partial water vapor pressure is intentionally neglected due to its small influence. Most TLSs use near-infrared light for measuring distances. As known, the speed of light traveling through the atmosphere's different layers is diminished in comparison to the speed of light in vacuum. Independent of the method used for determining the distance, either time-of-flight or phase

difference (Rüeger, 1990), the atmospheric correction increases proportionally with the measured distance. At close range (e.g. ranges up to 200 m), errors in the measurement of the atmospheric parameters lead to erroneous corrections, but due to their magnitude, they may be neglected. However, the situation changes at long ranges and they cannot be neglected for long-range scanners (e.g., Riegl VZ-2000, Teledyne Optech Polaris) that measure up to a few km. Depending on the strived level of precision, the on-site atmospheric parameters should be known to a certain degree (Rüeger, 1990).

According to the manufacturer's specifications, the Riegl scanner has an atmospheric correction model implemented in the instrument, meaning that distances are corrected based on the introduced parameters for temperature, pressure, and relative humidity. The approach is described in the RiSCAN Pro software documentation (Riegl Laser Measurement Systems GmbH, 2015b) and follows the IAG 1999 resolutions (International Association of Geodesy, 1999). The relevant resolutions are shortly presented here, followed by an explanation of their integration into the elementary error model.

The propagation speed of electromagnetic waves is determined by the group refractive index and is dependent on the wavelength λ_L itself. The IAG 1999 resolutions recommend computing the group refractivity N_{Gr} of standard air with 0.0375% CO_2 content at T= 273.15 K (0°C), air pressure p=1013.25 hPa, and partial water vapor e = 0.0 hPa as follows:

$$N_{Gr} = (n_{Gr} - 1) \cdot 10^6 = 287.6155 + \frac{4.88660}{{\lambda_L}^2} + \frac{0.06800}{{\lambda_L}^4}, \tag{4.4}$$

where N_{Gr} is the group refractivity, λ_L the wavelength and n_{Gr} is the corresponding group refractive index. The same resolution specifies that these coefficients are available for wavelengths from 650 nm to 850 nm. This doubts the universal character of the eq. 4.4, since Peck & Reeder (1972) give another formula that is recommended for wavelengths from 720 nm to 1690 nm. Nonetheless, eq. 4.4 is used for atmospheric correction in the Riegl software, despite the fact that the scanner in case uses a wavelength of 1550 μm. Because of this, it is further used in this work. Next, the standard atmosphere must be reduced to real atmospheric conditions by the following equation (cf. Joeckel and Stober, 2008):

$$N_L = (n_L - 1) \cdot 10^6 = N_{Gr} \cdot \frac{273.15}{1013.25} \frac{p}{T} - \frac{11.27 \cdot e}{T}, \tag{4.5}$$

where N_L is the reduced group refractivity for the standard atmosphere to the current atmosphere, n_L the group refractive index with the current atmosphere, p is the air pressure and T is the temperature in Kelvin ($T[K] = t[°C] + 273.15$) and e the partial water vapor pressure. It should be noted, that eq. 4.5 is valid for temperatures between -40°C…+100°C, air pressure between 800 hPa and 1200 hPa, and the equivalent of relative humidity (conversion formula not given here) from 0%...100%.

The change in the group refractive index n_L (in literature usually addressed as n) with regard to each of the atmospheric condition parameters T, p, e is approximated with the total differential:

$$\partial n_L = \frac{\partial n_L}{\partial t} \cdot dt + \frac{\partial n_L}{\partial p} \cdot dp + \frac{\partial n_L}{\partial e} \cdot de. \tag{4.6}$$

Substituting numeric values in eq. 4.6 gives the individual values for the partial derivatives according to temperature, pressure, and water vapor pressure. To exemplify this numeric values are computed for a mean atmosphere of 17 °C, 1000 hPa pressure, and water vapor pressure of 11 hPa. The wavelength of λ_L = 1550 nm is used in eq. 4.4 as it is common for both scanners in this work. This yields:

$$\frac{\partial n_L}{\partial t} = -0.93 \cdot 10^{-6} \left[\frac{1}{°C}\right]; \quad \frac{\partial n_L}{\partial p} = 0.27 \cdot 10^{-6} \left[\frac{1}{hPa}\right]; \quad \frac{\partial n_L}{\partial e} = -0.038 \cdot 10^{-6} \left[\frac{1}{hPa}\right]. \tag{4.7}$$

Finally, if the change in the distance measurement is of interest, the numeric values are used as follows:

$$\Delta n_L \cdot 10^{-6} = -0.93 \cdot \Delta t + 0.27 \cdot \Delta p - 0.038 \cdot \Delta e, \tag{4.8}$$

$$\Delta R = -R \cdot \Delta n_L, \tag{4.9}$$

where Δn_L is the change in the group refractive index of light, Δt is the change in temperature (°C) and Δp is the change in pressure (hPa). Finally, the change in range ΔR is given. Note that these parameters are calculated for mean atmospheric parameters indicated before (t = 17 °C, p = 1000 hPa, e = 11 hPa). Interpreting this in terms of parts per million (ppm) depending on the atmospheric parameters in standard conditions, a change in t of 1 °C affects the distance and refractive index by 0.93 ppm, a change in air pressure of 10 hPa yields a −2.7 ppm correction on the distance, whereas the humidity effect is around 0.04 ppm even if the conditions suddenly change from 0% to 100%, it is negligible. Air humidity may not be neglected if it is needed for very precise absolute distances with overall uncertainties under 0.1 ppm (e.g. calibration laboratories, baselines, etc.) and it can be reliably measured in indoor as well as outdoor settings by means of optical hygrometers (Pollinger et al. 2012). Since this is not the case in the current work, air humidity is left out in all upcoming equations, therefore the influence on the distance with regard to humidity is neglected. For more details about this topic, the reader can consult literature like Rüeger (1990) or Kahmen (2006).

4.4.2 Influence on the vertical angle measurement

In addition to the effects on distance measurements of any electro-optical measurement, atmospheric refraction also influences vertical angle measurements. This effect causes image scintillation, often obvious in its extreme case when temperature vertical gradients near the ground are high for example in the desert or on a highway on hot summer days (cf. Brunner, 1984a, Reiterer, 2012). Eschelbach (2009) emphasizes the dominant effect of the vertical temperature gradient and presents an approach to taking turbulences into account. The effects on vertical angle measurements are likewise important in classical geodetic observations, like transferring heights by trigonometric levelling or geometric levelling. Nevertheless, similar effects also affect TLS measurements and have been lately studied and explained by Friedli, et al. (2019) and Friedli (2020). The reader is advised to consult these publications for understanding how refraction angles can be determined with the aid of reference values from total station measurements.

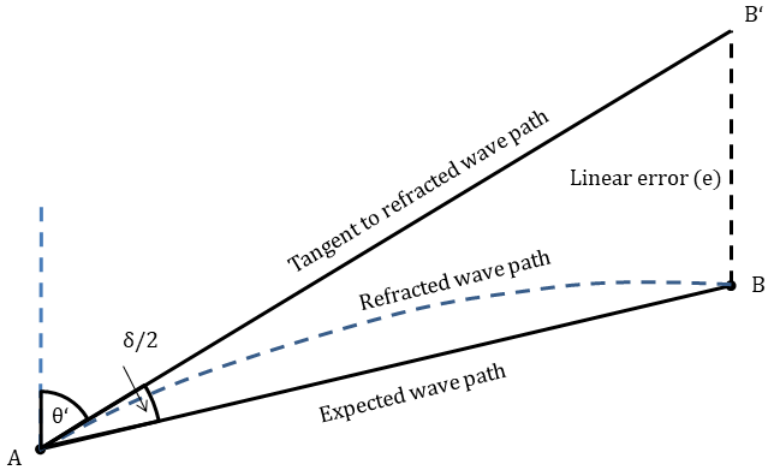

Figure 4.8. The effects of atmospheric refraction on vertical angles - excluding the earth radius that is not represented (after Ogundare, 2016).

Figure 4.8 denotes the effects of atmospheric refraction out of which the refraction angle correction $\delta/2$ is of further interest. This angle is given between the expected wave path and apparent line of sight also called tangent to refracted wave path. For more details about how $\delta/2$ is deduced, refer to Joeckel et al. (2008). There are different ways of expressing the refraction angle correction (cf. Rüeger, 1990), but the current one has been chosen based on its derivable equation and implemented in the elementary error model. The corrected vertical angle is (cf. Joeckel et al., 2008):

$$\theta = \theta' + \frac{\delta}{2} \; and \; \frac{\delta}{2} = \frac{R}{2 \cdot E_R} \cdot k \cdot \rho, \tag{4.10}$$

where θ is the corrected vertical angle, θ' is the measured vertical angle, R measured range, E_R Earth's middle radius (6381 km), k refraction coefficient, and ρ the conversion constant between angle measurement units (degrees or grads) and radians. The coefficient of refraction k is usually needed to account for the curved light path from one point to another. It is defined as the ratio between the Earth radius and the radius of the line of sight which is mostly convex (Kahmen, 2006). Very often, the well-known Gaussian value of $k = +0.13$ is used by default, assuming that it holds true for most applications (Brunner, 1984b). Nevertheless, k strongly varies throughout the day and directly depends on the temperature gradient $\partial T/\partial z$ (K/m) (cf. Brocks, 1939; Rüeger, 1990; Hennes, 2002; Kahmen, 2006), as observed in eq. 4.11. If the refraction coefficient of a small area is of interest, the local refraction coefficient k_{loc} is given as a function dependent on temperature, pressure, and the VGT within that area (cf. Joeckel et al., 2008; Brocks 1939):

$$k_{loc} = 503 \cdot \frac{p}{T^2} \cdot \left(0.0343 + \frac{\partial T}{\partial z}\right), \tag{4.11}$$

where p is pressure (hPa or mbar), T is the temperature in (K) and $\partial T/\partial z$=VGT (K/m) is the temperature gradient at a certain point. The term k_{loc} is used instead of an average k in eq. 4.10 for further purposes. As noticed in eq. 4.11, temperature gradient strongly influences the size of the local refraction coefficient; hence, its variation is the most relevant for the vertical angles. A numeric example underlines this fact. Similar to section 4.4.1, the influencing coefficients are determined after computing the partial derivatives of eq. 4.10.

Therefore, numeric values have been exemplary computed with similar conditions as stated before (t = 17 °C, p = 1000 hPa) and VTG = −0.01 K/m at a distance of 1000 m:

$$\frac{\partial\theta}{\partial t} = -0.08 \cdot 10^{-6} \left[\frac{1}{K}\right]; \quad \frac{\partial\theta}{\partial p} = 0.01 \cdot 10^{-6} \left[\frac{1}{hPa}\right]; \quad \frac{\partial\theta}{\partial VGT} = 468.1 \cdot 10^{-6} \left[\frac{1}{K/m}\right]. \tag{4.12}$$

The change in the measured vertical angle (in radians) is given by:

$$\Delta\theta \cdot 10^{-6} = -0.08 \cdot \Delta t + 0.01 \cdot \Delta p + 468.17 \cdot \Delta VGT, \tag{4.13}$$

where $\Delta\theta$ is the change in the measured vertical angle, Δt is the change in temperature (°C), Δp is the change in pressure (hPa) and ΔVGT is the change in vertical temperature gradient. In other words, a change in temperature of 10 °C affects the vertical angle by −0.08 μrad ($-0.005 \cdot 10^{-3}$ mgon), a change in air pressure of 10 hPa affects the vertical angle by 0.01 μrad ($0.006 \cdot 10^{-4}$ mgon) and the most significant factor, a change in the VGT of 1 K/m results in a change of the angle with 468.17 μrad (29.8 mgon). This is not to be confused with the systematic effect of the refraction angle correction $\delta/2$. For comprehension, at the above-stated conditions and at 1000 m, $\delta/2$ has a value of 0.7 mgon, which leads to a value of the linear error e = 11.4 mm (see fig. 4.8). The intention is not to correct these systematic effects, but to show how the variations in temperature, pressure, and VGT influence the error of position in TLS observations.

As noticed in eq. 4.10, the vertical angle also depends on the measured range *R*, which is likewise affected by the atmospheric elementary errors (sec. 4.4.1). The changes in temperature and air pressure in the example above (Δt = 10°C, Δp = 10 hPa) lead to a change of the same measured range (R = 1000 m) of 6.6 ppm in this case. If this change is introduced in eq. 4.10 and the influencing coefficients (cf. eq. 4.12) are recalculated and compared with the ones from eq. 4.12, the obtained differences are as follows: for temperature $3 \cdot 10^{-8}$ mgon, for air pressure $-4 \cdot 10^{-9}$ mgon, and finally the VGT $2 \cdot 10^{-4}$ mgon. Consequently, the impact on the vertical angle in this case is so small that it can be practically neglected. However, vertical angles and measured ranges will be correlated to each other due to the elementary errors that affect both, as shortly presented at the end of section 4.5.

4.5 Application to the elementary error model

The atmospheric elementary errors have been classified in the stochastic correlating group due to their inseparable effect on the observations. After having a fully populated VCM as the one described by eq. 4.1 for the atmospheric parameters (sec. 4.3) and knowing their effect on the TLS observations (sec. 4.4), the contribution in the SVCM defined by the elementary error theory is obtained.

The influencing matrices for the observation types considered in this section (distances and vertical angles) are presented based on the partial derivatives seen in eq. 4.7 and 4.12. The influencing matrix $\boldsymbol{G_{atm}}$ needs to be defined as a block diagonal matrix as mentioned in sec. 2.4.3 and not a simple diagonal matrix. Every single block contains the influencing parameters arranged according to the conventions in sec. 2.4.3, but also to the defined physical dependencies in this chapter. The general form $\boldsymbol{G_{atm}}$ is given here, whilst the specific form for distances and vertical angles treated in this chapter $\boldsymbol{G_i}$ is described by:

$$\boldsymbol{G_{atm}} = \begin{bmatrix} G_1 & 0 & \cdots & 0 \\ 0 & G_2 & 0 & \vdots \\ \vdots & 0 & \ddots & \vdots \\ 0 & \cdots & \cdots & G_n \end{bmatrix}, \quad \boldsymbol{G_i} = \begin{bmatrix} \frac{\partial \lambda}{\partial t} & \frac{\partial \lambda}{\partial p} & \frac{\partial \lambda}{\partial g} \\ \frac{\partial \theta}{\partial t} & \frac{\partial \theta}{\partial p} & \frac{\partial \theta}{\partial g} \\ \frac{\partial R}{\partial t} & \frac{\partial R}{\partial p} & \frac{\partial R}{\partial g} \end{bmatrix} = \begin{bmatrix} 0 & 0 & 0 \\ \frac{\partial \theta}{\partial t} & \frac{\partial \theta}{\partial p} & \frac{\partial \theta}{\partial g} \\ \frac{\partial R}{\partial t} & \frac{\partial R}{\partial p} & 0 \end{bmatrix}. \tag{4.14}$$

The corresponding elementary error group in the SVCM is obtained by multiplication with the VCM $\boldsymbol{\Sigma_{\gamma\gamma_{atm}}}$ (cf. eq. 4.1):

$$\boldsymbol{\Sigma_{ll-atm}} = \boldsymbol{G_{atm}} \cdot \boldsymbol{\Sigma_{\gamma\gamma_{atm}}} \cdot \boldsymbol{G_{atm}}^{\boldsymbol{T}}. \tag{4.15}$$

Based on the matrix structure, the result from eq. 4.15 should be a fully populated matrix. However, according to the introduced novelty in the elementary error model with influencing block matrices (cf. sec. 2.4.3) and the specific matrix structure presented in eq. 4.14., the resulting $\boldsymbol{\Sigma_{ll-atm}}$ is likewise a block matrix in which only the following elements are populated: variances of vertical angles, variances of distances, and the covariances between vertical angles and distances (of one observation and between all other observations). The rest of the elements will be 0. This extends the definition of the stochastic correlating group by two new aspects: first by introducing correlations between observations that are influenced by the same elementary errors (e.g. distances and vertical angles) and second by introducing correlations between different types of stochastic correlating errors (e.g. air temperature and VGT) (cf. eq. 4.1).

This demonstrates on one side, that different observations of one observation line are correlated because they are affected by the same stochastic correlating errors, and on the other side that correlations between different observation lines occur due to their position in space (e.g. observations lines that travel through the same layers and have the same length). A more detailed analysis with numerical examples is given for a study case in sec. 6.1.2.

5. Object surface-related errors

5.1 Object surface properties as elementary errors

Besides instrument-specific elementary errors and atmospheric elementary errors, other TLS errors are caused by the interaction between the laser beams and object surfaces. Depending on the intended application, many studies have dealt with different properties of natural and artificial surfaces. For example, in airborne LiDAR studies (cf. Large and Heritage, 2009) much of the attention goes to the properties of natural surfaces covered by water, snow, vegetation, earth, etc., whereas TLS studies focus mostly on man-made surfaces covering structures made of concrete, metals, wood, etc. Obviously, there are many more examples of natural and artificial surfaces, and even within the same material group (e.g. wood), surface properties can vary so much that there is no general rule to how laser light interacts with that class of surfaces. Many scientists have searched for systematic effects and strived to define dependencies based on different surface attributes (cf. Boehler and Marbs, 2003; Mechelke et al., 2007; Voelgtle and Wakaluk, 2009; Zámečníková et al., 2014; Schäfer, 2017; Bolkas and Martinez, 2018). However, up to now, there is no overarching rule that can be applied to all surfaces. This is due to the complexity of surface properties. But it is beyond the scope of this thesis to offer detailed information about material science; therefore, for in-depth knowledge in the vast field of material science, the reader can start with Shackelford (2016).

Since the dependencies of surface attributes (e.g. roughness, color, and reflectance) are very complex and different for each material, they are classified in the same group of elementary errors and modeled as stochastic correlating errors as proposed by Kauker and Schwieger (2017). In addition to the aforementioned publication, a more detailed approach is defined based on the surface's physical properties and empirical correlations.

In the upcoming subchapters, details are given about the definition of the influencing matrix, variances, and covariances of this error group. From all TLS observations, it is considered that only the measured distance is affected by object-related errors. Especially for the definition of the covariances, correlation functions depending on surface features and the spacing between neighboring TLS points are considered. The main challenge is to quantify the effect of surface properties on the stochastic model according to the elementary error theory.

5.2 Interaction between laser beam and object surface as influencing factor

The fundamental working principle of any LiDAR system implies the interaction between laser beams and reflecting objects. Independent of the LiDAR working range, whether airborne or terrestrial, the emitted laser light interacts with matter encountered in the direction of emission. If the beam is not totally deflected or absorbed, a certain amount of energy is reflected back to the emitter. This amount is influenced by several factors (cf. Rees, 2013) like range between emitter and object, emitting source, surface reflectance, angle of incidence, and atmospheric attenuations. Since the latter has already been treated in the previous chapter and double modeling must be avoided, the focus in this chapter is set only on surface-related factors.

Firstly, the influencing terms of the $\boldsymbol{G_h}$ matrices (cf. eq. 2.41) and afterwards variances and covariances of the $\boldsymbol{\Sigma_{\gamma\gamma}}$ matrices are discussed starting from the radar equation (cf. eq. 5.1). This equation holds true for the ratio between the emitted and received intensity in laser scanners.

Multiple forms of the radar equation are found in literature under slightly varying forms according to the authors and considered sensor types. For TLS instruments, an adaption according to Fröhlich (1996) and Besl (1988) is used:

$$P_R = k_l \cdot P_E \cdot \chi \cdot \frac{{d_0}^2 \cdot \cos(\beta)}{16R^2}, \tag{5.1}$$

where P_R is the received energy, P_E transmitted energy, k_l transceiver constant, χ surface reflectivity, d_0 aperture diameter, β angle of incidence between surface normal and laser beam direction (fig 5.1), R distance to a reflecting object. Note that in contrast to how the radar equation is given in many sources, the range-dependent term is defined as suggested by Jelalian (1992) for narrow laser beams by $1/R^2$. Out of these variables and constants, the geometry-dependent ones (β, R) and the surface reflectance (χ) play a role in the final VCM as explained in the upcoming sections. Reflectance as depicted in this formula should be understood as the combination of the surface's physical properties – roughness and reflectivity. Both are treated in detail in sec. 5.3.

Consequently, if the received energy P_R reaches a predefined threshold at the receiver (TLS), the distance between the emitting unit and the respective obstacle can be determined. However, the distance measurement and implicitly its uncertainty strongly depend on the surface properties and scanning geometry (see eq. 5.1). From the two factors, only the latter may be chosen to a certain extent by the user. Scanning geometry can be influenced in such a way that the distance R from scanner to object and angle of incidence β (eq. 5.2) are appropriate for the pursued goal (see sec. 6.3 later). This is especially important for recent permanent laser scanning (PLS) applications (Kuschnerus et al. 2021).

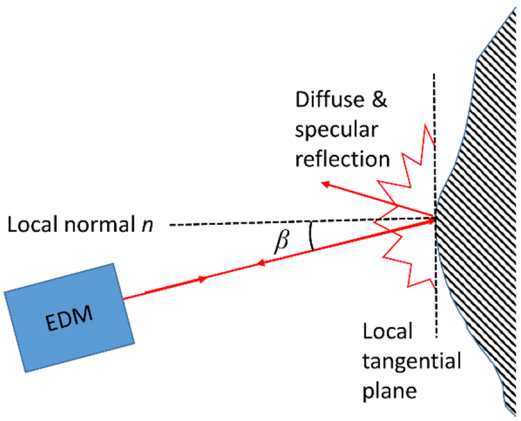

Figure 5.1. Angle of incidence as used in this thesis

The angle of incidence β depicted in fig. 5.1 is computed as follows:

$$\beta = \operatorname{acos}\left(\frac{\boldsymbol{d} \cdot \boldsymbol{n}}{|\boldsymbol{d}| \cdot |\boldsymbol{n}|}\right), \tag{5.2}$$

where $\boldsymbol{d}$ is the direction vector of the incident beam and $\boldsymbol{n}$ is the normal vector on the surface. In this case, $\boldsymbol{n}$ is considered perpendicular to the tangent plane of that surface at the intersection point between the incident beam and surface.

By nature, it is impossible to have a scan configuration with favorable angles of incidence on all parts of an object, therefore a compromise must always be reached. This implies accepting an interval in which the angles of incidence fall. Even within a favorable scan configuration with all values for β <65° (cf. Lichti, 2007) laser light backscattering strongly depends on the surface properties and is classified into three classes by Jutzi et al. (2017) for simplicity. Other complex types of scattering can be found in Rees (2013), but only three are named here.

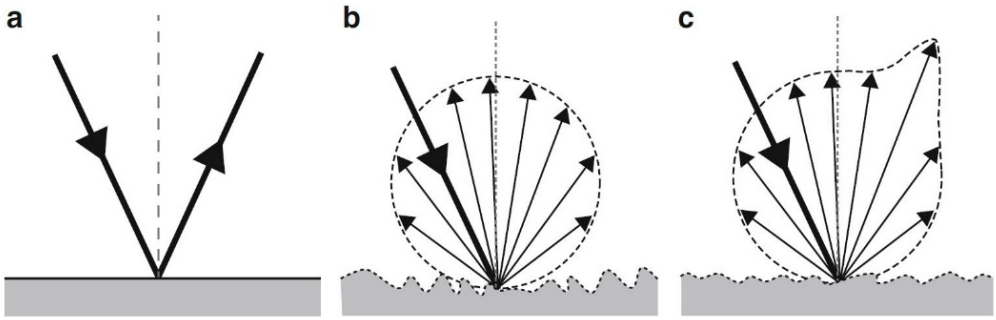

Figure 5.2. (a) Specular reflection, (b) diffuse reflection (c) mixed diffuse and specular reflection (Jutzi et al. 2017).

The first two types (fig. 5.2a and 5.2b) are idealizations, whereas the third type (fig. 5.2c) describes real surfaces as a mixture of specular and diffuse reflection.

Judging by the beam scattering seen above, only an oversimplified view of how light interacts with matter is obtained. In reality, each laser beam that encounters an object covers an area commonly known as the laser footprint. The theory about laser footprint and general manifold properties of lasers can be read in Eichler et al. (2018). Without getting into details, the size and shape of the footprint depend functionally on the distance from the emitter to the object, the angle of incidence β, and beam divergence given by the full angle 2γ. Its form resembles the shape of an ellipse and the semi-axes can be computed as follows (Sheng, 2009):

$$a_f = d_0 + 2 \cdot R \cdot \frac{\sin(2\gamma)}{\cos(2\beta) + \cos(2\gamma)}, \qquad b_f = d_0 + 2 \cdot R \cdot \frac{\sin(2\gamma)}{\cos(\beta)\,(1 + \cos(2\gamma))}, \tag{5.3}$$

where a_f is the major footprint semi-axis, b_f the minor footprint semi-axes, d_0 the beam diameter at aperture (TLS), γ beam half-divergence angle, and β angle of incidence and R range. Based on eq. 5.3 and 5.1, the geometry-dependent parameters are introduced as influencing factors in the stochastic correlating group. This is done on one side using an inverse cosine law (see sec. 5.5) and introducing a distance-dependent function useful for obtaining variances (sec. 5.4).

Additionally, the size of the footprint can be used to define the area over which variances caused by surface roughness are calculated (sec. 5.3.1).

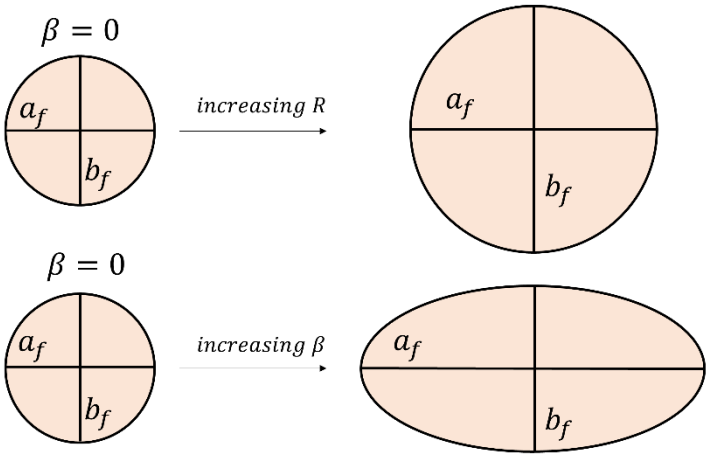

Figure 5.3. Footprint shape with increasing angle of incidence and range.

Usually, the object normal in a TLS point cloud is computed with the help of neighboring points within a certain region based on the object shape and scan resolution (Schaer et al., 2007) and the geometry-dependent parameters are known if the point cloud is available. The other necessary two parameters (d_0, γ) can be extracted from the technical specifications of the laser scanner in most cases. Most of the scanners have a beam diameter at the aperture of a few mm (e.g. 3.5 mm) and beam divergence of a few mrad (e.g. half-angle 0.3 mrad), which corresponds to an increase of 30 mm of the beam diameter per 100 m distance. Following this simple rule, the footprint at 100 m will have a diameter of 3.5 mm + 100·0.6 = 63.5 mm. This increase is alternatively given as an expansion factor (e.g. 1cm@10m) due to its linearity at large ranges (Lichti and Gordon, 2004). There are multiple definitions for the footprint diameter, but one of the most commonly used by TLS manufacturers is the $1/e^2$ rule. In other words, the footprint radius (or semi-axes) is considered only up to the point where the intensity has fallen to $1/e^2$ of its on-axis maximum value (Weichel, 1990). Out of the on-axis maximum value (the equivalent to the total intensity of the Gaussian beam), ca. 86% remains within this region and this is simultaneously the circumference of the footprint. An estimation of the footprint area, and implicitly diameter, is necessary for later presented roughness analysis. The footprint size determines the area over which roughness should be analyzed as seen later in sec. 5.3.1.

An important object surface property considered in this work is the surface reflectivity χ. Dependent on the type of laser and wavelength, each material shows different reflectance values (cf. Voegtle and Wakaluk, 2009). Reflectance is the amount of electromagnetic power reflected from a surface. It is usually given as a ratio between the emitted and received energy (e.g. from 0% to 100% or normalized from 0 to 1 as in fig. 5.4). There are many theories about reflection from rough surfaces, but according to Jelalian (1991), none are both general and rigorous at the same time. Therefore, the best approach is to use existing measurements from spectrometers and consult spectral libraries that give the reflectance based on wavelength and different materials. If a-priori knowledge about the object surface is available, e.g. from the constructor or designer of a structure, then searching in a spectral library for similar materials is easy. Spectral measurements made with laboratory and field spectrometers are available online with detailed sample descriptions. An example of a special concrete mixture is extracted from the freely available USGS Spectral Library (spilb07a) created by Kokaly et al. (2017) and can be seen in figure 5.4. Older publications like Jelalian (1991) and Wolfe and Zissis (1985)

present similar graphics, but recent spectral measurements are preferred due to the performance of newer spectrometers.

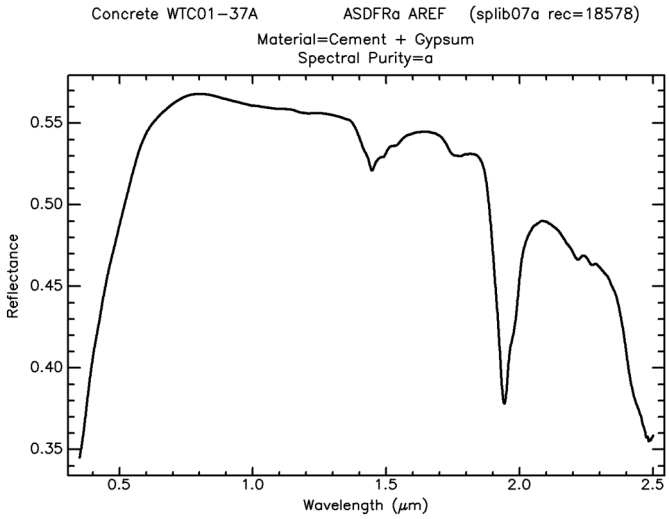

Figure 5.4. Example of a reflectance diagram for a concrete mixture for different wavelengths (Kokaly et al. 2017).

From such a diagram, the user can extract the value of reflectivity for the needed wavelength (e.g. for 1.5 μm reflectance is around 54% for this type of concrete). It serves only as an approximate value since the sample may not resemble the complete surface coverage and even in this case inhomogeneity of the same material mixture can lead to slightly different values. However, some of the TLS manufacturers give indications about reflectance for some typically measured natural and manufactured objects. Fröhlich (1996) counts among the first studies that present the influence of reflectivity on distance measurements for the AMCW Laser measurement system. Other TLS manufacturers like Riegl Laser Measurement Systems GmbH give direct information about the longest measurable distance with regard to reflectivity. For example, in the Riegl VZ400i datasheet (Reigl Laser Measurement Systems GmbH, 2022) the user can find reflectance values for coniferous trees (15%), dry asphalt (20%), deciduous trees (30%), terra cotta (35%), construction concrete (40%), cliffs, sand, and masonry (60%), etc.

There is also an alternative method of obtaining reflectance values directly on-site. Currently, there are commercially available laser scanners that deliver calibrated reflectance values beside intensity (amplitude). Examples of such scanners are the Riegl V series, which have this capability, and users can access the so-called apparent reflectance for each measured point. The values are in given in decibels (dB) and are almost entirely distance independent as presented in Pfennigbauer and Ullrich (2010). The user additionally obtains an indication about the reflection type (cf. fig. 5.2). Negative dB reflectance values are obtained for diffuse reflecting surfaces, whereas positive values are obtained for retro-reflecting surfaces. The conversion of reflectance χ from dB to % is straightforward:

$$\chi(\%) = 10^{\frac{\chi(dB)}{10}} \cdot 100. \tag{5.4}$$

Several studies (cf. Calders et al., 2017; Hartzell et al., 2013) have asserted the quality of the apparent reflectance values obtained with Riegl VZ Scanners. Calders et al. (2017) conclude that measured reflectance deviations compared to reference values of Spectralon plates are within an interval of 0% to 7.4%. Exceptions to this rule occur for strong reflecting surfaces (e.g. $\chi(\%) > 95\%$), for which the uncertainties were larger. Nevertheless, this is a very

practical method (compared to measurements on samples with spectrometers) of directly deriving reflectance for the studied objects.

Out of all object properties that can be analyzed, only surface roughness and reflectivity together with influencing factors based on scanning geometry are introduced in the elementary error model presented in this thesis. Roughness and reflectivity are considered the most important sources of errors caused by object surface properties. For each of these, an explanation of the conventions in this work is given first, and afterwards their role in the elementary error model is explained. Based on existing empirical studies in literature and technical specifications from TLS manufacturers, the geometry influences (here distance and angle of incidence) are introduced into the model, not as error sources, but as influencing coefficients. All matrices or vectors that refer to these two properties will have the indices ***rou*** for roughness and ***ref*** for reflectivity.

In the following sections, a stepwise approach for defining variances and covariances for the TLS distances is presented. Firstly, details are given about the relation between the two elementary errors and distance measurements. Afterwards, the definition of variances (main diagonal elements of $\boldsymbol{\Sigma}_{\gamma\gamma}$) is given. Finally, covariances are determined with the help of correlation functions. This is necessary due to the limited knowledge about roughness and reflectivity over the entire object area.

5.3 Surface properties for variance

On one side, roughness is the main surface property that permits the backscattering of light. In optics, a surface is considered capable of backscattering (e.g. fig. 5.2. case b and c) if the surface's physical irregularities fulfill the Rayleigh criterion. For a surface to be classified as rough, these irregularities must be larger than about λ_L /8 at a normal incidence angle (Rees, 2013). Without this condition, laser scanning would not be appropriate for many surfaces. On the other side, surface reflectance determines the amount of backscattered light (cf. Jelalian, 1992). These two properties are interrelated and it can be affirmed that one may influence the other, but this combined effect is not addressed in this thesis. In the next subsections, an approach for quantifying their effects on TLS measurements is presented for both of them.

5.3.1 Roughness

Surface roughness is one of the main sources of variations in EDM measurements. The standardized surface parameters describing roughness can be determined for either 1D samples (profiles) or 2D samples (areas) of a surface. Independent of the sampling method, some of the characteristics do not change for the same surface, therefore the 1D case will be presented further for simplicity.

Within this dissertation, the basic assumption regarding distance measurement and roughness is that distance variances are directly related to roughness. Another assumption is that surface roughness does not only influence the variance but also the covariance (correlations) due to the periodicity or randomness of surface features. Following this principle, correlation functions are defined based on the characteristics of different materials. This will be explained after the basic concepts are highlighted.

Not all properties of the roughness profile are relevant to the definition of this elementary error group; therefore, some characteristics are presented only for understanding purposes.

The definition of all parameters used to describe roughness and more details can be found in the following norms: DIN EN ISO 4287, DIN 25178-2, DIN EN ISO 11562.

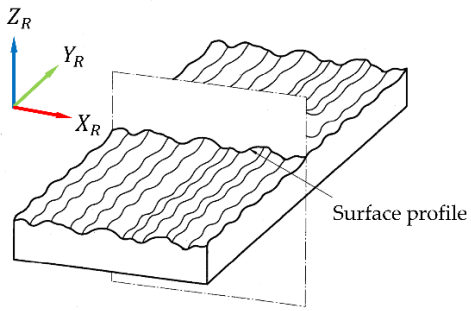

Figure 5.5. Sample profile of a surface according to DIN EN ISO 4287:2010-07

Surface profiles are measured in two dimensions using either tactile or optical systems with resolutions of a few nm (e.g. 10 nm) to a few µm. An evaluation length (fig. 5.6 and 5.8 – depicted as ln) is chosen and the resulting profile is analyzed. Afterwards, this region is divided into smaller intervals lr called sampling lengths. At least 5 such intervals should be considered. Initially, the unfiltered primary measured profile (P-profile) is represented by a continuous line with hills and valleys along an ordinate. After filtering with phase correction filters (cf. DIN EN ISO 11562), the waviness profile (W-profile) and roughness profile (R-profile) are extracted (fig. 5.6). All profile features can be computed for each of the profile types; the difference is given by the nominator (first letter) of the parameter like seen in fig. 5.6 for the total height (maximum height between the highest peak and deepest valley) Pt, Wt, Rt of the respective profile. If the analysis is conducted on a sample area (not only profile), the nominator for all surface parameters is S (e.g. St, Sz).

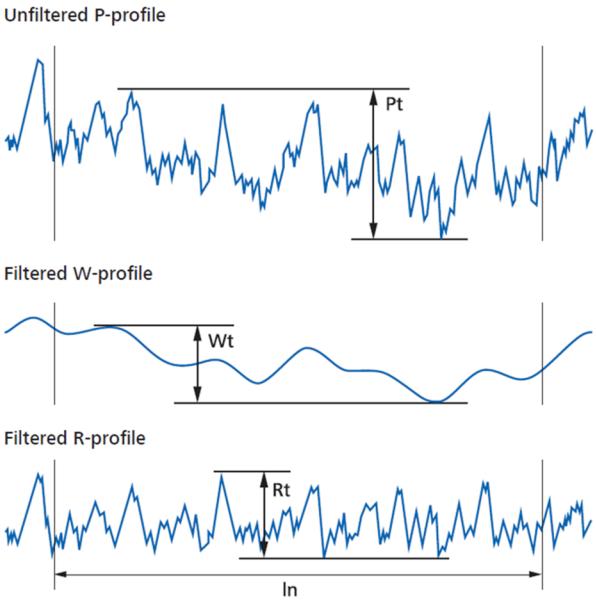

Figure 5.6. Division of a roughness profile measurement (Jenoptik, 2020)

Many parameters describe the roughness profiles along both dimensions (X_R and Z_R in fig 5.5), however, the vertical parameters (peak heights and valley depths) are the relevant ones. Only the one considered to describe the TLS distance variation is highlighted here and for more details, the reader is advised to consult the aforementioned ISO and DIN norms.

A parameter that gives information about the average values of differences between peaks and valleys is more appropriate. The total height Rt (cf. fig. 5.6 and 5.7) is calculated only with extreme values of the ordinates. If Rt is not available or not mentioned, the established descriptor, called the maximum height a profile Rz can be used instead. It is a representative descriptor of the profile (not prone to single maxima or minima) defined as the medium interval of all Rz_i, $(i = 1..n_R)$ along the sampling lengths (e.g. five sampling lengths lr fig 5.8.) Note that in some publications or technical specifications the notations Rt and Rz are used to describe the same feature. If in doubt, Rt should be used as recommended in ISO 4287.

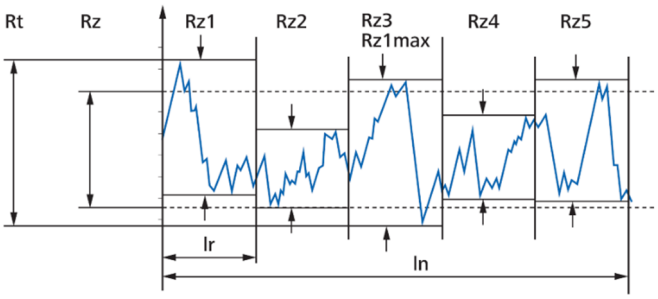

Figure 5.7 Total height of a profile (Rt) and maximum height of a profile (Rz) and $ln \geq 5 \cdot lr$ (Jenoptik, 2020)

$$Rz = \frac{1}{n_R}(Rz1 + Rz2 + \cdots + Rzn_R) \; and \; Rt = z_{max} - z_{min}. \tag{5.5}$$

If a center line of the interval Rz or Rt is drawn in fig. 5.7, the center line of the profile corresponds with the average of the Rz values. This means that Rt covers the total area in which peaks and valleys fall, and can be used as a quantitative indicator for how much peaks and valleys are spread around the center line. If we consider the definition of standard deviation, it expresses how widely a random variable is spread around a mean value, under the assumption of a normal distribution. For TLS distance measurements on a rough surface, the assumption is that the most probable value of the measured distance will lie on the center line (fig. 5.8 yellow dot). The actual measured distance, however, may vary along the measurement direction within the interval given by the surface profile. In this sense, the complete interval can be defined by the Rt value, or in its absence Rz (fig. 5.8 see the histogram on the right). The profile height distribution is assumed to follow a normal distribution, which is mostly the case in surfaces with irregular profiles (e.g. fig. 5.8).

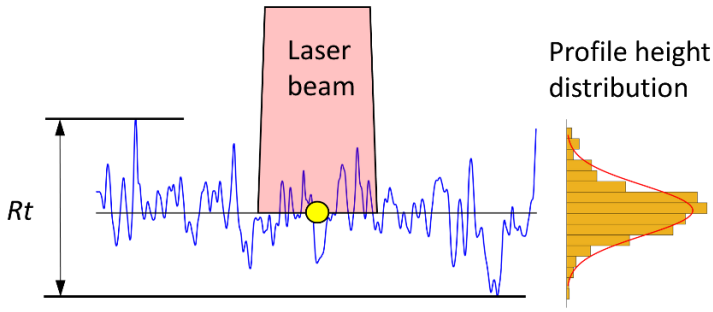

Figure 5.8. Definition of standard deviation for the distance measurement based on the Rz value

Following the conventions and recommendation of Pelzer (1985) with regard to the maximum influence of elementary errors and their standard deviation (see sec. 2.4.4), the variances for distance are defined under the assumption of normal distributions as:

$$\sigma_{R-Rt} = Rt \cdot 0.3. \tag{5.6}$$

If the profile height distribution is closer to another type of distribution (e.g. rectangular, triangular), then the value for σ_{R-Rt} is determined by multiplication with other factors as shown in sec. 2.4.4.

With this definition, the main diagonal of the VCM $\boldsymbol{\Sigma}_{\gamma\gamma-rou}$ of the stochastic correlating group for object properties can be filled. The challenging part is to find values for Rt for the object surface. In the ideal case, roughness measurements can be performed for a sample of the surface, but this is not always possible due to inaccessible areas of the objects or the unavailability of mobile roughness measurement instruments. An alternative is to use values from scientific publications or reports. A few examples of numeric values for Rt in the case of profile analysis and St for surface analysis are provided in table 5.1.

Table 5.1 Examples of roughness values for *Rz* for different materials

Material class	Material	Roughness parameters (source)	Literature source
Wood	Spruce planed	*Rt* = ~ 67 µm	Csanády et al. (2015)
	Oak planed	*Rt* = ~ 108 µm	Csanády et al. (2015)
	Birch	*Rt* = ~ 52 µm	Vitosytė et al. (2015)
Alloy	Sand blasted aluminum	*Rt* = ~32 µm … 54 µm	Slătineanu et al. (2011)
	Blasted Structural Steel	*Rt* = ~87 µm … 102 µm	Draganovská et al. (2018)
Concrete	Concrete C35/45	*St* = 1.7 mm … 3.5 mm	Possler (2009)
	Exposed aggregate concrete	*St* = ~ 4 mm	Jirovský (2021)
	Concrete pavement	*Rt* = ~ 5 mm	Schulz (2008)

In all cases, the user must be aware of the scale at which the profile needs to be analyzed and for which kind of surfaces is the standard deviation representative. More precisely, the recommendation is to define the evaluation length ln based on the footprint size that can be approximately determined (eq. 5.3) if the scanning configuration is known. And this should be done on several areas of the object's surface. Therefore, in the following paragraphs scales at which such profiles analysis are appropriate for TLS measurements are shortly discussed.

Depending on the application, different scales of the surface profile can be analyzed. Many classifications are possible, but in this study, the one presented by Jutzi et al. (2017) for airborne LiDAR and RADAR is adapted for TLS measurements. It differentiates between three classes of roughness profiles, namely macro-, meso- and microstructures based on the irregularities, the laser footprint size of the measurement system, and the wavelength of the same system (fig. 5.9). The term "irregularities" covers the variations of the roughness profile along both (height and width of hills and valleys). The classification is explained based on the irregularities dimensions along the surface.

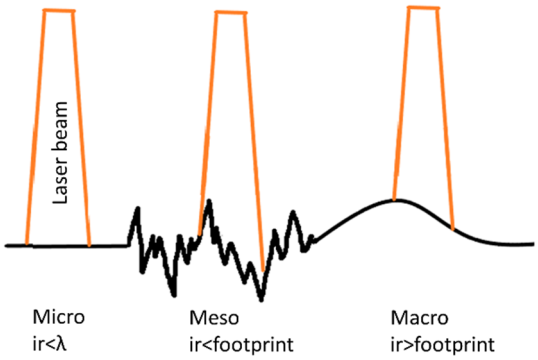

Figure 5.9. Scales of the analyzed profile with regard to footprint size. The irregularities are depicted by "ir".

The macro structures category comprises every object that shows profile irregularities larger that the smallest footprint and spacing between two consecutive footprints. For TLS point clouds, all clearly identifiable surface features (shapes) belong to this category. Exceptions to this rule are surface imperfections like cracks or pores that may still not be identified in the point cloud due to their small dimensions and available scanning resolution. Recently, Chaudhry et al. (2021) and Schmitz et al. (2020) have made an in-depth analysis of the resolution capability of high-end laser scanners, giving recommendations about which scan setting is appropriate for different TLS applications.

The second category of meso structures contains all structures with irregularities of dimensions smaller than the footprint and larger than the wavelength of the EDM. For TLS applications, almost every material falls into this category, which means that their dimensions (surface features) are larger than the wavelength, typically $>\lambda_L$ =1550 nm, and smaller than the footprint size (e.g. < 35 mm), depending on scanning geometry. This may have a big impact on the distance measurement due to physically varying distances from the source to different parts of the object within the footprint. Most likely, the measurement is biased by these variations leading to an effect like mixed voxels at the edges.

For micro structures, the irregularities' dimensions are smaller than the wavelength. Therefore, variations within this interval become negligible for TLS purposes. In some cases, the object may not be even measurable due to specular reflection (cf. fig 5.2a). According to the Rayleigh criterion, for a surface to be classified as smooth (specular reflections), the irregularities must be smaller than about λ_L /8 as mentioned before (Rees, 2013). However, more attention will not be devoted to this category, since objects of interest captured by TLS mainly show variations larger than 0.2 μm (e.g. for λ_L =1550 nm).

Based on this classification, the roughness analysis can be performed at different scales according to two factors: the footprint size and roughness profile within the footprint area. In most cases, it is possible to obtain an estimate of the footprint size (see sec. 5.2). Starting from this, sample roughness profiles should be extracted on several areas of the object. Next, standard deviations for the distance measurements are determined from this analysis at the meso level (for TLS). The extracted profiles may show periodic variations, which means that the TLS measured points are correlated due to the surface nature. This fact will be explained in section 5.4.

In this section, an approach for obtaining variances of distance measurements based on roughness has been introduced. It relies on the total profile height and probability distribution functions of the irregularities within the laser footprint. Covariances for roughness are treated in sec. 5.4 and the final application in the elementary error model is explained in sec. 5.5.

5.3.2 Reflectance

General facts on reflectivity have been presented in sec. 5.1. In this part, an approach for quantifying the effect of reflectivity on TLS observations is presented. The relation between surface reflectivity and TLS distance measurements cannot be defined as a function in a similar manner as seen in chapter 3 for instrument-specific errors. According to TLS manufacturers (e.g. Riegl Laser Measurement Systems GmbH, Teledyne Optech Inc.), the longest measurable distance strongly depends on surface reflectivity, meaning that the measurement is possible if reflectance is above a certain threshold at a given range.

Other TLS manufacturers (e.g. Zoller+Fröhlich GmbH, 2021, Basis Software Inc., 2021) give direct information about the distance measurement noise with regard to reflectivity and range in form of lookup tables. With the help of these values, the user is able to estimate the uncertainty of range measurements depending on approximate distances and surface reflectivity. Because these values are discrete, not all scenarios (e.g. different distances or reflectivity than those in the table) can be covered. A workaround is to use interpolated functions. To outline this principle, such a table is taken from the Z+F Imager 5016 technical specifications (Zoller+Fröhlich GmbH, 2021), and a polynomial surface is interpolated. Based on these values, the standard deviations for distances are obtained and introduced in the $\boldsymbol{\Sigma}_{\gamma\gamma-ref}$ matrix. For completeness, the discrete values from the technical specification are given in table 5.2. The reason for choosing this type of scanner is the availability of data for ranges up to 200 m and reflectance for three levels, despite the fact that indications for 100 m and 200 m are given as "not fully tested values" by the manufacturer. This data set is preferred for interpolation due to their coverage of distance and reflectance intervals (see fig. 5.10). In technical specifications from other scanners (e.g. Leica RTC360 or Faro S350Plus) the indications are given only for one reflectance level (e.g. 89 %) or for short ranges (e.g. up to 25 m). Therefore, they are not appropriate for interpolation purposes. Some scientific papers (cf. Voegtle and Wakaluk, 2009), also present values from experiments with ranges up to 25 m.

Table 5.2 Distance measurement noise (1σ) dependence on distance and reflectance as given in Z+F 5016 Datasheet

Dist(m)/Reflectance	14%	37%	80%
10	0.30 mm	0.25 mm	0.20 mm
25	0.39 mm	0.28 mm	0.25 mm
50	0.80 mm	0.50 mm	0.30 mm
100	2.60 mm	1.10 mm	0.70 mm
200	9.60 mm	3.60 mm	1.70 mm

Discrete values are plotted and a polynomial function is interpolated, therefore values for the range standard deviation can be directly obtained.

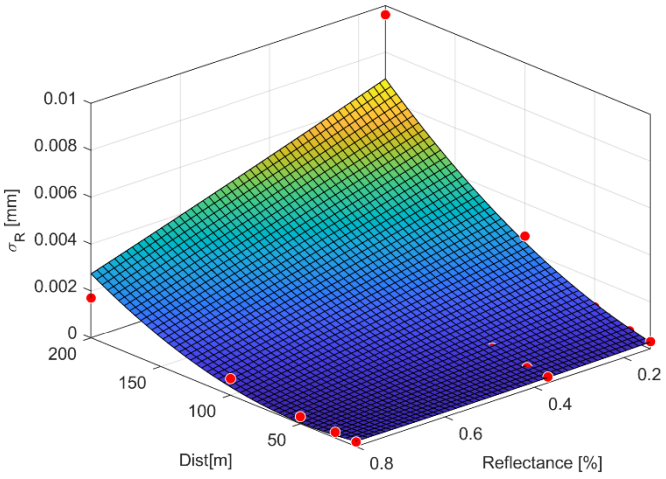

Figure 5.10. Polynomial function describing distance measurement standard deviation (Z+F Imager 5016) with regard to range and reflectance. Red points are values from table 5.2.

There are multiple types of surfaces that can be estimated based on these discrete values, but after empirical tryouts, it was seen that a weighted polynomial function of second order leads to the smallest residuals for the given values (tab 5.2). As weights, the inverse squared distance is used in order to avoid overfitting the data.

This surface in fig. 5.10 is described analytically by the following function:

$$\sigma_R = p_{00} + p_{10}\,\mathrm{R} + p_{01}\,\chi + p_{20}\,\mathrm{R}^2 + p_{11}\,\chi\,\mathrm{R} + p_{02}\,\chi^2, \tag{5.7}$$

where the coefficients are:

$$\begin{aligned} p_{00} &= 0.0001864; \\ p_{10} &= 1.429e-05; \\ p_{01} &= -0.0001207; \\ p_{20} &= 1.186e-07; \\ p_{11} &= -3.256e-05; \\ p_{02} &= 0.0003875. \end{aligned}$$

Higher order surfaces may be estimated as well, but this leads to overfitting of the data, therefore some areas without data points (e.g. empirical values at reflectance 60 %) lead to estimations that are not realistic. For example, a third-order function results in a surface "valley" at 60 % reflectance, suggesting that σ_R is better in that area compared to values at 80 % reflectance. Since this is the opposite of what literature studies affirm, higher-order surfaces are not used. This function is valid only for the scanner in case (see tab. 5.2). If similar empirical values as in table 5.2 are provided, other functions can be estimated. In this work, this is the only data set available for ranges that occur in the study cases.

Up to now, only the main diagonal of both VCM of the object surface elementary errors have been treated. In the next section, the approach for deriving covariances of the same matrixes is explained.

5.4 Surface properties for covariance & correlation functions

Surface features vary throughout the whole analyzed surface. For example, knowing the mean surface roughness does not imply that the surface profile is constant along the complete surface. There are surfaces with identical values for the profile total height Rt or maximum profile height Rz and cannot be discriminated based only on this parameter (Lynch, 2012). For some surfaces (e.g. wood), reoccurring patterns can be observed for features like reflectance along the grain direction. Some surfaces have natural irregularities in form of pores, stripes, wholes, etc. (fig. 5.12).

Therefore, using only Rt or Rz does not give information on whether the hills and valleys of the surface profile are close together or whether they are far apart. There is however another indicator for this measure, namely the autocorrelation function or autocorrelation coefficient that describes this aspect of the surface (Beckmann & Spizzichino, 1963). By this means, the occurrence of irregularities along one direction is described by the function's correlation length. It is simultaneously a direct measure of the width of the surface's irregularities (Rees, 2013). The advantage is that it can be considered in each of the dimensions of the surface (e.g. longitudinal and transversal, diagonal, etc.).

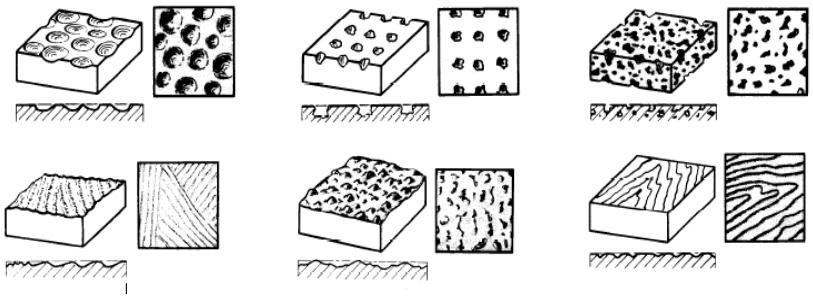

Figure 5.12. Surface character after DIN 4761 (DIN 4761:1978 – outdated)

Based on this principle, covariances are computed with the help of empirically identified correlation lengths for different materials. The first step is to choose a set of correlation (autocorrelation) functions. Common models found in literature (cf. Beckmann & Spizzichino 1963; Ishimaru, 2017; Lynch, 2012, Rees, 2013; Jurek et al., 2017) mostly use Gaussian functions (eq. 5.8) or negative exponential functions (eq. 5.9) to describe the correlations along an analyzed direction. The following functions for the correlation coefficient are sufficiently general:

$$\rho(\Delta R)_G = exp\left(-\frac{\Delta R^2}{{L_0}^2}\right), \tag{5.8}$$

$$\rho(\Delta R)_N = exp\left(-\frac{|\Delta R|}{L_0}\right), \tag{5.9}$$

where ΔR is the distance between analyzed features and L_0 the correlation length.

Within this function, the value of the correlation length (L_0) defines the function decay, implicitly determining the feature (e.g. reflectivity, roughness) correlation with previous points on the function. The term "length" should not be confused in this case with any metrical unit because it is strictly related to the correlation function and the units are defined over the function domain. A large value of the correlation length indicates that the feature is varying

slowly over the studied distance, while a small value shows rapid variations (Griffiths et al., 2011). By definition $\rho(0) = 1$ and $\rho(\infty) = 0$. To gain an impression of the correlation function decay with regard to correlation length, exemplary functions with different correlation lengths are shown in fig. 5.13.

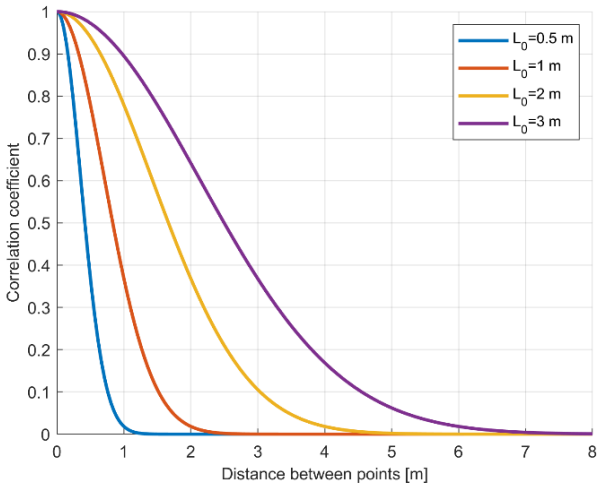

Figure 5.13. Examples of Gaussian correlation functions (cf. eq. 5.8) with different correlation lengths

This is a useful tool for defining spatial correlations in TLS point clouds for specific surfaces. However, finding appropriate correlation lengths for the Gaussian function is one of the biggest challenges. On one hand, roughness measurements are always done on a small sampling distance/area, relevant only for the meso scale. TLS point clouds, on the other hand, often cover a much bigger area than the one for which roughness analysis can be conducted, therefore the only alternative is to rely on the fact that the surface is homogenous with regard to the small sampled distance/area. To avoid general statements, the variety of TLS applications that can benefit from this assumption is reduced to monitoring applications in which the surface nature of the monitored object is known in advance (e.g. concrete, natural stone, wood, metal, etc.) This is mostly the case, and it is hardly imaginable that the surface nature cannot be remotely visually inspected (e.g. with a camera or UAV) even for inaccessible objects like rock cliffs, water dams, towers, etc.

In order to derive appropriate correlation lengths and verify if the correlation functions for surface properties can be generalized, an empirical approach based on image processing is used. The scope is to obtain measures of similarity for the respective surface property (e.g. reflectivity) from a sample of the surface or the entire surface. This can be achieved as suggested in the DIN EN ISO 25178-2 after computing the multidimensional autocorrelation function (ACF) for a defined sample area, further depicted by $\boldsymbol{A}$ to maintain coherence with the norm. Specifically, the values for reflectivity and roughness will be analyzed. The 2D autocorrelation function $f_{ACF}(t_x, t_y)$ is given by:

$$f_{ACF}(t_x, t_y) = \frac{\iint_A A(x,y) \cdot A(x - t_x, y - t_y)\, dx\, dy}{\iint_A A(x,y) \cdot A(x,y)\, dx\, dy} \tag{5.10}$$

where $\boldsymbol{A}$ is the definition area (sample area), t_x, t_y are the shifts (lags) of the same definition area and $A(x, y)$ describes a certain feature (e.g. height above mean plane) at position (x, y).

In any type of analysis, if the ACF is plotted, it will have a peak in the middle (cf. fig. 5.14 left), a point at which the sample is perfectly correlated with itself ($t_x = t_y = 0$) and present a specific decay according to the nature of that surface. At the same shift values, the ACF gives the variances.

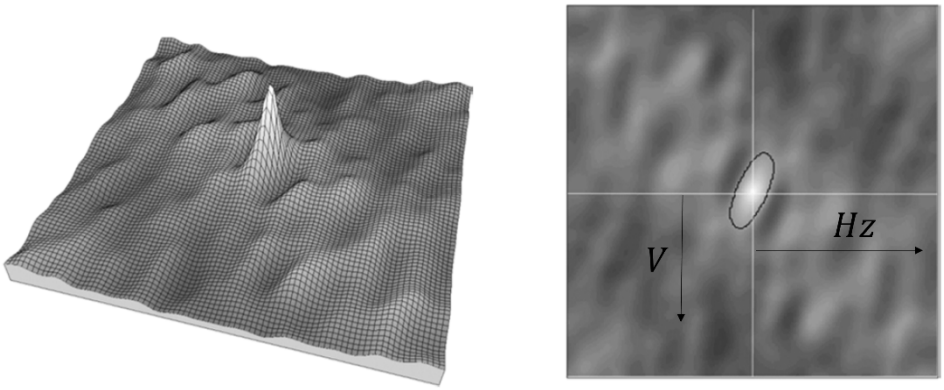

Figure 5.14. Left: the autocorrelation function in 3D and its peak at maximum correlation. Right: same function in 2D and the extraction of empirical correlations along two directions (white lines).

Having the 2D ACF, it is possible to extract empirical values along directions of interest. The t_x, t_y shifts (lags) are set equivalent to TLS scan lines directions (horizontal and vertical) as explained in the next sections. With the help of empirical values along each direction, correlation functions as stated in eq. 5.8 or 5.9 can be estimated for generalizing purposes or correlation coefficients can be directly extracted from the obtained 2D ACF (eq. 5.10).

An alternative to obtain the ACF in eq. 5.10 is to use a discrete autocovariance function (Agterberg, 1974; Meier and Keller, 1990) that directly yields an estimation of the covariances:

$$C(t_x, t_y) = \frac{1}{(u_c - t_x - 1) \cdot (v_c - t_y - 1)} \cdot \sum_{x=1}^{u_c - t_x} \sum_{y=1}^{v_c - t_y} (A(x,y) - \bar{A}) \cdot (A(\mathrm{x} + t_x, \mathrm{y} + t_y) - \bar{A}). \tag{5.11}$$

Here u_c and v_c represent the number of features of $\boldsymbol{A}$ over which the autocovariance function is computed and t_x, t_y depict the shifts (lag) along both directions, $A(x,y)$ depicts the value on the surface at position (x,y). Due to statistical reasons, a reliable approximation is only possible up to the point $t_x = u_c\,/10$ and $t_y = v_c/10$ (cf. Heunecke et al., 2013). A specific property of the autocovariance function is that at shift 0, the empirical variance is obtained, meaning that the autocovariance implicitly contains the variance. For more details, consult chapter 9 in Heunecke et al. (2013). Consequently, the ACF is:

$$f_{ACF} = \frac{C(t_x, t_y)}{C(0,0)}. \tag{5.12}$$

These 2D ACFs can be empirically determined for a small sample area or the entire area of the object. If the characteristics of a surface differ strongly, several sample areas can be studied, but if the surface is (theoretically) homogeneous, it is assumed that the ACF is valid for other parts of the object, therefore only one correlation length can be used for all directions. This implies that the mean and autocorrelation estimated from a small sample of the surface

provide unbiased estimates for the entire assemblage (Agterberg, 1974). As with atmospheric parameters, stationarity is assumed for the analyzed surface sample for which the samples are equidistant. This is implicitly the case when using eq. 5.10 and 5.11.

For surfaces with varying characteristics along one direction, like different wood types with pronounced fiber direction, two separate correlation functions are recommended, due to differences between the features in each direction. Numerical examples are given with the help of a working example.

5.4.1 Correlations for reflectance

In section 5.3.2, the relation between the measured distance variances and reflectance was presented. With this, the variance is directly obtained based on the technical specifications of laser scanners or empirical values. In what concerns the covariances caused by reflectance, the two-step approach must be used. With the known ACF for reflectance (cf. eq. 5.10) and variances caused by reflectance for distances (cf. eq. 5.7), the covariances for distances are determined as explained next.

The approach is presented briefly by a workflow chart (fig. 5.15), followed by a detailed explanation accompanied by an example of a real object. It comprises four steps. In the first one, the 3D point cloud together with its reflectance information (e.g. reflectance value for each point) is needed (fig. 5.15 step 1). The coordinate system origin is considered the TLS station point (0, 0, 0).

In the second step, the point cloud is projected onto a 2D grid in form of an image in which each pixel represents the reflectance value of one measured point (fig. 5.15 step 2). The value for reflectance can be given as a percent or scaled between 0 and 1. The pixels are arranged according to the horizontal and vertical angles derived from the point cloud. Grid spacing is directly defined by the angular scanning resolution, a setting usually known by the user. Other projection methods imply equidistant (metrical unit) spacing on the object. In the current approach equidistant spacing is not an option because, in TLS scans, the distances between single points are never equidistant, rather constantly changing based on the object shape and scanning configuration. In the ideal case, the surface should be represented by equally spaced samples, but this can only be obtained from independent sources (e.g. UAV) and not directly from the TLS. Nevertheless, angular increments defined by the scanning resolution are approximately constant for the entire point cloud and independent of the object shape or scanning configuration. This type of representation is also found in different TLS processing software, usually used for displaying the point cloud as a panorama or 2D image (e.g. Riegl RiScan, Faro Scene, etc.).

In the third step, the ACF (eq. 5.9) is computed on the previously obtained 2D image (grid). The shifts (lags) for the ACF represent discrete steps (pixels) in each direction, e.g. t_x along the horizontal angle direction and t_y along the vertical angle direction (fig. 5.15 step 3).

Finally, the correlation coefficients between the points (pixels) are extracted from the ACF and converted into angular units. The conversion is necessary because they are obtained from these observations. Afterwards, the covariances are obtained with the help of correlation coefficients between different points according to their position relative to the ACF middle point (shift=0) (fig. 5.15 step 4). This fact is explained in detail in the example with the real object.

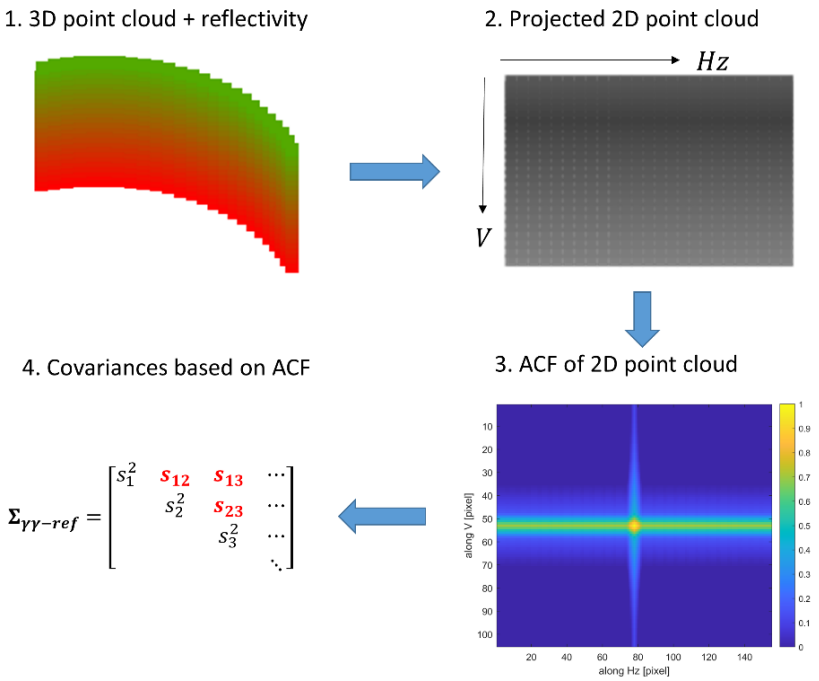

Figure 5.15. Workflow applied for determining covariances originating from the surface reflectivity.

A segmented point cloud of the Kops water dam (fig. 5.16) acquired from around 90 m is used for exemplifying the resulting correlation functions in a real study case. More details about the scanned object are given in the practical experiments section 6.3. It was scanned with a Riegl VZ 2000 scanner and surface reflectance information for each point is directly available. The conversion to % is made as stated in eq. 5.4. The result is presented in fig. 5.16. As a side note, it is noticeable that there are certain areas of the dam that show rather low reflectance values (less than 40 %) in the lower left part. After an on-site inspection, this is because of the different concrete mixtures in this area. There are also parts of the dam that show very good reflectance values (nearly 100%). These are actually deposits caused by water infiltrations that result in nearly white patches on the dam's surface. However, a more detailed analysis of the dam's surface reflectivity is not the subject of this work.

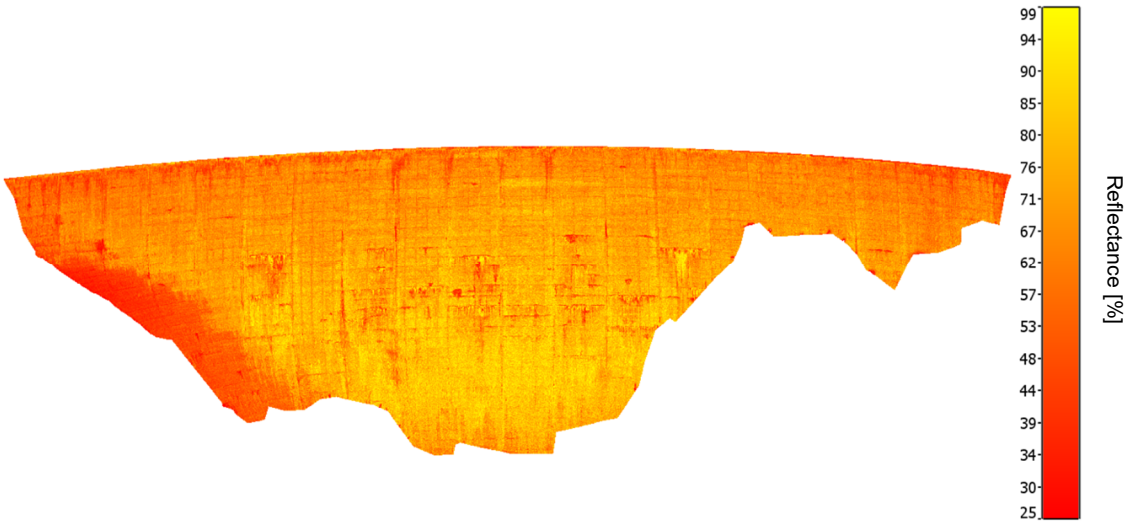

Figure 5.16. Point cloud of the water dam Kops colored according to reflectance obtained with the Riegl VZ 2000 scanner.

As seen in eq. 5.10, the ACF is computed for a sample area in which z depicts the feature of interest. In order to compute the same function for the complete point cloud, the projection explained in step 2 is used. The scanning resolution in this case was set to 0.033 gons for both vertical and horizontal angles, therefore each pixel in the projected point cloud (grid) has a constant spacing of 0.033 gons. The numeric value of each pixel is the reflectance value directly in %. Next, an ACF of the projected point cloud is computed. The resulting function has the same units (here pixels). Since the relation between pixels and angles is known from the projected point cloud, the conversion from pixel to angle from the ACF is also possible. This means that correlation coefficients (values of the ACF pixels) between two pixels in the ACF can be directly interpreted as correlation coefficients between two points in the point cloud. The spacing is defined by angular units as explained previously.

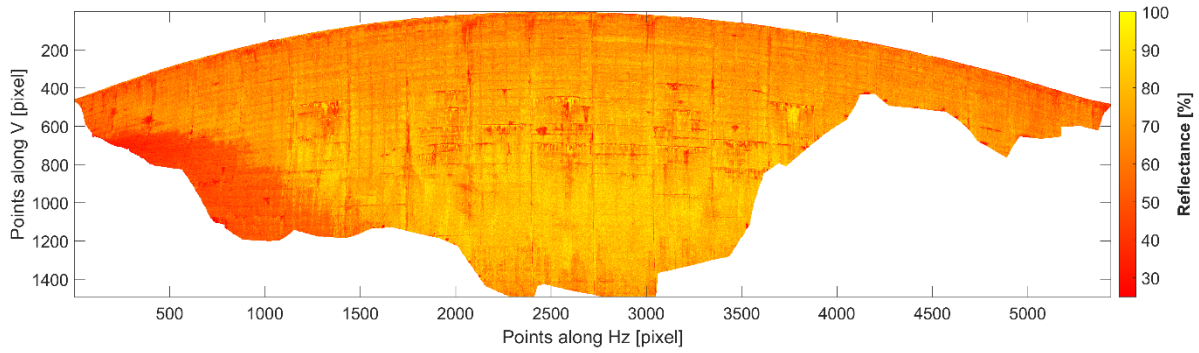

Figure 5.17. 2D panorama created from the point cloud of the water dam Kops.

Next, the ACF is computed for the 2D image (Ursell, 2021) and represented (fig. 5.18). Note that the representation is made in 3D only to emphasize the function shape. The axes' directions correspond to the axes of the analyzed image (fig. 5.17), therefore it is possible to extract correlation coefficients directly along horizontal and vertical directions out of the empirical ACF and retrieve 1D correlation functions. Fig. 5.18 also shows the function decay along both directions. Data points from the ACF are extracted along the vertical direction and horizontal direction for discussion purposes.

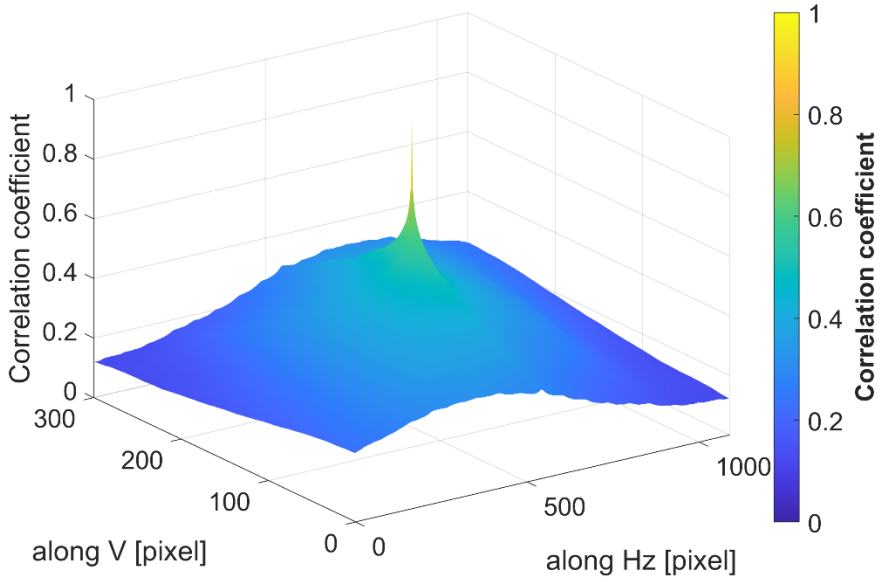

Figure 5.18. The ACF of the 2D panorama for reflectivity (fig. 5.17)

As noticed, the correlation coefficient reaches its peak value in the middle, where the lags t_x, t_y are 0. Starting from this middle point, data is extracted up to the borders of the ACF representation. The discrete data represented by pixels with correlation coefficients is visualized in fig. 5.19. At the beginning of this section, two general correlation functions have been presented (eq. 5.8 and 5.9). The negative exponential function led to smaller residuals (best fit) for both horizontal and vertical directions (fig. 5.19 detail boxes). However, this fact is valid only for a small interval of the data, as concluded after empirical tryouts. The exponential function general form is: $co_1 \cdot e^{\left(-\frac{x}{co_2}\right)} + co_3 \cdot e^{\left(-\frac{x}{co_4}\right)}$, where $co_i, i = (1..4)$ represent the estimated coefficients and x represents the discrete data for which the function is estimated. In each case, after a certain point, e.g. 9 pixels in the horizontal direction and 15 pixels in the vertical direction, the correlation coefficients show a nearly linear decay. In other words, a single correlation function cannot be estimated for the entire interval covered by the empirical data. More likely, separate functions need to be estimated for given intervals. This is a decision that can be taken only based on the analyzed data and should not be generalized.

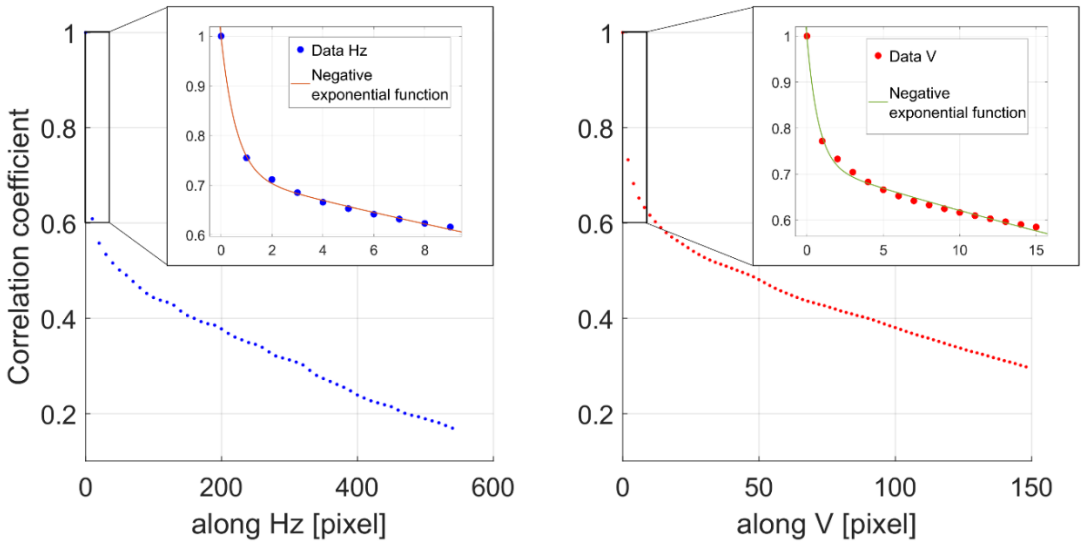

Figure 5.19. Correlation functions along two directions. Empirical data (red) and estimated negative exponential correlation functions with their corresponding correlation length (blue and green).

Figure 5.19 additionally shows that surface features such as reflectance are, on one side correlated with each other, and on the other, correlation functions can be represented by exponential functions. It is arguable that another type of function could also fit the data (e.g. power function), but the exponential is preferred due to its recommendation in literature and validity for natural features (cf. Beckmann & Spizzichino, 1963).

The estimated exponential equations are unnecessary for further processing because the correlation coefficients for any pair of points and arbitrary directions are extracted directly from the ACF, as described in the next paragraph.

Let points *S* and *T* be 1 gon (~30 pixels) in the horizontal and in the vertical direction apart from one another. The conversion is done based on the known size of one pixel in gons, here 0.033 gon = 1 pixel for Hz and 0.033 gon = 1 pixel for V. Finally, the value of the correlation coefficient between points *S* and *T* is obtained directly from the table cell at a specific position in the ACF (peak + 30, peak + 30) – corresponding to the 1 gon spacing in each direction and

gives the value of ρ_{ST}=0.47. The same procedure is applied for all point pairs and therefore, correlation coefficients for the property reflectivity are obtained.

To gain an impression of the correlation coefficients for different scanning resolutions, examples are given for two object points considered on the same horizontal or vertical scan line. The mean distance from TLS to the dam is 90 m in this case and the spacing between neighboring points is chosen according to pixel size as multiples of the aforementioned values. The column "equivalent distance" refers to the point spacing on the object for the respective resolution at 90 m.

Table 5.3 Example of correlation coefficients for reflectance along scanning lines (Hz & V) on the surface of the Kops dam scanned from 90 m.

Angular spacing (gon)	Equivalent distance between 2 points (m)	$\boldsymbol{\rho(\Delta Hz)}$	$\boldsymbol{\rho(\Delta V)}$
0.033	0.047	0.755	0.772
0.066	0.093	0.711	0.733
0.132	0.187	0.666	0.683
0.264	0.373	0.623	0.633
0.528	0.746	0.574	0.580
1.056	1.493	0.529	0.522
2.112	2.987	0.487	0.444
4.224	5.980	0.429	0.330
$@t_y = 4.950$	7.012	-	0.297
$@t_x = 17.985$	26.124	0.167	-

The correlation coefficient values among points situated at these distances confirm the gradual decay observed in fig. 5.19. Moreover, the general intuition about high correlations for neighboring points on a surface with similar properties is also confirmed.

5.4.2 Correlations for roughness

Similar to the workflow presented before, correlation functions for roughness can be used to derive the covariances resulting from this object property. The main difference is that variances and covariances can be simultaneously obtained (cf. eq. 5.10) due to the direct dependency between roughness and distance measurements defined in sec. 5.3.1. In the ideal case, roughness measurements should be made for the entire analyzed surface, but for large objects, this is not practically realizable.

Unfortunately, an example of the same dam surface as for the reflectivity analysis is not available. Therefore, no specific values for Rt or the equivalent parameter St are available, but measurements of a concrete sample similar to the one of the dam's outer layer were used instead. The sample was used in literature (Schulz, 2008) for roughness analysis in another context. For current purposes, data for the same sample was cordially provided by the author (Schulz, 2008) in form of a very dense point cloud. The concrete sample represents a small area of 10.0 x 7.8 cm of aggregate concrete (fig. 5.20). It is obtained with a triangulation camera and the average point spacing is 0.1 mm. More details about how the sample was obtained, can be read in Schulz (2008).

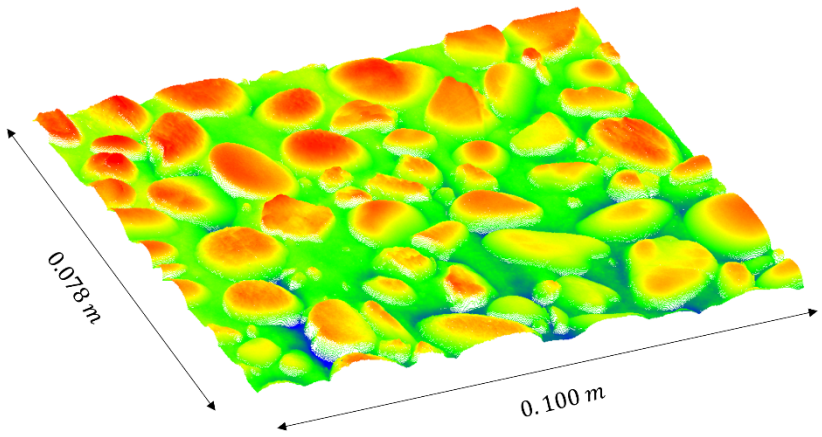

Figure 5.20. Sample of concrete surface captured by triangulation camera (Schulz, 2008).

From the sample, the maximum height of profile Rt can be directly calculated from the minimum and maximum values of z. If larger samples are available, the laser footprint size (cf. sec. 5.2) can be used to restrict the area over which the Rt value is computed. This is not the case here, since the available sample is very small. The value computed over the complete sample is 5.3 mm. As explained in sec. 5.3.1 the main diagonal of VCM $\boldsymbol{\Sigma_{\gamma\gamma-rou}}$ can now be filled.

For the covariances resulting from roughness, the surface analyzed feature is the height above the mean plane of the sample. This height depicts the irregularities (peaks and valleys) directly in metric units. In contrast to the workflow used for reflectivity, no projection onto a 2D plane is needed, because the height of the irregularities necessary for the ACF equation (cf. eq. 5.10) or covariance function (eq. 5.11) are directly available at each of the x and y positions in these equations as recommended in the DIN EN ISO 25178-2. In other words, at each position for the given sample, the height is known. The ACF computed with the shifts $t_x = 1\ cm$ and $t_y = 0.78\ cm$ is depicted in fig. 5.21.

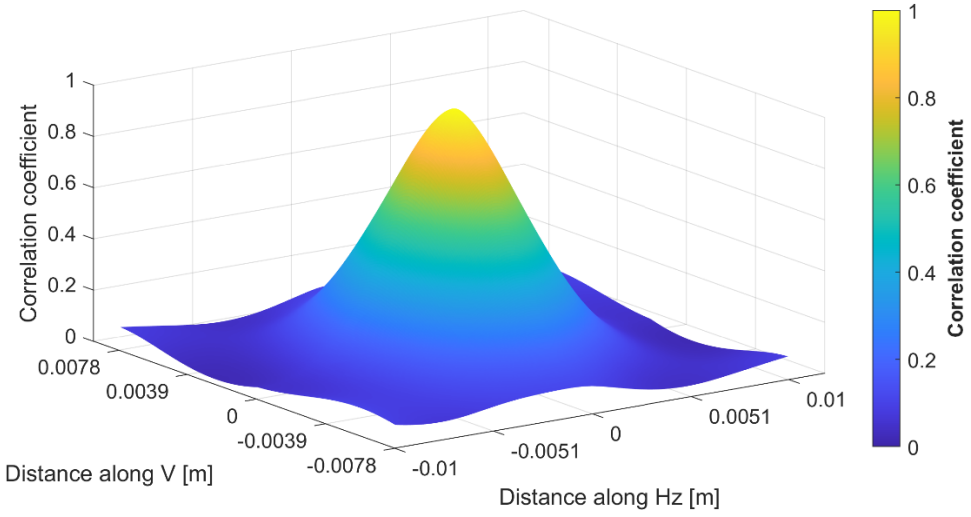

Figure 5.21. The ACF of roughness for small concrete sample from fig. 5.20

The correlation lengths in this case are directly retrieved in metrical units, as the original sample. It can be seen that the function follows a Gaussian decay in both directions (fig. 5.21).

For clearness, 1D functions are estimated analog to those for reflectance. In contrast to the functions used for reflectance, the empirical data resembles a Gaussian function (fig. 5.22) better than a negative exponential (cf. eq. 5.8 and 5.9). Once more, it is seen that correlations for natural features are very well represented by exponential functions. Along both directions, the obtained correlation lengths are relatively small, $L_{0\_Hz} = 4.3\ [mm]$ and $L_{0\_V} = 4.5\ [mm]$.

It is mentioned that the ACF obtained with this sample leads to high correlations only for very high scanning resolutions (e.g. point spacing less than 5 mm), in which the laser footprints overlap. For the sampling distances shown in tab. 5.3, the correlation coefficients are 0, therefore no table is presented here. The approach explained in sec. 5.4.1 is used for determining covariances between pairs of arbitrary points. Now the upper and lower part of VCM $\boldsymbol{\Sigma_{\gamma\gamma-rou}}$ can be filled.

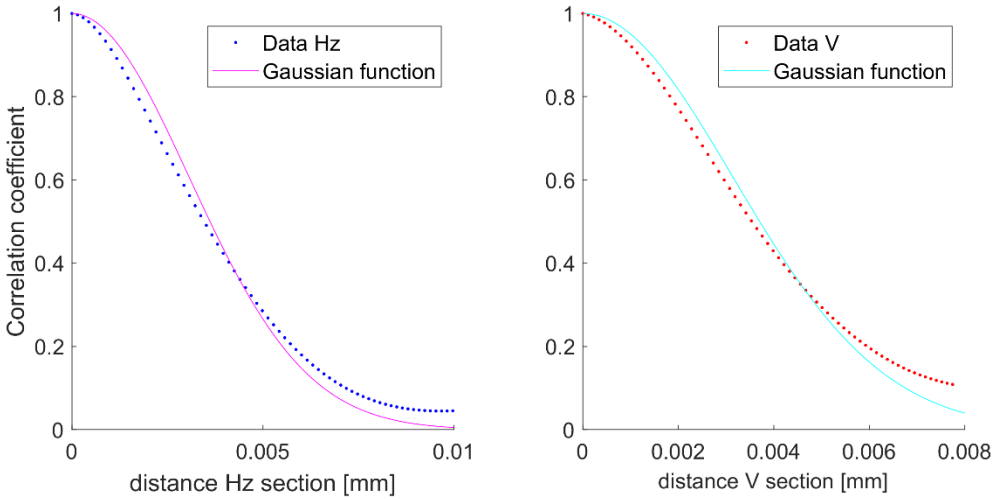

Figure 5.22. Extracted ACF of roughness along two sections fig. 5.20

This concludes the workflow for retrieving variances and covariances for the matrixes $\boldsymbol{\Sigma_{\gamma\gamma-rou}}$ and $\boldsymbol{\Sigma_{\gamma\gamma-ref}}$. In the next section, they are introduced into the elementary error model.

5.5 Application to the elementary error model

The object surface elementary errors presented here have been likewise classified in the stochastic correlating group. It was seen that they can be correlated within the same group and a strict separation into stochastic independent groups is not possible.

Besides the VCM for reflectivity and roughness, the influencing matrices for the object surface properties errors (cf. sec. 4.1) have to be defined. Similar to the case of atmospheric errors, the object-related errors influencing matrix is constructed out of block matrices with diagonal elements defined as follows:

$$\boldsymbol{G_{obj}} = \begin{bmatrix} G_1 & 0 & \cdots & 0 \\ 0 & G_2 & 0 & \vdots \\ \vdots & 0 & \ddots & \vdots \\ 0 & \cdots & \cdots & G_n \end{bmatrix}, \quad \boldsymbol{G_i} = \begin{bmatrix} 0 & 0 & 0 \\ 0 & 0 & 0 \\ 0 & 0 & gi \end{bmatrix}, \tag{5.13}$$

with each submatrix $\boldsymbol{G_1}$, $\boldsymbol{G_2}$…$\boldsymbol{G_n}$, generic called $\boldsymbol{G_i}$ as a 3x3 matrix corresponding to the observation order. As seen at the beginning of this chapter (sec. 5.1), only the distance

measurements are affected by the object's surface properties. According to the way observations are arranged in the SVCM, the distances measurements are on the (3,3) position in each submatrix, therefore only this element will receive a value in this group of errors. Unlike in the case of instrumental functional correlating errors, the influencing factors cannot be obtained by partial derivatives, because there is no direct functional relation between the distance measurement and the object surface properties' roughness, respectively reflectivity. However, influencing coefficients can be defined starting from the radar equation and based on experimental evidence. In this sense, the influencing matrixes for both groups, further denoted by $\boldsymbol{G_{ref}}$ and $\boldsymbol{G_{rou}}$ are constructed based on the currently available knowledge from scientific publications.

Starting with reflectance, in sec. 5.3.2 the eq. 5.7 gives the functional dependency of TLS distance variances, reflectance, and distance between TLS and object. It was seen that the elements of the VCM $\boldsymbol{\Sigma_{\gamma\gamma-ref}}$ contain variances and covariances that are dependent on reflectivity and distance between the scanner and the object. Based on the radar equation and findings from literature, a scan geometry-dependent factor based on the angle of incidence (β) is introduced in the $\boldsymbol{G_{ref}}$ matrix. This is done to model variances that occur at large angles of incidence in a plausible way. The underlying principle is that with increasing values for β, the uncertainty also increases. In other words, the variance of the distance measurement increases at large angles of incidence (cf. Rachakonda et al., 2015). This resembles the statement according to which the distance variance is inversely proportional to the received signal strength (Fröhlich, 1996) and is supported by the form of the laser footprint at high incidence angles (cf. fig. 5.3). A commonly used model to express this is by cosine function (cf. Jutzi, 2007; Kaasalainen et al., 2011; Grant et al., 2012; Soudarissanane, 2016; Chaudhry, 2021) in a variety of forms. In this thesis, the chosen cosine function is based on the radar equation (eq. 5.1) and uses the inverse cosine of the angle of incidence of each observation. Therefore, in each $\boldsymbol{G_{ref\_i}}$ block of the influencing matrix $\boldsymbol{G}$, the term gi for individual observations is defined as:

$$gi = \frac{1}{\cos(\beta)}. \tag{5.14}$$

The influencing factor in gi is dimensionless, therefore no conversion constants are needed.

As regards roughness, the existence of surface roughness is one of the main factors that make TLS distance measurements possible in the first place. This is related to the diffuse and mixed reflection (cf. fig. 5.1 & 5.2) explained in sec. 5.1. Numerous studies strived to define a functional relation between roughness and distance measurements, but this has not been achieved up to date. There are common findings in these studies that can be used to define the influencing factors for roughness. Kukko et al. (2008) conducted experiments with TLS measurements of materials with different roughness levels. One of the very interesting findings is that their results indicate an independent behavior of the intensity relative to the angle of incidence. This may be caused by the roughness profile hills and valleys which leads to a higher amount of reflected light for rough surfaces. A similar phenomenon is observed in the experiments of Zámečníková and Neuner (2017). More recently, the effects of roughness together with angle of incidence have been presented by Linzer et al. (2021) and confirm that for angles of incidence from 15 gon to 60 gon, there is almost a constant influence on the distance measurement. All in all, the studies show that the distance measurement uncertainty

does not necessarily depend on the geometry-related term, angle of incidence. Due to this, the influencing matrix $\boldsymbol{G_{rou}}$ of the elementary error roughness is filed with ones on the corresponding position, therefore $g_{i\_\mathrm{rou}} = 1$ and all other elements are 0.

For clearness, the complete part of the elementary error model $\boldsymbol{\Sigma_{ll-Object}}$ caused by object surface properties is presented once more.

$$\boldsymbol{\Sigma_{ll-Object}} = \boldsymbol{\Sigma_{ll-ref}} + \boldsymbol{\Sigma_{ll-rou}}, \tag{5.15}$$

$$\boldsymbol{\Sigma_{ll-ref}} = \boldsymbol{G_{ref}} \cdot \boldsymbol{\Sigma_{\gamma\gamma-ref}} \cdot \boldsymbol{G_{ref}}^{\boldsymbol{T}}, \tag{5.16}$$

$$\boldsymbol{\Sigma_{\gamma\gamma-ref}} = \begin{bmatrix} 0 & 0 & 0 & 0 & 0 & 0 & \cdots & 0 & 0 & 0 \\ & 0 & 0 & 0 & 0 & 0 & \cdots & 0 & 0 & 0 \\ & & \sigma_{R1}^2 & 0 & 0 & \sigma_{R1R2} & \cdots & 0 & 0 & \sigma_{R1Rn} \\ & & & 0 & 0 & 0 & \cdots & 0 & 0 & 0 \\ & & & & 0 & 0 & \cdots & 0 & 0 & 0 \\ & & & & & \sigma_{R2}^2 & \cdots & 0 & 0 & \sigma_{R2Rn} \\ & & & & & & \ddots & \vdots & \vdots & \vdots \\ & & & & & & & 0 & 0 & 0 \\ & & & & & & & & 0 & 0 \\ & & & & & & & & & \sigma_{Rn}^2 \end{bmatrix}, \tag{5.17}$$

where σ_R is obtained as in eq. 5.7.

$$\sigma_{RiRn} = \rho \cdot \sigma_{Ri} \cdot \sigma_{Rj}, \tag{5.18}$$

where i, j indices up to n number of observations and $i \neq j$. For ρ see ACF example in fig 5.18.

$$\boldsymbol{\Sigma_{ll-rou}} = I \cdot \boldsymbol{\Sigma_{\gamma\gamma-rou}} \cdot I^{\boldsymbol{T}} = \boldsymbol{\Sigma_{\gamma\gamma-rou}}, \tag{5.19}$$

$$\boldsymbol{\Sigma_{\gamma\gamma-rou}} = \begin{bmatrix} 0 & 0 & 0 & 0 & 0 & 0 & \cdots & 0 & 0 & 0 \\ & 0 & 0 & 0 & 0 & 0 & \cdots & 0 & 0 & 0 \\ & & \sigma_{R1}^2 & 0 & 0 & \sigma_{R1R2} & \cdots & 0 & 0 & \sigma_{R1Rn} \\ & & & 0 & 0 & 0 & \cdots & 0 & 0 & 0 \\ & & & & 0 & 0 & \cdots & 0 & 0 & 0 \\ & & & & & \sigma_{R2}^2 & \cdots & 0 & 0 & \sigma_{R2Rn} \\ & & & & & & \ddots & \vdots & \vdots & \vdots \\ & & & & & & & 0 & 0 & 0 \\ & & & & & & & & 0 & 0 \\ & & & & & & & & & \sigma_{Rn}^2 \end{bmatrix}, \tag{5.20}$$

where $\sigma_R = Rt \cdot 0.3$ and σ_{RiRj} are obtained as explained in sec. 5.4.2.

This concludes the object surface-related elementary error group. The contribution to the SVCM has been explained and in the next chapter, numerical examples are given for simulated and real objects.

6. Study cases

The possible applications of a stochastic model in form of a VCM are manifold and depend on the pursued scope. In this chapter, they are restricted to four applications for objects of different sizes. The subchapter names and object sizes are as follows:

6.1 The SVCM of a simulated wall – size up to a hundred meters;
6.2 Relevance of the SVCM in sphere estimation – size up to a few decimeters;
6.3 Deformation analysis of a wooden tower – size up to a few meters;
6.4 TLS optimal station point, exemplary for an arch dam scan– size up to a few hundred meters.

With exception of the first study case, all other cases use real data obtained with different types of laser scanners. The first study case offers an in-depth analysis of the SVCM defined with the elementary error model for a simulated wall that resembles a high-rise building. The following three study cases are common applications that practitioners encounter in TLS reality capture and TLS deformation analysis.

It should be noted, that the VCM based on the elementary error theory cannot not be applied to all groups of elementary errors as described in chapters 3, 4, and 5 for all study cases. This is due to the continuous development of the TLS elementary error model and the planning of measurement campaigns concomitantly. Therefore, in some cases, the unavailability of supplementary information, like surface roughness measurement, reflectance information of the surface, or atmospheric parameters obtained on-site, does not allow the integration of the VCM with all groups of errors for all study cases. Nevertheless, the contributing elementary errors are presented in tables for each case. Some results are partly published in previous papers of the author or in other joint papers.

6.1 The SVCM of a simulated wall

The first application addresses one of the most common questions among TLS practitioners. It offers an answer to the inquiry about the expected uncertainty for TLS point clouds. As formulated in previous chapters, this answer depends on multiple factors and is not straightforward. Therefore, in this first application, SVCMs have been generated for simulated point clouds of a wall. This wall is the same as in the example for the atmospheric elementary errors in sec. 4.3. It is 66 m wide and 114 m tall (fig. 6.1) and is assumed to be made of concrete as in the examples presented in sec. 5.4.2. In total, the point cloud of the wall contains 1972 points with a distance of 2 m in the horizontal and vertical directions. Regarding the object's dimensions, they have been chosen to gain an impression of the spatial distribution of variances and covariances that may occur in situations with real objects like high-rise buildings, bridge pillars, water dams, etc. The atmospheric parameters have been simulated as in sec. 4.3 with weather stations distributed in the measurement area. The same DTM was used.

In the following sections, SVCMs have been computed according to the methodology from chapters 2 to 5. Different scanning configurations have been simulated for two types of scanners – panoramic and hybrid (cf. sec. 3.4 and 3.5), namely the Leica HDS 7000 and Riegl VZ2000. The examples are restricted to four station points in which the horizontal distances from the scanner to the wall vary in discrete steps from 20 m to 200 m (fig. 6.1).

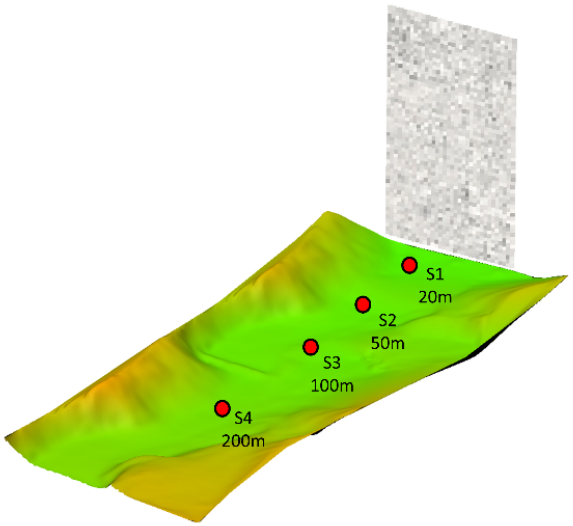

Figure 6.1. Overview with the simulated concrete wall, the DTM and the TLS station points.

The focus is set on the dependency of variances in relation to the scanning distance. Inevitably, with the varying distances, the angles of incidence also change. Regarding the coordinate space, each TLS station point defines the origin of a local coordinate system, therefore all values of variances given in Cartesian coordinates are relative to the TLS local coordinate system.

Table 6.1 Simulated station points for each type of scanner at different distances.

Distance from scanner to wall	Leica HDS 7000	Riegl VZ 2000
20 m	**x**	
50 m	**x**	**x**
100 m	**x**	**x**
200 m		**x**

For these simulated TLS station points, the technical restrictions of each scanner have been considered, therefore SVCMs are only generated for station points from which the complete wall can be scanned. For example, the Leica HDS7000 has a working range of 187 m, therefore the station point at 200 m is not simulated. Also, for the Riegl VZ2000, the station point at 20 m is not simulated because the scanner has a vertical field of view of +60°, meaning that only the lower part of the wall (up to 34 m) can be scanned. These are the reasons for only having two overlapping simulated scenarios at 50 m and 100 m, respectively. For a clear separation, the results from different station points contain the station point name together with an indicator for the scanner, e.g. S1_L stands for the first station point acquired with the Leica scanner, whilst S3_R stands for the third station point acquired with the Riegl scanner. There is no intention of comparing the capabilities of these scanners here, rather the focus is on the SVCMs.

The elementary errors that are introduced in each SVCM have been presented in different sections up to now, therefore a table that jointly shows the numeric values used in this analysis is necessary (tab. 6.2). Note that this is only one level of variance for which upcoming results will be presented. It is possible to change the level of variance either globally (e.g. multiply all standard deviation values with a factor), or change individual values, as seen later.

Table 6.2 Values for elementary errors for both scanners.

Elementary error group	Panoramic scanner – Leica HDS700		Hybrid scanner – Riegl VZ 2000	
	Elementary error name [unit]	**Standard deviation**	**Elementary error name [unit]**	**Standard deviation**
Non-correlating errors	Angular noise Hz [mgon]	3.1	Angular noise Hz [mgon]	0.55
	Angular noise V [mgon]	3.1	Angular noise V [mgon]	1.66
	Range noise [mm]	0.5	Range noise [mm]	5
Functional correlating errors	x_{1n} [mm]	0.140	a_0 [mm]	0.34
	x_{1z} [mm]	0.220	a_1 [ppm]	40
	x_2 [mm]	0.020	b_4 [mgon]	3.18
	x_3 [mm]	0.130	b_6 [mgon]	1.91
	x_4 [mgon]	0.448	c_0 [mgon]	1.08
	x_{5n} [mgon]	1.738	c_1 [mgon]	1.85
	x_{5z} [mgon]	1.598	c_4 [mgon]	0.64
	x_6 [mgon]	0.272		
	x_7 [mgon]	1.929		
	x_{10} [mm]	0.060		
Stochastic correlating errors	Air temperature [°C]	Observation specific. At ground level σ = 5 °C		
	Air pressure [mbar]	Observation specific. At ground level σ = 2.41 mbar		
	VGT [°C/m]	Observation specific. σ = 0.06°C/m		
	Roughness = 0.3* Rt [mm]	1.6		
	Reflectivity (40% for concrete)	Observation specific - see sec. 5.3.2		

The values presented here are based on chapters 3, 4, and 5 and serve as the theoretical base for the upcoming variance and covariance (correlation) analysis.

6.1.1 Variance analysis

6.1.1.1 Space-wise analysis

Firstly, the main diagonal of the SVCM is analyzed. The variances of individual points are used to compute the mean error of position after Helmert for each of them:

$$\sigma_{xyz} = \sqrt{\sigma_x^2 + \sigma_y^2 + \sigma_z^2} \tag{6.1}$$

It serves as an indicator of the point uncertainty in the local coordinate system.

Each point is represented according to its coordinates and colored based on the magnitude of the error of position (fig. 6.2). With this information, the user is able to make decisions based on the pursued level of accuracy, which may be necessary for the whole object or only for specific parts of like (e.g. top or base). Only the point cloud of the wall is represented here. For the position of the station points, see fig. 6.1.

Figure 6.2 describes the uncertainty budget for different scanning configurations for the given elementary errors (tab. 6.2). In all cases, it can be seen how the error of position increases with increasing distance from the bottom of the wall to the top. This effect is more pronounced in scanning configurations that are close to the wall (e.g. S1-L and S2-R). For example, in S1-L distances from the scanner to the object points change from 20 m to 115 m at the top, which leads to errors of position in mm level (e.g. 2-4 mm) at the base of the wall and values of 12-19 mm at the top of the wall. This is due to the high angles of incidence that occur in this kind of

setup, a fact that will be highlighted by the individual contribution of elementary errors later. A similar, but less pronounced effect is observed at S2-R.

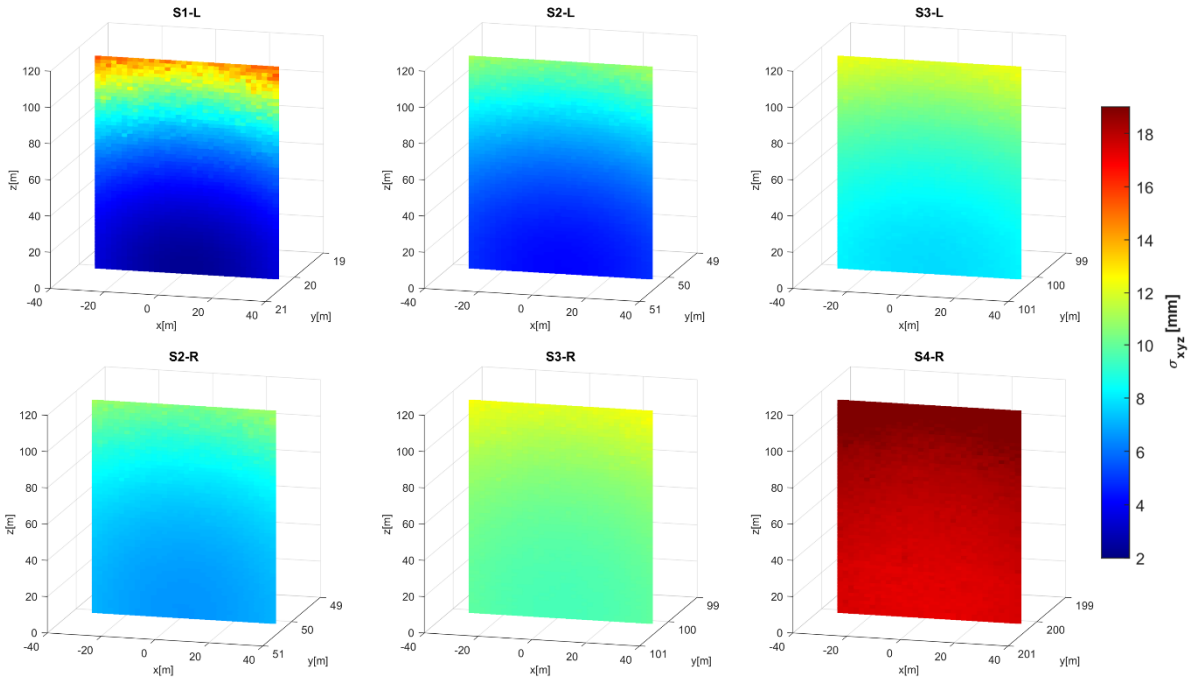

Figure 6.2. Error of position for the simulated wall scanned from different station points (varying distance). S1-L to S3-L represent the results from the SVCM of the Leica scanner, whilst S2-R to S4-R represent the results from the SVCM of the Riegl scanner.

As the distance from the object to scanner increases, so does the error of position. Simultaneously, the interval defined by the lowest and highest error of position decreases (cf. color scale fig. 6.2). For example, at 100 m, both S3-L and S3-R change from ca. 7-11 mm and 9-13 mm with increasing height, respectively. At the longest distance presented here (S4-R) the change is even less pronounced with differences from base to top of 17 mm to 19 mm. This is because of the more homogeneous distance measurements and angles of incidence that result from this configuration.

6.1.1.2 Contribution to the SVCM trace

This type of analysis gives information about the magnitude of the errors of position on the object but does not show which elementary errors are responsible for the complete uncertainty budget. Therefore, a more in-depth analysis is performed with the aim to identify the most influential sources of errors in each case. This is the equivalent of the so-called screening (Saltelli et al., 2008) in the variance-based sensitivity analysis (Razavi et al., 2021). However, a sensitivity analysis using different sampling methods is not performed here, since it is subject to ongoing research. Nevertheless, the contribution of each elementary error group and individual elementary errors can be obtained from the SVCM directly. The main diagonal is analyzed here and the contribution of each group of errors is given in percent relative to the SVCM trace. The trace is the sum of all variances, therefore knowing which groups of errors lead to this sum, directly indicates the relative contribution of that group. This is presented in form of pie charts (fig. 6.3 & 6.4) for all station points depicted in fig. 6.2. These must be interpreted together with the previous results (cf. fig. 6.2) because they are extracted from the same matrices.

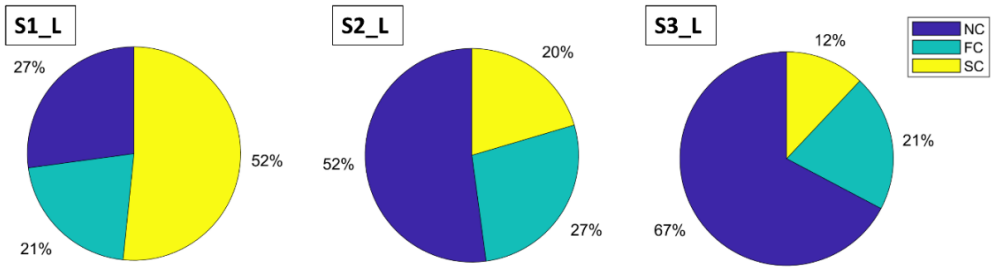

Figure 6.3. Relative contribution of elementary error groups on the SVCM traces for station points S1, S2 and S3 of the Leica scanner. NC=non-correlating group, FC= functional correlating group, SC=stochastic correlating group.

Figure 6.3 shows the relative contribution of the elementary error groups for the panoramic scanner. The effect related to high angles of incidence mentioned at S1_L can be observed again in the relative contribution of the stochastic correlating group (SC) in fig. 6.3. More than half of the SVCM trace is caused by the SC group in this case. For the same station point, the contribution of measurement noise (NC group) is, compared to other station points, the lowest. It is true that for short distances (e.g. from the scanner to the wall base) the impact of measurement noise is much smaller than for observations to the top of the wall from the same station point. As seen later, the highest contribution within the NC group is attributed to the angular noise (horizontal and vertical). This effect is identical to that of angle measurement noise in directions measured by total stations. The other two station points S2_L and S3_L confirm this by the increasing contribution of the NC group with increasing distance. At the same time, the SC group shows a smaller contribution, specifically for S2_L, the roles are almost inverted between the SC and NC groups. In what concerns the functional correlating errors (FC), they remain at approximately the same level of contribution for this global analysis. The situation is available for the specified level of variances and cannot be generalized. A detailed overview of the individual contribution of the FC errors is also offered (fig. 6.5).

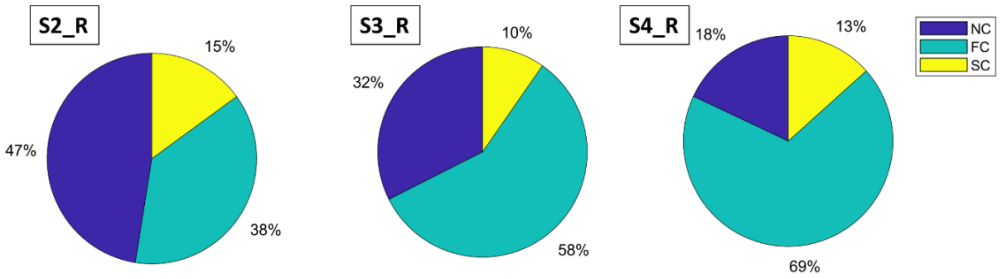

Figure 6.4. Relative contribution of elementary error groups on the SVCM traces for station points S2, S3 and S4 of the Riegl scanner. NC=non-correlating group, FC= functional correlating group, SC=stochastic correlating group.

The same analysis is performed for the hybrid scanner and shown in fig. 6.4. One might be tempted to compare the findings directly with those from the panoramic scanner (fig. 6.3), but such a comparison is not justified due to several reasons. First, the level of noise (NC group) is different for both scanners, especially for the range measurement noise there is an order of magnitude difference. Moreover, the effects of the NC group are also dependent on the scanning geometry, e.g. angular noise has a greater impact at longer distances. Secondly, both scanners have different scanning mechanisms, which are modeled differently (cf. sec. 3.5) and

contain only a few calibration parameters that have equivalents in both models (cf. tab. 3.4). Therefore, it is not a surprise that the relative contribution is different. For the FC group, an increase is observed with increasing distance, pointing out the importance of the scanner calibration procedure. The SC group remains in all three scenarios at approximately the same relative contribution level. This does not mean, that the absolute value of the contribution to the error of position is the same, therefore, the pie diagrams must always be interpreted together with the absolute values seen in fig. 6.2. They are presented in the next paragraphs only for the S2 set-ups, where the individual role of the elementary errors on the complete matrix is shown. All other results can be consulted in Appendix 2.

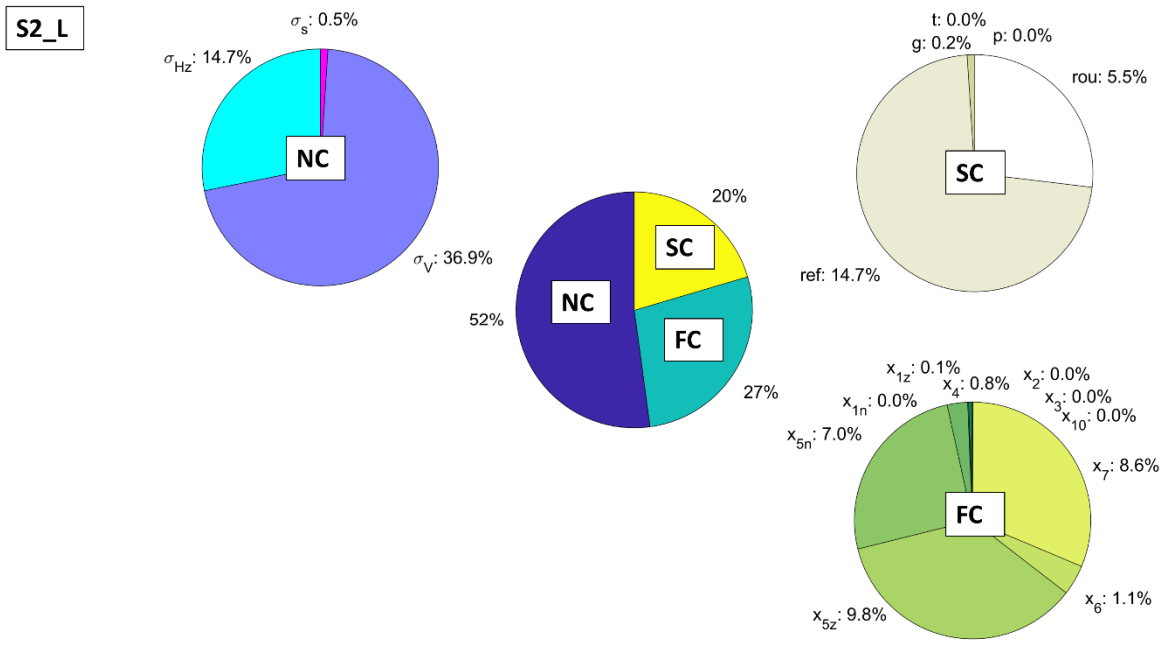

Figure 6.5. Relative contribution of elementary error groups and individual elementary errors on the SVCM traces for S2_L (panoramic scanner).

The central pie chart in fig. 6.5 shows the contribution of the elementary error group and it has already been seen in fig. 6.3, but it is represented for completeness. The other pie charts show the relative contribution within one group. The highest relative contribution for S2_L is given by the NC group, more precisely by the vertical angle noise, which contributes by almost 37% to the SVCM variances sum (trace). Within the same group, the range noise is the least important at this level of standard deviation (0.5 mm). For the functional correlating instrumental errors that contribute in total by 27%, only some CPs play a role at the given level of variance and for this scan configuration. The three most important are the angular errors: x_{5n}, x_{5z}, and x_7 with contributions from 7% to nearly 10%. In comparison to the other CPs, their variance level is also the highest (tab. 6.2). The relative contribution of other CPs is low, e.g. x_{1n}, x_2 x_3, and x_{10} show contributions only in µm level (relative less than 0.1 %) and are not decisive for the TLS error budget as analyzed here. In what concerns the stochastic correlating errors (SC group), the object surface properties are the dominant error sources in this group. Surface reflectivity (*ref*) contributes by almost 15% out of the total 20% in the SC group. Following it, is surface roughness (*rou*) with 5.5%. As expected, the atmospheric elementary errors air temperature (*t*) and air pressure (*p*) have a negligible contribution (less than 0.1%), whilst the vertical temperature gradient (*g*) contributes by only 0.2% at this level of variance.

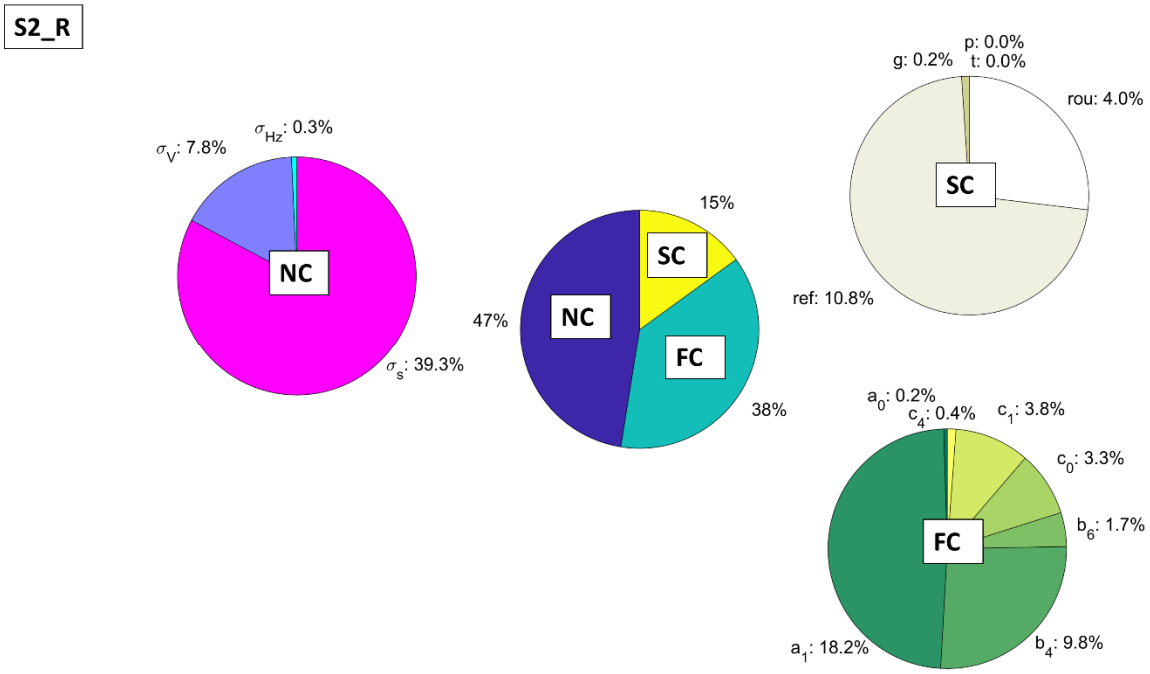

Figure 6.6. Relative contribution of elementary error groups and individual elementary errors on the SVCM traces for S2_R (hybrid scanner).

In the case of the hybrid scanner setup at S2, the central pie chart shows the relative contribution of the three groups (fig. 6.6). For the group of non-correlating errors, the highest contribution (~39%) is given by the range noise, as expected at this level of variance (tab. 6.2). Next, is the vertical angle noise with almost 8 % and the smallest contribution here is given by the horizontal angle measurement noise, for which the standard deviation is more than three times smaller in absolute value than the vertical angle noise. As regards the other instrumental errors, the functional correlating group contributes by 38% out of which the most relevant CPs are a_1 the scale factor and b_4 the horizontal circle eccentricity. Other CPs remain in a low percent interval (e.g. less than 4%). For one straightforward comparison between the two TLS functional models, it can be seen that the zero point error a_0 also has a negligible contribution (0.2%) as was in the case of the panoramic scanner (fig. 6.5). The stochastic correlating group in this set-up is comparable with the one for the panoramic scanner. The same error sources affect the observations in this case.

6.1.1.3 Contribution of single elementary errors and pointwise analysis

Up to now, only the total effect of elementary errors on the main diagonal of the SVCM has been presented in form of pie charts. A more detailed analysis is necessary if the interest is on a certain area of the wall. The same analysis is conducted for individual points and in the following graphics, the relative contribution of each elementary error on each point in the point cloud is shown. The color scale for the relative contribution is set from 0 % to 50% for visualization reasons. If it would have been from 0% to 100%, the contrast between the individual graphics would be too low. Each cell in the graphic presents the influence of single elementary errors. As presented previously, the analysis is shown here for the setups at S2 and the other can be consulted in Appendix 2.

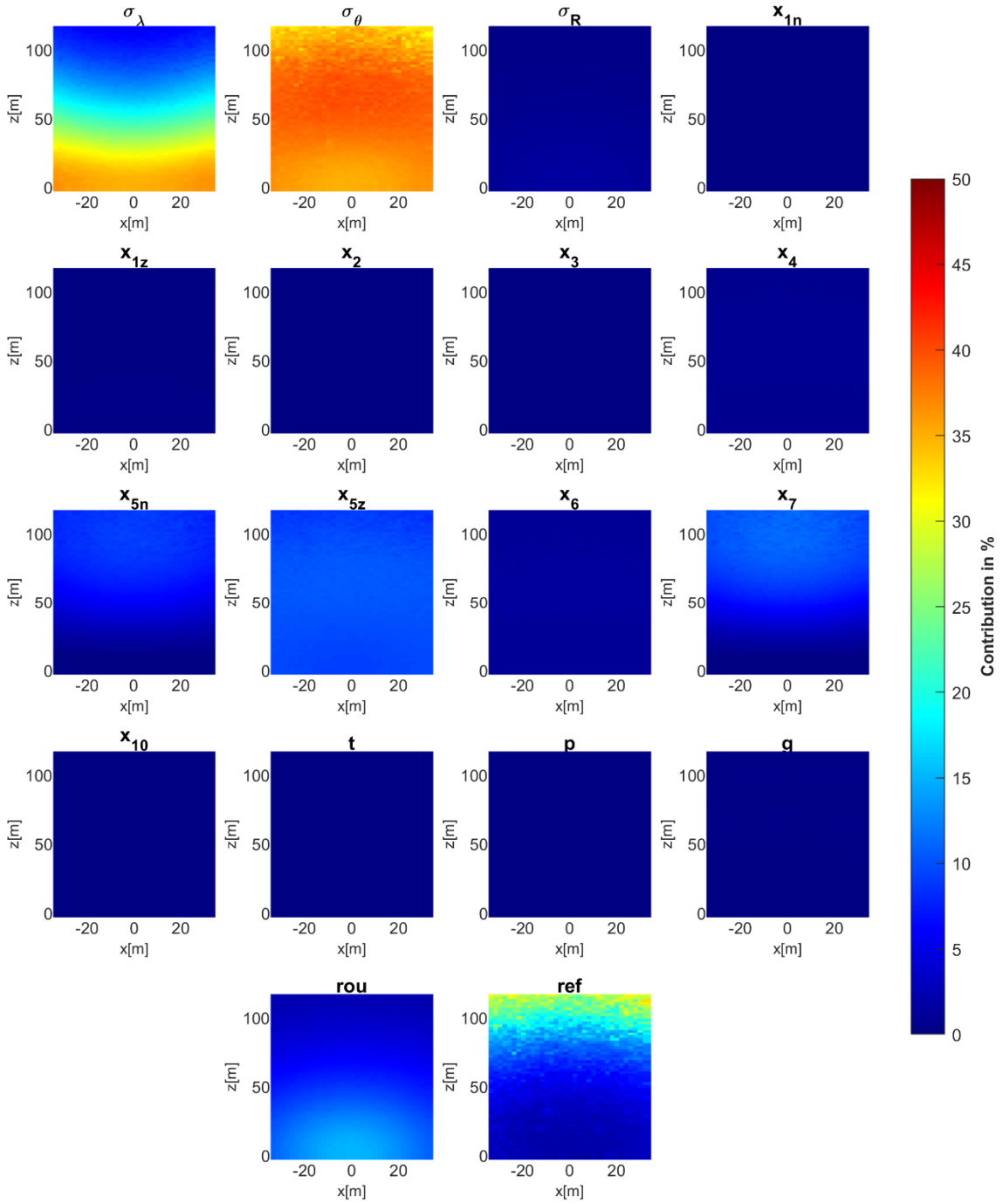

Figure 6.7. Relative contribution of individual elementary errors on the error of position from S2_L (panoramic scanner).

In fig. 6.7 the color represents the contribution of each elementary error to the error of position of all points. If all cells from fig. 6.7 would be superimposed, they result in 100% of the error budget. It can be seen that the contribution strongly depends on the point position with regard to the station point. This effect is especially seen with increasing height for some elementary errors. The influence of horizontal angle σ_λ is the highest at the base of the wall. Regarding the vertical angle noise, σ_θ, it remains on a relatively high level, between 30% and 39% with exceptions at the top part of the wall. In this area, the influence of reflectivity (*ref*) increases up to 30%, which results from the effect of high angles of incidence. In case of roughness (*rou*), a

light radial effect is seen directly in front of the wall. Especially at shorter distances (e.g. S1_L), the effect of roughness is seen with better contrast, as shown in the appendix (fig. A2.5).

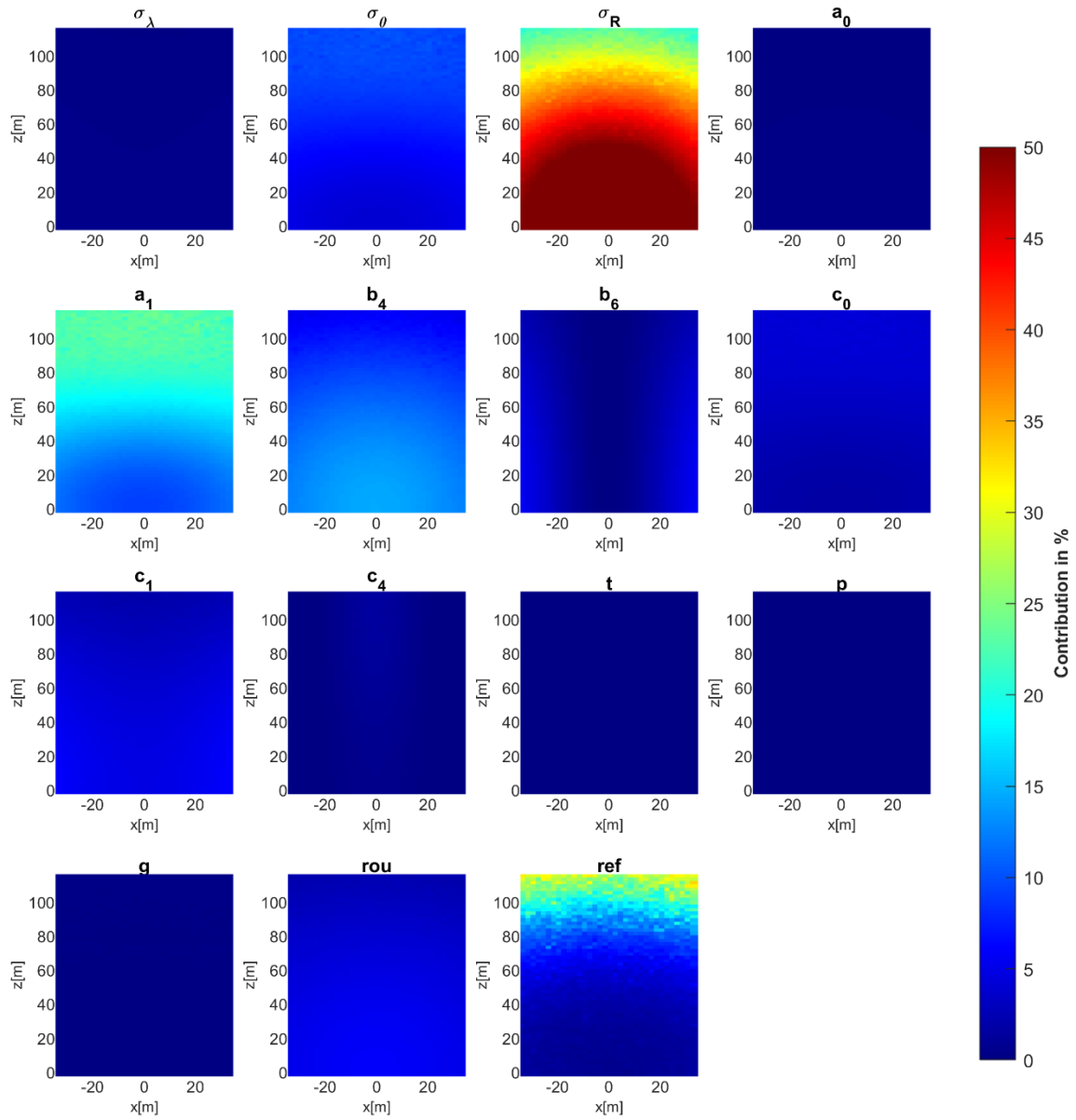

Figure 6.8. Relative contribution of individual elementary errors on the error of position from S2_R (hybrid scanner).

The most dominant contribution in the case of the hybrid scanner is clearly the range noise. This is available for the base of the wall because, with increasing height, other elementary errors increase in contribution (e.g. the scale factor a_1). The latter is proportional to increasing distances. At the same time, the effect of reflectivity is observed at the wall's upper part, like in the case of the panoramic scanner.

With this information, the user may choose a different scanning configuration that reduces the contribution of certain elementary errors (e.g. reflectance at high angles of incidence), or attribute more attention to determining other elementary errors on site (e.g. temperature). There might be also cases in which some elementary errors have such a small contribution to the uncertainty budget, that they can be neglected at that level of variance and for the specific

scanning configuration, as demonstrated in the above analysis. This can additionally save time or enhance the computational efficiency in deformation analysis or surface estimations, e.g. by neglecting some instrumental errors that contribute by less than 1% to the error budget.

6.1.2 Correlation analysis

In the previous section, only the main diagonal of the SVCM was of interest. Aside from the main diagonal, the fully populated SVCM contains covariances between different groups of observations. In this section, the covariances are studied. For visualization purposes, instead of presenting numeric values of the covariances, the resulting correlations are used. One possibility is to visualize the complete correlation matrix that results from the SVCM. In the case of a reduced number of points in the analyzed point cloud, this is possible. Additionally, correlations are studied along selected sections of the object. This is done in the same manner as in Kerekes & Schwieger (2021), where sections of the studied object have been selected and the correlations along one coordinate axis were presented. A vertical section in the middle of the wall (fig. 6.9) is extracted and SVCMs are generated for the points of this section. The points are arranged in ascending order according to their height. This helps at interpreting the correlations between points in different regions of the wall directly from the correlation matrix, as seen later.

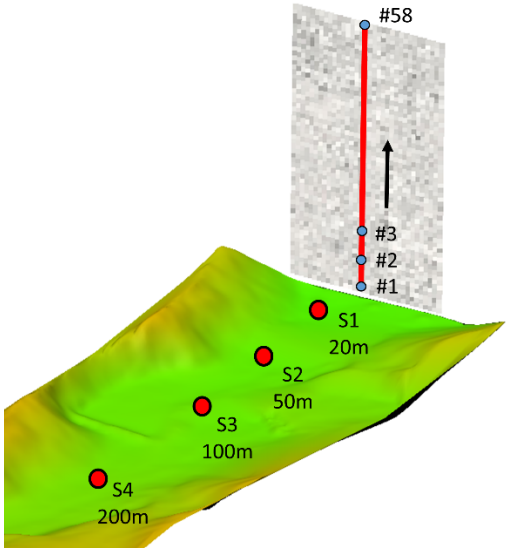

Figure 6.9. Vertical section of the wall (red line) for which the spatial correlations are analyzed. Ascending order starting from the base of the wall.

Analog to the variance analysis, the correlations resulting from the SVCMs of the four set-ups (S1 to S4) are analyzed for both scanners only for the selected station points (tab. 6.1). The correlation matrices that result from the SVCM are presented first. The numeric indication on the side and bottom of the matrix represents the point number according to the order presented in fig. 6.9. The points in the section are numbered 1, 2, 3 up to 58 with increasing height. Therefore, with the reduced amount of points, the correlation coefficient between any combinations of points can be directly interpreted from the matrix. The color represents the correlation coefficient directly. The first analysis is made for the panoramic scanner setups.

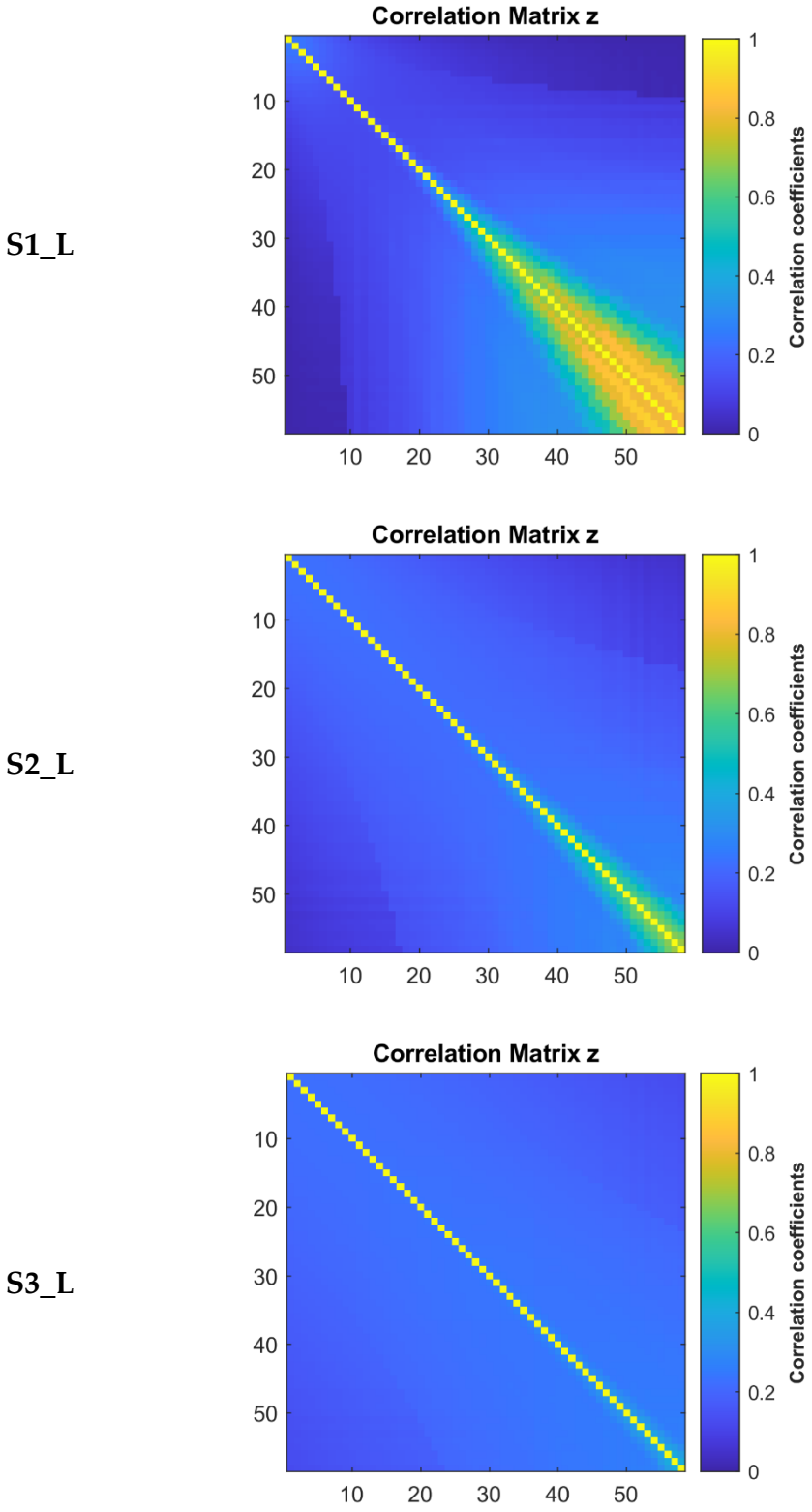

Figure 6.10. Structure of correlation matrix for vertical wall section from station points S1-L, S2-L and S3-L (panoramic scanner).

As with any correlation matrix, the main diagonal contains only the values 1. All other elements are actually of interest. A first observation that can be made out of the correlation matrix structure is that the correlation coefficients between points at the top of the wall are higher than points at the bottom (fig. 6.10 S1_L bottom right side). Especially in the case of S1_L high correlation coefficients occur in the same area with the highest errors of position (cf.

fig. 6.2). At a closer analysis, this phenomenon is caused by the stochastic correlating group, more precisely by the reflectivity part. The high angles of incidence (up to 80 gon) at the top of the wall, lead to highly correlated distances as described in sec. 5.4.1. This effect decreases with increasing distance from the wall, as can be seen for S2_L and S3_L, where the yellow area from the bottom right corner (high correlation coefficients) is reduced in each case.

Out of these correlation matrices, single matrix lines can be extracted for visualization purposes. These lines represent individual correlation coefficients between the selected point and all other points on that line. In this sense, representing the first line of the matrix shows the correlation coefficients between the first point (#1 - the lowest) and all others (fig. 6.11 first column). The same representation is made for the last line in the matrix which shows correlations between the highest point (#58) and all others in decreasing height order (fig. 6.11 second column). Simultaneously, the graphic presents the standard deviations of single points in the height component according to the point height difference.

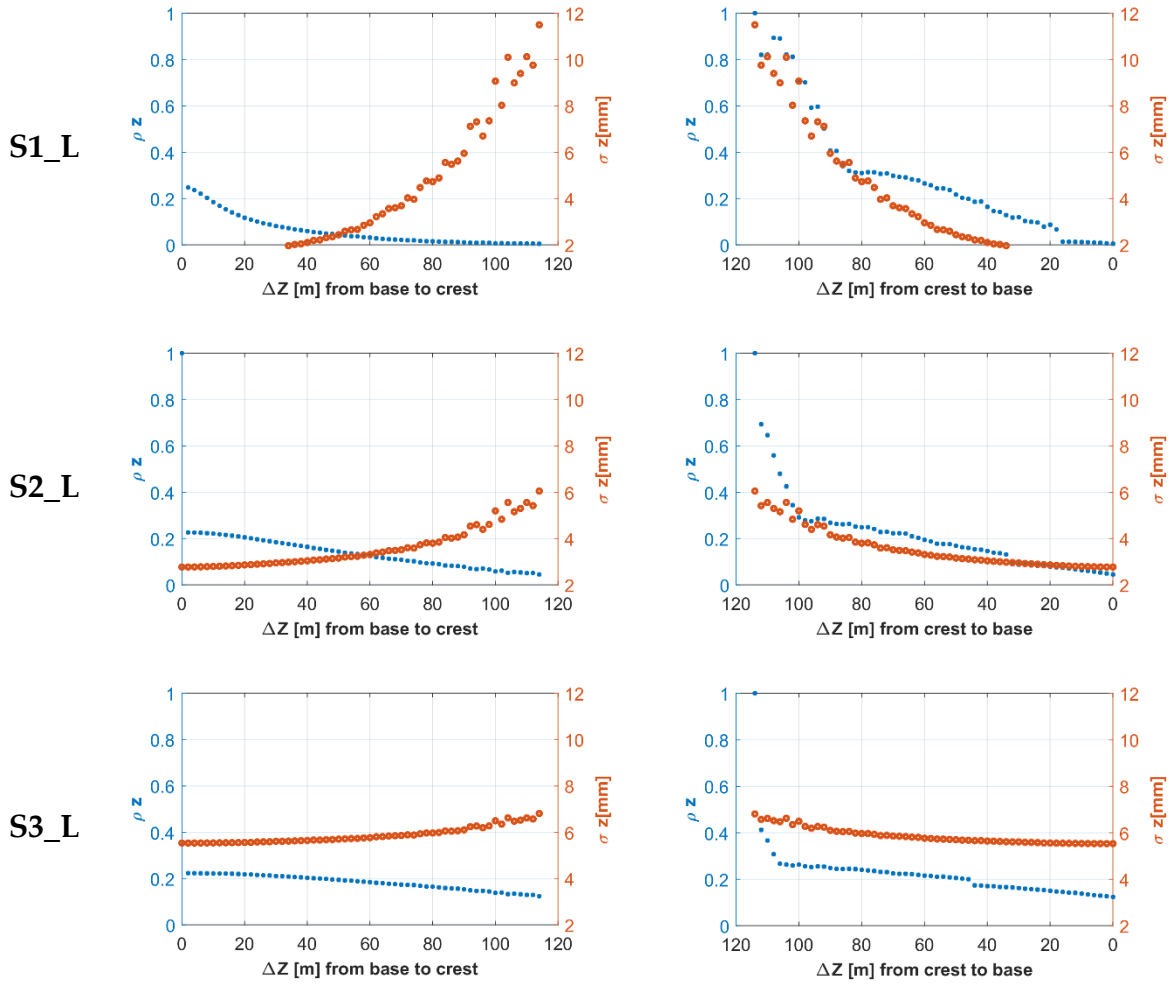

Figure 6.11. Correlation coefficients (blue) extracted from the matrices in fig. 6.10 for the set-ups S1-L, S2-L and S3-L. Orange dots represent the standard deviations in height (panoramic scanner).

The first column of fig. 6.11 depicts a nearly linear decrease in the correlation coefficients between the lower and upper parts of the wall. They remain all at a relatively low level of correlation (less than 0.3). In relation to the standard deviation values of the same points, an inversely proportional relation is observed. The situation changes if the correlation coefficients of the last line in the correlation matrix are analyzed (fig. 6.11 second column). Here it can be

clearly seen that the high correlation coefficients follow the same trend as the variances. Especially in S1_L, where the most dominant error source was reflectivity, as mentioned previously for the variance analysis. The influencing terms for reflectivity are inverse cosine functions that depend on the angle of incidence, therefore at these extreme values, they account for most of the error budget. The noisy pattern of standard deviations and implicit correlation coefficients values of neighboring points at S1_L (fig. 6.11 first line) above 100 m is explainable by the different values of concrete reflectance at that part of the wall (cf. fig. 6.2. upper left image). If eq. 5.7 is recalled, the distance standard deviation is dependent on reflectance as well as distance and the combination of these two leads to slightly different values (noisy pattern) at the upper part of the wall. For surfaces with very similar values for reflectivity (approximately no texture), there would have been no noisy pattern. The effect becomes less obvious with increasing distances at S2_L and S3_L. In the case of these set-ups, a parallel between the change of standard deviation and correlation coefficients can also be observed. This finding shows that high correlations are closely related to high variances in that specific region of the object.

One may ask, what error sources contribute to these correlations? In order to identify these, SVCMs can be computed with only one type of elementary error at a time. This shows, as in the case of variances, the contribution of each elementary error to the correlation budget. According to the elementary error model as presented in chapter 2, several facts can be highlighted here.

The non-correlating errors, by nature, do not cause correlations between the observations. The functional correlating errors do lead to correlations between the same type of observations on one side (e.g. horizontal angles), but also to correlations between groups of observations on the other side (e.g. vertical angles and distances) as demonstrated in sec. 3.4. In this specific case, due to the small correlations caused by the instrumental errors (not shown here), the analysis is restricted to the remaining groups of errors. Regarding the third group of errors, an analysis of correlation matrixes from SVCMs generated with the stochastic correlating errors is possible and shows which of the elementary error types play a role in the correlation matrices.

This is done only for S1_L since this correlation matrix presented the most interesting structure (fig. 6.12). The same representation style as for the complete matrix in fig. 6.10 is used. The difference is that individual correlation matrices are presented for the stochastic correlating errors: air temperature, air pressure, vertical temperature gradient, reflectivity, and roughness. Note that only one elementary error is presented at a time, meaning that in the complete SVCM, their impact leads to other values for the covariances based on the level of variances which occupy the main diagonal (see contribution to the variances in sec. 6.1.1).

Figure 6.12 shows different patterns, from which several facts are revealed. Starting with the correlation matrix obtained from a SVCM with air temperature only, one observes different blocks of yellow patterns (points with high correlation coefficients). These blocks are caused by the synthetic points on the observation lines between the wall and scanner that are in different air layers. The observation lines that fall within the same air layers as seen in chapter 4, are more correlated with each other, than observation lines that fall in two or three layers, resulting in a block structure of the matrix. However, their influence on the main diagonal (cf.

sec 6.1.1) is so small, that the pattern is not decisive for the complete correlation matrix in fig. 6.10.

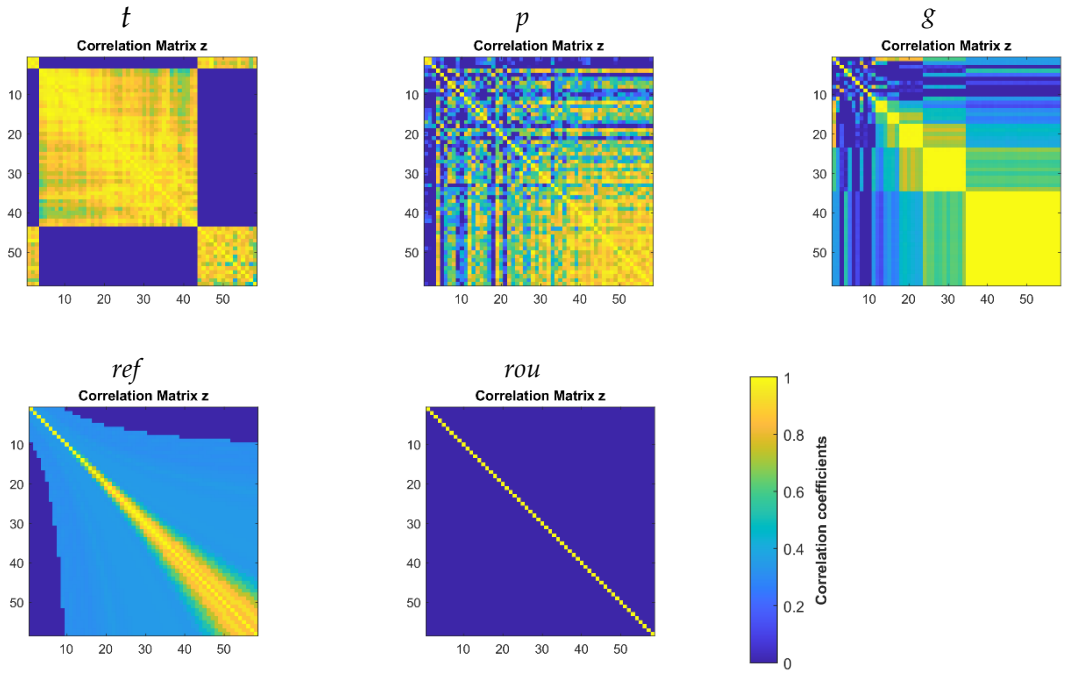

Figure 6.12. Correlation matrices with the single stochastic correlating errors at S1_L. Each cell depicts the correlating matrix for the elementary errors *t*-air temperature, *p*-air pressure, *g*-vertical temperature gradient, *ref*-reflectivity and *rou*-roughness (panoramic scanner).

For the other two atmospheric elementary errors, the matrix patterns suggest that with increasing height, the correlations between neighboring points increase, especially for the vertical temperature gradient (*g*), but as in the case of temperature, their contribution on the main diagonal is so small, that the pattern does not play the decisive role.

Moving on to reflectivity, one can observe that this is the dominant cause in the pattern of the correlation matrix. In fact, reflectivity is the defining source in this case. This is seen by comparing the pattern of the reflectivity matrix from fig. 6.12 with the one in fig. 6.10. Roughness does not lead, in this case, to any correlations, due to the large point spacing. As seen in section 5.4, the correlation length for roughness is small (a few mm), therefore the chosen point spacing in this study case does not lead to any correlations caused by roughness.

This analysis presented the principle of finding the main contribution source to spatial correlations. It is expected that for different levels of variances (other than in tab. 6.2) the correlation coefficients may be different, although the patterns remain the same.

This concludes the analysis of SVCM of the panoramic scanner. In the next paragraphs, the same analysis is conducted for the hybrid scanner. Only the interpretation is given, after each graphic.

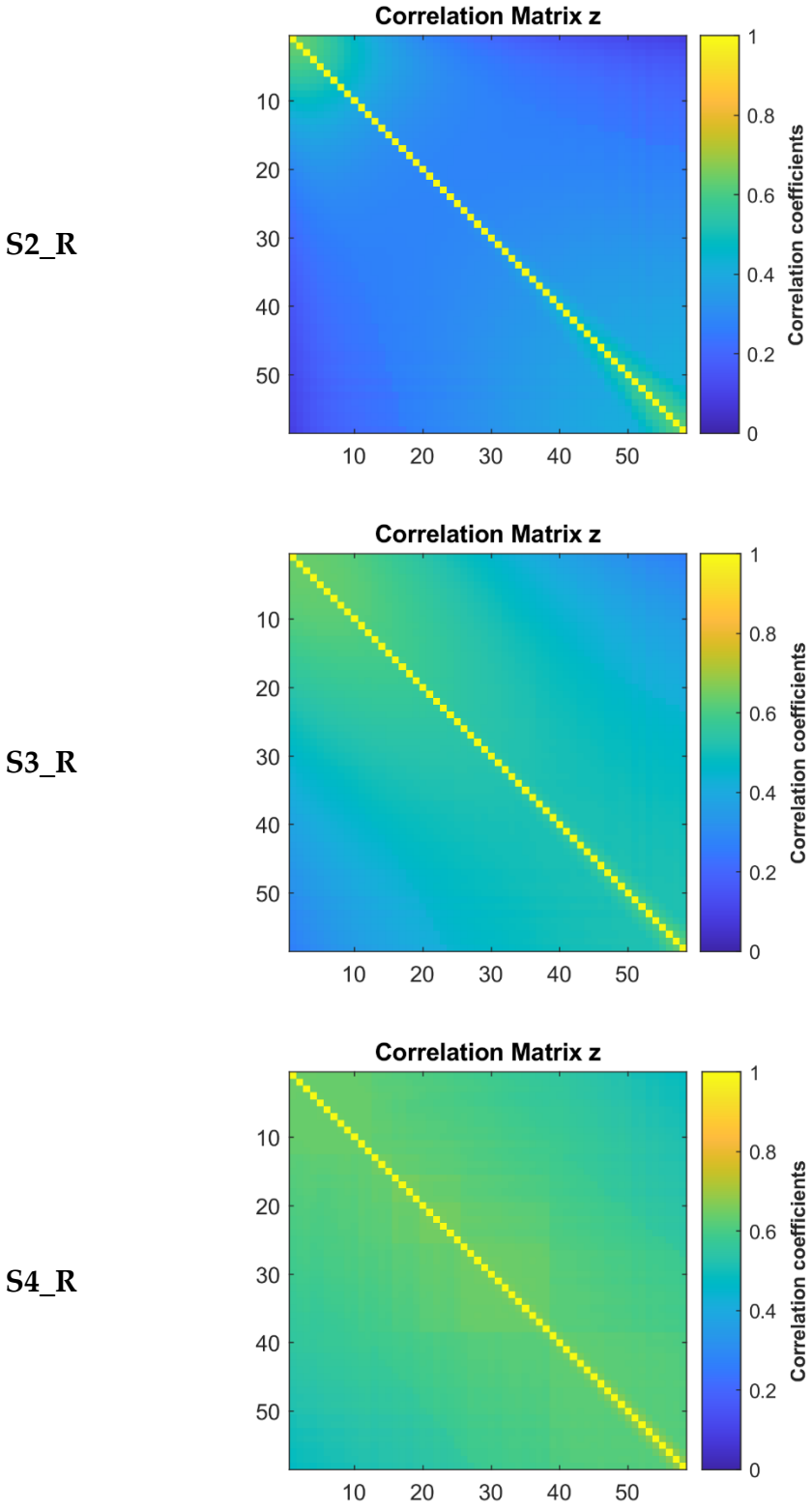

Figure 6.13. Structure of correlation matrix for vertical wall section from station points S2-R, S3-R and S4-R (hybrid scanner).

A first remark about the patterns of the correlation matrices (fig. 6.13) is that the same effect observed for points at the top of the wall is not evident (S2_R). In general, the correlation between observations increases at other station points (S3_R) and (S4_R) with increasing distance and remains at a higher level, in comparison with those of the panoramic scanner. Another observation is that neighboring points remain correlated with each other independent

of their position in height on the vertical section. This phenomenon can be seen at S3_R in the gradient pattern defined from the main diagonal in the upper and lower matrix triangle. For a better example of this effect, the single lines from the matrices are extracted as before from base to crest and inverse (cf. fig. 6.11).

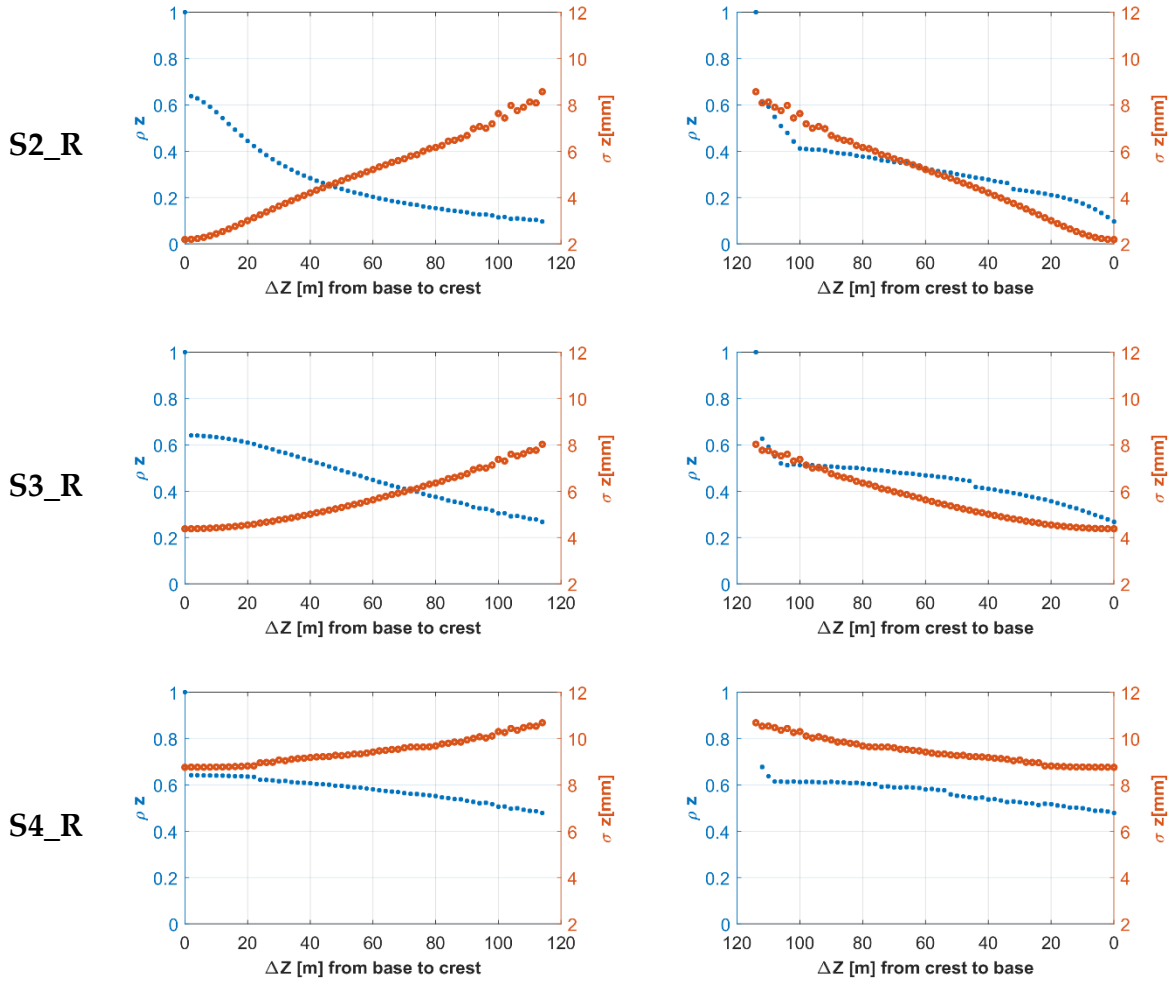

Figure 6.14. Correlation coefficients (blue) extracted from the matrices in fig. 6.13 for the set-ups S2-R, S3-R and S4-R. Orange dots represent the standard deviations in height (hybrid scanner).

A similar effect as for the panoramic scanner is observed for the decrease of correlations with increasing height in the first column of fig. 6.14 (from bottom point to top point). The main difference is the level of correlation, which is higher overall than for the panoramic scanner. Note that only the TLS station points at S2 and S3 may be compared because S4 has no equivalent for the panoramic scanner. If the correlation line from top to bottom is analyzed (second column of fig. 6.14) a strong dependency between the standard deviations and the correlations is likewise identified.

For the relative contributions to the correlation level, the same approach as before is used but applied for the S4_R case in which the correlations are the highest. Additionally, the contribution of one functional correlating instrumental error together with the non-correlating errors is presented. The instrumental error $c1$ is studied due to its influence on the height component of coordinates.

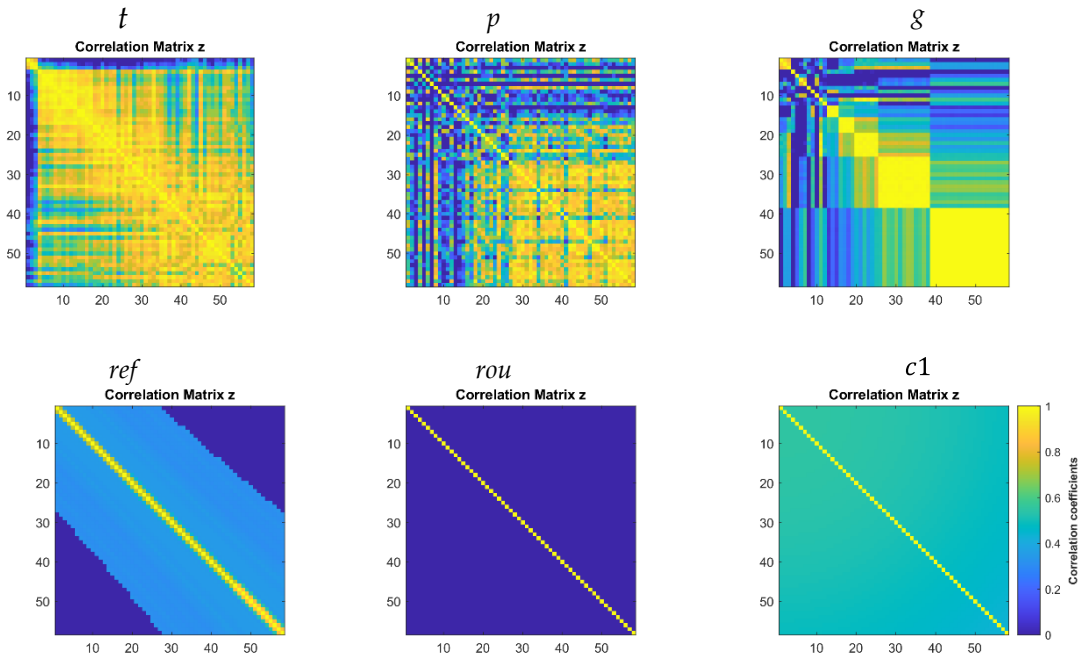

Figure 6.15. Correlation matrices with the single stochastic correlating errors and one functional correlating error at S4_R. Each cell depicts the correlating matrix for the elementary errors t-air temperature, p-air pressure, g-vertical temperature gradient, ref-reflectivity and rou-roughness, c1-vertical circle eccentricity (hybrid scanner).

The resulting patterns depicted in fig. 6.15 are not directly interpretable in relation to the complete correlation matrix from 6.13. It can be observed that a similar gradient from the main diagonal towards the upper and lower triangle is obvious for reflectivity. In what concerns the influence of *c1*, it can be seen that a constant level of correlation results for all points. Superimposing the correlation matrix from *ref* with the correlation matrix from *c1* results in a correlation matrix that resembles the total one from fig. 6.13 for S4_R.

6.2 Relevance of the SVCM in sphere estimation

In many practical applications, TLS targets in spherical forms are used for georeferencing or registration. The coordinates of the sphere center are determined after an adjustment; a procedure that mostly happens directly in the TLS proprietary software. As an output, the user obtains the sphere's center coordinates but does not always receive detailed information about the coordinate's precision for each coordinate. For example, in Leica Cyclone (v. 2020.1.0) the user can only evaluate the fit quality by a few global indicators, the mean error, and a standard deviation. This may be an issue if the sphere center coordinates are needed for deformation analysis (Yang et al., 2021) where the stochastic properties of the estimated coordinates are used for statistically based decisions, or in other cases where the georeferencing uncertainty must be taken into account. The user may also use the points on the sphere and conduct an adjustment independent of the TLS software in order to obtain a measure for the uncertainty estimation, but usually, the high number of points on the sphere leads to results that are in most cases too optimistic (cf. Yang et al., 2021). The opposite may also be possible; in any case, results will be treated as unrealistic. This phenomenon is due to the inconsideration of an appropriate stochastic model in the adjustment.

In order to prove the effects of including a SVCM in the estimation of a sphere's center coordinates, an example is given with a scanned TLS sphere in laboratory conditions. It is an

ordinary 14 cm diameter TLS sphere made out of plastic composite. It was scanned from around 3.7 m from the scanner and the points on the sphere were manually segmented. The coordinates serve as input for the upcoming sphere adjustment. In total, there are 516 points on the sphere's surface with an average point spacing of 6 mm.

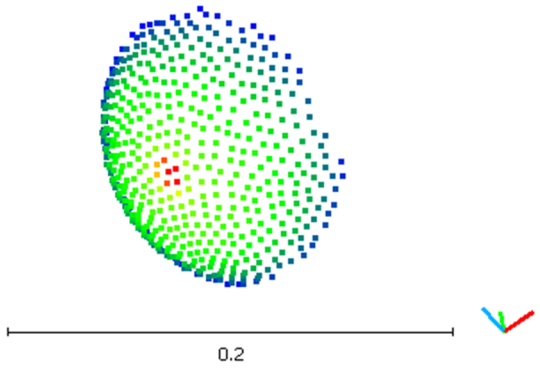

Figure 6.16. Points on a TLS sphere (radius = 14 cm).

Niemeier (2008) gives the theoretical background for the Gauß-Helmert-Model (GHM) used to estimate the center coordinates of points observed on a circle, whilst the same model is presented for a sphere in Jäger et al. (2005) and implemented in Matlab by Kisser (2011). The general GHM model used here is presented in eq. 6.2 and functional model for the sphere estimation in eq. 6.3:

$$\boldsymbol{B} \cdot \boldsymbol{v} + \boldsymbol{A} \cdot \hat{\boldsymbol{x}} + \mathbf{w} = \mathbf{0}, \tag{6.2}$$

$$(x_i - x_C)^2 + (y_i - y_C)^2 + (y_i - y_C)^2 - R^2 = 0, \tag{6.3}$$

where the $\boldsymbol{B}$ matrix contains partial derivatives with respect to the observations (x_i, y_i, z_i), $\boldsymbol{w}$ is the misclosure vector, the $\boldsymbol{A}$ matrix contains partial derivatives with respect to the four unknowns (x_C, y_C, z_C, R), v represents the residuals vector and $\hat{\boldsymbol{x}}$ is the parameter vector**.**

The entire algorithm and construction of each matrix can be consulted in the aforementioned handbooks and will not be presented in this dissertation again. The code published by Kisser is used for the current demonstration.

The focus is set on the role of the stochastic model in the adjustment, therefore emphasis is put on using the SVCM in the GHM. The analysis implies varying the stochastic model of the sphere adjustment in which the stochastic model has different forms as follows:

a) $\boldsymbol{\Sigma_{ll}}$ is the identity matrix $\boldsymbol{I}$;
b) $\boldsymbol{\Sigma_{ll}}$ is the main diagonal of the SVCM;
c) $\boldsymbol{\Sigma_{ll}}$ is the fully populated SVCM.

Comparing these stochastic models shows the influence of the variances and the covariances on the adjusted coordinates of the sphere center points and their corresponding uncertainties. A similar analysis for a more complex surface has already been performed by Raschhofer et al. (2021).

The SVCM used in this adjustment is established starting with the same values presented in sec. 6.1 for the Leica HDS7000 scanner. Table 6.3 presents these values and the two exceptions that apply in this study case. The first one is that the stochastic correlating error group of atmospheric errors is not included in the adjustment due to the small distances from the scanner to the sphere and laboratory conditions. Second, the values for surface roughness are adapted to a smaller value that is more appropriate for the smooth plastic surface of the sphere ($Rt = 0.1\ mm$) and reflectance is set to 80% instead of 40% that was used for concrete before. Both adaptions are however assumptions necessary in lack of real values. This can be improved in the future by actual roughness measurements and reflectivity measurements with spectrometers or from scanners that have this capability (cf. sec. 5.3.2).

Table 6.3 Values for elementary errors used in the SVCM.

Elementary error group	Panoramic scanner Leica HDS7000	
	Elementary error name [unit]	**Standard deviation**
Non-correlating errors	Angular noise Hz [mgon]	3.1
	Angular noise V [mgon]	3.1
	Range noise [mm]	0.5
Functional correlating errors	x_{1n} [mm]	0.140
	x_{1z} [mm]	0.220
	x_2 [mm]	0.020
	x_3 [mm]	0.130
	x_4 [mgon]	0.448
	x_{5n} [mgon]	1.738
	x_{5z} [mgon]	1.598
	x_6 [mgon]	0.272
	x_7 [mgon]	1.929
	x_{10} [mm]	0.060
Stochastic correlating errors	Roughness = 0.3* *Rt* [mm]	0.030
	Reflectivity (80% for this type of plastic)	Observation specific

In the following table the results are shown for the estimated center coordinates, their standard deviations, the weighted least-square sum, and finally the square root $\hat{s}_0$ of the a posteriori variance factor $\hat{s}_0^2$ as a global indicator for the adjustment. Although not all decimals would be of interest in most cases, they are presented here for discussion purposes. The assumed a priori variance factor of $s_0^2 = 1$ (dimensionless) is used in common cases.

Table 6.4 The influence of the SVCM in estimating the sphere center coordinates in a GHM.

Stochastic model	x (m)	y (m)	z (m)	σ_x (mm)	σ_y (mm)	σ_z (mm)	v^tPv	$\hat{s}_0$
$\Sigma_{ll} = I$	1.69791	2.75280	-2.04346	0.0404	0.0548	0.0444	0.00004	0.0003
$\Sigma_{ll} = D$	1.69790	2.75278	-2.04344	0.0398	0.0543	0.0438	179.9558	0.5929
$\Sigma_{ll} = SVCM$	1.69790	2.75278	-2.04344	0.1559	0.1598	0.1600	704.6848	1.1732

The first important finding is that the difference in the estimated values of the sphere center coordinates in all three stochastic models is very small (in μm level).

Regarding the uncertainties, the previously mentioned phenomenon of over-optimistic results for case *a)* is also identified here. The standard deviations are in the order of tenths of μm. Moving on to case *b),* introducing the SVCM main diagonal has only a small influence on the standard deviations. From this point of view, introducing only the main diagonal of the SVCM

does not change the results or their uncertainties much. The change happens only if the fully populated SVCM is used in case *c)* where there is an increase in the standard deviations up to the submillimeter level. They may still be considered too small, but these kind of changes make a difference in the decisions of deformation analysis (Yang et al., 2021).

Next, the more relevant parameter $\hat{s}_0$ for the adjustment is analyzed. An obvious change is observed in all three cases. The value of the square root a posteriori factor increases in size from 0.0003 for case *a)* to 1.17 for case *c)*. In theory, the closer it approaches the value 1, the more appropriate the stochastic model is. If the level of variance and covariances are chosen too optimistic, then $\hat{s}_0 > 1$, and if they are too pessimistic $\hat{s}_0 < 1$ (Heunecke et al., 2013). Acceptance intervals generally considered in geodesy for adjustments are between [0.7 … 1.3] (cf. Möser et al., 2012), although the upper and lower acceptance boundaries should be rigorously obtained from the critical values of the F-distribution function (cf. Jäger et al., 2006; Niemeier, 2008).

Returning to the sphere estimation, it can be seen that equally weighting all observations (case *a*) leads to too pessimistic results from this point of view. By not using any stochastic model, $\hat{s}_0$ does not approach the value of 1. In case *b*, observations are weighted according to the diagonal SVCM and a slight improvement can be seen with $\hat{s}_0 = 0.59$, however, it is still not satisfactory. For completeness, the same estimation was performed with a simple diagonal VCM (not included in tab. 6.4) that contains only non-correlating errors as taken from the technical specifications of the scanner (see tab. 3.1). This resembles a choice that most users would make. With this stochastic model, a value of $\hat{s}_0 = 3.49$ is obtained, showing that this is clearly a too pessimistic choice.

Finally, the fully populated SVCM in case *c)* offers the best result of $\hat{s}_0 = 1.17$ compared with the other. It is considered more realistic in comparison to the other cases and demonstrates that including the spatial correlations is beneficial for sphere estimation.

By this application, the relevance of including correlations in a GHM sphere estimation was presented on real data. The same approach is also possible for other geometric primitives like planes, cylinders, etc. For example, Chen et al. (2015) include the stochastic information in form of a VCM into a plane adjustment, concluding that the residuals can be reduced for planar and non-planar surfaces. Without explicitly mentioning it, the authors also consider correlations between neighboring points in their proposed method by computing the intersection volume of neighboring error ellipsoids. The importance of fully populated matrices is likewise emphasized in the following application.

6.3 Deformation analysis of a wooden tower

In this section, a two-epoch comparison of the scanned surface of a constructed wooden tower is analyzed. The results are also published in one of the author's joint conference papers, Kerekes et al. (2022) and the methodology was developed by Harmening et al. (2021). The approach is used to exemplify the workflow of a deformation analysis that uses B-splines estimated with the SVCM as a stochastic model. Details about B-spline theory are omitted, because the focus is set on the matrix influences on the quality of approximating surfaces and deformation analysis results. For fundamentals about B-splines, the interested reader is referred to Cox (1972), de Boor (1972), Piegl and Tiller (1997) and Harmening (2020).

6.3.1 Measurement setup

The monitored object is a unique double-curved wooden 14 m tall tower, called the Urbach Tower (fig. 6.17). It was designed and constructed in 2018 with new self-shaping processes for the curved wooden components and constitutes the first worldwide structure made from self-shaped building-scale components (Institute for Computational Design and Construction, 2019). This makes it an interesting and challenging object for area-wise deformation analysis.

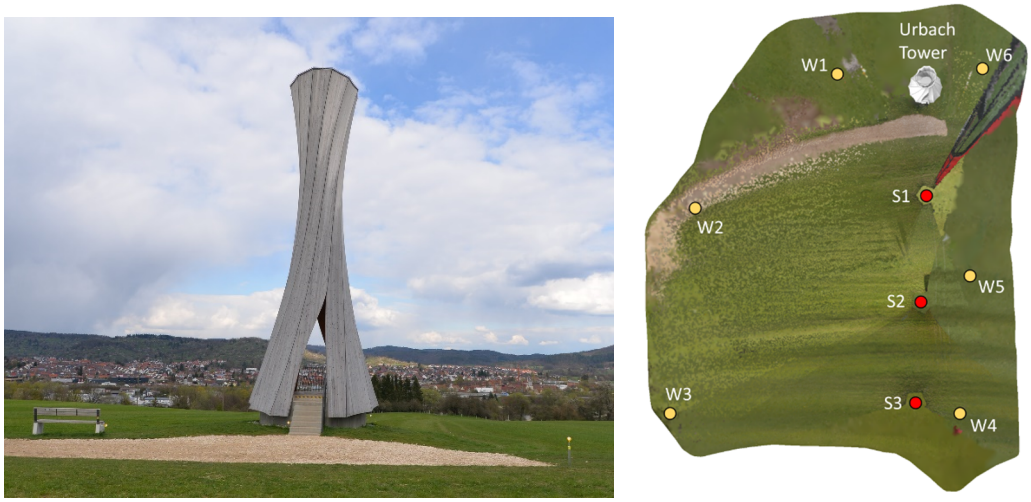

Figure 6.17 Left: the Urbach Tower (own image), Overview of TLS scan set-up. The station points (Sx) and weather points (Wx) are shown relative to the Urbach tower.

The wooden tower was scanned in two measurement campaigns with a Riegl VZ2000 scanner in the summer of 2020 and spring of 2021. Three locations for the station points are chosen in each epoch in order to evaluate the impact of different scanning geometries. The scanning positions were chosen approximately along a line in order to scan the façade of the tower's front part (fig. 6.17 left) for reasons related to the local topography. Any other part would have made the choice for the necessary network points even more difficult as explained in the next paragraph. Figure 6.17 right depicts the three scanning distances of 20 m, 40 m, and 60 m from the tower.

Additionally, the weather parameters air temperature and air pressure were measured with a precision Thermo-Barometer, Greisinger GTD1100 for both campaigns (tab. 6.5) as described in chapter 4 at the locations depicted by the W points in fig. 6.17 right. In addition to the Riegl scans, the reference (nominal) value of the tower façade is created with a second more precise scanner, the Surphaser 100 HSX-SR. This industrial scanner is appropriate in this case due to its very low range noise <1 mm at distances up to 4 m (Basis Software Inc., 2021). This is of course insufficient for the whole façade element which has a height of about 14 m, but it is sufficient if a smaller part is analyzed, as presented later. An external company (Limess Messtechnik & Software GmbH) was contracted to conduct the nominal scan due to the unavailability of this type of scanner at the IIGS. The scan covered several wooden plates near the entrance of the tower, but only one has been chosen for analysis.

Table 6.5 Average atmospheric conditions for both epochs.

Station point - Epoch	Average temperature [°C]	Average pressure [mbar]
S1 – E0	26.2	987.6
S1 – E1	11.6	995.6
S2 – E0	25.7	987.8
S2 – E1	10.1	995.4
S3 – E0	25.5	987.8
S3 – E1	14.4	996.0

A common geodetic datum is needed for two purposes: firstly for referencing scans obtained with both scanners in a single epoch and secondly for referencing scans from both epochs. Therefore, fixed points of this created geodetic network were marked in the spring of 2020 before the actual measurement campaigns.

As seen in fig. 6.17 left, the tower is located in the middle of a field with few choices of stable and protected areas (e.g. from tractors) that have a TLS favorable geometric distribution. Nevertheless, five network points were marked around the tower and the planned TLS station points. Three of them were marked with concrete dowels in the tower's concrete base and in the nearby bench concrete foundation, one with a wooden dowel in a wooden electricity pole and the other with an 80 cm aluminum peg near the access road. The aluminum head peg allows mounting targets and adapters by forced centering, thus assuring the same mechanical center between different TLS target types and reflectors (e.g. contrast targets and reflecting foil targets).

The stability of the network points was verified for both epochs with a 0.5" Leica TS30 Total Station (TS). After network adjustment and deformation analysis (congruence test), no significant differences (α=5%) are present, indicating that the coordinates of the reference network can be used for transforming the TLS point clouds without inducing errors due to different datums.

In what concerns the atmospheric elementary errors, these are included in the SVCM as explained in chapter 4. It is possible to have specific values for covariances of air temperature, and air pressure based on the measured values on-site and interpolated values. For the vertical temperature gradient, assumed values are used as the ones in chapter 4. The digital terrain model (DTM) in the area (cf. fig. 6.18) is extracted from panoramic scans of the area. An example of a station point in the first epoch is given in fig. 6.18. One may argue, that at these distances (up to 60 m) the contribution of atmospheric parameters to the TLS uncertainty budget can be ignored. This is true for the variances because atmospheric parameters do have a small contribution in this case (cf. sec. 6). However, the covariances (thereafter correlations) that result from the atmospheric elementary errors together with the instrumental functional correlating errors are important, as demonstrated later, for the statistically based decisions.

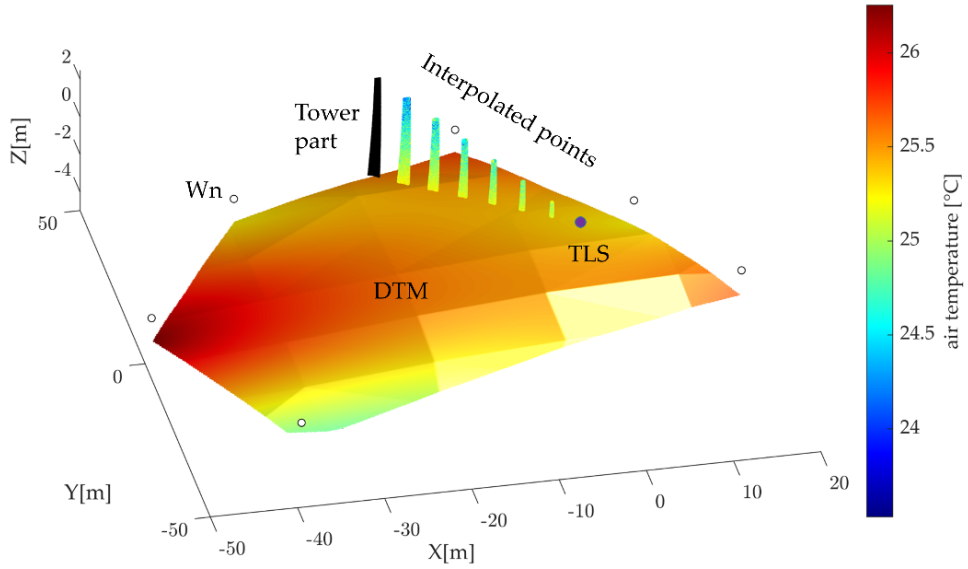

Figure 6.18 An example of interpolated synthetic points with temperature along the observation lines.

6.3.2 Deformation analysis and evaluation

The approach for the B-spline based deformation analysis is shortly presented here (fig. 6.19) and explained for understanding purposes. It allows the determination of rigid body movements and the identification of distorted areas. Above all, it is a statistically based approach in which the identified deformation parameters are tested for significance. For more details, Harmening et al. (2021) must be consulted.

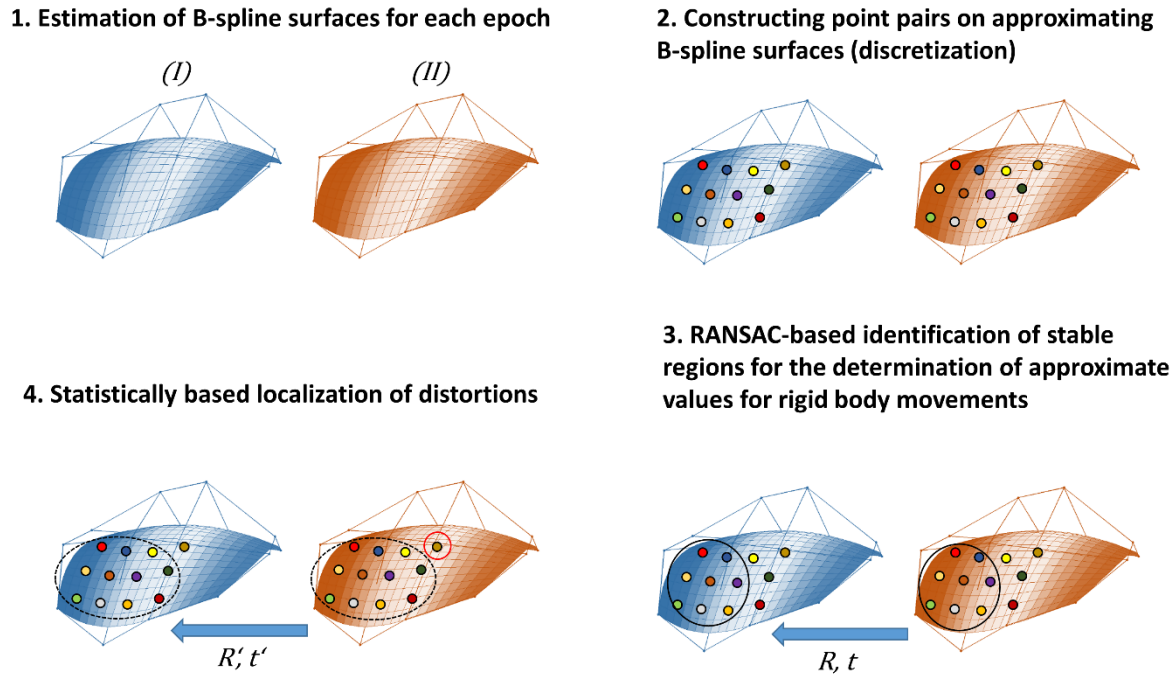

Figure 6.19 Workflow of the B-spline based deformation analysis (clockwise starting from upper left corner). Created after the approach presented in Harmening et al. (2021).

The method requires 4 steps and can be applied for TLS point clouds acquired in subsequent epochs. An underlying assumption for this approach is that stable areas on the object (e.g. subject only to rigid body movement) exist.

In the first step (fig. 6.19 – 1), point clouds of each epoch are introduced together with their SVCMs as observations in B-spline estimation (cf. Raschhofer et al., 2021). For each epoch, a surface is estimated separately, but with the same parametrization (e.g. no. of control points, knot vectors, degrees of freedom) (Harmening and Neuner, 2017).

In the second step (fig. 6.19 – 2), points are sampled on a regular grid of the surface. Choosing the point spacing is a decision based on the specific surface shape. Additionally, the point spacing can be different in each direction. This step is also referred to as discretization or surface sampling. Next, point pairs from each epoch are constructed. This is only possible because B-splines are parametric surfaces and therefore allow the definition of point correspondences.

In a third step (fig. 6.19 – 3), a RANSAC-based algorithm is used to randomly selected pairs of points created at step 2 and transform them from one epoch to the other. The transformation can be a 6-parameter transformation or 7-parameter transformation, in case the point clouds are obtained by different methods (e.g. photogrammetry). Using the randomly selected point pairs, the rotations, and translations between epochs are estimated. This process is ran iteratively and in each run, a user-defined criterion is verified and a global statistical test is performed. The purpose is to obtain a consensus set of point pairs that describe the rotations and translations and simultaneously indicate the stable area. There may be points that are superimposed by rigid body movements and distortions, but it is possible to discern between them with this robust approach. The criteria for allocating pairs in the consensus set is the 3D distance between the points after the transformation. It must be smaller or equal to the error of position multiplied by a free parameter (e.g. $d_k \leq \tau \cdot \sigma_{d,k}$), where d_k is the 3D distance, $\sigma_{d,k}$ is the error of position obtained from the SVCM and τ is a free parameter (e.g. varying from 1 to 6 depending on the interval of uncertainty that needs to be covered). This iterative process can be influenced either by a user-defined number of iterations (*itr*) or ran until a minimum number of point pairs (e.g. n_{min}) are included in the consensus set. After the n pairs are found and the criteria is not met anymore, the rigid body movement parameters as well as the consensus set are available.

Finally, step 4 (fig. 6.19 – 4) is necessary to evaluate the remaining points that may be subject to distortions. Based on the choice of the free parameters τ and the number of iterations *itr*, there may be other pairs that also belong to the non-distorted area, but have not been identified in step 3. Therefore, the consensus set of points is extended stepwise by neighboring pairs of the points in undistorted areas and the rigid body movement components are re-estimated by an extended Gauss Markov model (Harmening et al., 2021). A statistical test is defined as follows:

$$H_0: E(\widehat{\boldsymbol{\nabla}}) = 0, \tag{6.4}$$

$$H_A: E(\widehat{\boldsymbol{\nabla}}) \neq 0. \tag{6.5}$$

If there are no significant differences in the model, in other words, the estimated gross error $\widehat{\boldsymbol{\nabla}} = \mathbf{0}$, the null hypothesis H_0 (eq. 6.4) is accepted and the consensus set is extended with these point pairs. Contrarily, point pairs that lead to outliers in the re-estimation $\widehat{\boldsymbol{\nabla}} \neq \mathbf{0}$ (H_A eq. 6.5), are considered to belong to the distorted areas. With this approach, the statistically-based identification of distorted points is possible.

This algorithm has been applied for one element from the lower part of the tower façade with a height of 5 m. The complete façade element that is 14 m high could not be included in the estimation due to the limited coverage of the Surphaser scan. This fact is related to the limited working range of the scanner (up to 7 m) and the very good spatial precision ($0.35\,mm \leq \sigma_{xyz} \leq 0.70\,mm$; error of position after Helmert) obtainable for this region according to the scanner's technical specifications.

Figure 6.20 Selected surface of the tower façade, which is analyzed for deformations.

The estimated B-spline surface from the Surphaser point cloud (fig. 6.20) of the first epoch in 2020 serves as the reference surface and all sequent surfaces are estimated based on this parametrization. It is mentioned that for this surface, the identity matrix has been used instead of the SVMC. As seen in Raschhofer et al. (2021), the differences between using an identity, diagonal, or fully populated matrix as a stochastic model in the absolute position of control points for an estimated surface can be neglected at close range (~ 6 m).

For the joint B-spline parameterization, all Riegl point clouds from both epochs are projected onto this reference surface in order to obtain surface parameters (cf. step 1). Furthermore, the number of control points and the knot vectors are maintained for the estimation.

As for the used stochastic model of other scans, a SVCM for the Riegl scanner (hybrid scanner) as presented in chapter 3 is generated and introduced into the estimation. The values for the standard deviations shown in chapter 3 tab. 3.1 and 3.5 had to be adapted during the surface estimation based on the a posteriori variance factor $\hat{s}_0^2$ (Raschhofer et al., 2021). Table 6.5 presents the values of the standard deviations used for the non-correlating errors. The functional correlating errors were not changed and their contribution can be seen later when the fully populated SVCM is compared with the diagonal SVCM.

Table 6.6 Standard deviations for the elementary errors. E0 depicts the first epoch; E1 the second and S1 to S3 depict the station points.

Correlation type	Parameter	Standard deviations / epoch					
		S1 – E0	**S1 – E1**	**S2 – E0**	**S2 – E1**	**S3 – E0**	**S3 – E1**
Non-correlating errors	Range noise [mm]	5	5	5	5	5	5
	Angle noise (λ) [mgon]	5.0	6.1	2.5	2.8	2.2	2.7
	Angle noise (θ) [mgon]	15.0	18.3	7.5	8.7	6.5	8.3
Functional correlating errors	a_0 [mm]	0.34					
	a_1 [ppm]	40					
	b_4 [mgon]	3.18					
	b_6 [mgon]	1.91					
	c_0 [mgon]	1.08					
	c_1 [mgon]	1.85					
	c_4 [mgon]	0.64					
Stochastic correlating errors	Air temperature [°C]	Observation and epoch specific. (cf. tab. 6.5)					
	Air pressure [mbar]	Observation and epoch specific. (cf. tab. 6.5)					
	VGT= -0.2 [°C/m]	Observation and epoch specific.					

The applied standard deviations for the non-correlating errors are slightly different between epochs. One reason is the missing object surface properties (as stochastic correlating errors) in the SVCM due to the unavailability of data for roughness and reflectivity for this type of wood at the moment of conducting this research. Judging by a visual inspection, the tower façade visibly changed between the epochs, varying from birch natural light yellow colour to light grey.

The epoch-wise estimated approximating B-spline surfaces are discretized in a regular grid of corresponding points (step 2). The level of discretization presented here contains 20 x 15 points along the knot vector directions u_k and v_k and indicates the number of points in the respective parameter direction. Therefore, 300 points are generated in each epoch. The average point distance on the surface is in this case 10 cm. Other discretization sets are presented in Kerekes et al. (2022) and excluded from here due to high resemblance.

The intention of this deformation analysis was to detect rigid body movements and distorted areas of this tower element and if possible, they should be detected by the Riegl scans. This is challenging because the measurement accuracy of the Riegl scanner is on one side, in another class (e.g. 5 mm range noise) than that of the Surphaser, and on the other, the scanning distances are larger (20 m – 60 m). In this experimental setup, the scans from both epochs of the Surphaser scanner are used as references. In this sense, the results are considered as benchmark test. Scans obtained with the other scanner are verified against the Surphaser scans.

A first finding from the Surphaser scans was that no rigid body moments could be identified. This fact is in concordance with the tower designer's simulations (Institute for Computational Design and Construction, 2019). They expected movements to occur at the top of the tower, not at the base. In what concerns distortions, a small area was identified as statistically distorted after running steps 3 and 4.

All representations of the deformation analysis are made by visual means with the following conventions. Deformations are represented by colour depending on the deformation

magnitude at the corresponding area of the tower element. The ones that are highlighted by circles (contours) have been identified as significantly distorted. The level of significance is set empirically to $\alpha = 3\%$ in order to exclude more type I errors, as shown in the following results. All other points with no circles depict undistorted regions. The stochastic model for the Surphaser is a simple diagonal SVCM. The main diagonal is filled with values of range noise $\sigma_R = 0.3\ mm$ and angle noise $\sigma_{\lambda,\theta} = 4.6\ mgon$ (Basis Software Inc., 2021). Figure 6.21 shows the distorted regions detected using the Surphaser point clouds.

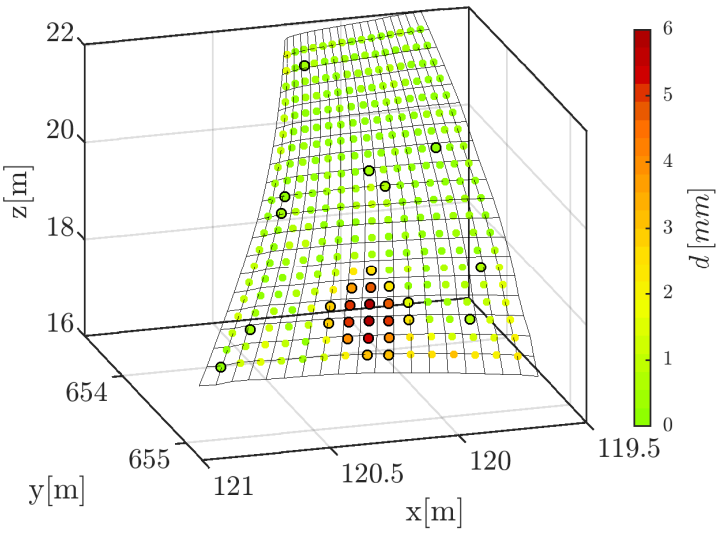

Figure 6.21 Distorted regions - Surphaser @ 6 m

The lower region in the middle of the wooden element shows significant deformations of the discretized points with values of a few mm (fig. 6.21). They are highlighted with black circles. Since they are concentrated in one region, the deformation is considered real. Other points outside of this area are also identified as significantly deformed, although their values are less than 1 mm. This clearly indicates an error of type I that cannot be completely avoided, since the subject is still under research. Next, the estimated surfaces from the Riegl scans are analyzed with the same workflow. For the first station point at 20 m, the results of the deformation analysis are shown in fig. 6.22.

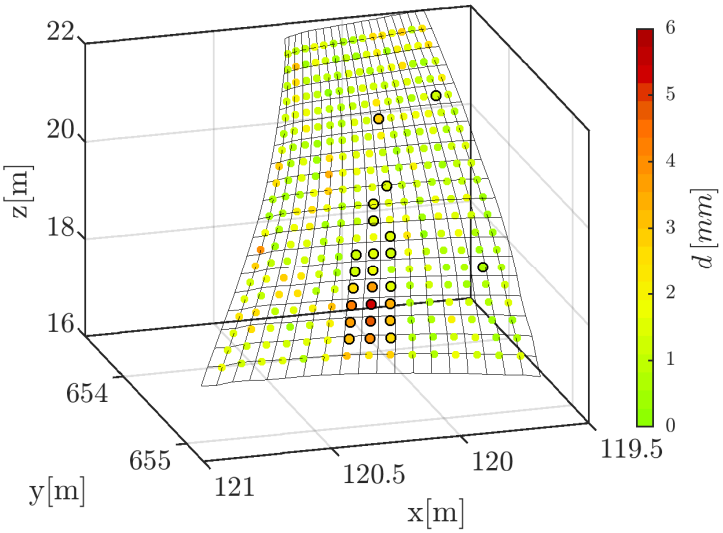

Figure 6.22 Distorted regions – Riegl S1 (from 20 m)

If compared to the reference results in fig. 6.21, the same area is identified as deformed. Points have the same order of magnitude (less than 6 mm). Despite the scanning distance of 20 m from the tower and the higher range measurement noise of this scanner, the existing deformations are successfully identified in the same area.

For the second station point at 40 m, the results for S2 are comparable with those from S1, and the deformed area is also successfully identified. Some points are still type I errors on the boundary areas (fig. 6.23).

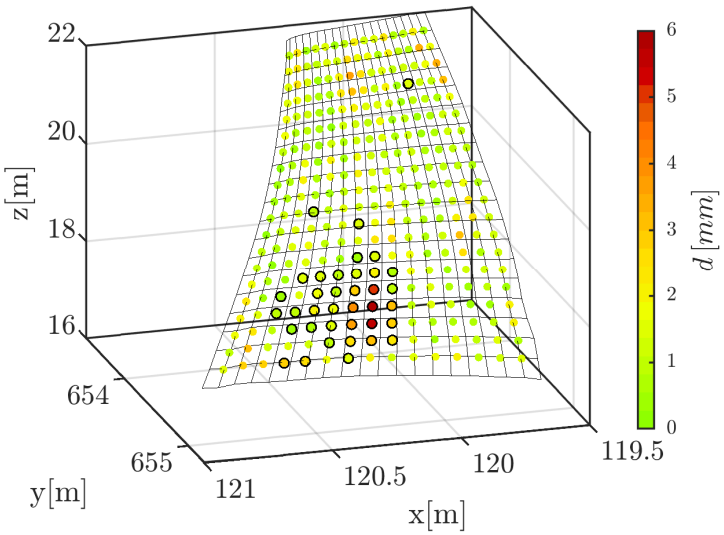

Figure 6.23 Distorted regions – Riegl S2 (from 40 m)

At 60 m, the algorithm also identifies the largest deformations, but unlike in the previous cases, there is a comparatively high number of deformed points observed over the entire surface (fig. 6.21). This fact is caused by the georeferencing of the second epoch for this station point. The standard deviations of the transformed points in the TS network are between 11 mm and 14 mm, which is the main cause for the less accurate joint B-spline parameterization. This issue has been discussed in Harmening and Neuner (2017) and the authors point out that reasonable comparison is only possible if the B-spline surfaces are based on the same parameterization.

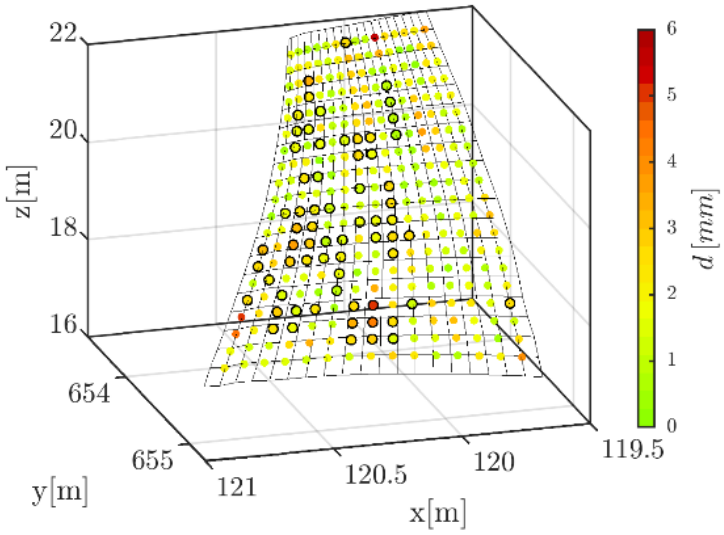

Figure 6.24 Distorted regions – Riegl S3 (from 60 m)

Throughout this comparison, the deformed regions are detected by different data sets obtained from different scanning setups. It is seen that type I errors cannot be completely avoided, even at a high confidence probability of $1 - \alpha$ ($\alpha = 3\%$). On the other side, type I errors usually do not occur in neighbouring parts in groups, therefore, most of them can be identified by investigating surrounding areas. If in the neighbouring area, only a single point is identified as deformed, it can be assumed that a type I error exists (Harmening et al., 2021).

Comparing the deformation analysis for all Riegl scans (fig. 6.22 to 6.24) with the reference values in fig. 6.21 it can be seen that the regions of small deformations (max. 6 mm) are successfully detected. It must be emphasized once more, that the range noise of the Riegl scanner is much higher (5 mm) than the one of the Surphaser (0.3 mm) and a large extent of the measurement noise is reduced during the deformation analysis using B-spline surfaces together with an appropriate stochastic model. This shows that realistic results are achieved using this approach.

Additionally, the role of the fully populated SVCM in TLS based deformation analysis is highlighted. A simple comparison of the results obtained with the fully populated SVCM and a diagonal SVCM (fig. 6.25), shows the clear advantage of including it in the surface estimation and statistical tests. If only a diagonal matrix is used in the deformation analysis, the outcomes of a deformation analysis become blurred with regard to the statistical test results. Figure 6.25 right shows the result of the data set S2 (@ 40m), but instead of a fully populated matrix as a stochastic model, it uses only the main diagonal of it. Here, many points are identified as significantly deformed (circled), even though they are outside the deformed area, as known from the benchmark scans (fig. 6.21). This proves that the inclusion of an appropriate stochastic model (cf. Jäger et al., 2005) in form of a fully populated SVCM is necessary for the correctness of statistically based decisions.

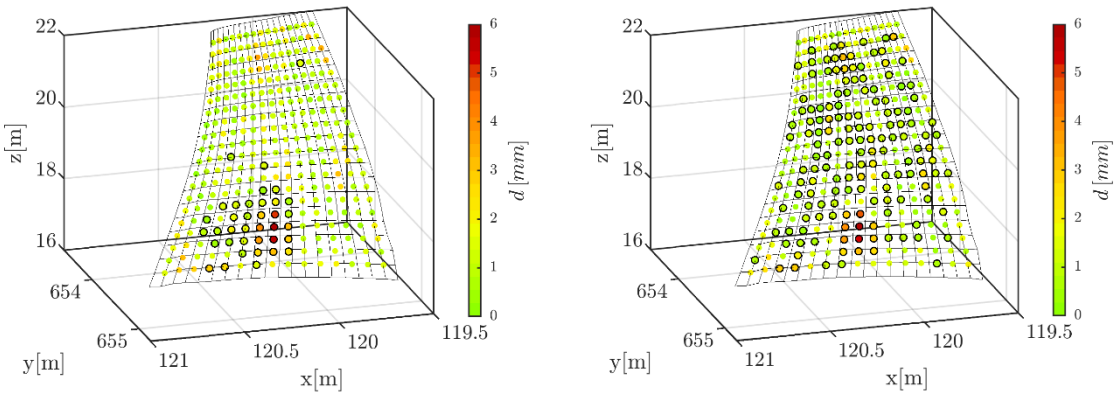

Figure 6.25 Left: distorted regions – Riegl S2 (from 40 m) with fully populated SVCM; right: the same deformation analysis with diagonal matrix as stochastic model

This study case highlighted an approach based on B-spline deformation analysis supported by the developed SVCM. Out of all findings, the most important are:

1. by means of appropriate modelling with B-splines and inclusion of appropriate stochastic information, small deformations are identified, despite the relatively high measurement noise of the scanner in use;
2. distorted regions are identified by statistical testing and not just compared visually;
3. covariances (correlations) in the full SVCM make a difference in decision-making with regard to distorted regions.

6.4 TLS optimal station point, exemplary for an arch dam scan

There are many studies that deal with TLS station point planning for different purposes, like object coverage, overlapping areas, reduction of angles of incidence, finding optimal scanning parameters or minimizing point density (cf. Heine et al., 2009; Soudarissanane, 2016; Wujanz and Neitzel, 2016; Jia and Lichti, 2017; Aichinger and Schwieger, 2018; Cabrera Revuelta et al., 2021). All of them intend to optimize processes, either for data acquisition or post-processing, by reducing the number of station points, reducing the acquisition of unnecessary data (overlapping), or simply reducing the processing time. With regard to the term optimization and thinking of geodetic network observations, a VCM or cofactor matrix can be used to evaluate the quality of the network. Similar to this aspect, the defined SVCM in this work can also be used to evaluate the prospective errors in the point cloud coordinates. The purposes of such an analysis are manifold. They reach from knowing where to place the station point with regard to the scanned object, to choosing the best suitable location for installing a permanent laser scanner. The latter application is gaining intensive attention in recent times (cf. Kuschnerus et al., 2021; Schröder and Nowacki, 2021; Voordendag et al., 2021) and would benefit from the following analysis.

In this section, the criteria used for finding an optimal station point is defined based on geodetic adjustment theory. One criterion for the global precision indicators of the adjusted parameters is the trace or variance criteria (Niemeier, 2008). It uses the VCM of the parameters as a basis and the purpose is to minimize its trace. In a similar manner, the defined SVCM in this thesis contains the variances of the observations on the main diagonal. Finding a TLS station point that has the lowest value of the trace is considered the optimal station point in this approach. This is a brute force approach, in which multiple configurations are first defined and then verified.

As seen through chapters 3 to 5, most of the elementary errors are dependent on the scanning geometry, which means that the user is able to influence the values in the SVCM by choosing different scan locations in a given situation. Therefore, finding the best suitable station point requires simulating several positions and choosing the one that meets this criterion. For practical reasons, an equation based on the variance criterion (Niemeier, 2008) is adapted to a more concrete indicator, namely the average variance:

$$\bar{\sigma}_{sp}^2 = tr(\boldsymbol{\Sigma}_{ll}) \cdot \frac{1}{u_p}, \tag{6.6}$$

where u_p is the number of points multiplied by 3 (for each coordinate dimension).

This indicator is used in the upcoming section to exemplify the analysis with the help of a real arch dam. Additionally, the contribution of each elementary error group is indicated for the simulated station points. This scenario may be encountered in TLS deformation analysis.

6.4.1 Study case: arch dam Kops

For this example, a point cloud acquired with the Leica HDS 7000 of the Kops dam is used as reference data. This means that the user needs to know the form and shape of the object approximately, e.g. from a field recognition measurement campaign or based on airborne LiDAR data. The point cloud was acquired in the summer of 2019, at the Kops dam in the

Austrian Alps. A short presentation of the dam is given in order to gain a sense of the object's dimensions, constructive materials, and local conditions.

The Kops water dam (fig. 6.26) is a storage concrete dam that was built between 1962 and 1969. Unlike other arched dams, it is considered a hybrid dam comprised out of a gravity dam and an arch dam with an artificial counterfort or abutment (Ganser, 1975). It retains a volume of almost 43 Mil. m^3 of water, creating the 1 km^2 "Kopssee" lake (Illwerke vkw AG, 2022). The crown spans over 400 m and in the middle, it has a height of 122 m from foundation to crest with a crest width of 6 m.

Figure 6.26 Side view of the arch dam Kops in August 2019

At the airside of the arch dam, there is no artificial or natural river drainage, thus making this area ideal for terrestrial measurements. Although not entirely free from vegetation like bushes and pine trees, the valley on the airside resembles a small plateau that extends transversal from the dam's middle point in the side that was once a river valley (fig. 6.27).

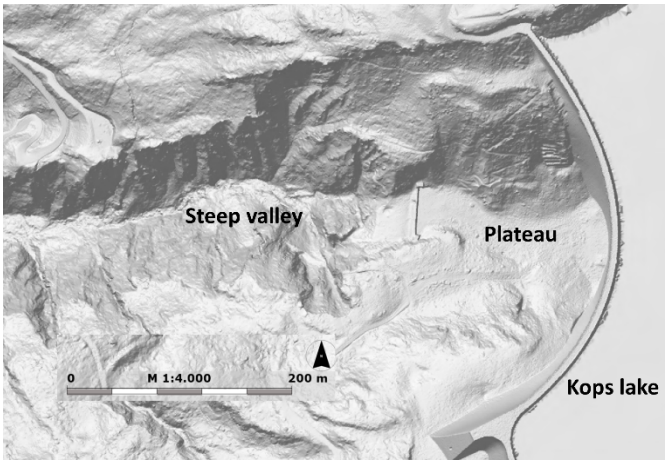

Figure 6.27 Overview of topography at the airside of the Kops arch dam (Background source: ©Land Voralberg LVA, Vogis)

Even though laser scanning is not used by the Vorarlberger Illwerke AG measurement team for monitoring the Kops dam yet, the International Commission on Large Dams (ICOLD) recommends terrestrial laser scanning as a recent development for dam monitoring (International Commission on Large Dams, 2018). Therefore, practitioners see potential in TLS area-wise monitoring for dams. The same fact is emphasized in the scientific community (cf. Scaioni et al. 2018).

6.4.2 Defining restrictions for the candidate positions

Searching for an optimal TLS station point is made based on analytic geometry (also called coordinate geometry or Cartesian geometry). The initial scan contains coordinates relative to the station point, also referred to as the scanner's own coordinate system (SOC). Using the technical specifications, the maximal and minimal measurable ranges of the scanner are known. For the Leica HDS7000, the longest measurable distance is 187 m and the shortest is 1.4 m. Both values are restrictive factors for the coverage of each scan, but the longest measurable is the main restrictive parameter for objects of such dimensions. Placing the scanner at locations that lead to larger distances, means a lower coverage of the scanned object because the object parts that are outside of the measurable range will not be scanned. Therefore, using this restriction is essential for defining the areas with possible locations for the station point without compromising coverage. The positions of these station points are generically called candidates in the upcoming paragraphs.

It is assumed that approximate knowledge of the scanned object is available, e.g. in form of a point cloud from previous scans (see fig. 6.28 green object), or a CAD model. A first step is to identify the lowest and highest value in the point cloud coordinates relative to the SOC along the plane axes (x and y). Since the whole algorithm is developed for terrestrial (and not airborne) laser scanning, the height component is ignored at this stage, because the user is not interested in obtaining candidate positions that are not on the ground. Therefore, only the values along the x and y axis are necessary at this stage. Later the height of the candidate position is calculated based on the 2D position projected onto the DTM.

Using the coordinates with the minimum and maximum along each axis, plane circles are drawn with centers in both the maximum and minimum of x and y. The radius of each circle is the longest measurable TLS distance (here 187 m). In total, there will be four circles, one for each min and max value along both axes (see fig. 6.28 hollow circles). In fig. 6.28 only three circles can be distinguished, although it was mentioned above that four are generated. This is due to a coincidence in this case, explainable by the fact that the maximum along y corresponds with the minimum along x (blue circle). At the same position, two circles are created, but they cannot be visually distinguished in fig. 6.28. Note that the visualization is only done for understanding and explanation purposes here. The intersection area given by all four circles defines the area in which all TLS distances are shorter than 187 m (see fig. 6.28 blue area). Therefore, any station point placed within this intersection area will respect the condition of distances shorter than 187 m. The next step is to make a selection within this area.

As observed, the blue intersection area stretches from the airside of the dam up to the waterside. Obviously, the user is interested only in the air side of the object, therefore a supplementary condition is introduced by specifying which side should be eliminated. The remaining side can be sampled and candidate positions are generated at user-defined intervals. In the current example, a grid (see fig. 6.28 red points) with a spacing of 40 m between the candidates has been generated in the intersection area. This raster can be denser or less dense, but here the value of 40 m has been chosen due to reduced computation time and ease of visualization. Out of all raster points (red) only a few are on the airside of the dam and within the blue area. They are highlighted in yellow in fig. 6.28. For each of the 12 candidates, only the plane coordinates are available at this stage. The height is then retrieved by projecting the plane position onto the DTM (cf. fig. 6.27) and adding the instrument height. In this case, 2 m were added as instrument height above ground level.

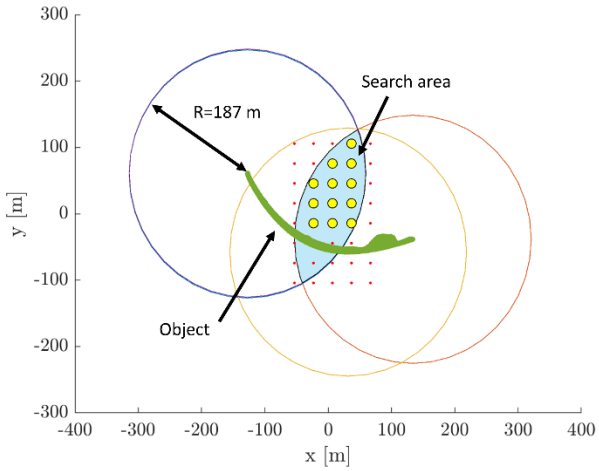

Figure 6.28 Area that defines the possible station point positions (light blue) with regard to the point cloud (green). Yellow points represent a raster of plausible candidates. Circles have radii the longest measurable distance.

6.4.3 SVCM for the candidate positions

Having candidate positions for the TLS station points means that the SVCM can be computed for each candidate and the user can decide which point is best suitable according to the criteria defined at the begging of the section – matrix trace the lowest, or the equivalent average coordinate precision the lowest. The values used in the establishment of the SVCM are presented in tab 6.7.

Table 6.7 Values of the elementary errors introduced in the SVCM

Correlation type	Elementary error name [unit]	Standard deviation
Non-correlating errors	Angular noise Hz [mgon]	3.1
	Angular noise V [mgon]	3.1
	Range [mm]	0.5
Functional correlating errors	x_{1n} [mm]	0.140
	x_{1z} [mm]	0.220
	x_2 [mm]	0.020
	x_3 [mm]	0.130
	x_4 [mgon]	0.448
	x_{5n} [mgon]	1.738
	x_{5z} [mgon]	1.598
	x_6 [mgon]	0.272
	x_7 [mgon]	1.929
	x_{10} [mm]	0.060
Stochastic correlating errors	Air temperature [°C]	5.00
	Air pressure [mbar]	2.41
	VGT= - 0.2 [°C/m]	0.06
	Roughness – *Rt* [mm]	1.6
	Reflectivity	See sec. 5.2.2

The values for standard deviations of the non-correlating elementary errors correspond with the ones derived from laboratory experiments (Raschhofer et al., 2021); for the functional correlating errors the same as in chapter 3 and in the stochastic correlating group a distinction has to be made for both types. In what concerns the values for the atmospheric conditions, the

measured values from the measurement campaign are used. A mean air temperature of 23.8°C and air pressure of 832.9 mbar were recorded. The VGT was not measured. Instead, the same value as for the Urbach tower (cf. tab. 6.6) of -0.2 °C/m with a standard deviation 0.06 °C/m is exemplarily used. Weather recordings were made on several points on-site (fig. 6.29 greed squares) at the instrument height of ca. 2 m above ground height with a precision Thermo-Barometer, Greisinger GTD1100. According to the technical specifications, air temperature is measured with an accuracy of +/−1% of the reading in the interval −10 °C to +50 °C and air pressure with +/−1.5 hPa in the interval of 750 hPa to 1100 hPa (GHM Messtechnik GmbH, 2020). These accuracies are likewise considered in the interpolation process.

Regarding the variances and covariance, the approach presented in chapter 4 was applied with the DTM presented in fig. 6.29 and leads to unique values for all observations after the interpolations (fig. 6.30).

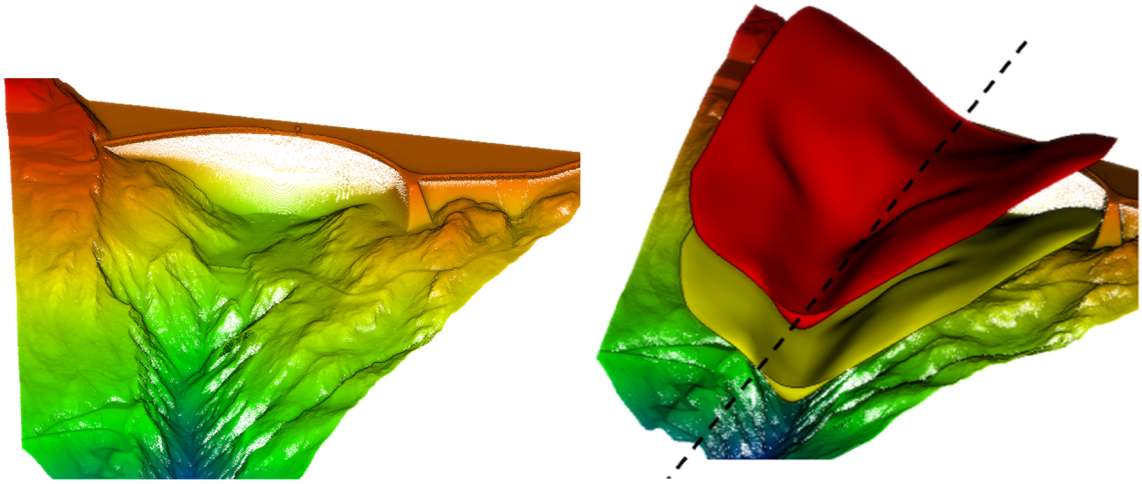

Figure 6.29. (Left) Digital Terrain model and part of the water dam (courtesy: Landesamt für Vermessung und Geoinformation, Land Vorarlberg, Austria); (right) Spatial separation of vertical temperature gradient (VGT) layers.

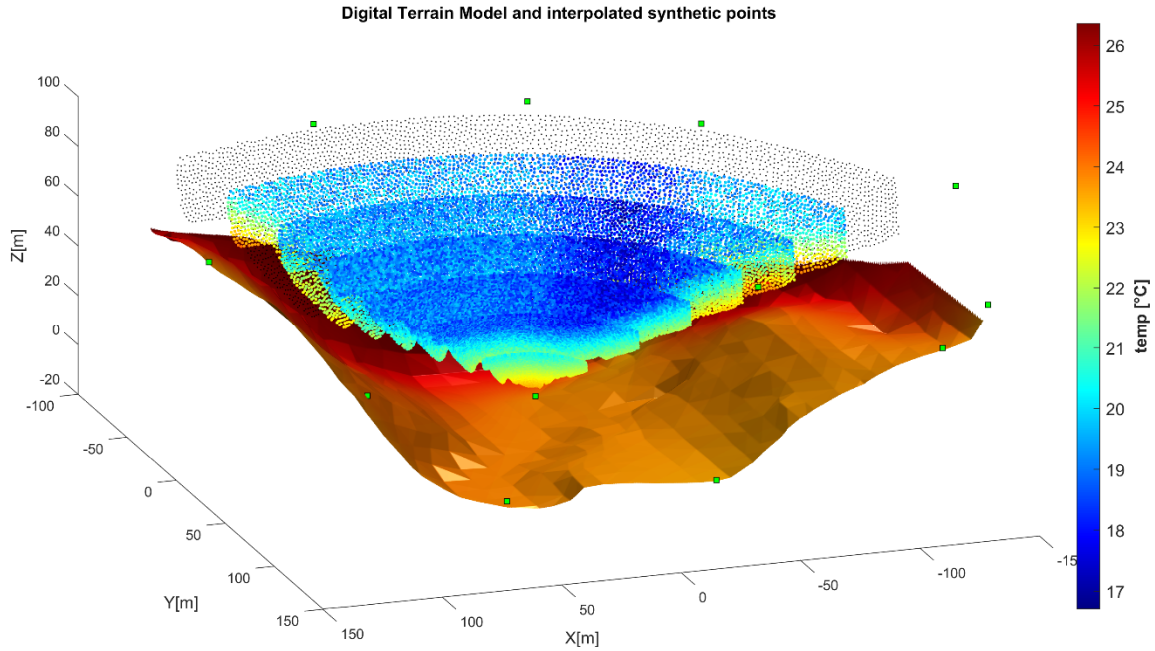

Figure 6.30. Interpolated values for the synthetic points colored according to temperature at the airside of the Kops water dam. Green squares represent the locations of weather data measurements.

For the other type of stochastic correlating errors, object surface properties, the same values as in sec. 5.4.1 are used. The reflectance values were obtained directly on-site and converted to % values using eq. 5.4 (see sec. 5.2). As regards roughness, the value obtained from the concrete sample of Rt = 5.3 mm is used (standard deviation of 1.6 mm). As mentioned at the beginning of sec. 6.4, only the main diagonal of the SVCM is used as a criterion, therefore correlations do not play any role in this analysis.

6.4.4 Optimal station point results

Based on the present workflow, the user obtains results in form of a table and individual graphics with the on-site situation and the relative contribution of each group of elementary errors to the main diagonal of the SVCM. Out of all 12 candidate points, only the results for four of them are graphically presented (fig. 6.31 – 6.34) because the others are very similar. The rest of them can be seen in Appendix 2. Each graphic also contains the value for the mean error of position after Helmert (HPE) in the title and the individual points are colored based on their HPE value computed as in sec. **Fehler! Verweisquelle konnte nicht gefunden werden.**. Representations like these are made based on the ones in the author's previous publication Kerekes and Schwieger (2021).

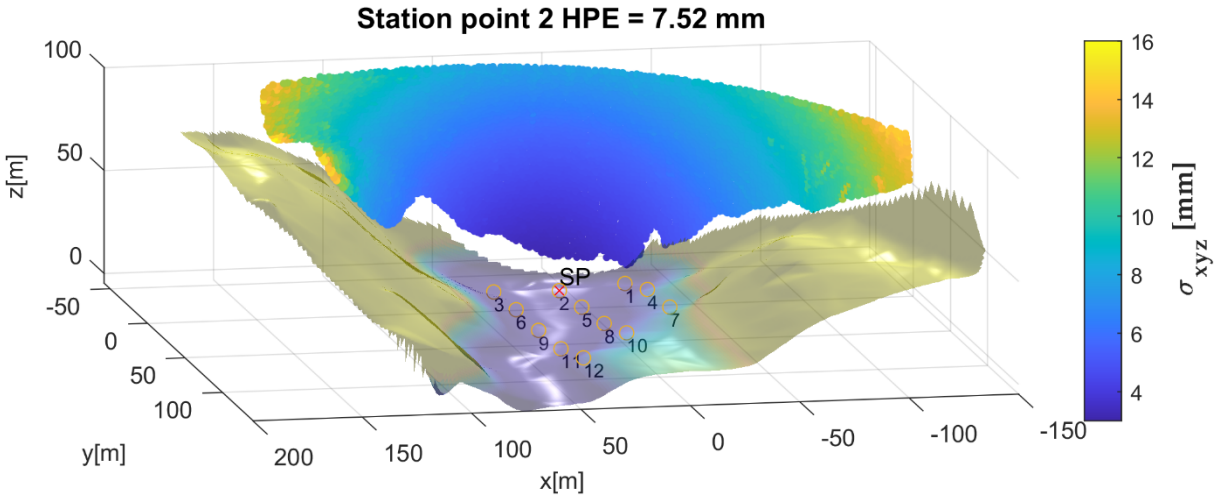

Figure 6.31 Analysis of candidate point 2 – average distance from object 96 m.

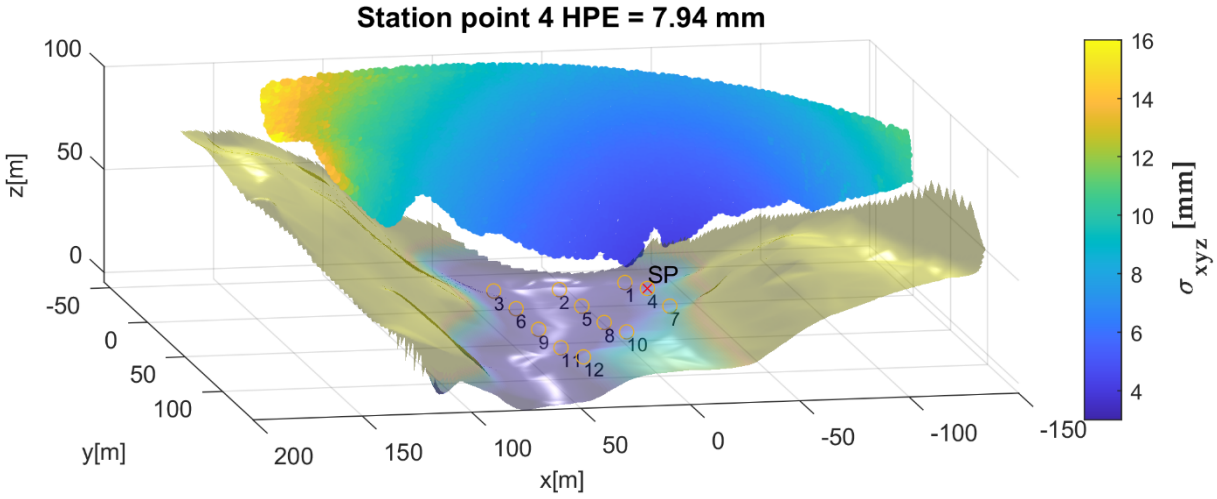

Figure 6.32 Analysis of candidate point 4 – average distance from object 103 m.

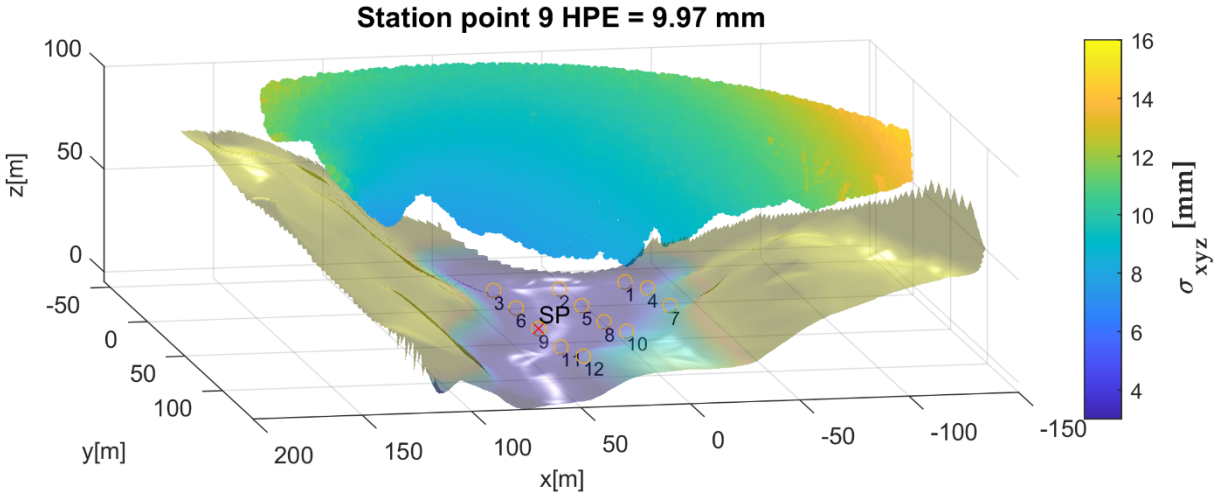

Figure 6.33 Analysis of candidate point 9 – average distance from object 131 m.

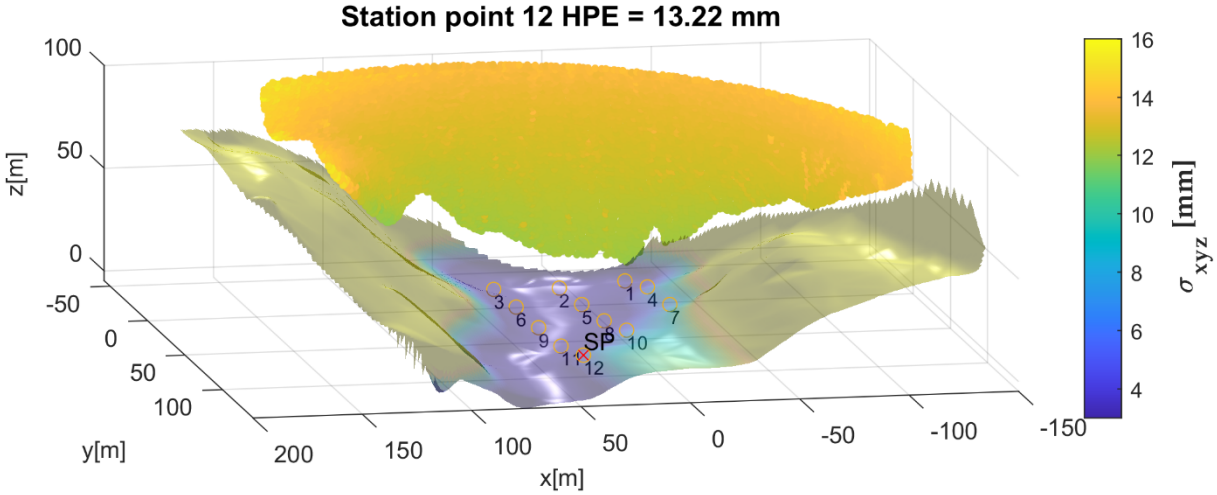

Figure 6.34 Analysis of candidate point 12 – average distance from object 172 m.

The results indicate that candidate 2 leads to the lowest error of position, even though the difference to candidate 4 is in the submillimeter level. However, the distribution of the HPEs on the dam's surface is different. It can be seen how candidate 2 leads to a radial distribution starting from the lower middle area of the dam, almost symmetric, whilst candidate 4 leads to the same effect, but the center of this radial distribution is shifted.

The other two candidates presented here, 9 and 12 are further away from the dam and the slight increase in the average coordinate precision is due to the contribution of elementary errors at higher distances. Note that the average coordinate precision is a global indicator here and does not reflect the individual error of position. If the user is interested in this, it can be deduced according to the color of each point.

Finally, candidate 2 leads to the lowest trace of the SVCM, and this can be considered for the on-site mission planning or installation of a permanent TLS location.

Similar to the simulated examples in which the contribution of each elementary error to the total variance was shown (cf. sec. 6.1), for the selected four candidates, the relative contribution of each group is presented here.

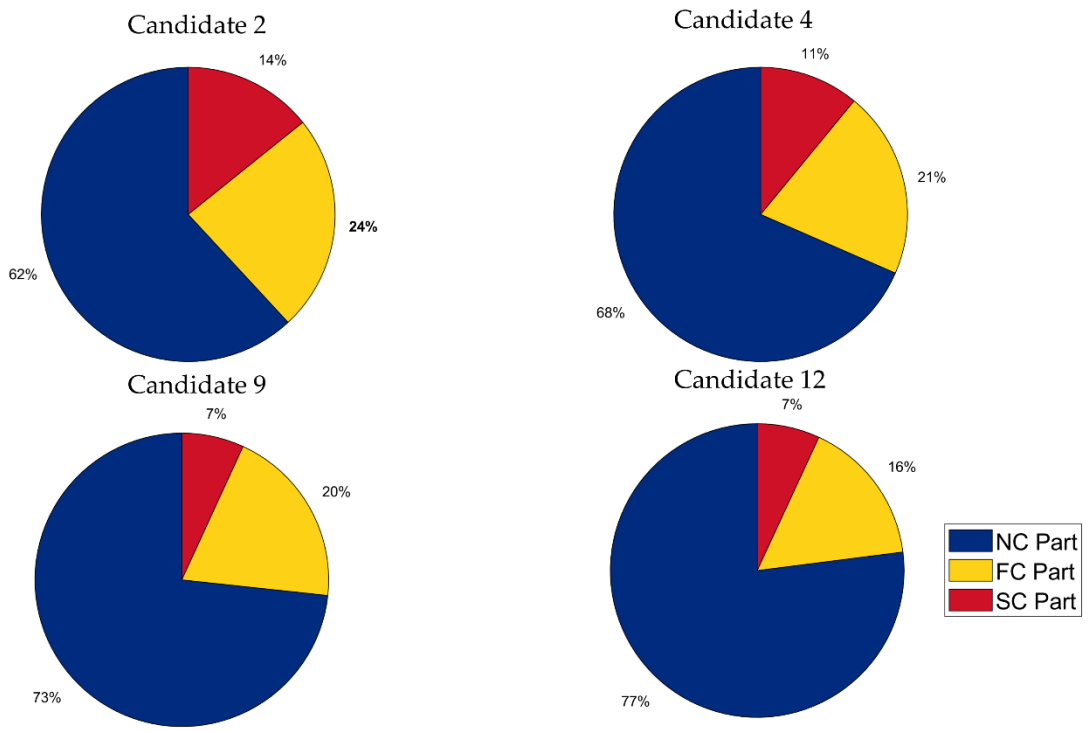

Figure 6.35 Variance analysis of candidate points on the SVCM trace.

From fig. 6.35 several conclusions can be drawn with regard to the importance of each elementary error group. An important notice is that these charts must be interpreted as a global measure of contribution. The same analysis is possible for single points in the point cloud as seen in sec. 6.1.1, but since the SVCM is treated as a whole in this optimization approach, the charts are representative of all points in the point cloud. Detailed analysis may be of interest if only some specific parts of the dam are attributed more attention than the others, e.g. the crow middle area that is most prone to deformations (Heine et al., 2009). But this is out of scope for the current application.

Like in the simulated examples with the panoramic scanner (sec. 6.1), the most influential group of elementary errors, was the non-correlating group, to be exact, the angle noise for both horizontal and vertical angles. The same finding is obvious here as well. For all of the analyzed candidates, the non-correlating group (NC Part) is dominant. Even at the closest candidate (1) at about 95 m (see fig. 6.35) the contribution reaches 59%. More than half of the variances are caused by these errors in this case. With increasing distance, the contribution also increases, as intuitive for any kind of angular error. This fact is reflected in all other charts for candidates at larger distances. At the furthest candidate situated at 173 m, almost three quarters of the SVCM trace is influenced by the non-correlating group.

Regarding the functional correlating group, if the absolute contribution is analyzed by converting the percent indication into a metric measure (e.g. proportion of error of position), a geometry-dependent behavior can be observed as in the case of non-correlating errors. This shows once more, that the scanning configuration does not need to be treated as a supplementary error source, since all groups of errors are strictly related to the geometry by their nature. In the previous applications, they proved to play a less important role in the variances, but more important for the covariances (cf. sec. 6.1.2). This subject can be studied

independently for each candidate, if the scope is to see the impact of correlations on the deformation analysis as in sec. 6.3.

As concerns the stochastic correlating group, the geometry dependence is similar to that of the non-correlating errors. This fact is directly related to the influencing terms in object surface properties. More precisely, the points at high angles of incidence lead to increased values in the distance variances (cf. sec. 5.2.1). This phenomenon occurs at the candidates that are relatively close to the dam (e.g. 1-5), and it is also visible by the higher values for the error of position at the dam's crest extremities. With increasing distance, the angles of incidence become more uniform, therefore less extreme values affect the error of position. This is reflected by the reduced relative contribution of the stochastic correlating group at the candidates further away (9 and 12).

6.4.5 Conclusion for optimal station point

All in all, this analysis can be a useful tool for decision-making, which aids in choosing the optimal station point regarding the mentioned criteria. The prerequisites are a representation of the area of interest (scanned object) and a DTM of the area. If neither is available in advance, a preview scan can be performed and then the object can be selected by the user. The same preview scan can be used for creating a local DTM. In the author's view, such an application can be easily included in the laser scanner's on-board software, making it possible to derive the optimal station point directly on-site.

The algorithm can be extended by other criteria, for e.g. finding the scan position that leads to a reduced level of correlations along a preferred direction or in a limited area of the object. Or analyzing which of the elementary errors are most dominant along one direction and choosing the station point to reduce their effect along that direction. Some instruments have special adapters that permit setting up the scanner at fixed inclined angles (e.g. Riegl VZ scanners), making it possible to reduce the effect of some instrument-specific errors (e.g. errors at steep zenith angles) in certain areas of the object. Another possible application is in approximating the precision of certain features within a scan, e.g. targets necessary for registration. In this sense, the user would know where to place the scanner so that the strived level of accuracy is obtained and not rely entirely on their intuition, as most users do. In any case, the full potential of the SVCM remains only partly explored at the time of writing this thesis.

The findings from this study case can be summed up as follows:

1. A workflow for determining the optimal TLS station point position has been presented based on the SVCM. It requires pre-knowledge about the local conditions (DTM) and on-site information about the weather conditions. Additionally, the object's shape and size need to be known, at least approximately;
2. The best "candidate" is the one with the lowest average variance and its position was obtained based on the on-site conditions. Several simulations can be performed before deciding where to set up the most appropriate station point in the search area;
3. The relative contribution of each elementary error group shows which elementary errors contribute the most to the uncertainty in a real test scenario. Here, the non-correlating group is the dominant one

7. Conclusions

7.1 Reached goals

Throughout this contribution, a stochastic model for TLS observations is defined in form of a VCM based on the elementary error theory. Three groups of elementary errors are considered with regard to the nature of their correlations. All three are jointly introduced into the created SVCM. In each group of elementary errors, different types of errors that affect TLS measurements have been classified according to pre-knowledge, assumptions, and empirical data. The instrument-specific errors are treated as non-correlating and functional correlating errors in this work. In the last group called the stochastic correlating errors, two types of errors have been included, the atmosphere-specific and object surface-related errors. Each type of error was treated in a separate chapter. The overall scope of this thesis is to define a stochastic model for TLS measurements that can aid in quantifying the uncertainty budget, surface estimation, or TLS based deformation analysis.

For the first group of instrument-specific errors, the standard deviations are retrieved from the TLS technical specifications. This resembles what most practitioners would do if they need a precision indication for the individual points in the point cloud. However, the situation becomes more complex with the second group of instrument errors. These are errors related to the calibration parameters of a TLS. After calibration, these parameters are determined with a certain level of uncertainty. If this is known (e.g. made available by the calibration institute), the variances can be included in the elementary error model, therefore the impact on the observation's uncertainty becomes more realistic. The used functional models for panoramic and hybrid scanners are adopted from available recent literature sources on the topic.

Regarding the atmosphere-specific errors, an approach has been presented that considers the spatial distribution of atmospheric parameters and their effect on distances and vertical angles. The method is based on well-established knowledge of EDM measurements in the lower atmospheric layer and uses interpolation methods based on time series and the spatial distribution of TLS observations. Out of all atmospheric parameters, only air temperature, air pressure, and vertical temperature gradient are included in the SVCM. With empirical values for variances and the computed covariances based on local atmospheric conditions, it can be affirmed, that even at relatively short ranges (cf. sec 6.3), the resulting influences matter in the statistically based decision. The approach presented in chapter 4 has been developed for long-range scanning (e.g. distances > 400 m) and is meant for validation in future studies.

In what concerns the influences of object surface properties on TLS measurements, the presented approach requires knowledge of two characteristics of the object surface properties: roughness and reflectivity. In many disciplines, roughness is necessary for evaluating the quality of a surface, e.g. for friction reduction or adherence with different adhesives. Here it is used as an influencing factor for the TLS distance standard deviation. Additionally, the radiometric properties of a surface are used to determine standard deviations for distance measurements with respect to the technical capabilities of the scanner as a function of reflectivity and distance from the object to the scanner. Covariances of this group of errors are obtained by empirically estimated correlation/covariance functions. This assures a relation to the physical properties of the object surface and improves past approaches used in the elementary error model.

Several study cases have been used to demonstrate the utility of the defined TLS stochastic model in form of a SVCM. In the first study case, scans for a simulated object were used to exemplify the TLS uncertainty budget and influences of scanning geometry. Moreover, the contribution of variances and covariances was analyzed for a defined level for the elementary errors. The relative contribution of elementary errors was additionally shown. A second short study case presented the influence of introducing a stochastic model for estimating the sphere center coordinates for commonly used TLS sphere targets. A more realistic estimate of the uncertainty was obtained in this case. The third application used the SVCM for multiple purposes on a real wooden tower scanned in two epochs in outdoor conditions. It was used to estimate B-splines in different epochs and afterwards used for deformation analysis. The most important finding for this scenario is that including an appropriate SVCM in the deformation analysis reduces the number of falsely identified deformed areas. Finally, a fourth study case shows the utility of a SVCM for planning purposes and estimation of the expected variances from different TLS station point locations. Additional to the indication of the optimal station point with regard to minimal SVCM trace, the relative contribution of each elementary error group on the variance of the coordinates is shown. This also highlights the relation between different groups of errors, scan configuration, and the resulting estimated variances.

7.2 Outlook

Functional calibration models of current TLS were adopted based on scientific publications. The models may not correspond to those used by laser scanner manufacturers, but as long as they remain proprietary information, the real calibration model cannot be included in the elementary error model. In the hope that this will change in the future, the approach in chapter 3 could be improved.

The atmosphere for microclimates is described based on empirical data at the ground level and existing studies about the behavior of some atmospheric parameters in this region. In reality, the situation is so complex, that there is no generic modelling approach valid for all conditions. In the author's view, the only possibility to have realistic values for the atmospheric parameters within the whole volume of the microclimate, is to determine these parameters from empirical data on-site. This is possible nowadays with so-called meteorology drones that capture weather data in a relatively small volume by flying in different patterns within the needed volume (cf. Jacob et al., 2018; Meteomatics AG, 2019). The approach is based on interpolation, like the one presented in chapter 5, but the spatial discretization would be more realistic in this way.

For object surface properties possible improvements are also related to obtaining on-site data for a sample part of the object for both roughness and reflectivity. Mobile optical profilometers and mobile spectrometers can be used to have realistic values of the two surface properties. Additionally, the model has to be validated with reference surfaces for which the roughness profile and reflectivity values are well-known. This can be done similarly to the experiments in laboratory conditions.

The current work relies on the variance propagation law and assumes normally distributed variables. The same approach can be made with Monte Carlo simulations and the outcomes can be compared. This was not shown in this thesis because it was out of scope, but similar to the results presented for the elementary error relative contribution, a variance-based sensitivity analysis can be conducted to obtain the influence of the input parameter's

uncertainty (elementary errors) on the uncertainty of the results. The findings can put light on which elementary errors are the most relevant in the stochastic model, according to this different approach.

A final improvement is related to the SVCM between multiple epochs. The inter-epochal variances and covariances have not been treated here because it is subject to ongoing research.

Resources

Agterberg, F.P. (1974). *Geomathematics - Mathematical Background and Geo-Science Applications*. Amsterdam, London, New York: Elsevier Science & Technology.

Aichinger, J. and Schwieger, V. (2018). Influence of scanning parameters on the estimation accuracy of control points of B-spline surfaces. *Journal of Applied Geodesy*, 12(2).

Alkhatib, H., Neumann, I. and Kutterer, H. (2009). Uncertainty modeling of random and systematic errors by means of Monte Carlo and fuzzy techniques. *Journal of Applied Geodesy*, 3(2).

Andrews, L.C. (2019). *Field Guide to Atmospheric Optics*. 2nd ed. Bellingham, Washington, USA: SPIE Press.

Augath, W. (1985). Lagenetze. In: *Geodätische Netze in Landes-und Ingenieurvermessung*. Konrad Wittwer, pp.373–428.

Basis Software Inc. (2021). Data sheet Surphaser 3D Laser Scanners. [online] surphaser.com. Available at: *https://www.surphaser.com/pdf/Surphaser%20100HSX.pdf* [Accessed 10 Nov. 2021].

Beckmann, P. and Spizzichino, A. (1963). *The scattering of electromagnetic waves from rough surfaces*. Frankfurt am Main: Pergamon Press.

Beiser, L. (1992). *Laser scanning notebook*. Bellingham, Wash.: Spie Optical Engineering Press.

Beraldin, J.A. and Blais, F. (2010). Laser Scanning Technology. In: G. Vosselman and H.-G. Maas, eds., *Airborne and Terrestrial Laser Scanning*. Whittles Publishing.

Besl, P.J. (1988). Active, optical range imaging sensors. *Machine Vision and Applications*, 1(2).

Bessel, F.W. (1838). Untersuchungen über die Wahrscheinlichkeit der Beobachtungsfehler. *Astronomische Nachrichten*, 15.

Boehler, W. and Marbs, A. (2003). Investigating Laser Scanner Accuracy. In: *Proceedings of XIXth CIPA Symposium.*

Bolkas, D. and Martinez, A. (2018). Effect of target color and scanning geometry on terrestrial LiDAR point-cloud noise and plane fitting. *Journal of Applied Geodesy*, 12(1).

Borovkov, K.A. (2014). *Elements of Stochastic Modelling*. New Jersey: World Scientific Publishing Co Pte Ltd.

Box, G.E.P., Jenkins, G.M. and Reinsel, G.C. (2008). *Time series analysis: forecasting and control*. 4th ed. Hoboken, NJ : Wiley, 2008.

Brocks, K. (1939). Vertikaler Temperaturgradient und terrestrische Refraktion, insbesondere im Hochgebirge. *Publications Meteorological Institute University of Berlin*, Band III (Heft 4).

Brunner, F.K. (1984a). Modelling of Atmospheric Effects on Terrestrial Geodetic Measurements. In: F.K. Brunner, ed., *Geodetic Refraction - Effects of Electromagnetic Wave Propagation through the Atmosphere*. Berlin, Heidelberg, Germany: Springer-Verlag.

Brunner, F.K. (1984b). Overview of Geodetic Refraction Studies. In: F.K. Brunner, ed., *Geodetic Refraction - Effects of Electromagnetic Wave Propagation Through the Atmosphere*. Berlin, Heidelberg, Germany: Springer-Verlag.

Buchner, A., Hadrath, S., Burkard, R., Kolb, F.M., Ruskowski, J., Ligges, M. and Grabmaier, A. (2021). Analytical Evaluation of Signal-to-Noise Ratios for Avalanche- and Single-Photon Avalanche Diodes. *Sensors*, 21(8).

Cabrera Revuelta, E., Chávez, M.-J., Barrera Vera, J.A., Fernández Rodríguez, Y. and Caballero Sánchez, M. (2021). Optimization of laser scanner positioning networks for architectural surveys through the design of genetic algorithms. *Measurement*, 174(2021).

Calders, K., Disney, M.I., Armston, J., Burt, A., Brede, B., Origo, N., Muir, J. and Nightingale, J. (2017). Evaluation of the range accuracy and the radiometric calibration of multiple terrestrial laser scanning instruments for data interoperability. *IEEE Transactions on Geoscience and Remote Sensing*, 55, pp.2716–2724. doi.org/10.1109/TGRS.2017.2652721.

Caspary, W. and Wichmann, K. (2007). *Auswertung von Messdaten: Statistische Methoden für Geo- und Ingenieurwissenschaften*. München, Wien: Oldenbourg Verlag.

Chaudhry, S., Salido-Monzú, D. and Wieser, A. (2021). A Modeling Approach for Predicting the Resolution Capability in Terrestrial Laser Scanning. *Remote Sensing*, 13(4).

Chen, X., Hua, X., Zhang, G., Wu, H., Xuan, W. and Li, M. (2015). Evaluating point cloud accuracy of static three-dimensional laser scanning based on point cloud error ellipsoid model. *Journal of Applied Remote Sensing*, [online] 9. doi:10.1117/1.JRS.9.095991.

Chow, J., Lichti, D.D. and Teskey, W.F. (2012). Accuracy assessment of the Faro Focus 3D and Leica HDS6100 panoramic type terrestrial laser scanner through point-based and plane-based user self-calibration. In: *Proceedings of FIG Working Week 2012, Rome, Italy*.

Chow, J., Lichti, D.D., Glennie, C. and Hartzell, P. (2013). Improvements to and Comparison of Static Terrestrial LiDAR Self-Calibration Methods. *Sensors*, 13(6).

Ciddor, P.E. (1996). Refractive index of air: new equations for the visible and near infrared. *Applied Optics*, 35(9).

Collins Cobuild advanced learner's dictionary (2018). Glasgow: Harper Collins Publishers.

Cox, M.G. (1972). The Numerical Evaluation of B-Splines. *IMA Journal of Applied Mathematics*, 10(2).

Csanády, E., Magoss, E. and Tolvaj, L. (2015). *Quality of Machined Wood Surfaces*. 1st ed. Cham Springer International Publishing.

De Boor, C. (1972). On calculating with B-splines. *Journal of Approximation Theory*, 6(1).

DeGroot, M.H. and Schervish, M.J. (2011). *Probability and statistics*. 4th ed. Addison-Wesley.

Deutscher Wetterdienst (2022). Wetter und Klima - Deutscher Wetterdienst - Glossar. [online] www.dwd.de. Available at: *https://www.dwd.de/DE/service/lexikon/lexikon_node.html* [Accessed 20 Feb. 2020].

De Wekker, S. and Kossmann, M. (2015). Convective boundary layer heights over mountainous Terrain—A review of concepts. *Frontiers in Earth Science*, [online] 3. doi:10.3389/feart.2015.00077.

DIN German Institute for Standardization (1978) *DIN 4761:1978-12 Oberflächencharakter – Geometrische Oberflächentextur-Merkmale*. Ed., DIN German Institute for Standardization.

DIN German Institute for Standardization (1998) *DIN EN ISO 11562:1998-09 Geometrical Product* Specifications (GPS*) - Surface texture: Profile method - Metrological characteristics of phase correct filters*. Ed., DIN German Institute for Standardization.

DIN German Institute for Standardization (2012) *DIN EN ISO 25178-2:2012-09 Geometrical product specifications (GPS) - Surface texture: Areal - Part 2: Terms, definitions and surface texture parameters (ISO 25178-2:2012)*. Ed., DIN German Institute for Standardization.

DIN German Institute for Standardization (2010) *DIN EN ISO 4287:2010-07 Geometrical Product Specifications (GPS) – Surface texture: Profile method – Terms, definitions and surface texture parameters*. Ed., DIN German Institute for Standardization.

Draganovská, D., Ižaríková, G., Guzanová, A. and Brezinová, J. (2018). General Regression Model for Predicting Surface Topography after Abrasive Blasting. *Metals*, 8(11).

Dr. Johannes Heidenhain GmbH (2022). Modular Angle Encoders with Optical Scanning. [online] Available at: *https://www.heidenhain.de/fileadmin/pdf/en/01_Products/Prospekte/PR_Modular_Angle_Encoders_with_Optical_Scanning_ID1222041_en.pdf* [Accessed 15 Jan. 2022].

Duma, V.-F. (2017). Polygonal Mirror Laser Scanning Heads: Characteristic Functions. In: *Proceedings of the Romanian Academy (18), 1/2017*. The Publishing House of the Romanian Academy.

Eichler, H.J., Eichler, J. and Lux, O. (2018). *Lasers - Basics, Advances and Applications*. 1st ed. Springer International Publishing.

Fialovszky, L. (1991). Instruments for Measuring Angles. In: L. Fialovszky, ed., *Surveying Instruments and their Operational Principles*. Amsterdam, Oxford, New York, Tokyo: Elsevier, pp.70–241.

Fischer, H. (2011). *A History of the Central Limit Theorem: from Classical to Modern Probability Theory*. New York: Springer Science+Business Media.

Flach, P. (2000). *Analysis of refraction influences in geodesy using image processing and turbulence models*. PhD Thesis, ETH Zürich.

Freedman, D., Pisani, R. and Purves, R. (2007). *Statistics*. 4th ed. New York: W. W. Norton & Company.

Friedli, E. (2020). *Point Cloud Registration and Mitigation of Refraction Effects for Geomonitoring Using Long-Range Terrestrial Laser Scanning*. PhD Thesis, ETH Zürich.

Friedli, E., Presl, R. and Wieser, A. (2019). Influence of atmospheric refraction on terrestrial laser scanning at long range. In: *Proceedings of the 4th Joint International Symposium on Deformation Monitoring (JISDM), Athens, Greece, 15–17 May 2019*.

Fröhlich, C. (1996). *Aktive Erzeugung korrespondierter Tiefen- und Reflektivitätsbilder und ihre Nutzung zur Umgebungserfassung*. PhD Thesis. Technical University Münich, Pro Universitate Verlag.

Ganser, O. (1975). Staumauer Kops, Anlage der Drainagebohrungen, Auswirkung dieser Massnahmen auf die Höhe des Bergwasserspiegels und die Grösse des Sohlenwasserdruckes. In: *Die Talsperren Österreichs Vol. 22*. Vienna, Austria: Springer.

Gauß, C. F. (1823). *Theoria combinationis observationum erroribus minimis obnoxiae*. Translation by G.W. Stewart - Theory of the combination of observations least subject to errors. Part one, part two, supplement. ed. Philadelphia 1995, USA: Society for Industrial and Applied Mathematics.

Geiger, R., Aron, R.H. and Todhunter, P. (2003). *The climate near the ground*. Oxford, UK: Rowman & Littlefield Publishers Inc.

Geomares (2022). Terrestrial Laser Scanners Buyers' Guide 2022. [online] geo-matching.com. Available at: *https://geo-matching.com/terrestrial-laser-scanners* [Accessed 20 Jan. 2022].

GHM Messtechnik GmbH (2020). Product specifications GTD 1100. [online] Available at: *https://www.greisinger.de/files/upload/de/produkte/kat/k19_095_DE_oP.pdf*.

González-Aguilera, D., Rodríguez-Gonzálvez, P., Armesto, J. and Arias, P. (2011). Trimble GX200 and Riegl LMS-Z390i sensor self-calibration. *Optics Express*, 19(3).

Gordon, B. (2008). *Zur Bestimmung von Messunsicherheiten terrestrischer Laserscanner*. PhD Thesis, Technical University Darmstadt.

Gotthardt, E. (1960). Zur Ermittlung von Korrelationen. *Zeitschrift für Vermessungswesen 1960*, 85(6).

Grant, D., Bethel, J. and Crawford, M. (2012). Point-to-plane registration of terrestrial laser scans. *ISPRS Journal of Photogrammetry and Remote Sensing*, [online] 72. doi.org/10.1016/j.isprsjprs.2012.05.007.

Graybill, F. A. (1969). *Introduction to matrices with applications in statistics*. Belmont, Calif., Wadsworth Pub. Co.

Griffiths, D. V., Huang, J. and Fenton, G.A. (2011). Probabilistic infinite slope analysis. *Computers and Geotechnics*, 38(4).

Habib, A. (2009). Accuracy, Quality Assurance, and Quality Control of LiDAR Data. In: J. Shan and C.K. Toth, eds., *Topographic Laser Ranging and Scanning*. CRC Press.

Hagen, G. (1837). *Grundzüge der Wahrscheinlichkeitsrechnung*. 1st ed. Berlin: Dümmler.

Harmening, C. (2020). *Spatio-Temporal Deformation Analysis Using Enhanced B-Spline Models of Laser Scanning Point Clouds.* PhD Thesis, Technical University Vienna.

Harmening, C. and Neuner, H. (2016). Detecting rigid body movements from TLS-based areal deformation measurements. In: *Proceedings of the FIG Working Week 2016 Christchurch, New Zealand, 2-6 May*.

Harmening, C. and Neuner, H. (2017). Choosing the optimal number of B-spline control points (Part 2: Approximation of surfaces and applications). *Journal of Applied Geodesy*, 11(1).

Harmening, C., Hobmaier, C. and Neuner, H. (2021). Laser Scanner–Based Deformation Analysis Using Approximating B-Spline Surfaces. *Remote Sensing*, 13(18).

Hartzell, P. J., Gadomski, P. J., Glennie, C. L., Finnegan, D. C. and Deems, J. S. (2015). Rigorous error propagation for terrestrial laser scanning with application to snow volume uncertainty. *Journal of Glaciology*, 61(230).

Hartzell, P.J., Glennie, C.L. and Finnegan, D.C. (2013). Calibration of a Terrestrial Full Waveform Laser Scanner. In: *ASPRS 2013 Annual Conference*. Baltimore, Maryland.

Heine, E., Reiner, H. and Weinold, T. (2009). Deformationsmessungen mit terrestrischen Laserscannern am Beispiel der Kops Staumauer. In: G. Chesi and T. Weinold, eds., *Proceedings of 15. Internationale Geodätische Woche Obergurgl.* Herbert Wichmann Verlag.

Hennes, M. (2006). Das Nivelliersystem-Feldprüfverfahren nach ISO 17123-2 im Kontext refraktiver Störeinflüsse. *Allgemeine Vermessungsnachrichten*, 2006/1(3).

Heunecke, O. (2004). Nochmals über Korrelationen in der Messtechnik. In: *Festschrift Univ. Prof. H. Pelzer zur Emeritierung Schriftenreihe der Fachrichtung Vermessungswesen der Universität Hannover Vol. 120*.

Heunecke, O., Kuhlmann, H., Welsch, W., Eichhorn, A. and Neuner, H. (2013). *Auswertung Geodätischer Überwachungsmessungen*. 2nd ed. Berlin, Germany: Handbuch Ingenieurgeodäsie, Wichmann, p.198.

Hirt, C., Guillaume, S., Wisbar, A., Bürki, B. and Sternberg, H. (2010). Monitoring of the refraction coefficient in the lower atmosphere using a controlled setup of simultaneous reciprocal vertical angle measurements. *Journal of Geophysical Research*, 115(D21).

Holst, C., Klingbeil, L., Esser, F. and Kuhlmann, H. (2017). Using point cloud comparisons for revealing deformations of natural and artificial objects. In: *Proceedings of INGEO 2017, 7th International Conference on Engineering Surveying*.

Illwerke vkw AG (2022). Website Kopssee. Available at: *https://www.illwerkevkw.at/kopssee.htm* [Accessed 10 Jan. 2022].

Institute for Computational Design and Construction (2019). Urbach Tower | Institute for Computational Design and Construction | University of Stuttgart. [online] www.icd.uni-stuttgart.de. Available at: *https://www.icd.uni-stuttgart.de/projects/remstal-gartenschau-2019-urbach-turm/*.

International Association of Geodesy (1999). IAG resolutions adopted at the XXIIth General Assembly in Birmingham. Available at: *https://office.iag-aig.org/doc/5d7b8fda0c032.pdf* [Accessed 2 Feb. 2020].

International Civil Aviation Organization (2019). Website ICAO. [online] Icao.int. Available at: *https://www.icao.int/Pages/default.aspx*.

International Commission on Large Dams (2018). *Dam surveillance guide, Bulletin 158*. CRC Press.

International Organization for Standardization (2008). *ISO/IEC Guide 98-3:2008: Uncertainty of Measurement—Part 3: Guide to the Expression of Uncertainty in Measurement (GUM: 1995)*. Genève, Switzerland, 2008.

International Organization of Legal Metrology (2007). *International Vocabulary of Metrology – Basic and General Concepts and Associated Terms (VIM)*. International Organization of Legal Metrology (OIML).

Ishimaru, A. (2017). *Electromagnetic wave propagation, radiation, and scattering*. 2nd ed. Hoboken, New Jersey: Wiley & Sons, Inc.

Jacob, J., Chilson, P., Houston, A. and Smith, S. (2018). Considerations for Atmospheric Measurements with Small Unmanned Aircraft Systems. *Atmosphere*, 9(7).

Jacobson, M. Z. (2005). *Fundamentals of Atmospheric Modeling*. 2nd ed. [online] Cambridge: Cambridge University Press. doi: 10.1017/CBO9781139165389.

Jäger, R., Müller, T., Saler, H. and Schwäble, R. (2006). Klassische und robuste Ausgleichungsverfahren: Ein Leitfaden für Ausbildung und Praxis von Geodäten und Geoinformatikern. Heidelberg: Herbert Wichmann.

Janßen, J., Kuhlmann, H. and Holst, C. (2021). Assessing the Temporal Stability of Terrestrial Laser Scanners During Long-Term Measurements. In: *Contributions to International Conferences on Engineering Surveying, 8th INGEO International Conference on Engineering Surveying and 4th SIG Symposium on Engineering Geodesy; Kopáčik, A., Kyrinovič, P., Erdélyi, J., Paar, R., Marendić, A., Eds.;* Berlin/Heidelberg: Springer International Publishing.

Jelalian, A. V. (1992). *Laser radar systems*. Boston: Artech House.

Jenoptik Industrial Metrology Germany GmbH (2020). Precise roughness measurement - Surface texture parameters in practice. [online] www.jenoptik.com. Available at: *https://www.jenoptik.com/-/media/websitedocuments/metrology/neu/parameters/roughness-leaflet-en.pdf*. [Accessed 18 Oct. 2021].

Jia, F. and Lichti, D. (2017). A Comparison of Simulated Annealing, Genetic Algorithm and Particle Swarm Optimization in Optimal First-Order Design of Indoor TLS Networks. *ISPRS Annals of the Photogrammetry, Remote Sensing and Spatial Information Sciences*, IV-2/W4. doi:10.5194/isprs-annals-iv-2-w4-75-2017.

Jirovský, L. (2021). *Automatisierte Auswertung von Betonoberflächen*. Masterarbeit, Institute of Structural Engineering (IKI), University of Natural Resources and Life Sciences, Vienna. Available at: *https://permalink.obvsg.at/AC16130177*.

Joeckel, R., Stober, M. and Huep, W. (2008). *Elektronische Entfernungs- und Richtungsmessung und ihre Integration in aktuelle Positionierungsverfahren*. 5th ed. Stuttgart: Wichmann.

Jurek, T., Kuhlmann, H. and Holst, C. (2017). Impact of spatial correlations on the surface estimation based on terrestrial laser scanning. *Journal of Applied Geodesy*, 11(3).

Jutzi, B., Meyer, F. J. and Hinz, S. (2017). Aktive Fernerkundungssensorik - Technologische Grundlagen und Abbildungsgeometrie. In: C. Heipke, ed., *Photogrammetrie und Fernerkundung*. Springer Spektrum.

Kahmen, H. (2006). *Angewandte Geodäsie: Vermessungskunde*. 20th ed. Berlin: Walter De Gruyter.

Kassera, W. and Pietsch, P. (2020). *Motorflug kompakt das Grundwissen zur Privatpilotenlizenz*. Stuttgart Motorbuch Verlag.

Kauker, S. and Schwieger, V. (2015). Approach for a Synthetic Covariance Matrix for Terrestrial Laser Scanner. In: *Proceedings on 2nd International workshop on "Integration of Point- and Area-wise Geodetic Monitoring for Structures and Natural Objects." Stuttgart, Germany*.

Kauker, S. and Schwieger, V. (2017). A synthetic covariance matrix for monitoring by terrestrial laser scanning. *Journal of Applied Geodesy*, 11(2).

Kauker, S., Harmening, C., Neuner, H. and Schwieger, V. (2017). Modellierung und Auswirkung von Korrelationen bei der Schätzung von Deformationsparametern beim terrestrischen Laserscanning. In: *Proceedings of 18. International Ingenieurvermessungskurs in Graz*. Wichmann Verlag: Berlin, Germany, 2017.

Kerekes, G. and Schwieger, V. (2020). Elementary Error Model Applied to Terrestrial Laser Scanning Measurements: Study Case Arch Dam Kops. *Mathematics*, 8(4).

Kerekes, G. and Schwieger, V. (2021). Determining Variance-Covariance Matrices for Terrestrial Laser Scans: A Case Study of the Arch Dam Kops. In: *Contributions to International Conferences on Engineering Surveying, 8th INGEO International Conference on Engineering Surveying and 4th SIG Symposium on Engineering Geodesy; Kopáčik, A., Kyrinovič, P., Erdélyi, J., Paar, R., Marendić, A., Eds.;* Berlin/Heidelberg: Springer International Publishing.

Kerekes, G., Raschhofer, J., Harmening, C., Neuner, H. and Schwieger, V. (2022). Two-epoch TLS deformation analysis of a double curved wooden structure using approximating B-spline surfaces and fully-populated synthetic covariance matrices. In: *Proceedings of 5th Joint International Symposium on Deformation Monitoring (JISDM), 20-22 June 2022, Valencia, Spain*.

Kersten, T. P. and Lindstaedt, M. (2022). Geometric accuracy investigations of terrestrial laser scanner systems in the laboratory and in the field. *Applied Geomatics*. [online] doi:10.1007/s12518022004422.

Kisser, W. (2011). Ausgleichende Kugel im Gauß-Helmert-Modell | kisser.online. [online] Waldemar Kisser. Available at: *https://kisser.online/ausgleichung/ghm/kugel* [Accessed 13 Jun. 2022].

Klügel, T., Böer, A., Schüler, T. and Schwarz, W. (2019). Atmospheric data set from the Geodetic Observatory Wettzell during the CONT-17 VLBI campaign. *Earth System Science Data*, [online] 11,. doi:10.5194/essd-11-341-2019.

Koch, K.-R. (1990). *Bayesian Inference with Geodetic Applications*. Berlin, Heidelberg: Springer Verlag.

Koch, K.-R. (2008). Determining uncertainties of correlated measurements by Monte Carlo simulations applied to laserscanning. *Journal of Applied Geodesy*, 2(3).

Kokaly, R. F., Clark, R. N., Swayze, G. A., Livo, K. E., Hoefen, T. M., Pearson, N. C., Wise, R. A., Benzel, W. M., Lowers, H. A., Driscoll, R. L., and Klein, A. J. (2017) USGS Spectral Library Version 7: U.S. Geological Survey Data Series 1035. Available at: *https://doi.org/10.3133/ds1035*.

Kuhlmann, H. and Holst, C. (2018). Flächenhafte Abtastung mit Laserscanning-Messtechnik, flächenhafte Modellierung und aktuelle Entwicklungen im Bereich des terrestrischen Laserscanning. In: *Ingenieurgeodäsie-Handbuch der Geodäsie*. Berlin, Germany: Springer.

Kuhlmann, H., Schwieger, V., Wieser, A. and Niemeier, W. (2014). Engineering Geodesy - Definition and Core Competencies. *Journal of Applied Geodesy*, 8(4).

Kukkamäki T. J. (1938). *Über die nivellitische Refraktion*. Helsinki: Suomen Geodeettinen Laitos.

Kukko, A., Kaasalainen, S. and Litkey, P. (2008). Effect of incidence angle on laser scanner intensity and surface data. *Applied Optics*, 47(7). doi:10.1364/ao.47.000986.

Kuschnerus, M., Schröder, D. and Lindenbergh, R. (2021). Environmental Influences on the Stability of a Permanently Installed Laser Scanner. *The International Archives of the Photogrammetry, Remote Sensing and Spatial Information Sciences*, XLIII-B2-2021.

Lafarge, T. and Possolo, A. (2015). The NIST Uncertainty Machine. *NCSLI Measure*, 10(3). doi:10.1080/19315775.2015.11721732.

Lafarge, T. and Possolo, A. (2020). NIST Uncertainty Machine — User's Manual V. 1.4. [online] Available at: *https://uncertainty.nist.gov/NISTUncertaintyMachine-UserManual.pdf*.

Large, A. R. G. and Heritage, G. L. (2009). Laser Scanning – Evolution of the Discipline. In: *Laser Scanning for the Environmental Sciences* (eds G.L. Heritage and A.R.G. Large). Chichester, Uk: Wiley-Blackwell.

Leica Geosystems AG (2011). Datasheet HDS 7000 Laser Scanner. [online] Available at: *http://w3.leica-geosystems.com/downloads123/hds/hds/HDS7000/brochuresdatasheet/HDS7000_DAT_en.pdf*, [Accessed on 20.01.2020].

Lichti, D. D. and Skaloud, J. (2010). Registriation and Calibration. In: G. Vosselman and H.-G. Maas, eds., *Airborne and Terrestrial Laser Scanning*. Whittles Publishing - CRC Press.

Lichti, D. D. (2007). Error modelling, calibration and analysis of an AM–CW terrestrial laser scanner system. *ISPRS Journal of Photogrammetry and Remote Sensing*, 61(5).

Lichti, D. D. (2010). Terrestrial laser scanner self-calibration: Correlation sources and their mitigation. *ISPRS Journal of Photogrammetry and Remote Sensing*, 65(1).

Lichti, D. D. (2017). Ray-Tracing Method for Deriving Terrestrial Laser Scanner Systematic Errors. *Journal of Surveying Engineering*, 143(2).

Lichti, D. D. and Lampard, J. (2008). Reflectorless total station self-calibration. *Survey Review*, 40(309).

Linzer, F., Papčová, M. and Neuner, H. (2021). Quantification of systematic distance deviations for scanning total stations using robotic applications. In: A. Kopáčik, P. Kyrinovič, J. Erdélyi, R. Paar and A. Marendić, eds., *Contributions to International Conferences on Engineering Surveying, 8th INGEO International Conference on Engineering Surveying and 4th SIG Symposium on Engineering Geodesy*. Berlin/Heidelberg: Springer International Publishing.

Lipkowski, S. and Mettenleiter, M. (2019). Terrestrische Laserscanner – Im Fokus der Genauigkeit. In: *Proceedings of 184th DVW-Seminar, Terrestrisches Laserscanning 2019 Fulda, Germany*.

Long, N. Q., Buczek, M. M., Hien, L. P., Szlapińska, Sylwia A, Nam, B. X., Nghia, Nguyen Viet and Cuong, Cao Xuan (2018). Accuracy assessment of mine walls' surface models derived from terrestrial laser scanning. *International Journal of Coal Science & Technology*, [online] 5(3). doi:10.1007/s4078901802181.

Lynch, J. (2012). *Rough surface scattering theory - Lecture notes #12*, course 2.682 Acoustical Oceanography at Massachusetts Institute of Technology. Available at: https://ocw.mit.edu. [Accessed 12 Oct. 2021].

Martin, P. C. (1968). *Measurements and correlation functions*. New York: Gordon and Breach Science Publishers.

Matthias, H. J. (1992). *Bedeutung und Konstruktion von Kovarianzen in der Messtechnik*. PhD Thesis, ETH Zürich.

Mechelke, K., Kersten, T. and Lindstaedt, M. (2007). Comparative investigations into the accuracy behaviour of the new generation of terrestrial laser scanning systems. In: *Optical 3D Measurement Techniques VIII*.

Medić, T., Holst, C. and Kuhlmann, H. (2017). Towards System Calibration of Panoramic Laser Scanners from a Single Station. *Sensors*, 17(5).

Medić, T., Kuhlmann, H. and Holst, C. (2019). Sensitivity Analysis and Minimal Measurement Geometry for the Target-Based Calibration of High-End Panoramic Terrestrial Laser Scanners. *Remote Sensing*, 11(13).

Meier, S. and Keller, W. (1990). *Geostatistik - Einführung in die Theorie der Zufallsprozesse*. Berlin: Akademie-Verlag, pp. 171–172.

Meteomatics AG (2019). Meteomatics Whitepaper Drones. [online] Available at: *https://www.meteomatics.com/wp-content/uploads/2019/07/Meteomatics_Whitepaper_Drones.pdf*.

Metropolis, N. and Ulam, S. (1949). The Monte Carlo Method. *Journal of the American Statistical Association*, 44(247).

Mettenleiter, M., Härtl, F., Kresser, S. and Fröhlich, C. (2015). *Laserscanning phasenbasierte Lasermesstechnik für die hochpräzise und schnelle dreidimensionale Umgebungserfassung*. Munich, Germany: Süddeutscher Verlag onpact GmbH.

Möser, M., Hoffmeister, H., Müller, G., Staiger, R., Schlemmer, H. and Wanninger, L. (2012). *Handbuch Ingenieurgeodäsie - Grundlagen*. 4th ed. Heidelberg: Wichmann.

Mukupa, W., Roberts, G.W., Hancock, C.M. and Al-Manasir, K. (2016). A review of the use of terrestrial laser scanning application for change detection and deformation monitoring of structures. *Survey Review,* 49(353).

Mukupa, W., Roberts, G. W., Hancock, C. M. and Al-Manasir, K. (2017). Correction of Terrestrial LiDAR Data Using a Hybrid Model. In: *Proceedings of FIG Working week 2017, Helsinki, Finnland*.

Muralikrishnan, B. (2021). Performance evaluation of terrestrial laser scanners—a review. *Measurement Science and Technology*, [online] 32(7). Available at: https://tsapps.nist.gov/publication/get_pdf.cfm?pub_id=930840 [Accessed 22 Sep. 2021].

Muralikrishnan, B., Ferrucci, M., Sawyer, D., Gerner, G., Lee, V., Blackburn, C., Phillips, S., Petrov, P., Yakovlev, Y., Astrelin, A., Milligan, S. and Palmateer, J. (2015). Volumetric performance evaluation of a laser scanner based on geometric error model. *Precision Engineering*, 40.

National Institute of Standards and Technology (2016). *3D Laser Scanner Runoff Pushes New Standard Towards the Finish Line*. [online] Available at: https://www.nist.gov/news-events/news/2016/05/3d-laser-scanner-runoff-pushes-new-standard-towards-finish-line [Accessed 25 Jan. 2022].

Neitzel, F. (2006a). Gemeinsame Bestimmung von Ziel-, Kippachsenfehler und Exzentrizität der Zielachse am Beispiel des Laserscanners Zoller + Fröhlich Imager 5003. In: Luhmann and Müller, eds., *Photogrammetrie - Laserscanning - Optische 3D-Messtechnik, Beiträge der Oldenburger 3D-Tage 2006*. Heidelberg: Wichmann Verlag.

Neitzel, F. (2006b). Investigation of Axes Errors of Terrestrial Laser Scanners. In: Proceedings of 5th International Symposium Turkish-German Joint Geodetic Days, March 29th - 31st, 2006, Berlin, Germany.

Neitzel, F. (2006c). Untersuchung des Achssystems und des Taumelfehlers terrestrischer Laserscanner mit tachymetrischem Messprinzip. In: *Proceedings of 72nd DVW-Seminar, Terrestrisches Laserscanning 2006*. Fulda, Germany.

Neuner, H., Holst, C. and Kuhlmann, H. (2016). Overview on Current Modelling Strategies of Point Clouds for Deformation Analysis. *Allgemeine Vermessungsnachrichten*, 123(11-12).

Niemeier, W. (2008). *Ausgleichungsrechnung Statistische Auswertemethoden*. Berlin: Walter De Gruyter.

Nikolitsas, K. and Lambrou, E. (2019). A Methodology for Correcting Refraction in Vertical Angles for Precise Monitoring in Tunnels. In: *Proceedings of 4th Joint International Symposium on Deformation Monitoring (JISDM)*. Athens, Greece.

Ogundare, J.O. (2016). *Precision surveying: the principles and geomatics practice*. Hoboken: Wiley.

Peck, E. R. and Reeder, K. (1972). Dispersion of Air. *Journal of the Optical Society of America*, 62(8).

Pelzer, H. (1985). *Geodaetische Netze in Landes- und Ingenieurvermessung II : Vortraege des Kontaktstudiums Februar 1985 in Hannover*. Stuttgart: Konrad Wittwer.

Petrie, G. and Toth, C. H. (2018). Terrestrial Laser Scanners. In: *Topographic laser ranging and scanning: principles and processing.* CRC Press, Taylor & Francis Group.

Pfennigbauer, M. and Ullrich, A. (2010). Improving quality of laser scanning data acquisition through calibrated amplitude and pulse deviation measurement. In: M.D. Turner and G.W. Kamerman, eds., *International Society for Optics and Photonics*. [online] SPIE. doi.org/10.1117/12.849641.

Piegl, L. and Tiller, W. (1997). *The NURBS Book*. 2nd ed. Berlin/Heidelberg, Germany: Monographs in Visual Communication; Springer.

Pollinger, F., Hieta, T., Vainio, M., Doloca, N.R., Abou-Zeid, A., Meiners-Hagen, K. and Merimaa, M. (2012). Effective humidity in length measurements: comparison of three approaches. *Measurement Science and Technology*, [online] 23. doi:10.1088/0957-0233/23/2/025503.

Possler, H. P. (2009). *Oberflächenrauheit von Baustoffen*. Diploma Thesis. Available at: https://resolver.obvsg.at/urn:nbn:at:at-ubtuw:1-27302 [Accessed 13 Oct. 2021].

Possolo, A. and Elster, C. (2014). Evaluating the uncertainty of input quantities in measurement models. *Metrologia*, [online] 51(3). doi:10.1088/0026-1394/51/3/339.

Possolo, A. and Iyer, H. (2017). Invited Article: Concepts and tools for the evaluation of measurement uncertainty. *The Review of scientific instruments*, 88(1).

Precision Laser Scanning LLC (2022). POLYGON MIRRORS. [online] Courtesy to George Helser. Available at: *https://precisionlaserscanning.com/polygon-mirrors/*.

Rabinovich, S.G. (2018). *Evaluating measurement accuracy a practical approach*. Cham Springer.

Rachakonda, P., Muralikrishnan, B., Shakarji, C., Lee, V. and Sawyer, D. (2015). Evaluation of the Range Performance of Laser Scanners Using Non-Planar Targets. In: *Proceedings of 30th ASPE Annual Meeting, Austin, TX*.

Raschhofer, J., Kerekes, G., Harmening, C., Neuner, H. and Schwieger, V. (2021). Estimating Control Points for B-Spline Surfaces Using Fully Populated Synthetic Variance–Covariance Matrices for TLS Point Clouds. *Remote Sensing*, 13(16).

Razavi, S., Jakeman, A., Saltelli, A., Prieur, C., Iooss, B., Borgonovo, E., Plischke, E., Lo Piano, S., Iwanaga, T., Becker, W., Tarantola, S., Guillaume, J. H. A., Jakeman, J., Gupta, H., Melillo, N., Rabitti, G., Chabridon, V., Duan, Q., Sun, X. and Smith, S. (2021). The Future of Sensitivity Analysis: An essential discipline for systems modeling and policy support. *Environmental Modelling & Software*, [online] 137. doi:10.1016/j.envsoft.2020.104954.

Rees, W. G. (2013). *Physical principles of remote sensing*. Cambridge: Cambridge University Press.

Reiterer, A. (2012). Modeling Atmospheric Refraction Influences by Optical Turbulances Using an Image-Assisted Total Station. *Zeitschrift für Vermessungswesen*, 3.

Reshetyuk, Y. (2009). *Self-Calibration and Direct Georeferencing in Terrestrial Laser Scanning*. PhD Thesis. Royal Institute of Technology (KTH) Stockholm.

Riegl Laser Measurement Systems GmbH (2015a). *Datasheet of Riegl VZ-2000*.

Riegl Laser Measurement Systems GmbH (2015b). *RiSCAN Pro Software Help Documentation*.

Riegl Laser Measurement Systems GmbH (2022). Datasheet Riegl VZ400i. [online] Available at: *http://www.riegl.com/uploads/tx_pxpriegldownloads/RIEGL_VZ-400i_Datasheet_2022-09-27.pdf* [Accessed 4 Oct. 2022].

Rietdorf, A., Gielsdorf, F. and Gruendig, L. (2004). A Concept for the Calibration of Terrestrial Laser Scanners. In: *INGEO 2004 and FIG Regional Central and Eastern European Conference on Engineering Surveying Bratislava, Slovakia*.

Rinner, K. and Benz, F. (1966). *Handbuch der Vermessungskunde. Bd. VI : Die Entfernungsmessung mit Elektro-magnetischen Wellen und Ihre Geodätische Anwendung*. 10th ed. J.B. Metzlersche Verlagsbuchhandlung.

Rotach, M. W. and Calanca, P. (2003). Microclimate. In: J.R. Holton, ed., *Encyclopedia of Atmospheric Sciences*. Academic Press, pp.1301–1307.

Rüeger, J. M. (1990). *Electronic Distance Measurement: An Introduction*. 3rd ed. Berlin: Springer-Verlag.

Saltelli, A., Chan, K. and Scott, E.M. (2008). *Sensitivity analysis*. Chichester; New York: John Wiley & Sons, LTD.

Scaioni, M., Marsella, M., Crosetto, M., Tornatore, V. and Wang, J. (2018). Geodetic and Remote-Sensing Sensors for Dam Deformation Monitoring. *Sensors*, 18(11).

Schäfer. T. (2017). Berührungslose und flächenhafte Deformationsmessungen an Betonöberflächen unter Berücksichtigung der Interaktion zwischen Laserstrahl und Oberfläche. PhD Thesis, Technical University Munich. DGK Reihe C Heft Nr. 805.

Schmitz, B., Kuhlmann, H. and Holst, C. (2020). Investigating the resolution capability of terrestrial laser scanners and its impact on the effective number of measurements. *ISPRS Journal of Photogrammetry and Remote Sensing*, 159.

Schmitz, B., Kuhlmann, H. and Holst, C. (2021). Towards the empirical determination of correlations in terrestrial laser scanner range observations and the comparison of the correlation structure of different scanners. *ISPRS Journal of Photogrammetry and Remote Sensing*, [online] 182. doi:https://doi.org/10.1016/j.isprsjprs.2021.10.012.

Schneider, D. (2009). Calibration of a Riegl LMS-Z420i Based on a Multi-Station Adjustment and a Geometric Model with Additional Parameters. In: *Proceedings of Laser Scanning 2009, IAPRS, Vol. XXXVIII, Part 3/W8*.

Schönwiese, C.-D. (2013). *Praktische Statistik für Meteorologen und Geowissenschaftler*. 5th ed. Stuttgart: Geb. Borntraeger.

Schröder, D. and Nowacki, A. (2021). Die Atmosphäre als restriktiver Einfluss auf Messergebnisse eines Long Range Laserscanners. In: T. Weinold, ed., *Proceedings of 21. Internationale Geodätische Woche Obergurgl 2021*. Wichmann Verlag.

Schulz, R.-R. (2008). Roughness and anti-slip properties of concrete surfaces. *BTF International*, 74(9).

Schweitzer, J. and Schwieger, V. (2011). Modeling of quality for engineering geodesy processes in civil engineering. *Journal of Applied Geodesy*, 5(1). doi:10.1515/jag.2011.002.

Schwieger, V. (1999). *Ein Elementarfehlermodell für GPS-Überwachungsmessungen: Konstruktion und Bedeutung interepochaler Korrelationen*. PhD Thesis. Gottfried Wilhelm Leibniz University of Hannover. Schriftenreihe der Fachrichtung Vermessungswesen der Universität Hannover.

Shackelford, J. F. (2016). *Introduction to materials science for engineers*. Boston U.A.: Pearson.

Shan, J. and Toth, C. K. (2018). *Topographic laser ranging and scanning: principles and processing*. CRC Press, Taylor & Francis Group.

Sheng, Y. (2008). Quantifying the Size of a Lidar Footprint: A Set of Generalized Equations. *IEEE Geoscience and Remote Sensing Letters*, 5(3). doi:10.1109/LGRS.2008.916978.

Slătineanu, L., Potârniche, S., Coteaţă, M., Grigoraş, I., Gherman, L. and Negoescu, F. (2011). Surface Roughness at Aluminium Parts Sand Blasting. In: *Proceedings in Manufacturing Systems*, 6, (2/2011).

Soudarissanane, S.S. (2016). *The Geometry of Terrestrial Laser Scanning-identification of Errors, Modeling and Mitigation of Scanning Geometry*. PhD Thesis, Technical University Delft.

Spring, A. P. (2020a). A History of Laser Scanning, Part 1: Space and Defense Applications. *Photogrammetric Engineering & Remote Sensing*, 86(7).

Spring, A. P. (2020b). History of Laser Scanning, Part 2: The Later Phase of Industrial and Heritage Applications. *Photogrammetric Engineering & Remote Sensing*, 86(8).

Stahlberg, C. (1997). Eine vektorielle Darstellung des Einflusses von Ziel- und Kippachsenfehler auf die Winkelmessung. *ZfV - Zeitschrift für Vermessungswesen*, 5/1997.

Staiger, R. (2003). Terrestrial Laser Scanning Technology-Systems and Applications. In: *Proceedings of the 2nd FIG Regional Conference*. 2nd FIG Regional Conference, Marrakech, Morocco.

Stutz, G. E. (2012). Polygonal Scanners: Components, Performance, and Design. In: G.F. Marshall and G.E. Stutz, eds., *Handbook of Optical and Laser Scanning*. CRC Press.

Suchocki, C. (2020). Comparison of Time-of-Flight and Phase-Shift TLS Intensity Data for the Diagnostics Measurements of Buildings. *Materials*, 13(2).

Teunissen, G., S. Zaminpardaz and C. C. J. M. Tiberius (2020). On the integrity of deformation monitoring. *Geomatics, Natural Hazards and Risk*, [online] 11. doi:10.1080/19475705.2020.1716085.

Thompson, E. H. (1969). *Introduction to the algebra of matrices with some applications.* London: Adam Hilger.

Uren, J. and Price, B. (2010). *Surveying for engineers*. 5th ed. New York: Palgrave Macmillan.

Ursell T. (2021). Matlab Function autocorr2d. MATLAB Central File Exchange. Avialbe at: *https://www.mathworks.com/matlabcentral/fileexchange/67348-autocorr2d* [Accessed 21 Oct. 2021].

Vaníček, P. and Krakiwsky, E.J. (1982). *Geodesy: The concepts*. Amsterdam: North-Holland Publishing Company.

Vitosytė, J., Ukvalbergienė, K. and Keturakis, G. (2015). Wood surface roughness: an impact of wood species, grain direction and grit size. *Materials Science*, 21(2).

Voegtle, T. and Wakaluk, S. (2009). Effects on the measurements of the terrestrial laser scanner HDS 6000 (Leica) caused by different object materials. *IAPRS*, XXXVIII (Part 3/W8).

Voordendag, A. B., Goger, B., Klug, C., Prinz, R., Rutzinger, M. and Kaser, G. (2021). Automated and Permanent Long-Range Terrestrial Laser Scanning in a High Mountain Environment: Setup and First Results. *ISPRS Annals of the Photogrammetry, Remote Sensing and Spatial Information Sciences*, V-2-2021.

Vosselman, G. and Maas, H.G. (2010). *Airborne and terrestrial laser scanning*. Dunbeath, Scotland, UK: Crc Press.

Wang, L., Muralikrishnan, B., Lee, V., Rachakonda, P., Sawyer, D. and Gleason, J. (2020). A first realization of ASTM E3125-17 test procedures for laser scanner performance evaluation. *Measurement*, 153.

Wang, L., Muralikrishnan, B., Rachakonda, P. and Sawyer, D. (2017). Determining geometric error model parameters of a terrestrial laser scanner through two-face, length-consistency, and network methods. *Measurement Science and Technology*, 28(6).

Weichel, H. (1990). *Laser beam propagation in the atmosphere*. Bellingham, Washington: SPIE-The international Society for Optical Engineering.

Welsch, W. M. and Heunecke, O. (2001). *Models and Terminology for the Analysis of Geodetic Monitoring Observations, Official Report of the Ad-Hoc Committee of FIG Working Group 6.1*. [online] The International Federation of Surveyors (FIG). Available at: https://www.fig.net/resources/publications/figpub/pub25/figpub25.asp.

Wieser, A., Balangé, L., Bauer, P., Gehrmann, T., Hartmann, J., Holst, C., Jost, B., Kuhlmann, H., Lienhart, W., Maboudi, M., Mawas, K., Medić, T., Paffenholz, J., Pollinger, F., Rafeld, E., Schill, F. and Schwieger, V. (2022). Erfahrungen aus einem koordinierten Vergleich aktueller Scanner. In: *Proceedings of 214th DVW-Seminar Terrestrisches Laserscanning 2022 Fulda, Germany*.

Wieser, A., Kuhlmann, H., Schwieger, V. and Niemeier, W. (2018). Ingenieurgeodäsie - eine Einführung. In: *Ingenieurgeodäsie-Handbuch der Geodäsie*. Berlin, Germany: Springer.

Wieser, A., Pfaffenholz, J.-A. and Neumann, I. (2019). Sensoren, Features und Physik - Zum aktuellen Stand der Entwicklung bei Laserscannern. In: *Proceedings of 184th DVW-Seminar, Terrestrisches Laserscanning 2019 Fulda, Germany*.

Wolfe, W. L. and Zissis, G. J. (1985). *The infrared handbook*. Arlington, Va: Environmental Research Institute Of Michigan. Infrared Information and Analysis Center Office Of Naval Research, Dept. Of The Navy.

Wujnaz, D. (2016). *Terrestrial laser scanning for geodetic deformation monitoring*. PhD Thesis, Technical University of Berlin, Available at: 10.14279/depositonce-5136.

Wujanz, D., Burger, M., Mettenleiter, M. and Neitzel, F. (2017). An intensity-based stochastic model for terrestrial laser scanners. *ISPRS Journal of Photogrammetry and Remote Sensing*, 125.

Wunderlich, T. H., Wasmeier, P., Ohlmann-Lauber, J., Schäfer, T. H. and Reidl, F. (2013). *Objective Specifications of Terrestrial Laserscanners—A Contribution of the Geodetic Laboratory at the Technische Universität München*. Blaue Reihe des Lehrstuhls für Geodäsie, Vol. 21, Technical Unviersity of Munich.

Wunderlich, T., Niemeier, W., Wujanz, D., Holst, C., Neitzel, F. and Kuhlmann, H. (2016). Areal Deformation Analysis from TLS Point Clouds – the Challenge. *Allgemeine Vermessungsnachrichten*, 123(11-12).

Yang, Y., Balangé, L., Gericke, O., Schmeer, D., Zhang, L., Sobek, W. and Schwieger, V. (2021). Monitoring of the production process of graded concrete component using terrestrial laser scanning. *Remote Sensing*, 13. doi:10.3390/rs13091622.

Yoshino, M. M. (1987). *Local climatology*. *Encyclopedia of Earth Science*, Springer, Boston, MA.

Zámečníková, M. and Neuner, B. (2017). Untersuchung des gemeinsamen Einflusses des Auftreffwinkels und der Oberflächenrauheit auf die reflektorlose Distanzmessung beim Scanning. In: W. Lienhart, ed., *Proceedings of Ingenieurvermessung 2017*.

Zámečníková, M., Wieser, A., Woschitz, H. and Ressl, C. (2014). Influence of surface reflectivity on reflectorless electronic distance measurement and terrestrial laser scanning. *Journal of Applied Geodesy*, 8(4).

Zhao, X. (2019). *Terrestrial Laser Scanning Data Analysis for Deformation Monitoring*. PhD Thesis, Gottfried Wilhelm Leibniz University of Hannover. Available at: https://publikationen.badw.de/de/046282705.

Zhao, X., Kermarrec, G., Kargoll, B., Alkhatib, H. and Neumann, I. (2019). Influence of the simplified stochastic model of TLS measurements on geometry-based deformation analysis. *Journal of Applied Geodesy*, 13(3).

Zoller+Fröhlich GmbH (2021). Z+F IMAGER 5016 Datasheet. [online] Available at: *https://www.zofre.de*.

Acknowledgments

This research was conducted within a DFG (German Research Foundation) Project, under the project number SCHW 838/7-3. The title is IMKAD II "Integrated space-time modeling based on correlated measurements for the determination of survey configurations and the description of deformation processes". The other funding party of IMKAD II (I3869) was the Austrian Science Fund (FWF). The author expresses his gratitude to the DFG and the FWF for funding this project, likewise to all contributing scientists.

The author cordially thanks Illwerke vkw AG for supporting the measurement campaigns at the Kops Lake in 2019 and 2020.

Acknowledgment also goes to the Society for Calibration of Geodetic Devices (SCGD) and the Institute of Engineering Geodesy (IIGS) for providing calibration data of the Leica HDS 7000. Data were gathered within the COLLECTOR project.

The author cordially thanks the "Landesamt für Vermessung und Geoinformation" Land Vorarlberg, Austria for providing a digital terrain model of the area surrounding the Kops lake.

Finally, the author also thanks Prof. Dr. -Ing. R. Schulze for making data available for the roughness analysis (sec. 5.4.2).

Appendix 1 – Facts about polygon laser scanners

In section 3.5 the scanning mechanism of hybrid scanners was shortly described. In order to highlight the complex nature of scanners that use rotating polygon mirrors (cf. fig. 3.9), a few examples are given based on the recommendations from Stutz (2012) for manufacturing such a scanner.

The term "polygonal scanner" is often encountered and refers to scanners that incorporate an optical deflection element with three or more reflective facets. Such systems are commonly used for applications in inspection, laser printing, medical imaging, laser marking, displays, and ranging. They excel in applications that require unidirectional scans, high scan rates, large apertures, large scan angles, or high throughputs. There are many types of mirrors, but four categories cover most of them. These are only enumerated here for the sake of denomination: 1. Prismatic polygonal scanning mirrors, 2. Pyramidal polygonal scanning mirrors, 3. Monogons, 4. Irregular polygonal scanning mirrors. (Stutz, 2012). Only the first type is of interest in this section. A regular prismatic polygon (fig. A1) is defined as having a number of plane mirror facets that are parallel to, equidistant from, and face away from a central rotational axis (Stutz, 2012).

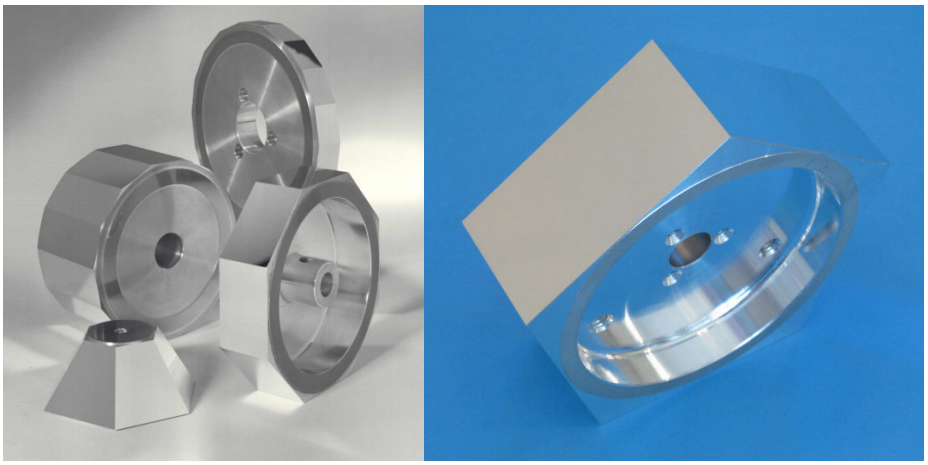

Figure A1. Left: Example of regular prismatic polygon mirrors and pyramidal polygonal scanning mirrors (left corner) with different number of facets. Right: pentagon regular prismatic polygon mirrors (Courtesy: Precision Laser Scanning LLC).

Additional to the mentioned reference, more exotic types of mirrors are presented, among others, in Beiser (1992). In his Laser Scanning Notebook, Beiser (1992) gives precise indications about how such a scanner should be designed (e.g. number of facets, the position of laser source), especially in his eighth and ninth article. If these dimensions would be available for the studied TLS, a huge step would be made toward defining a calibration model.

Polygon mirrors are also subject to manufacturing imperfections and there are specific indications that need to be made for each mirror in form of mechanical tolerances. These also lead to optical effects in the scanning process. All of them are enumerated for information purposes. By definition, the practical set of imperfections for polygon mirrors are (Stutz, 2012):

1. Facet-to-facet angle variance,
2. Pyramidal error,

3. Facet-to-axis variance (total and adjacent face),
4. Facet radius,
5. Facet surface figure (facet flatness),
6. Surface quality and scatter.

Although these mechanical terms and their definitions are very interesting, they are not detailed, because the TLS end-user does not have access to these specifications. They are rather discussion terms between the TLS manufacturer and the polygon mirror manufacturer. For this reason, details about the imperfections of polygon mirrors are not discussed further. In addition to the mirror, a functional scanner requires a bearing system and a drive mechanism. Once all three components are assembled, the system can be referred to as a polygonal scanner. (Stutz, 2012). These are additional sources of error caused by the bearing and drive system:

1. Dynamic track,
2. Jitter,
3. Speed stability,
4. Balance,
5. Perpendicularity,
6. Time to synchronize.

The interested reader may consult the aforementioned source for more details. Duma (2017) also provides evidence about such scanning systems with polygon mirrors, but not for TLS applications. Other sources that treat hybrid TLS scanners are Fröhlich (1996) and González-Aguilera et al. (2011).

Appendix 2 – Supplementary results

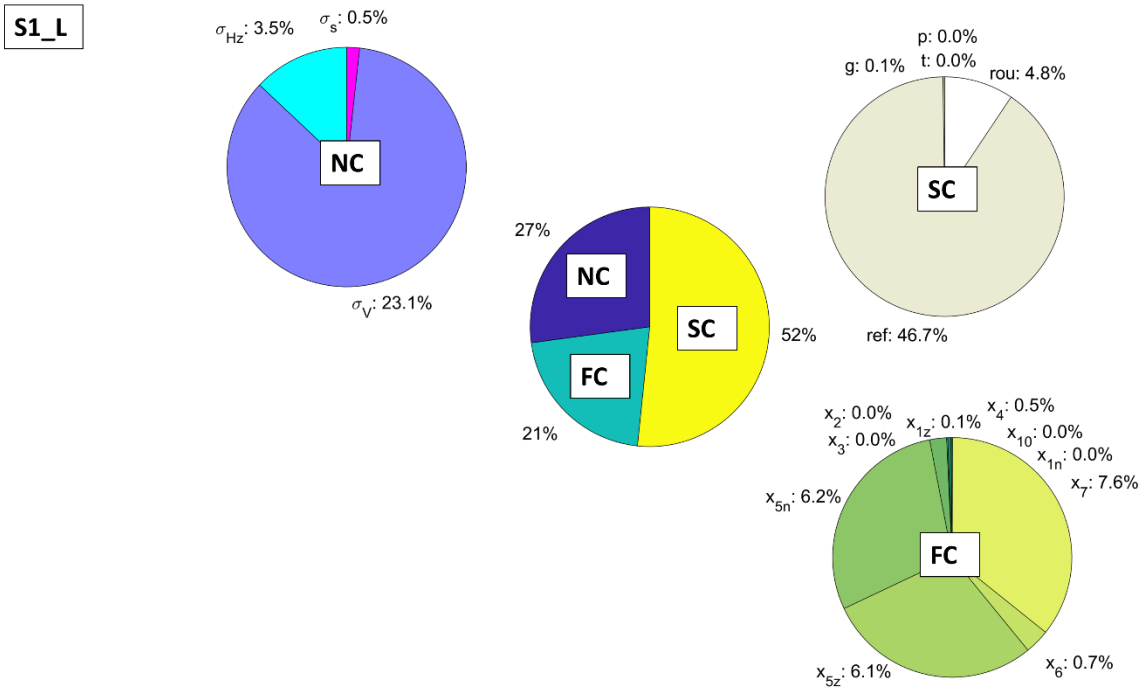

Figure A2.1. Relative contribution of elementary error groups and individual elementary errors on the SVCM traces for S1_L (panoramic scanner).

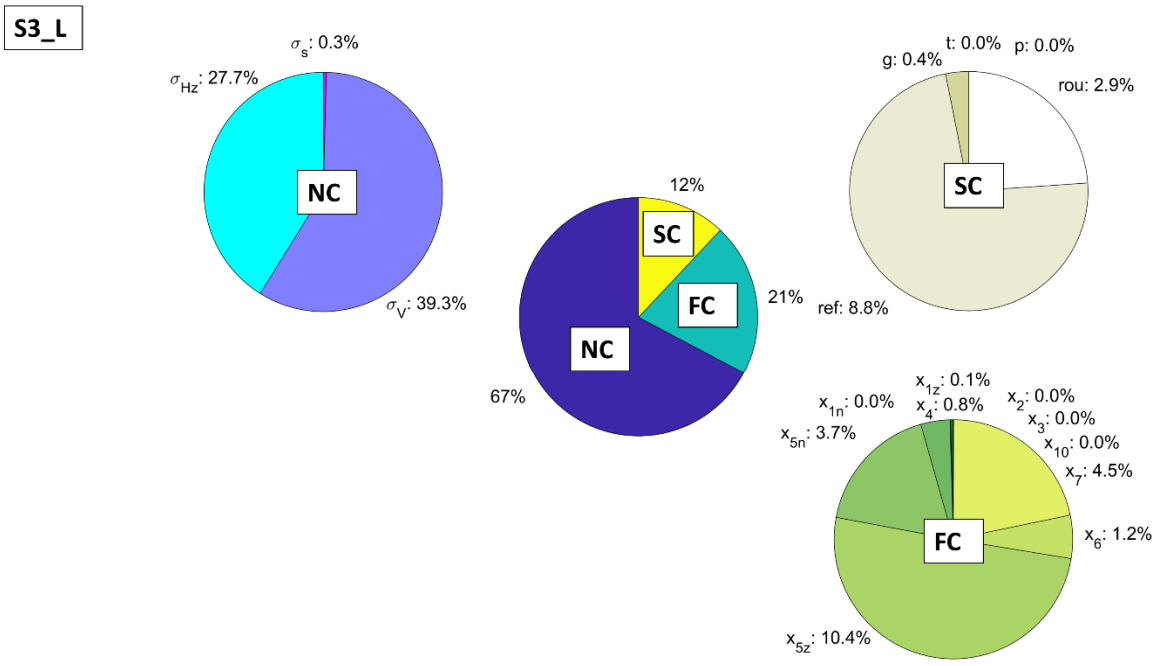

Figure A2.2. Relative contribution of elementary error groups and individual elementary errors on the SVCM traces for S3_L (panoramic scanner).

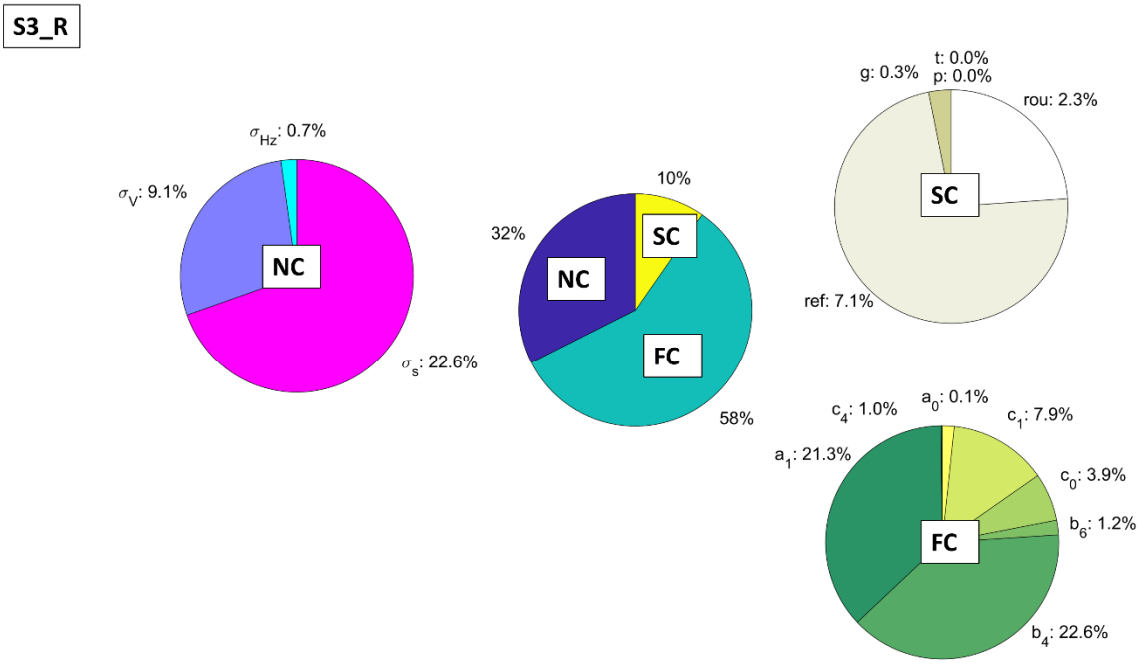

Figure A2.3. Relative contribution of elementary error groups and individual elementary errors on the SVCM traces for S3_R (hybrid scanner).

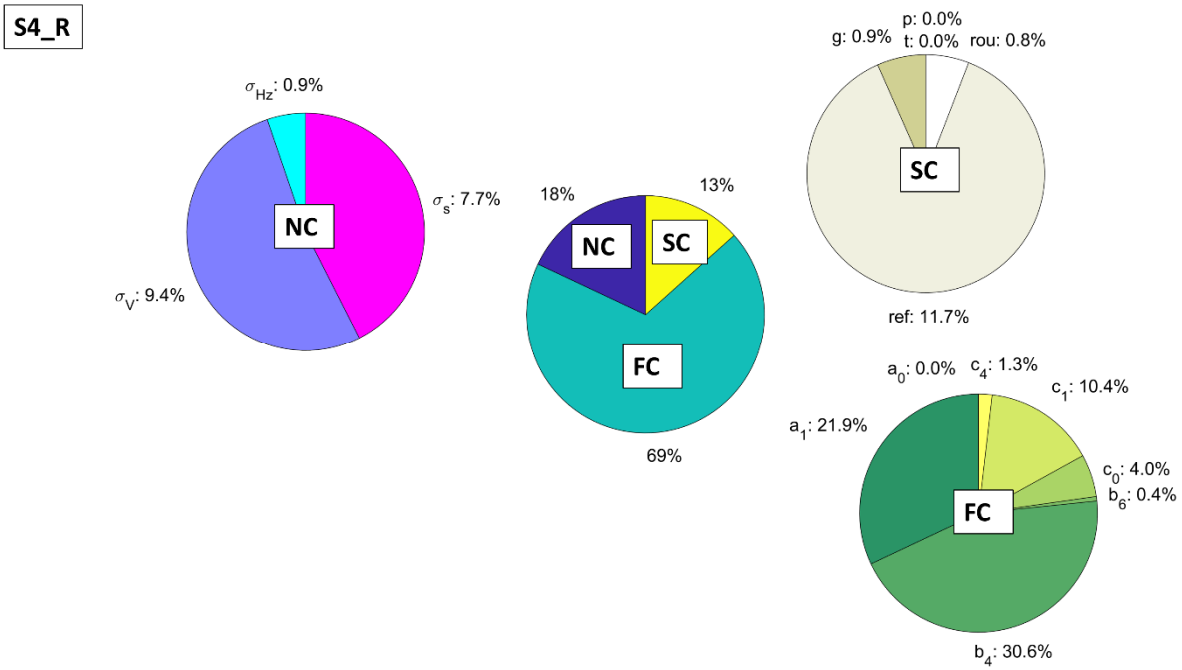

Figure A2.4. Relative contribution of elementary error groups and individual elementary errors on the SVCM traces for S4_R (hybrid scanner).

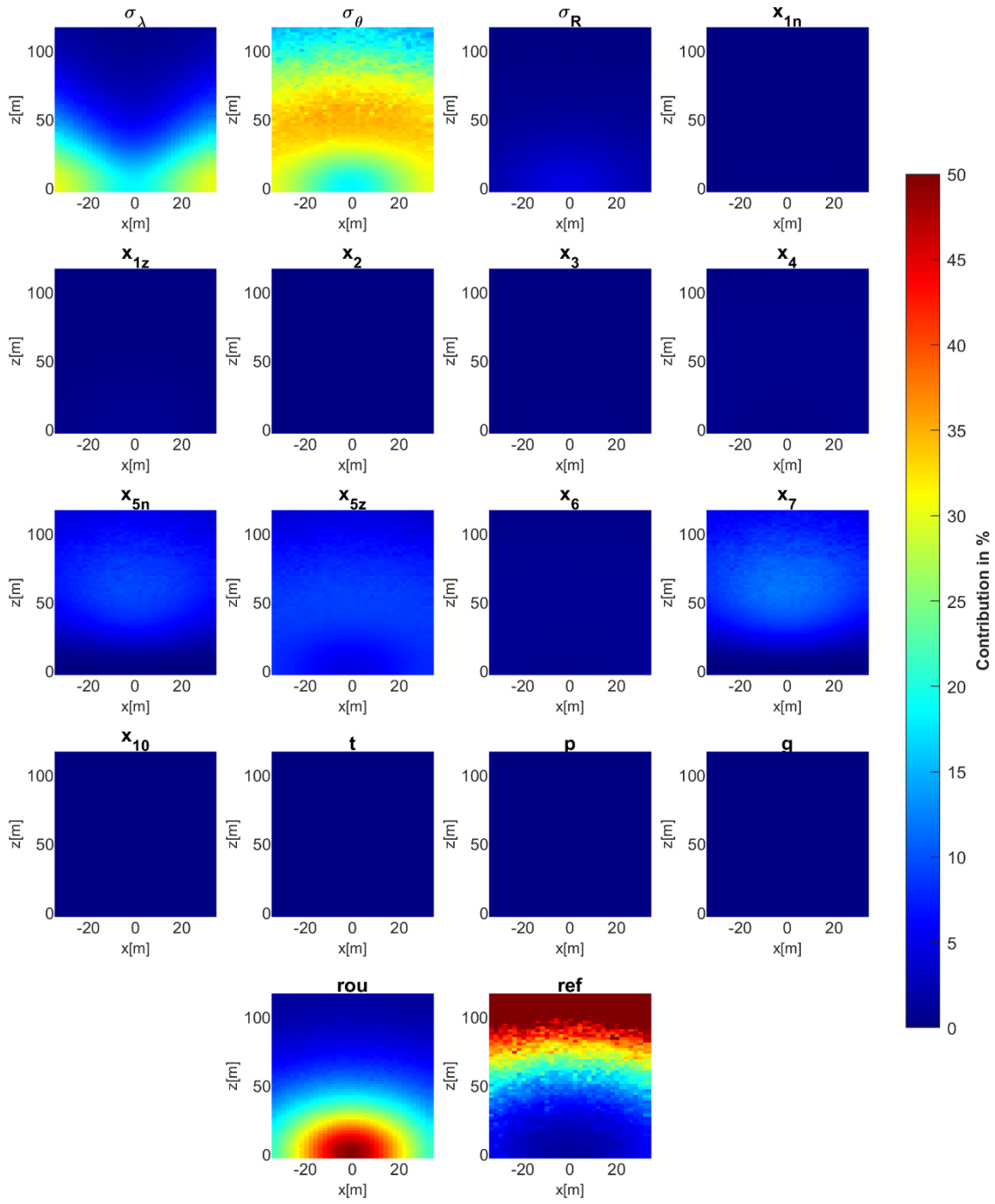

Figure A2.5. Relative contribution of individual elementary errors on the error of position from S1_L (panoramic scanner).

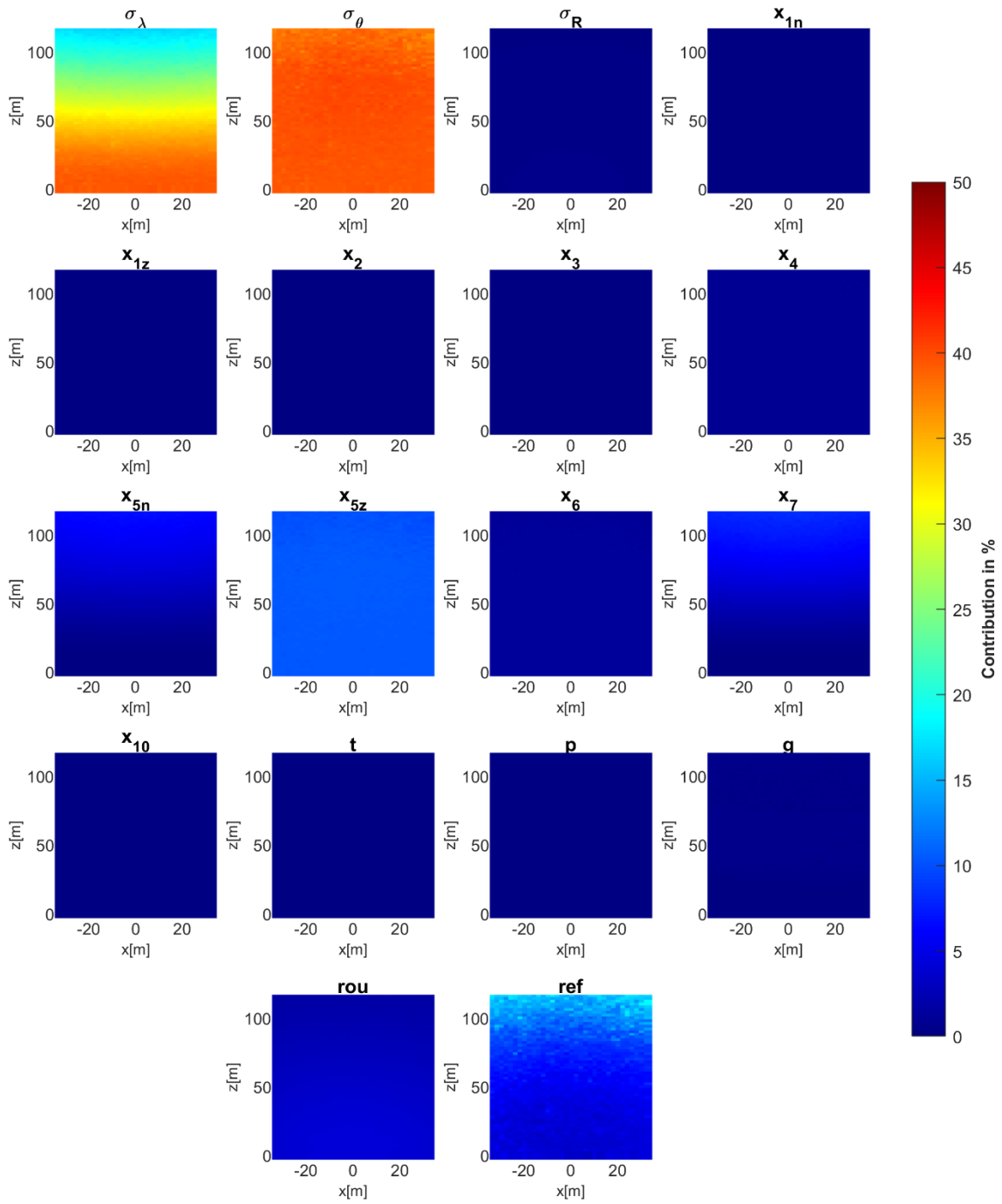

Figure A2.6. Relative contribution of individual elementary errors on the error of position from S3_L (panoramic scanner).

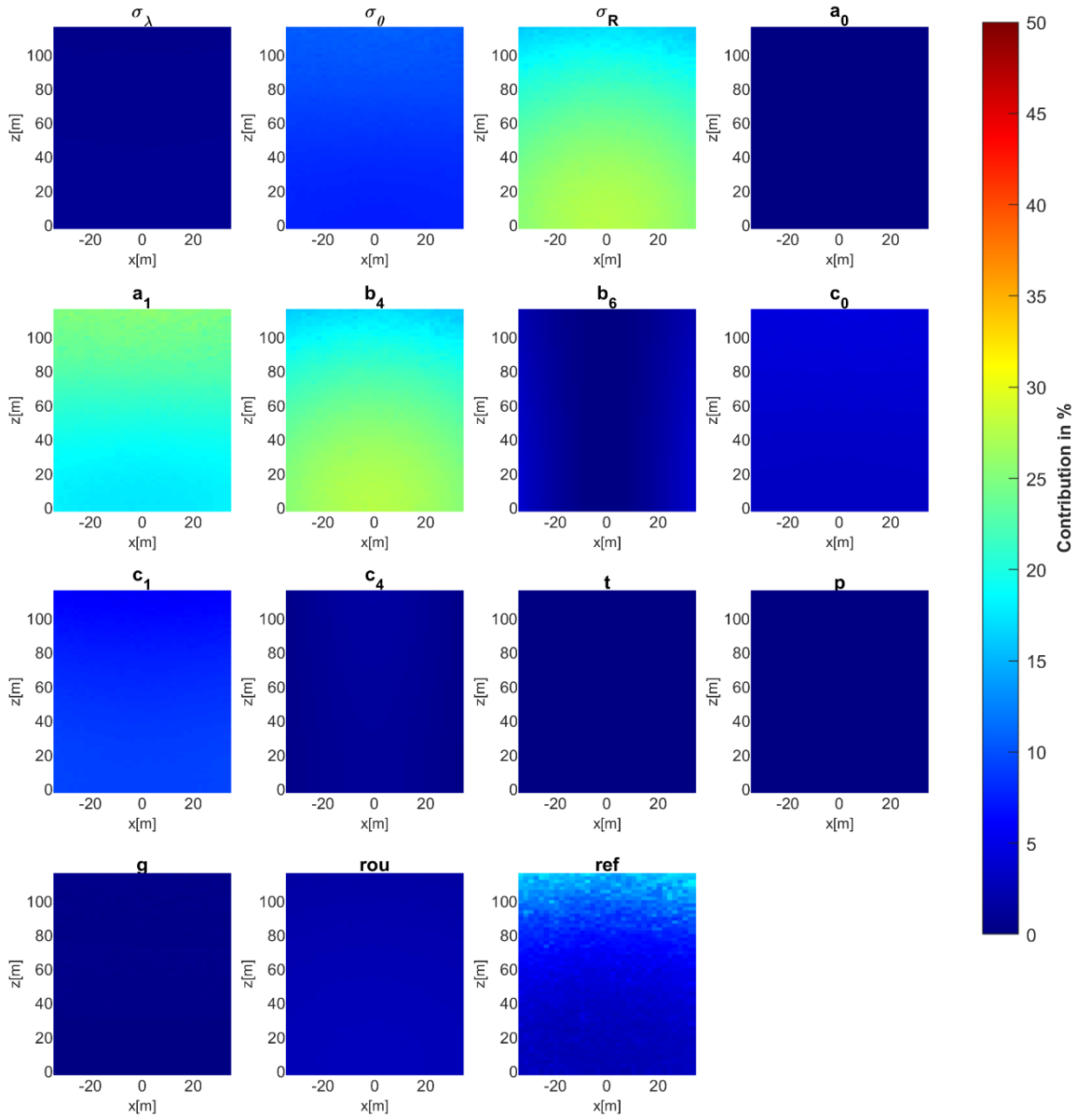

Figure A2.7. Relative contribution of individual elementary errors on the error of position from S3_L (hybrid scanner).

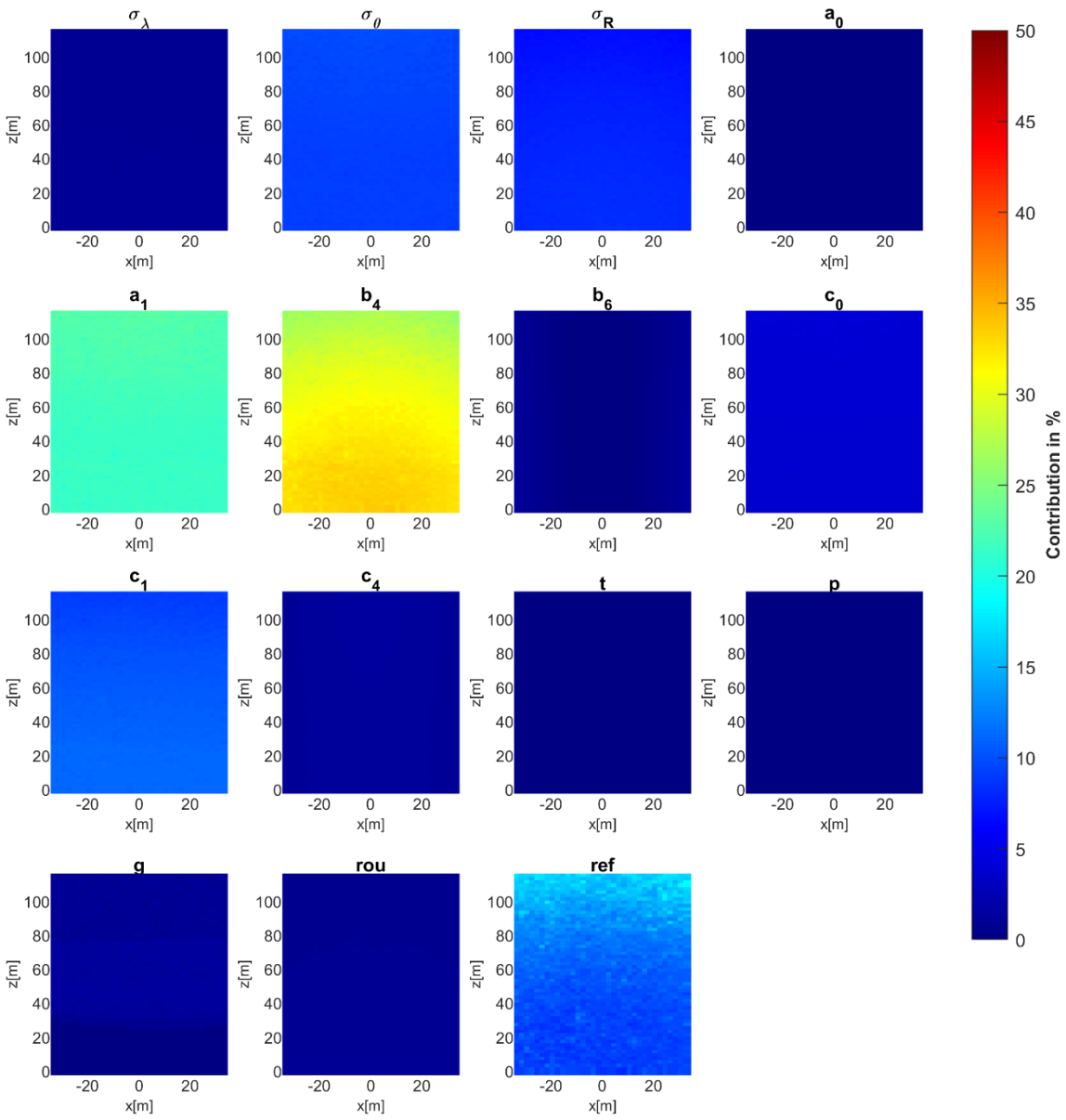

Figure A2.8. Relative contribution of individual elementary errors on the error of position from S3_L (hybrid scanner).

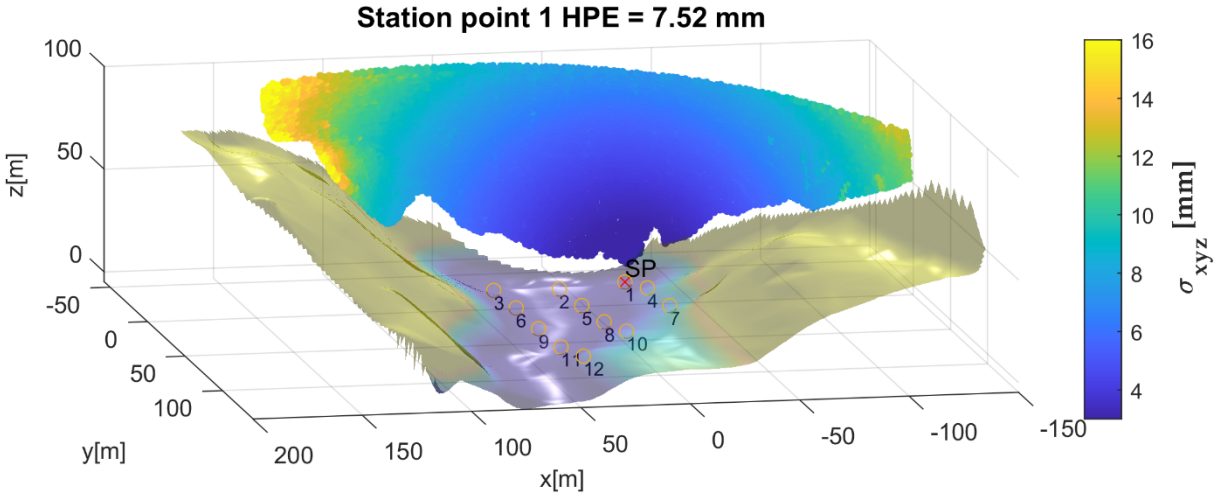

Figure A2.9. Analysis of candidate point 1 – average distance from object 95 m.

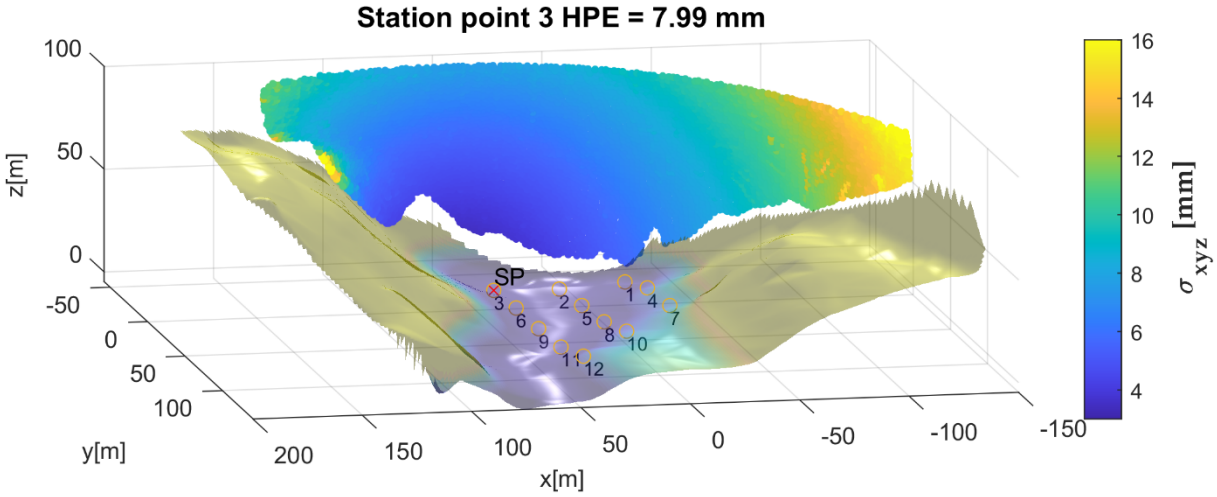

Figure A2.10. Analysis of candidate point 3 – average distance from object 103 m.

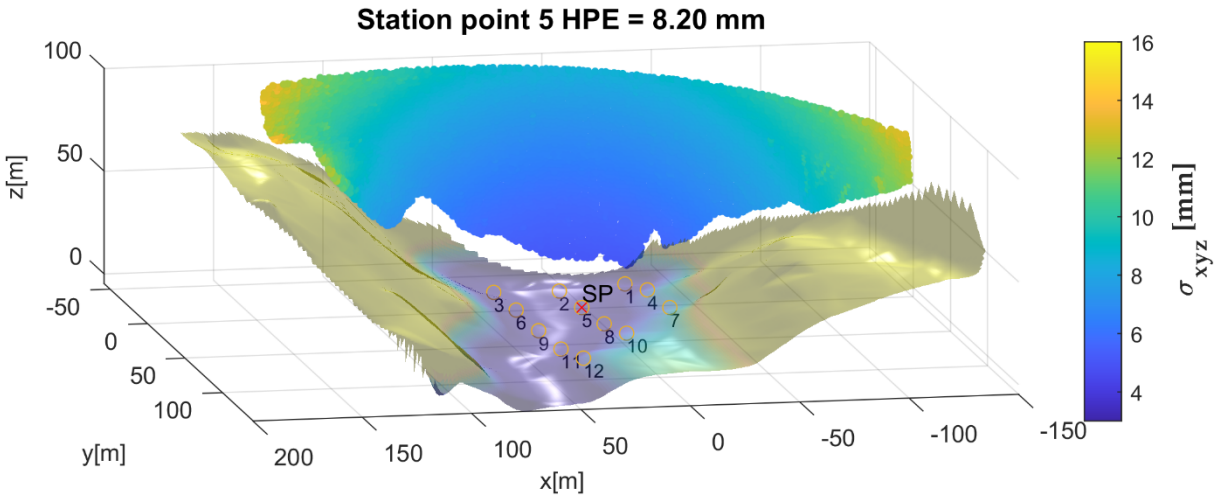

Figure A2.11. Analysis of candidate point 5 – average distance from object 107 m.

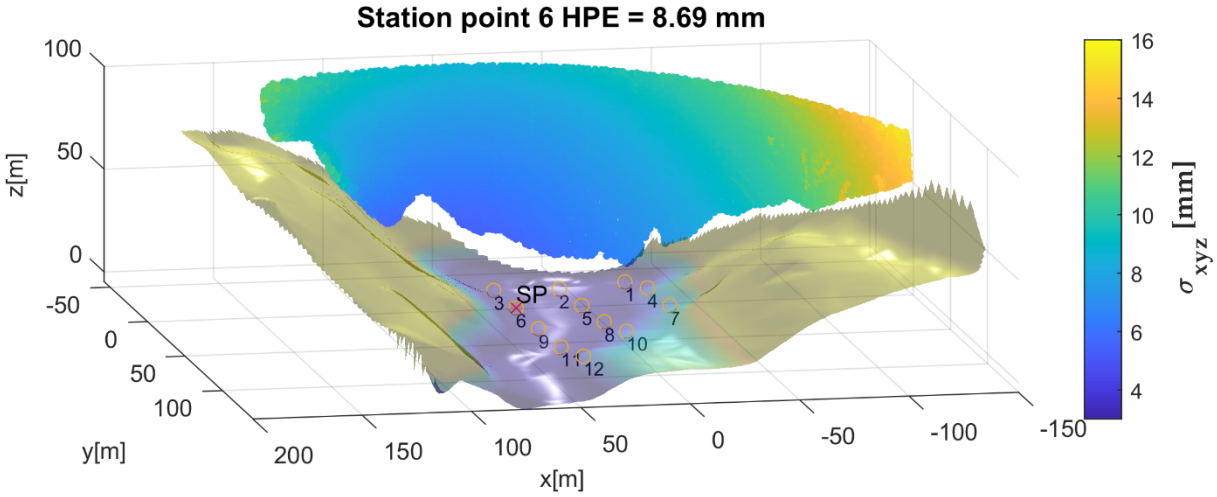

Figure A2.12. Analysis of candidate point 6 – average distance from object 114 m.

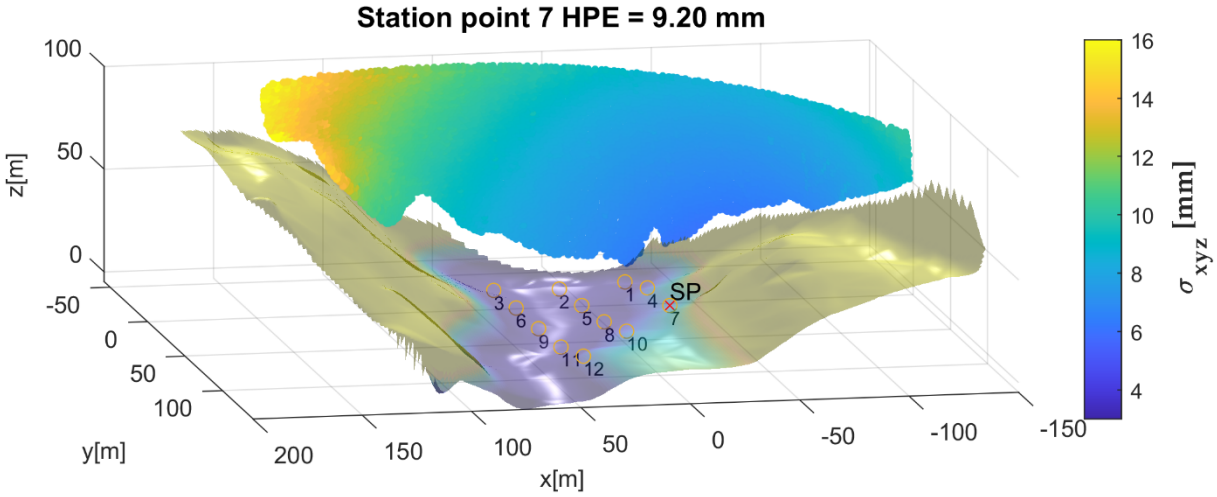

Figure A2.13. Analysis of candidate point 7 – average distance from object 120 m.

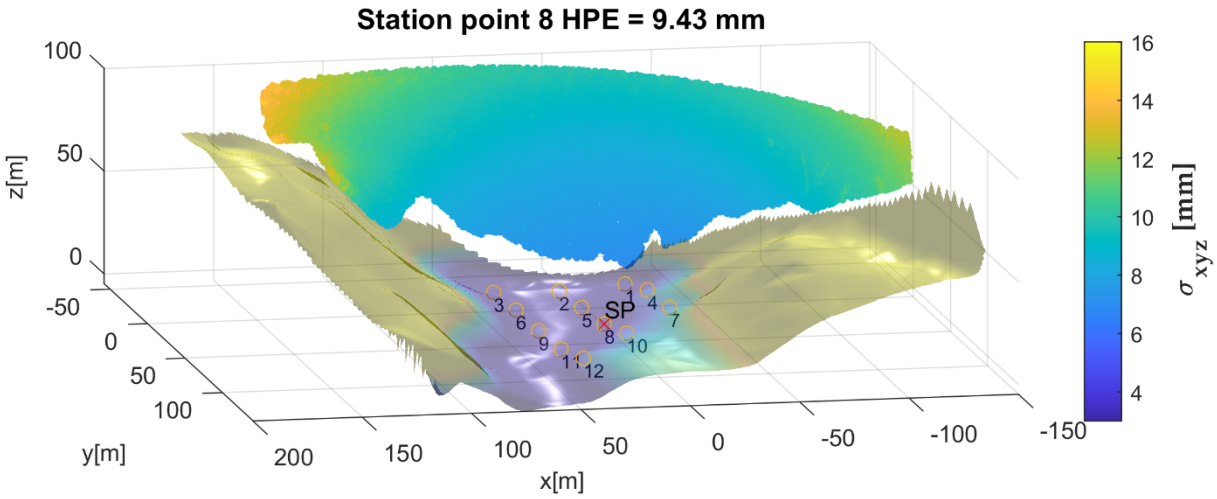

Figure A2.14. Analysis of candidate point 8 – average distance from object 124 m.

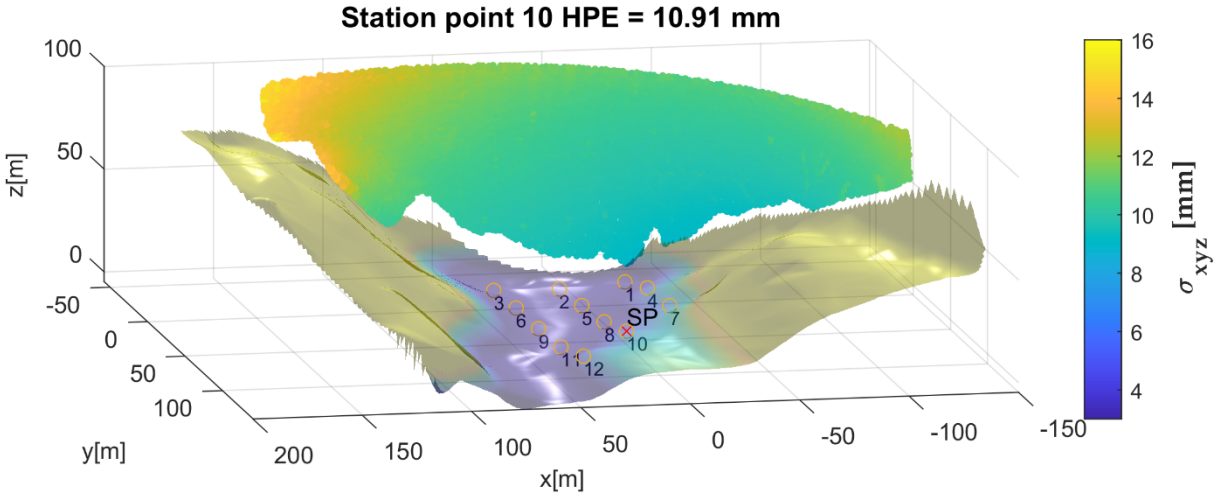

Figure A2.15. Analysis of candidate point 10 – average distance from object 143 m.

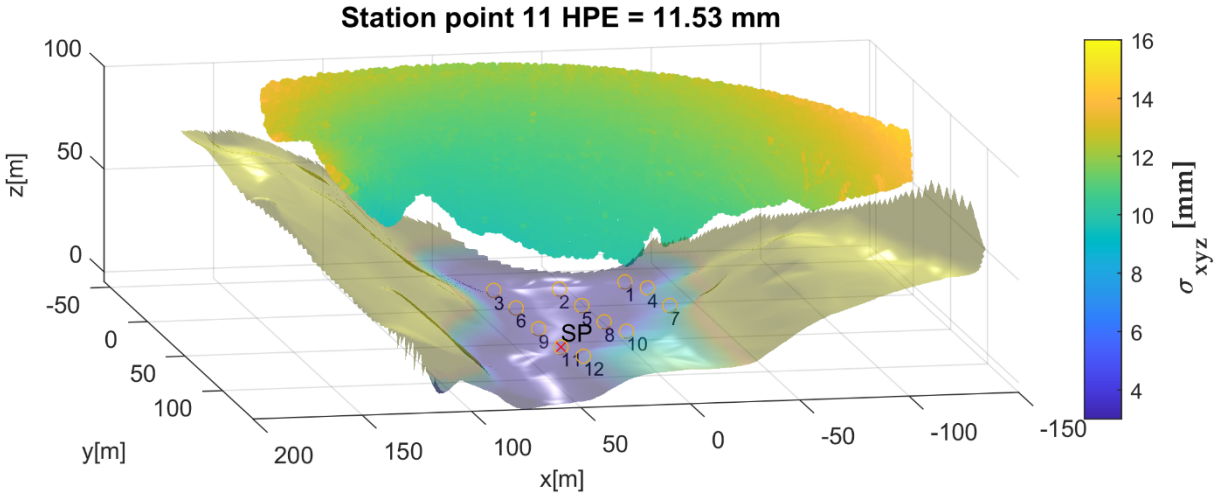

Figure A2.16. Analysis of candidate point 11 – average distance from object 152 m.

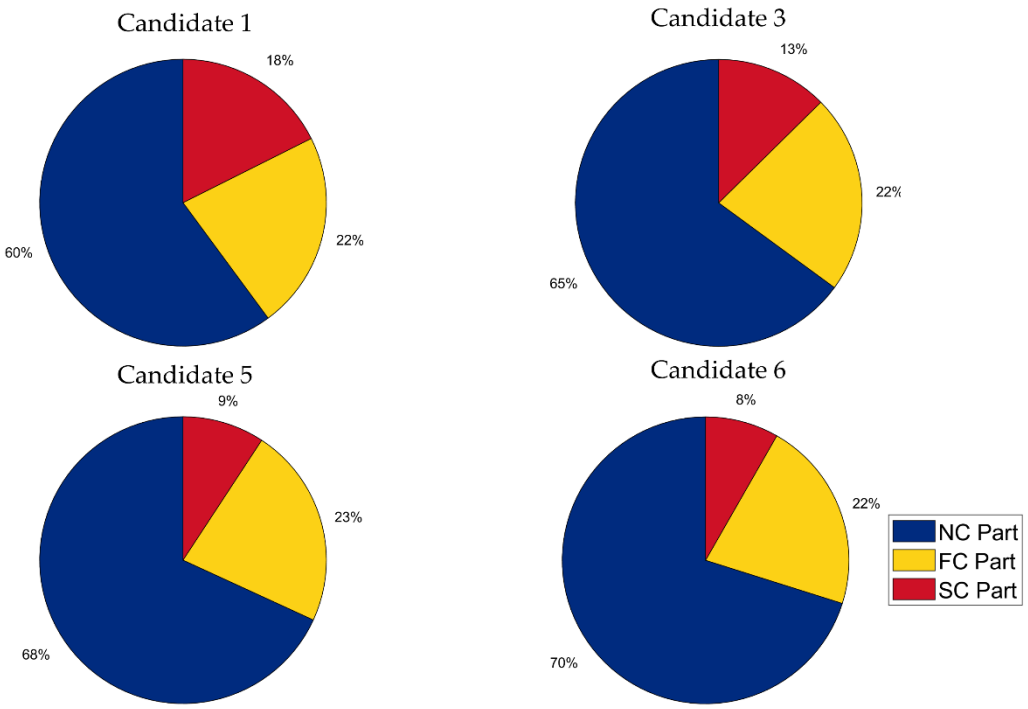

Figure A2.17. Contribution to the SVCM trace as presented in sec. 6.1.1.2.

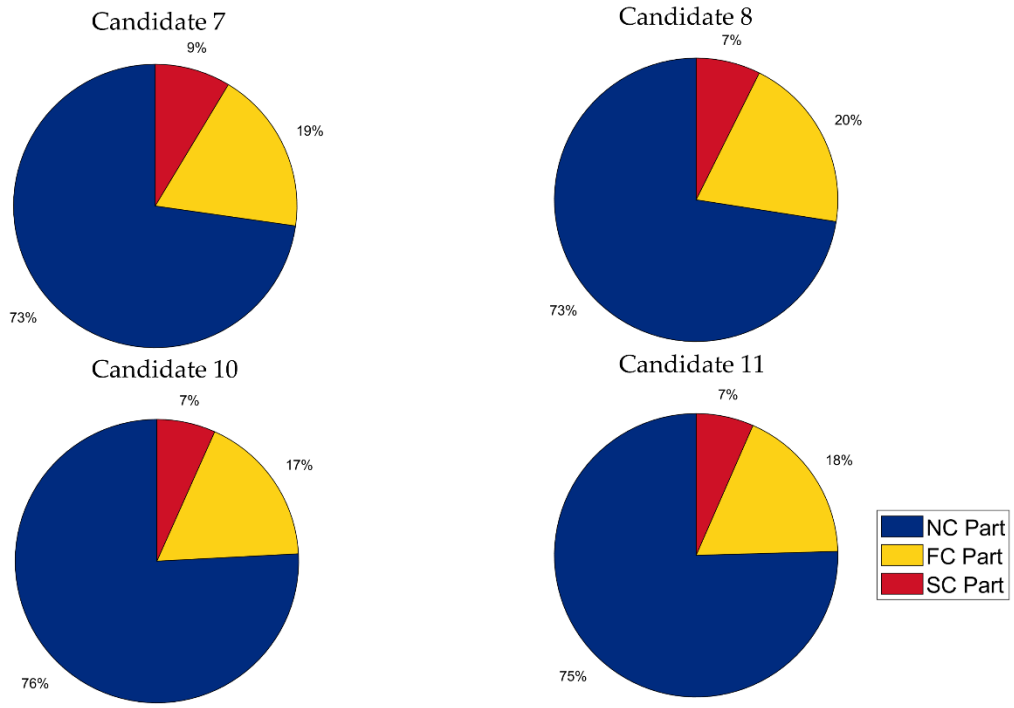

Figure A2.18. Contribution to the SVCM trace as presented in sec. 6.1.1.2.